Computer Simulations of Colloidal Fluids in Confinement

DISSERTATION

zur Erlangung des Grades
"Doktor der Naturwissenschaften"
am Fachbereich Physik, Mathematik und Informatik
der Johannes Gutenberg-Universität Mainz

vorgelegt von

Alexander Winkler

geboren in Koblenz

Mainz, Mai 2012

Alexander Winkler

Computer-Simulationen von Kolloidalen Fluiden in Beschränkten Geometrien

Kolloidale Suspensionen, die einen Phasenübergang aufweisen, zeigen eine Vielfalt an interessanten Effekten, sobald sie auf eine bestimmte Geometrie beschränkt werden, wie zum Beispiel auf zylindrische Poren, sphärische Hohlräume oder auf einen Spalt mit ebenen Wänden. Der Einfluss dieser verschiedenen Geometrietypen sowohl auf das Phasenverhalten als auch auf die Dynamik von Kolloid-Polymer-Mischungen wird mit Hilfe von Computer-Simulationen unter Verwendung des Asakura-Oosawa-Modells, für welches auf Grund der "Depletion"-Kräfte ein Phasenübergang existiert, untersucht.

Im Fall von zylindrischen Poren sieht man ein interessantes Phasenverhalten, welches vom eindimensionalen Charakter des Systems hervorgerufen wird. In einer kurzen Pore findet man im Bereich des Phasendiagramms, in dem das System typischerweise entmischt, entweder eine polymerreiche oder eine kolloidreiche Phase vor. Sobald aber die Länge der zylindrischen Pore die typische Korrelationslänge entlang der Zylinderachse überschreitet, bilden sich mehrere quasi-eindimensionale Bereiche der polymerreichen und der kolloidreichen Phase, welche von nun an koexistieren. Diese Untersuchungen helfen das Verhalten von Adsorptionshysteresekurven in entsprechenden Experimenten zu erklären.

Wenn das Kolloid-Polymer-Modellsystem auf einen sphärischen Hohlraum eingeschränkt wird, verschiebt sich der Punkt des Phasenübergangs von der polymerreichen zur kolloidreichen Phase. Es wird gezeigt, dass diese Verschiebung direkt von den Benetzungseigenschaften des Systems abhängt, was die Beobachtung von zwei verschiedenen Morphologien bei Phasenkoexistenz ermöglicht – Schalenstrukturen und Strukturen des Janustyps.

Im Rahmen der Untersuchung von heterogener Keimbildung von Kristallen innerhalb einer Flüssigkeit wird eine neue Simulationsmethode zur Berechnung von Freien Energien der Grenzfläche zwischen Kristall- bzw. Flüssigkeitsphase und Wand präsentiert. Die Resultate für ein System von harten Kugeln und ein System einer Kolloid-Polymer-Mischung werden anschließend zur Bestimmung von Kontaktwinkeln von Kristallkeimen an Wänden verwendet.

Die Dynamik der Phasenseparation eines quasi-zweidimensionalen Systems, welche sich nach einem Quench des Systems aus dem homogenen Zustand in den entmischten Zustand ausbildet, wird mit Hilfe von einer mesoskaligen Simulationsmethode ("Multi Particle Collision Dynamics") untersucht, die sich für eine detaillierte Untersuchung des Einflusses der hydrodynamischen Wechselwirkung eignet. Die Exponenten universeller Potenzgesetze, die das Wachstum der mittleren Domänengröße beschreiben, welche für rein zwei- bzw. dreidimensionale Systeme bekannt sind, können für bestimmte Parameterbereiche nachgewiesen werden. Die unterschiedliche Dynamik senkrecht bzw. parallel zu den Wänden sowie der Einfluss der Randbedingungen für das Lösungsmittel werden untersucht. Es wird gezeigt, dass die daraus resultierende Abschirmung der hydrodynamischen Wechselwirkungsreichweite starke Auswirkungen auf das Wachstum der mittleren Domänengröße hat.

Alexander Winkler

Computer Simulations of Colloidal Fluids in Confinement

Colloidal suspensions that exhibit a phase transition in the bulk show a wide spectrum of interesting effects when they are confined in geometries, such as cylindrical pores, spherical cavities or slit pores with planar walls. The influence of these various types of confinement on the phase behavior as well as on the dynamics of colloid-polymer mixtures is investigated by computer simulations using the Asakura-Oosawa model which describes the depletion force leading to phase separation.

In the case of cylindrical confinement an interesting phase behavior due to the system's quasi one-dimensional character is found. In the two-phase region the system is either filled with a polymer-rich or a colloid-rich phase when the system is confined to short cylindrical pores. However, when the length of the cylindrical pore exceeds a certain correlation length along the long axis, multiple quasi one-dimensional domains of the polymer-rich and colloid-rich phases start to form and coexist aside. These investigations help explain adsorption hysteresis curves of corresponding experiments.

When the colloid-polymer model system is confined to spherical cavities, the transition point from the polymer-rich to the colloid-rich phase is shifted. It is shown that this shift is a direct result of the wetting properties in the system and comes along with two different morphologies at phase coexistence – core-shell structures and Janus-type structures.

In the context of heterogeneous nucleation of crystals surrounded by liquid a new method to calculate wall surface free energies is developed. The results obtained for a hard sphere system and for a colloid-polymer mixture are used to derive contact angles for wall attached crystalline nuclei.

The phase separation dynamics in quasi two-dimensional systems after a quench from the homogeneous state into the demixed state is investigated by a mesoscale simulation method: The multi particle collision dynamics algorithm allows for a detailed study of the role of hydrodynamic interactions. The universal power law exponents of the domain growth dynamics known from the studies of strictly two- or three-dimensional systems are recovered for specific setups. The distinct dynamics perpendicular and parallel to the walls is studied as well as the influence of the solvent wall boundary condition. It is found that the screening of the effective hydrodynamic interaction range strongly modifies the domain growth behavior.

Parts of this work were published:

[1] D. Wilms, A. Winkler, P. Virnau & K. Binder, "Rounding of phase transitions in cylindrical Pores", *Phys. Rev. Lett.*, 105 (2010), 045701

[2] A. Winkler, D. Wilms, P. Virnau & K. Binder, "Capillary condensation in cylindrical pores: Monte Carlo study of the interplay of surface and finite size effects", *J. Chem. Phys.*, 133 (2010), 164702

[3] D. Wilms, A. Winkler, P. Virnau & K. Binder, "Monte Carlo simulations of the 2d-Ising model in the geometry of a long stripe", *Comput. Phys. Commun.*, 182 (2011), 1892

[4] K. Binder, P. Virnau, D. Wilms & A. Winkler, "Spurious character of singularities associated with phase transitions in cylindrical pores", *Eur. Phys. J. – Special Topics*, 197 (2011), 227

[5] D. Deb, A. Winkler, M.H. Yamani, M. Oettel, P. Virnau & K. Binder, "Hard sphere fluids at a soft repulsive wall: A comparative study using Monte Carlo and density functional methods", *J. Chem. Phys.*, 134 (2011), 214706

[6] D. Deb, D. Wilms, A. Winkler, P. Virnau & K. Binder, "Methods to compute pressure and wall tension in fluids containing hard spheres", *Int. J. Mod. Phys.* (2012)

[7] D. Deb, D. Wilms, A. Winkler, P. Virnau & K. Binder, "Monte Carlo studies of interfacial free energies in colloidal suspensions", *NIC Symposium 2012 Proceedings* (2012), 235

[8] D. Deb, A. Winkler, P. Virnau & K. Binder, "Simulation of fluid-solid coexistence in finite volumes: A method to study the properties of wall-attached crystalline nuclei", *J. Chem. Phys.*, 136 (2012), 134710

[9] A. Statt, A. Winkler, P. Virnau, & K. Binder, "Controlling the wetting properties of the Asakura-Oosawa model and applications to spherical confinement", *J. Phys.: Condens. Matter*, 24 (2012)

CONTENTS

CHAPTER

1

INTRODUCTION

Condensed matter physics belongs to the most fascinating branches in physics. It interconnects almost all the different parts of physics and even goes beyond physics providing connections to biology, medicine, mathematics and informatics. Two aspects are especially attractive. First of all, we are surrounded in our daily life by condensed matter in various phases (gases, liquids, liquid-crystals, crystals, etc.). The importance of materials with certain properties plays an outstanding role in our civilization (which is reflected by the names of some ages, like stone-age, bronze-age, etc.). Second, development of theories and, hence, the understanding of condensed matter is very challenging, but at the same time the formulation of the problem itself is very simple; consider, for example, hard spheres in a given volume which can be described by a single parameter, the packing fraction. In contrast to typical classical mechanics problems where a two or three particle problem is solved, in condensed matter physics one has to deal with macroscopic systems. Instead of single trajectories, quantities characterizing the system as a whole, like the temperature or the pressure, are in the focus of interest. The properties of condensed matter systems depend strongly on the microscopic details of the underlying particle interactions. However, in certain parameter ranges (critical regions) microscopically different systems behave identical with respect to specific quantities which leads to universality concepts allowing for the classification of all the various system types.

A special role in condensed matter physics play the so-called soft matter systems. In comparison to simple molecules they consist of large constituents between nm and several μm. Typical examples are colloids and polymers or mixtures of those components which are dispersed in a solvent. The term “soft” reflects the fact that, for instance, colloidal crystals are very easy to deform in comparison to molecular crystals. Colloids are particles (typically sphere- or rod-like) that are dispersed in a solvent and are much larger than the solvent molecules but still are small enough to be affected by thermal motion[1]. The terminus “colloid” goes back to the year

---

[1] An observation of thermal motion depends strongly on the timescales at which the observation

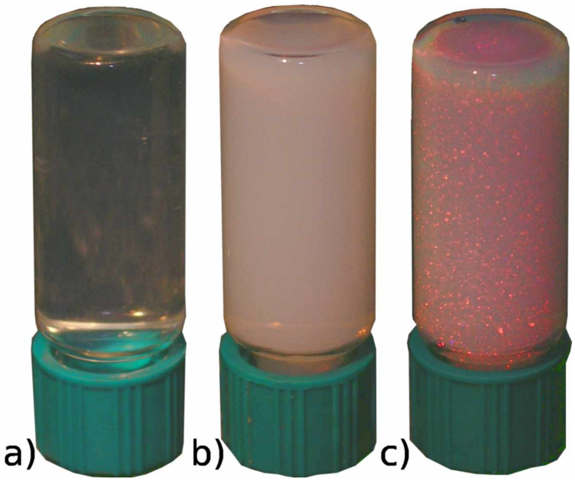

Figure 1.1: Gas (a), liquid (b), and crystalline (c) phase of a colloidal suspension containing charged colloidal spheres in deionized water. The pictures of these samples were kindly provided by Prof. Palberg, Komet 336, Johannes Gutenberg-Universität Mainz.

1861 when Thomas Graham distinguished between crystalloids which could pass a membrane and colloids which did not but were "glueing" at the membrane[2] [10]. Nowadays, we see colloids in a broad variety in our daily life such as milk, foams, gels, hand creme, etc. Another important area for colloidal research are industrial applications, for instance, colloidal ink, enamels or the enhancement of bullet proof clothes by colloid coating (causing shear thickening). Colloidal systems can also be regarded as models for molecular systems since they have a lot in common like phase transitions and critical phenomena (for instance, critical slowing down can be studied for systems such as colloid-polymer mixtures). However, in contrast to molecular systems, colloids can be observed easily due to their relatively large size (by light scattering or directly by confocal microscopy methods). Typical time scales range from microseconds up to seconds or beyond [11–13]. Apart from their role as models for atomistic systems, colloids also possess properties which do not exist in molecular systems caused by the various almost freely designable interaction potentials and very slow dynamics (for example in the case of gels).

The interactions of colloids can be tuned by grafting polymers or DNA to the surface or by screening their charges when adding salt to the dispersion. The interaction can also be tuned indirectly or effectively by admixing polymers to the system. This technique leads to an effective force, the so-called depletion force, whose range is controlled by the typical size of the polymers and whose strength depends on the amount of admixed polymers. This class of colloid-polymer mixtures is the main topic considered in this thesis. But it is not only possible to modify the interaction potentials among the colloidal particles, one can also create anisotropic compounds such as ellipsoids, colloidal polymers, tetrapods [14–16], etc. The variety of interactions and particle shapes enables scientists to obtain a highly complex phase behavior of such systems, ranging from gases and liquids (see Fig. 1.1a,b) over liquid-crystals and crystalline structures (see Fig. 1.1c) to macrostructure formations, micelles, etc. [17]. Furthermore, some methodologies of colloidal and polymer physics have a direct link to biology such as the investigation of bacteria [18–20], folded proteins [21], membranes [22, 23] or red blood cells [24].

The colloidal systems under consideration in this work are investigated by means of computer simulations. The history of computer simulations in the field of statistical

---

takes place.

[2] The Greek word $\kappa o \lambda \lambda \alpha$ stands for "glue".

physics is rather short. In the 50$^{\text{th}}$ of the last century METROPOLIS et al. [25] introduced the Metropolis Monte Carlo method. By creating random but Boltzmann weighted configurations of classical many particle systems they were able to show that it is possible with this method to calculate properties of a two-dimensional hard sphere system such as the pressure. Almost at the same time ALDER and WAINWRIGHT introduced the Molecular Dynamics simulation method [26–28]. Based on classical interaction potentials among the particles the phase space trajectory of each component is calculated using Newton's equations of motions. While the Metropolis Monte Carlo scheme samples the configuration space in a stochastic manner, in Molecular Dynamics simulations the trajectories of the individual particles are resolved in phase space. The initially questionable success of this kind of numerical investigations developed to become a well established part in the field of statistical mechanics and coexists aside theoretical and experimental studies. The main input into computer simulations of this kind is the precise knowledge of the particle interactions. Effects occurring in experiments such as polydispersity, impurities or particle shape anisotropy, can be excluded or separately investigated to clarify the exact origin of the macroscopic properties of the system under examination. Research in physics with the help of computer simulations is nowadays a two-fold challenge. On the one hand, one has to develop algorithms which describe correctly the considered physical problem and, on the other hand, one has to overcome restrictions due to the hardware regarding the system size and time scales. The latter aspect is typically addressed by the usage of highly parallel computer architectures which goes along with the very challenging development of the appropriate simulation software.

The main focus in this work lies on the investigation of models for colloid-polymer mixtures under various types of confinement by computer simulations. In general, a strongly confined system which is capable to undergo a phase separation into two coexisting phases shows an interplay between surface effects, e.g. wetting phenomena, finite size effects (the correlation length is typically restricted by the confinement) and effects related to the phase separation. Colloid-polymer mixtures are well suited to address the effects of the confinement since they allow, on the one hand, for a controlled and well understood setup of their bulk phase behavior and, on the other hand, the typical system sizes are in the order of μm for which the fabrication or setup of the confining geometry (e.g. parallel glass plates) is achievable with the desired precision. However, this kind of soft matter systems can be also regarded as a model for systems on the molecular or atomistic length scale which is especially expedient in the vastly growing research field of nanoconfinement or nanomaterials. Since almost a decade we are in touch with nanomaterials in our daily life in creams, sprays and even in our food. Especially the influence of nanoparticles on our health is a current debate [29]. The research and understanding of extremely confined systems is hence, a basic and pertinent necessity.

Outline

The investigation of equilibrium and non-equilibrium properties of colloidal suspensions is a highly challenging and complex task from the theoretical, experimental and computer simulations point of view. A crucial input for a successful investigation via computer simulations is a well defined model system and proper methodological and algorithmical approach. Chapter 2 introduces briefly the model system and Monte

Carlo simulation techniques which are used for the determination of equilibrium properties based on the calculation of free energy landscapes. A major attribute of computer simulations in general is the finite system size. Although thermodynamic fluctuations are in principal fully included in the mentioned simulation techniques, which is a great advantage over e.g. mean field theories, the finite system size limits the occurring maximum fluctuation amplitude, which leads to a rounding of phase transition properties in critical regions. Chapter 3 focuses on these effects and demonstrates how it is possible by the theory of finite size scaling to make predictions about the thermodynamic limit of critical properties of colloid-polymer mixtures in the bulk. From then on the influence of various confining geometries on the phase behavior is investigated. Colloid-polymer model mixtures confined between planar walls were successfully studied recently [30–32] and interesting and intricate behavior is found such as a crossover of the critical behavior from a two-dimensional character to a three-dimensional character or the interface localization transition when the walls inequivalently favor one of the particle species. Chapters 4 and 5 address the confinement in still lower dimensions. Chapter 4 focuses on colloid-polymer mixtures in quasi one-dimensional cylindrical pores, particularly the phase behavior close to critical regions when changing the length of the cylindrical tube. In chapter 5 the influence of spherical cavities on the phase transition behavior is studied. The role of the system size as well as the interplay with the wetting behavior is under investigation here.

One of the first models under investigation by computer simulations was the hard sphere model [26]. Despite its simplicity and thereby resulting suitability as a non-trivial reference system in the context of statistical mechanics, experiments on colloidal hard sphere systems are attainable and accomplishable. This simple and extensively studied system is still a topic in modern science, since not all of its properties are fully understood, as for example the equation of state [33], its wetting properties [34] or related aspects of heterogeneous nucleation of the crystalline phase. The latter aspect of heterogeneous nucleation at planar walls is addressed for hard sphere systems and colloid-polymer mixtures in chapter 6.

While in the chapters mentioned so-far static equilibrium properties of colloid-polymer model systems are investigated, eventually, the later chapters of this thesis explore the topic of non-equilibrium dynamics. When transport properties of the colloidal dispersion are considered, the solute starts to play a major role. Even before GRAHAM's introduction of the colloid nomenclature, ROBERT BROWN discovered that pollen grains show an erratic motion when suspended in a medium. In the beginning of the 20th century Brownian motion was extensively studied and finally understood as the imbalance between collision events of molecules on both sides of the suspended fluid particle [35–37]. The situation becomes complex when multiple fluid particles are present. Their motion in the solvent is influenced by each other due to hydrodynamic interactions. Although the suspended colloidal particles may have a short range hard sphere interaction, when moving they generate dynamical many-body forces among each other through the solvent. The large gap in time and length scales between the solvent molecules ($\sim 10^{-10}m$) and the embedded fluid compounds ($\sim 10^{-8}m - 10^{-6}m$) makes it impossible to use the well-established Molecular Dynamics simulation technique for colloidal suspensions when focusing on the solvent influence. Instead, mesoscale simulation techniques are required, which means that the solvent is treated in a coarse grained and hence computational less expensive way, typically directly related to the Navier-Stokes equations, while for the fluid particles the Molecular Dynamics framework is applied. Chapter 7 gives a detailed introduction on such a mesoscale method, the Multi Particle Collision Dynamics algorithm, which is used to study full non-equilibrium properties of colloid-polymer mixtures. The technique allows for the detailed study of the influence of certain solvent properties on the dynamics. In chapter 8 the spinodal decomposition of binary colloid-polymer mixtures in thin films (quasi two-dimensional systems) is addressed with the focus on hydrodynamic interactions with respect to the demixing dynamics. It can be shown that the underlying universal power law behavior of the phase separation dynamics is distinctly altered when including hydrodynamic interactions and even more that the solvent boundary conditions are related to the hydrodynamic interaction range which strongly influences the observed spinodal decomposition kinetics.

In collaboration with the group of ERIC LUIJTEN (Northwestern University of Chicago) systems of anisotropic particles with tetrapod morphology were investigated with regard to their phase behavior. The results of this study can be found in appendix A.

CHAPTER

2

MODEL AND BASIC ALGORITHMS

This chapter is meant to introduce the model system and basic algorithms which are commonly used throughout the thesis. The description of certain extensions and more specific algorithms are deferred to the corresponding chapters.

2.1. The Asakura-Oosawa Model

When studying a particular system in nature (or experiment) by means of theory, it is clear that not all the details of the system can be taken into account. A *model* is needed which has to be as simple as possible but still describes the basic and important properties. Asakura and Oosawa proposed such a model (AO model) to study a binary mixture of spherical colloids and polymers [38, 39] which was later analyzed by Vrij [40]. In this model, colloids and polymers are represented as spheres. Colloids are hard with respect to each other as well as with respect to the polymers. The polymer-polymer interaction is set to zero, which allows them to overlap without any energy costs. Such simple pair interactions can be regarded as a coarse grained model for colloids and polymers. The conformational degrees of freedom of the polymers are neglected assuming that the polymers are in a loose globular state so that they can easily penetrate each other but not the hard sphere-like colloids.

This purely entropic model leads to an effective attractive interaction between the colloids caused by the depletion force [41]. This force results from the increase of the number of microstates Ω in the system at fixed internal energy E [$S(E) = k_B \ln(\Omega(E))$] due to overlaps of so-called depletion zones. A depletion zone is defined as the volume which a center of a polymer is not allowed to enter due to the presence of the colloid, see figure 2.1. The interaction model has a single parameter, the ratio between polymer and colloid radius $q = r_p/r_c$. This parameter as well as the concentrations of both particle types determine the system properties.

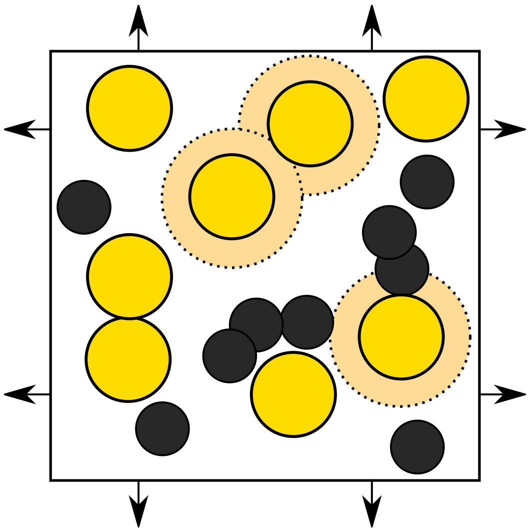

Figure 2.1: Schematic representation of the Asakura-Oosawa model in a simulation box with periodic boundary conditions. The colloids are represented as big yellow circles, the smaller polymers are drawn in black. The bright yellow zones around the colloids are the depletion zones.

2.2. Extensions of the Asakura-Oosawa Model

The Continuous Asakura-Oosawa Model The AO model and also other types of hard particle models do not allow to integrate out Newton's equation of motion based on the derivative of the interaction potential. Additionally, the fact that polymers do interact among each other is far away from reality, a more realistic but still simple interaction potential is desirable. Zausch et al. proposed the so-called *continuous* AO model [42] addressing the issues mentioned above. The hard sphere pair interactions are replaced by Weeks-Chandler-Andersen (WCA) potentials [43–45] which are truncated and shifted Lennard-Jones potentials:

$$U_{\mathrm{WCA}}(r;\sigma,\varepsilon) = \begin{cases} 4\,\varepsilon\left[\left(\frac{\sigma}{r}\right)^{12} - \left(\frac{\sigma}{r}\right)^{6} + \frac{1}{4}\right] & \text{, for } r < r_c = 2^{1/6}\sigma \\ 0 & \text{, else} \end{cases} . \tag{2.1}$$

Here, r is the distance between two particles, σ is the pair interaction range and ε is the interaction amplitude. At $\varepsilon \approx 1$, the WCA potential has the property to approximate to quite a high degree a pure hard sphere interaction. In the original proposal a smoothing function was used which leads to an analytic behavior of U_{WCA} at $r = r_c$. The resulting benefit of a higher accuracy in microcanonical Molecular Dynamics studies will not be exerted within the context of the problems addressed in this thesis, since stochastic thermostating methods are used.

In contrast to the original AO model, the polymer-polymer interaction is extended to an effective potential [46] which allows for a complete overlap of two polymers, however, with an energy penalty:

$$U_{\mathrm{pol}}(r;\sigma,\varepsilon) = \begin{cases} 8\,\varepsilon\left[1 - 10\left(\frac{r}{2^{1/6}\sigma}\right)^{3} + 15\left(\frac{r}{2^{1/6}\sigma}\right)^{4} - 6\left(\frac{r}{2^{1/6}\sigma}\right)^{5}\right] & \text{, for } r < 2^{1/6}\sigma \\ 0 & \text{, else} \end{cases} . \tag{2.2}$$

The parameters for the amplitudes and the radii are chosen the same as by Zausch et al. as $\sigma_{cc} = 1.0$, $\sigma_{cp} = 0.9$, $\sigma_{pp} = 0.8$ and $\varepsilon_{cc} = 1.0$, $\varepsilon_{cp} = 1.0$, $\varepsilon_{pp} = 0.0625$. The

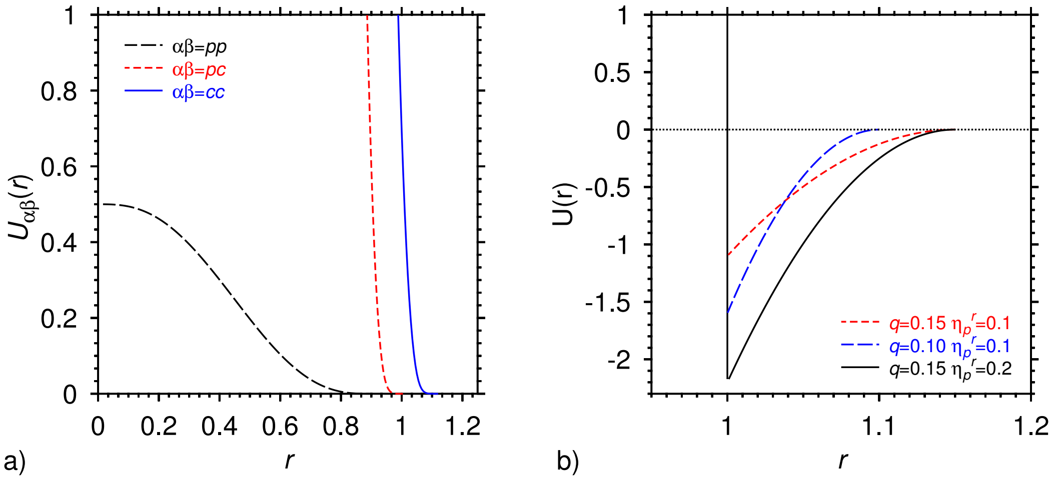

Figure 2.2.: (a) Pair interaction potentials of the extended AO model as a function of distance r. Here, $U_{cc}(r) = U_{\mathrm{WCA}}(r;1,1)$, $U_{cp}(r) = U_{\mathrm{WCA}}(r;0.9,1)$ and $U_{pp}(r) = U_{\mathrm{pol}}(r;0.8,0.0625)$. (b) Effective Asakura-Oosawa pair potential for various polymer-colloid diameter ratios q and polymer reservoir packing fractions η_p^r as indicated.

resulting behavior of the pair potentials is shown in figure 2.2. From the plot it is clear that forces can now be derived via $\boldsymbol{F}_i = -\nabla U_i$, but nevertheless due to the steep descent in the WCA potentials a relatively small Molecular Dynamics time step will have to be chosen when studying the dynamics of this model (see chapter 8). The continuous AO model (CAO) behaves very much the same in comparison to the original AO model. In the plane of extensive variables (η_p, η_c) the bulk phase diagrams of both models fall almost on top of each other [42].

The Effective Asakura-Oosawa Model Based on the original formulation of the AO model there exist further extensions and modifications. Especially for computer simulations so-called effective AO models are attractive. For a polymer-colloid diameter ratio $q < 0.156$ it is possible to integrate out exactly the polymer degrees of freedom [47], so that only the colloid particle species has to be explicitly simulated[1]. The result is an effective hard-core potential with an attractive well

$$U_{\mathrm{EffAO}}(r) = \begin{cases} \infty & \text{, for } r \in [0,\sigma) \\ -\eta_p^r \frac{(1+q)^3}{q^3}\left(1 - \frac{3r}{2(1+q)\sigma} + \frac{r^3}{2(1+q)^3\sigma^3}\right) & \text{, for } r \in [\sigma, \sigma(1+q)] \\ 0 & \text{, else.} \end{cases}$$

Here, σ is the colloid diameter, q is the ratio between the polymer diameter and the colloid diameter and η_p^r is the polymer reservoir packing fraction. The potential is shown in figure 2.2 for three different parameter sets. For the parameter choice of $q = 0.15$ and $\eta_p^r = 0.1$ the effective AO model was studied recently [49]. The phase diagram shows a transition from a colloidal liquid to a crystalline phase. The effective AO model will be studied in chapter 6 under the aspect of heterogeneous nucleation of crystals.

---

[1] For $q > 0.156$ there exist approximate versions of effective AO potentials [48].

2.3. Boundary Conditions

The boundary conditions are one of the most crucial aspects of computer simulations. Due to the limited amount of memory and operations per second a computer can perform, the simulated system is always restricted to a finite size and is in practice often very small in comparison to experimental setups. Periodic boundary conditions can be used in order to mimic large systems (two different realizations are presented below), but here, especially walls are in the main focus. Apart from a simple restriction in terms of the system size (and, hence, correlation lengths) walls represent an interface and, therefore, interesting phenomena such as wetting and heterogeneous nucleation appear. Understanding the interplay of these effects with the bulk phase behavior is a challenging problem.

2.3.1. $\mathcal{C}^3$ Boundaries

The label $\mathcal{C}^3$ from the title of this section stands for the Euclidean space with periodic boundary conditions, which simply means that a particle which leaves its simulation box, for instance, to the right, is entering the box from the left again. More formally, one can write $r_\alpha \to r_\alpha - \mathrm{sign}(L_\alpha, r_\alpha)$, where $\alpha \in \{x, y, z\}$, $\mathrm{sign}(\cdot,\cdot)$ returns the first argument with the sign of the second argument and L_α represents the linear dimensions of the cuboid simulation box. At first sight, this seems to model the infinite space since a particle can move as "far" as it wants. However, after considering interactions, it becomes clear that this is not the case. A particle can "feel" itself when the simulation box is shorter than the correlation length. This is exactly the reason why in finite systems with $\mathcal{C}^3$ boundary conditions a phase separation is observed in supercritical regions (in terms of the temperature, also see section 3.3).

2.3.2. $\mathcal{S}^3$ Boundaries

Periodic boundary conditions can also be applied to confine particles on the surface of a four-dimensional hypersphere $\mathcal{S}^3$, which is a closed, homogeneous, isotropic but curved three-dimensional space. This space combined with computer simulations was introduced by Caillol and Levesque [50, 51] to handle long range interactions of Coulombic systems as well as Lennard-Jones systems [52]. The condition for such a confinement is $w^2 + x^2 + y^2 + z^2 = R^2$, where $\boldsymbol{r} = \{w, x, y, z\}$ is the four-dimensional position vector of a particle and R is the radius of the hypersphere. The geodesic length, defined as $r_{ij} = R \arccos(\boldsymbol{r}_i \cdot \boldsymbol{r}_j / R^2)$, is the measure of distance. The big advantage of this special geometry is that no periodic images are present in it. This property means a great simplification for studying long range forces in contrast to the Euclidean space in which the computationally relatively expensive Ewald summation is used to provide a proper contribution of periodic images to the internal energy. Another advantage of the $\mathcal{S}^3$ boundaries is the isotropy of the space which leads to the fact that mirror reflections of anisotropic structures at planes, for instance, become self inverse (which is not the case in $\mathcal{C}^3$). The disadvantage of $\mathcal{S}^3$ is the curvature of the space, which gives rise to an additional finite size effect. Furthermore, it is not straightforward what the interaction potentials look like on a hypersphere surface. Solving the Poisson equation for point charges in $\mathcal{S}^3$ space

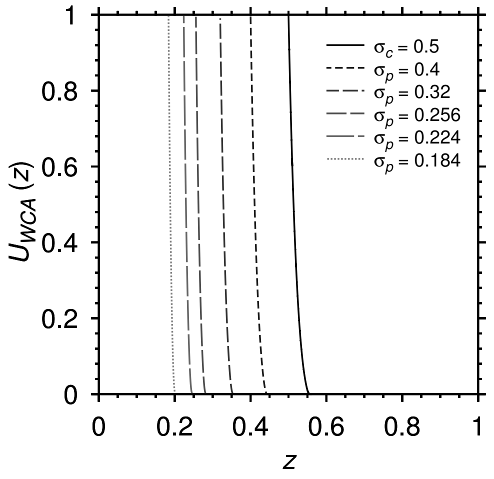

Figure 2.3: WCA wall potentials for different choices of the interaction range parameter σ_p. The wall is located at $z = 0$. The full line shows the potential a colloid feels near the wall, while the dashed lines show different choices of wall potentials acting on polymers.

or in $\mathcal{C}^3$ space leads to completely different pair interactions [53]. Studies involving the $\mathcal{S}^3$ boundary conditions are presented in appendix A.

2.3.3. Walls

In the context of this thesis, a very essential boundary condition is represented by walls. Rather than feeling periodic images the particles now interact (in a certain direction) with walls via a wall potential U_w. Walls introduce a new interface and, hence, an interfacial tension. A state of two phase coexistence confined by walls can result in a contact line (depending on the wetting properties). Furthermore, flat walls for instance induce order in gases, liquids, etc. resulting in layering effects. As a small appetizer for studies presented in the later chapters and as an illustration of these effects, various canonical simulations of the continuous AO model confined between two planar walls were performed. As wall potential the Weeks-Chandler-Anderson (WCA) potential is used with interaction amplitude $\varepsilon = 1$ and various choices of σ shown in figure 2.3. While the colloid-wall interaction was the same in all canonical simulations the polymer-wall interaction was varied from $\sigma_p = 0.4$ down to $\sigma_p = 0.184$ where the unit length scale is set by colloid diameter $\sigma_c \equiv 1$.

This asymmetric treatment of the particles with respect to the walls does not only have a big influence on the fluid layers close to the walls but influences such properties as the shape of the coexistence interface as well as the contact angle at the wall. The visualization of the latter effect is given in figure 2.4 by density contour plots. There, walls are present perpendicular to the z-axis at $z = \pm 6$, while in the x- and y-direction periodic boundary conditions were applied.

The curvature of the interface changes when varying the polymer-wall interaction and one can even recognize a change from complete wetting (note the colloid wetting layer for $\sigma_p = 0.4$) to partial wetting (all the other values of σ_p). Of course, this is not a rigorous study of the wetting behavior since strong finite size effects are present, but rather gives a first feeling for the differences of a confined system in comparison to the bulk and at the same time anticipates the topic of wetting and contact angles of wall attached nuclei both for liquids and gases of colloid-polymer mixtures (see chapter 5) and crystalline clusters (see chapter 6).

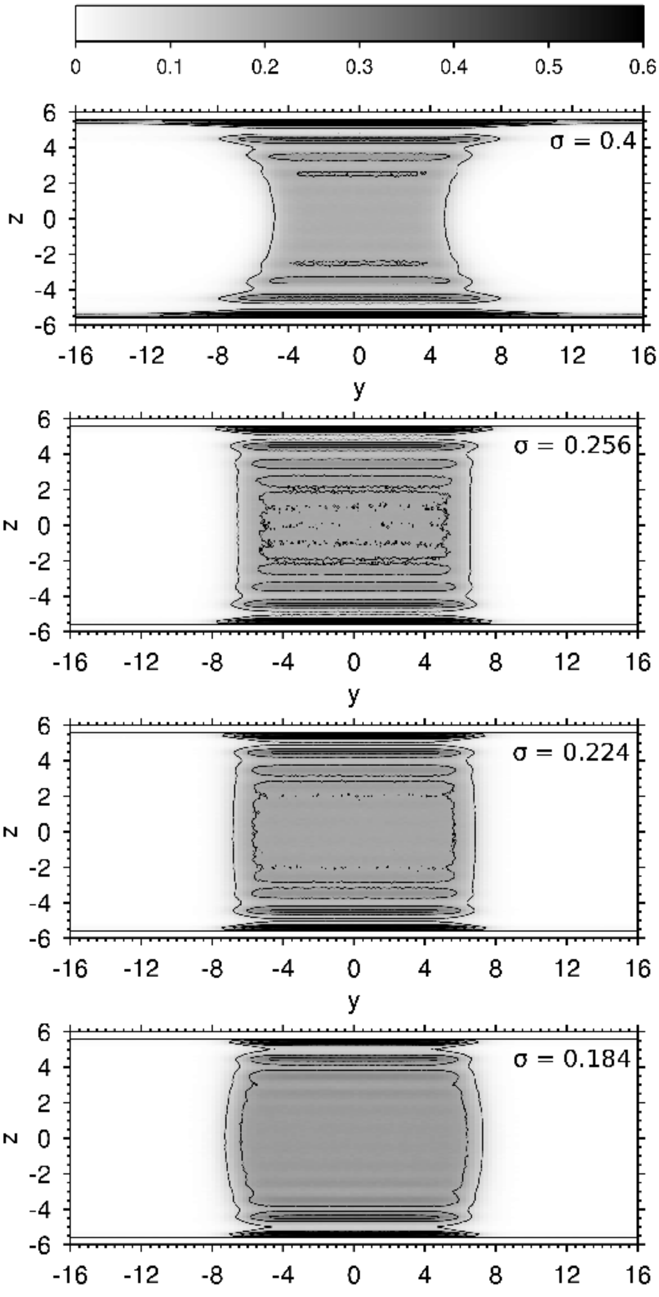

Figure 2.4.: Different planar density profiles for colloids (dark area) and polymers (bright area) in a slab geometry. The plots differ by the applied wall-polymer potential, indicated by the polymer interaction range parameter $\sigma_p = 0.4$, 0.256, 0.224, 0.184. To get a reasonable colormap, the data points were normalized by their maxima. Note the pronounced layering in the colloid-rich phase which is induced by the planar walls and can persist even in the center region (see $\sigma_p = 0.256$).

2.4. Basics of Monte Carlo Simulations

A Monte Carlo simulation solves a certain problem in a stochastic manner using random numbers. The results always have a statistical error and differ typically within this error when using different series of random numbers. One has to stress that this statistical error is not a problem of the method but in fact its strongest feature, since it is well under control (running the simulation longer will improve the statistics) and in contrast to other methods typically no systematical errors exist.

Within the context of equilibrium statistical mechanics a Monte Carlo simulation follows a stochastic trajectory in phase space in order to estimate certain quantities, for instance, thermal averages of observables. The efficient generation of a correct stochastic trajectory is the main aim of the simulation. There exist several rules how such a trajectory has to be constructed which are introduced within the next paragraphs.

In the following, a system with a discrete set of states $\{S_i\}$[2] (representing for instance a lattice site model) and a continuously treated Monte Carlo time t is considered. A continuity equation, the so-called master equation, describes the balance between a probability flux leaving a state S_j and leading into state S_j

$$\frac{dP(S_j,t)}{dt} = \sum_i W_{ij} P(S_i,t) - \sum_i W_{ji} P(S_j,t) \ . \tag{2.3}$$

Here, W_{ij} are the transition probabilities to go from state S_i to state S_j where it is assumed that the sequence of states $\{S_1, S_2, ...\}$ is a *Markov chain.* This means that state S_i can be generated from its predecessor without any knowledge of the trajectory of earlier states (such a generation of a state is called from now on Monte Carlo move). In thermal equilibrium the condition $\frac{dP(S_j,t)}{dt} = 0$ and thus $\sum_i W_{ij} P(S_i,t) - \sum_i W_{ji} P(S_j,t) = 0$ has to hold. The condition which certainly fulfills this statement is the *rule of detailed balance*

$$\frac{W_{ij}}{W_{ji}} = \frac{P(S_j)}{P(S_i)} \ . \tag{2.4}$$

In the canonical ensemble the probability to find the system in the states S_i with energy E_i is

$$P(S_i) = \frac{1}{\mathcal{Z}} e^{-E_i/k_B T} \ , \tag{2.5}$$

with $\mathcal{Z} = \sum_{\text{all states}} e^{\mathcal{H}/k_B T}$. The partition function $\mathcal{Z}$ is not needed since it cancels out when considering probability ratios. Metropolis et al. proposed in 1953 the following transition rate which fulfills equation 2.4:

$$W_{ij} \ = \ \begin{cases} e^{-(E_j - E_i)/k_B T} & , \ E_j - E_i > 0 \\ 1 & , \ E_j - E_i \leq 0 \end{cases} ,$$

Every move which lowers the energy is always accepted, moves which raise the energy are only accepted with a probability of $e^{-(E_j - E_i)/k_B T}$. With this technique

---

[2] A discrete set of states is used to simplify the notation but can be easily extended to a continuous set of states.

states are generated with the correct Boltzmann weight (see Eq. 2.5) and, therefore, an observable O in the canonical ensemble can be estimated by simply taking an arithmetic average

$$\langle O \rangle = \sum_{i=1}^{n} O_i$$

for a sufficiently large number of Monte Carlo steps n.

In the case of a system with particles which can move continuously through space the canonical Monte Carlo move is undertaken via changes in the particle position. The following algorithm shows a possible implementation.

Ordinary Translational Move

1. Choose a particle at random.
2. Generate a trial translation vector $\boldsymbol{t}$ with components randomly drawn from the interval $[-\Delta, \Delta]$, where Δ is the maximal translational amount determining the efficiency of the move.
3. Update the particle position $\boldsymbol{r} \to \boldsymbol{r} + \boldsymbol{t}$.
4. Calculate the energy difference $\Delta E = E_{\text{new}} - E_{\text{old}}$.
5. Generate a random number $g \in [0, 1)$.
6. Accept the move, if $g < \exp(-\Delta E / k_B T)$, otherwise, restore the old position.

Note that the first step is crucial to fulfill the detailed balance condition. A sequential update of all particles would not obey this rule since the probability that the reverse move for the same particle appears is zero. See reference [54] for details about the weaker “global balance” condition which still produces correct Monte Carlo results.

2.5. Cluster Moves

In contrast to ordinary single particle moves, cluster moves are able to explore the phase space much faster (in terms of CPU time) by handling not only a single particle but many within the same Monte Carlo step. There exists a rich collection of cluster moves in the literature that are very useful for lattice simulations [55–57]. The cluster moves developed by VINK et al. and LIU et al. are extremely helpful for simulations in the continuum, especially for binary mixtures [58–61]. The following sections introduce these cluster moves and possible modifications in detail.

2.5.1. Rejectable Canonical Cluster Moves

The idea of a canonical cluster move for a binary mixture of hard particles is very intuitive, especially when one type of particles, acting as a structureless component,

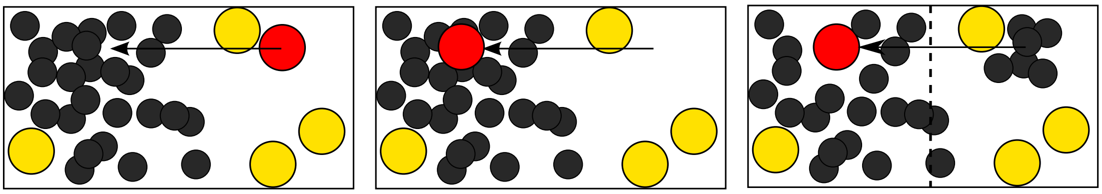

Figure 2.5.: Schematic illustration of the three steps of the rejectable cluster move for the translation: colloid selection, colloid translation, polymer mirror reflection at a plane perpendicular to the translation vector. In this example the move is accepted.

is only introduced for creating an effective depletion interaction, as e.g. the polymers in the Asakura-Oosawa model. Imagine the extreme case of a single colloid in a dense bath of ideal polymers. Despite dynamical effects, the colloid has to drift freely in a Monte Carlo simulation through the dense fluid of polymers. There exists a simple way to achieve this in a Monte Carlo simulation: when a colloid is moved and (illicitly) intersects with several polymer spheres, these polymers are removed and put into the empty space the colloid left at its original position. An obvious way to perform this is to apply to the polymers a simple mirror reflection at the center of the colloid translation vector. The situation becomes more difficult in the case of an arbitrary number of colloids. In this case, point reflected polymers could intersect with another colloid, and then the whole move has to be rejected. Note that the rejectability is a very important ingredient to this type of cluster move since it always allows for an improvement of the simulation speed in comparison to ordinary canonical moves regardless of the system's density. Additionally, one should note that this move is completely ergodic since in the case of a small translation it reduces to the ordinary canonical translation.

Figure 2.5 shows a modified version of this cluster move in the case of non-periodic boundary conditions, in a cylindrical confinement. Here, instead of a point reflection, a mirror reflection at the plane perpendicular to the cylinder axis is used. Furthermore, the x- and y-coordinates of the moved colloid are kept constant to ensure that the polymers do not leave the cylindrical simulation box [1, 2]. This move is not ergodic anymore, so it has to be combined with ordinary canonical moves or any type of moves that allows for a change in the x- and y-coordinates of the colloid.

2.5.2. Rejection Free Canonical Cluster Moves

The next logical step after the rejectable cluster move proposed in the previous section is to continue the mirror reflection of particles until there is no overlap anymore. This leads to a rejection free cluster algorithm proposed by Dress and Krauth [58]. This original formulation is limited to hard particle interactions. A great improvement was made by Liu and Luijten, who developed an extension of this algorithm to arbitrary potentials [59, 60], called the "Geometric Cluster Algorithm", providing an analog to the Wolff cluster algorithm for lattice gas simulations. The algorithm can be formulated as follows:

Geometric Cluster Algorithm

1. Choose a “seed” particle at random.
2. Choose a self inverse symmetry transformation $\mathcal{T} = \mathcal{T}(\boldsymbol{c})$, where $\boldsymbol{c}$ contains all the coordinates of the particle.
3. Add the seed particle to a queue, called in the following “the cluster“. Every particle i in the cluster has two configurations to be considered, $\boldsymbol{c}_i$ and $\boldsymbol{c}_i' = \mathcal{T}(\boldsymbol{c}_i)$.
4. Consider another particle j. Add it to the cluster with probability $P_{ij} = \max\{0, 1 - \exp(-\beta\Delta E_{ij})\}$, where $\Delta E_{ij} = E(\boldsymbol{c}_i', \boldsymbol{c}_j) - E(\boldsymbol{c}_i, \boldsymbol{c}_j)$.
5. Repeat step 4 for all particles which are not already a part of the cluster.
6. Repeat step 5 as long as the cluster grows, after that replace the coordinates $\{\boldsymbol{c}_i\}$ of all particles in the cluster by $\{\boldsymbol{c}_i'\}$, respectively.

Some comments about the algorithm are necessary. The choice of an array of coordinates $\boldsymbol{c} = \{c_1, c_2, \ldots, c_n\}$ rather than just the ordinary position $\boldsymbol{r} = \{r_x, r_y, r_z\}$ is made to point out the handling of anisotropic particles, which can consist of more than one molecule or have directors specifying their orientation. Furthermore, one could even include in $\boldsymbol{c}$ the simulation box label in the case if particles are moved from one simulation box to another, like in the restricted Gibbs ensemble (see appendix A). The self inverse symmetry transformation can be, for instance, reflections at an *arbitrary* point or plane or reflections at a *certain* point or a plane (biased moves). The highest performance of the algorithm is reached in the case of fluids containing different components of large size ratio. The performance breaks down when the system's volume fraction becomes too high, since then almost all particles are considered to be a part of the cluster and the computational expensive symmetry transformation $\mathcal{T}$ only leads to small changes in the configuration.

2.5.3. Grand Canonical Cluster Moves

While canonical moves have a tunable parameter – the maximum translational amount – which guarantees that configurations differ at least after a certain number of Monte Carlo steps, grand canonical particle insertion and particle deletion moves do not have such a parameter. So, it can happen (especially for hard particles and high densities) that even after millions and millions of MC steps no single insertion/deletion move is accepted. This shows how essential and important grand canonical cluster moves are for studying hard particle systems in the grand canonical ensemble.

The grand canonical cluster moves used in this thesis were developed by VINK and HORBACH [42, 61]. The basic idea of these moves is to swap the configuration of a single colloid with the random configuration of multiple polymers. Figure 2.6 illustrates schematically how the cluster move works. The figure can be read in both directions. The colloid insertion (read the figure from the left to the right) works as follows. The leftmost picture shows a dense polymer configuration in which a colloid

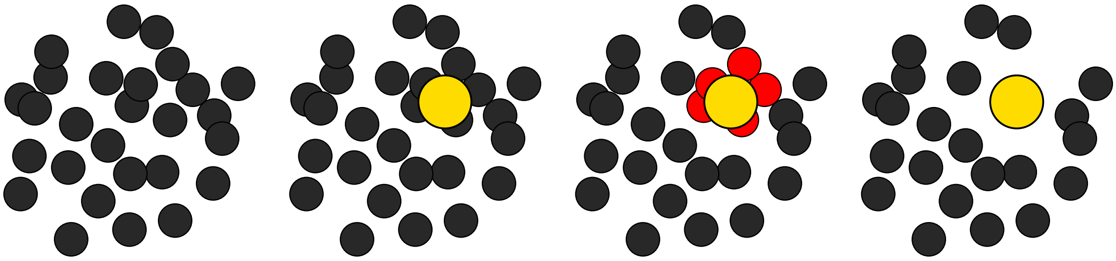

Figure 2.6.: Schematic illustration of the four steps of the grand canonical cluster move. The order of steps from the left to the right corresponds to the insertion of the colloid, from the right to the left – to the deletion. In this example both moves are accepted. The details of the move are explained in the text.

should be inserted. One randomly inserts a colloid (second scheme) and detects the overlapping polymers (third scheme). All overlapping polymers are removed (scheme at the right). For the colloid deletion (read now from the right to the left) one selects a random colloid, then one inserts randomly polymers into its depletion zone (third, second scheme). Finally, the colloid is removed.

The simplicity of the schemes should not conceal important non-trivial details. In order to fulfill the condition of detailed balance, one has to find appropriate acceptance probability rules (which are already asymmetric for ordinary grand canonical moves). For the colloid insertion one uses

$$\mathrm{acc}(|o\rangle \to |n\rangle) = \begin{cases} \min\left[1, \frac{V z_c n_p!}{(V_d z_p)^{n_p} m (N_c+1)} e^{-\beta(E_n - E_o)}\right] & , \text{for } n_p < m \\ 0 & , \text{else} \end{cases} , \tag{2.6}$$

while for the colloid removal

$$\mathrm{acc}(|o\rangle \to |n\rangle) = \min\left[1, \frac{(V_d z_p)^{n_p} m N_c}{V z_c n_p!} e^{-\beta(E_n - E_o)}\right] \tag{2.7}$$

is applied. Here, V is the volume of the system, N_c is the number of colloids, z_p and z_c stand for the polymer and colloid fugacities, respectively, and E_n and E_o are the energies of the new and the old configurations of the system. Special attention has to be paid to the variables n_p and m. In the case of a colloid removal, n_p is a random number drawn from the interval $[0, m)$, giving the number of polymers that have to be randomly inserted into the depletion zone of the colloid. In the case of the colloid insertion, n_p is the number of overlapping polymers. If $n_p \geq m$, in the latter case, the insertion attempt has to be rejected.

2.6. Free Energy Calculations

The partition functions of thermodynamic ensembles are directly related to the thermodynamic potentials like the Helmholtz free energy $\beta F(T, N, V) = -\ln Z(T, N, V)$

in the case of the canonical ensemble with partition function

$$\begin{aligned} Z(T,N,V) &= \frac{1}{h^{3N}N!}\int d\boldsymbol{r}_1\ldots\int d\boldsymbol{r}_N\int d\boldsymbol{p}_1\ldots\int d\boldsymbol{p}_N\, e^{-\beta\mathcal{H}(\{\boldsymbol{r}_i\}_N,\{\boldsymbol{p}_i\}_N)} \\ &= \frac{1}{\Lambda^{3N}N!}\int d\boldsymbol{r}_1\ldots\int d\boldsymbol{r}_N e^{-\beta U(\{\boldsymbol{r}_i\}_N)}\ , \end{aligned}$$

with the thermal wavelength $\Lambda = \frac{h}{\sqrt{2\pi m k_B T}}$ which includes the result of the momentum integration for a standard kinetic term inside the Hamiltonian $\mathcal{H}$. In the grand canonical ensemble, the grand potential or "Landau free energy" is related to the grand canonical partition function via $\beta J(T,\mu,V) = -\ln Y(T,\mu,V)$ with

$$\begin{aligned} Y(T,\mu,V) &= \sum_{N=0}^{\infty}\frac{1}{\Lambda^{3N}N!}\int d\boldsymbol{r}_1\ldots\int d\boldsymbol{r}_N e^{-\beta(U(\{\boldsymbol{r}_i\}_N)-\mu N)} \\ &= \sum_{N=0}^{\infty} z^N Z(T,N,V)\ , \end{aligned}$$

with fugacity $z = e^{\beta\mu}$. In computer simulations, distribution functions of quantities, such as the particle number N in a grand canonical simulation, are accessible via simple histogram recording. In the thermodynamic limit the distribution of the particle number $P(N)$ reads as

$$\begin{aligned} P(N;T,\mu,V) &= \sum_{N'=0}^{\infty}\frac{1}{\Lambda^{3N'}N'!}\int d\boldsymbol{r}_1\ldots\int d\boldsymbol{r}_{N'}\frac{e^{-\beta(U(\{\boldsymbol{r}_i\}_{N'})-\mu N')}}{Y(T,\mu,V)}\delta_{N'N} \\ &= e^{\beta\mu N}\frac{Z(T,N,V)}{Y(T,\mu,V)}\ . \end{aligned}$$

When considering now the logarithm of the distribution function

$$\begin{aligned} \ln P(N) &= \beta\mu N + \ln Z(T,N,V) - \ln Y(T,\mu,V) \\ &= \beta\mu N - \beta F(T,N,V) + \beta J(T,\mu,V)\,, \end{aligned}$$

one identifies the relation to the Helmholtz free energy $\beta F(T,N,V) = \beta\mu N - \ln P(N) + \text{const.}$

Of course, in computer simulations, the logarithm of the distribution function $P(N)$ is not related to a thermodynamic potential but rather to a finite size free energy function $\widetilde{F}(N;T,\mu,V)$ which converges for infinitely large systems at fixed N to the related thermodynamic potential. This convergence is non-trivial and may not exist dependent on the stability of the interaction potentials (see the rigorous derivation in [62]).

Whenever the free energy landscape of a system of interest possesses deep and widely spread minima, the system can be easily trapped in such a minimum. Sometimes very long simulation run times make it possible to overcome the free energy barriers between two minima, however, even then the *relative* weight between the two minima can show large statistical errors. Furthermore, the order parameter region of the free energy barrier itself is rarely visited, so that quantities connected with exact properties of the barrier, like the free energy of the interface between two coexisting phases, cannot be accurately determined.

In the early 90s Berg and Neuhaus [63, 64] addressed this problem by introducing an effective Hamiltonian in the probability distribution. Choosing exactly the negative of the Hamiltonian of the underlying probability distribution results in a completely flat distribution of states. Since one knows how the effective Hamiltonian was constructed, one can easily recalculate the thermodynamic quantities by reweighting the flat probability distribution with the inverse of the correction. Of course, in practice, one doesn't know a priori the effective Hamiltonian. Therefore, one constructs successive probability distributions that can be used in further simulations as effective Hamiltonians. These first estimates for the effective Hamiltonian can even be produced at different system parameters so that the system can overcome free energy barriers (for example, one starts with a higher temperature and lowers it from simulation to simulation until one reaches the desired probability distribution). Once a precise free energy function is achieved, the technique of histogram reweighting [65] can be applied to obtain estimates of the free energy function in the adjacent region in terms of the systems variables, such as the chemical potential or the temperature respectively.

The next two sections will introduce methods based on the idea of improving the performance by using an effective Hamiltonian without spending a lot of computer time for preliminary distributions, which are often not of interest.

2.6.1. Wang-Landau Algorithm

Wang and Landau proposed in 2001 the "Random walk in energy space with a flat histogram technique" commonly called "Wang-Landau sampling" [66, 67]. It belongs to the class of multicanonical simulations where a weight function is used to force the system to visit originally improbable states, similar to the successive umbrella sampling which will be introduced in the next section 2.6.2. However, the big difference is the way how the weight function is obtained. The weight function is iteratively directly improved during the simulation, which makes the "Wang-Landau" sampling a simple and robust method with no need for preceding Monte Carlo simulations.

In the original formulation the density of states in energy space in the canonical ensemble was considered:

$$Z(V,T,N) = \frac{1}{N!(2\pi\hbar)^{3N}} \int d\boldsymbol{r}_1 \ldots \int d\boldsymbol{r}_N \int d\boldsymbol{p}_1 \ldots \int d\boldsymbol{p}_N \, e^{-\beta \mathcal{H}(\{\boldsymbol{r}_i\}_N, \{\boldsymbol{p}_i\}_N)} \quad , \tag{2.8}$$

which can be rewritten with the function of the density of states $g(E) = e^{w(E)}$ as

$$Z(V,T,N) = \int dE \, g(E) e^{-\beta E} = \int dE \, e^{-\beta E + w(E)} \quad .$$

The function $w(E)$ can be identified as the weight function (or effective Hamiltonian) modifying the internal energy of the system. In terms of free energy landscapes, this algorithm fills the valleys and troughs until the resulting surface is flat, meaning $\beta E - w(E) = 0 \ \forall E$. The function $w(E)$ fulfilling this relation is obtained by the "Wang-Landau" algorithm:

Wang-Landau Sampling

1. Choose an initialization for the weight function, e.g. $w(E) = 0$ and define a weight update, e.g. $f = 1$.
2. Proceed with a Monte Carlo move leading from the old configuration $\{\boldsymbol{r}_i\}_{\text{old}} \equiv |o\rangle$ to the new configuration $\{\boldsymbol{r}_i\}_{\text{new}} \equiv |n\rangle$.
3. Calculate the acceptance probability as:

$$p(|o\rangle \to |n\rangle) = e^{-\beta(E_o - E_n) - w(E_o) + w(E_n)}, \text{ with}$$

$$E_o \equiv E(\{\boldsymbol{r}_i\}_{\text{old}}) \text{ and } E_n \equiv E(\{\boldsymbol{r}_i\}_{\text{new}}).$$

4. If a random number $r \in [0, 1)$ is smaller than $p(|o\rangle \to |n\rangle)$, accept the move, otherwise reject the move and continue with the state $|o\rangle$.
5. Update the weight function $w\left(E(\{\boldsymbol{r}_i\})\right) \to w\left(E(\{\boldsymbol{r}_i\})\right) + f$.
6. If the histogram $w(E)$ has not sufficient statistics and $f > 0$, continue with 2.
7. If the histogram $w(E)$ has sufficient statistics and $f > 0$, update $f \to f/2$ and continue with 2.

When the weight update approaches $f = 0$ and the $w(E)$ has reasonable statistics, one has found the free energy landscape of the system $w(e) = -\beta F(E)$ up to a constant. After reaching $f \gtrsim 0$ multicanonical simulations with a fixed weight function have to be performed to check that no systematic error is present. In practice, the simulation is stopped at a still finite value of f. In this work, $f_{\text{min}} = 10^{-9}$ is typically used.

In the present work where hard particle systems are studied in the grand canonical ensemble the number of colloids N_c was used as the reaction coordinate instead of the internal energy E in the “Wang-Landau algorithm”. An example for an application of the algorithm for a continuous reaction coordinate is given in chapter 6.

2.6.1.1. Linear Interpolation

In the grand canonical ensemble the natural resolution of the reaction coordinate is determined by the system size, since it is the number of colloids N_c which serves as a reaction coordinate. Going to larger systems increases automatically the number of states which have to be sampled and the free energy barriers typically increase. The increase in the number of possible states when increasing the system size becomes even more dramatic if a joint density of states (free energy landscapes depending on a whole set of reaction coordinates) is the subject of interest.

An easy solution to suppress this effect is to use an interpolation kernel which counts neighboring states additionally to the current one at once. The interpolating function as well as the range of interpolated neighbors have to be chosen properly according to the simulated system.

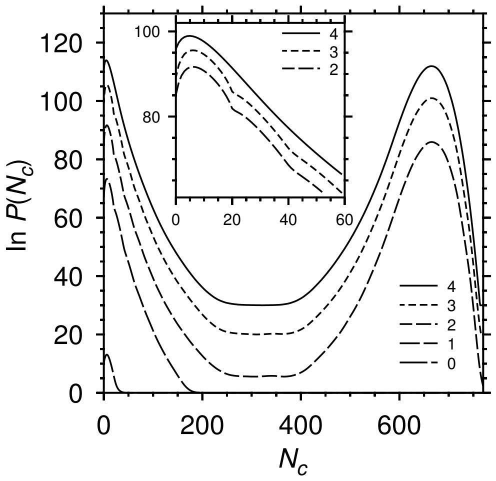

Figure 2.7: Progress in calculating a free energy landscape using a linear interpolation. First an interpolation over 40 next neighbors was done, which just took about 15 CPU hours and is shown by curves 0,1,2. Curve 3 was calculated taking 10 next neighbors into account. The final curve (4) was obtained using single bin updates for approximately one week. The inset shows the defects occurring from the interpolation and their disappearance when one goes back to single bin updates.

The interpolation method is explained in figure 2.7. A first estimate for the free energy landscape is already obtained after a few CPU hours. However, this estimate still has defects, shown in the inset of figure 2.7, which disappear when one proceeds with the original single bin updates.

2.6.1.2. Parallelization Scheme

One of the biggest advantages of the "Wang-Landau" algorithm in comparison to other methods calculating free energy landscapes is its potential for straightforward parallelization schemes. The most simple (pseudo-)parallelization scheme is the overlapping distribution method where the reaction coordinate space is cut into windows and each density of states is calculated in this restricted range by a single process [68]. Here, a parallel scheme based on message passing between the individual processes is presented which is very efficient without slicing a parameter range or preparing corresponding starting configurations.

The idea is very simple and so is its implementation. Every simulation process starts as in the case of the original "Wang-Landau" algorithm on a single CPU, e.g. a gas-like starting configuration is created randomly and the density of states is calculated iteratively. However, after a certain Monte Carlo time (which is measured, for instance, by the process 0) a data exchange via communication between all of the N_p processes takes place. This key feature is schematically shown in figure 2.8. The data which is exchanged between the a priori uncorrelated simulations on the different CPUs is the so far estimated weight function $w_i(\mathcal{C})$, where $\mathcal{C}$ corresponds to the reaction coordinate of choice. The weight function on every process i is then replaced by the average

$$w_i(\mathcal{C}) = \frac{1}{M_{\text{ges}}} \sum_{j=1}^{N_p} M_j w_j(\mathcal{C}) \ . \tag{2.9}$$

This leads to a correlation between the different simulation instances in the way that the typically sampled area in terms of the reaction coordinate $\mathcal{C}$ becomes statistically smooth. Due to the iterative character of the "Wang-Landau" algorithm the further progress in estimating the "perfect" weight function depends strongly on previous estimates used instantaneously as input. It is the statistical smoothness of the

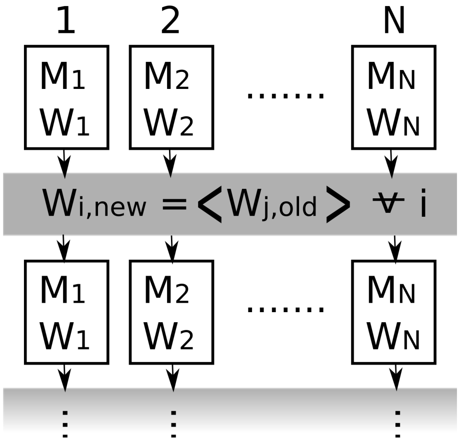

Figure 2.8: Parallelization scheme for the "Wang-Landau" algorithm. The first row is showing the CPU index. M_i stands for the number of Monte Carlo steps while W_i represents the weight function calculated by process number i. Brackets denote a weighted average over all processes. The full description of the algorithm is given in the text.

averaged weight function in comparison to non-communicating processes which leads to an improvement of the accuracy of the sampling behavior.

An important detail of equation 2.9 is the multiplication of the weight function $w_j(\mathcal{C})$ with the so far proceeded number of Monte Carlo steps M_j. This method takes care of the asymmetry in the simulated physics (cluster moves in the colloidal gas phase are much slower than in the colloidal liquid phase) as well as the used hardware architecture (e.g. different CPU speeds). A "slow" simulation result for the weight function is only weakly taken into account in contrast to the case where the simulation was able to increase the quality by performing a very large number of Monte Carlo steps.

The "Wang-Landau" algorithm is still under intensive investigation regarding its convergence properties, possible adaptive binning techniques, multi-dimensional density of states and advanced parallel schemes (see, for instance, Refs. [69, 70]). It is important to note that the effects of many of the improvements reported in literature, for instance, the modification of the weight update rule, the flatness criterion, the choice of certain binning techniques or parallel schemes, do strongly depend on the system under investigation.

2.6.2. Successive Umbrella Sampling

The successive umbrella sampling algorithm [71, 72] is a method in which computer time is no longer used for the calculation of an estimate of an effective Hamiltonian, but contributes immediately to the estimate of the probability distribution as well as to the weight function. The underlying idea is to split up the reaction coordinate of interest (for instance, the particle number N) into small windows, which are then processed successively. Since the window is small, small fluctuations in the reaction coordinate are enough to sample the probability distribution function in this window. In order to improve statistics, one can always extrapolate the probability distribution behavior from the previous window to the next window and use it as a weight function. The unnormalized probability distribution (here, as a function of the particle number N) is obtained via

$$P(N) = \prod_{n=1}^{N} \frac{P_w(n)}{P_w(n-1)}, \quad P_w(0) \equiv 1 \ , \tag{2.10}$$

where $P_w(n)$ stands for the probability distribution of a single window, n refers to the right border. Note that in practice typically the logarithm of the probability $\ln P(N) = \sum_{n=1}^{N} \{\ln P_w(n) - \ln P_w(n-1)\}$ is used so that a higher numerical precision is achieved.

The statistical error propagates quadratically from the beginning to the end of the window series. For the derivation and further insight in the error propagation see references [71, 72]. The biggest advantage of the successive umbrella sampling algorithm, especially in the case of grand canonical simulations in which the chemical potential μ dictates the linear slope of the free energy landscape, is its ability to overcome steepest slopes in the same time as moderate slopes. This ability is a crucial ingredient in grand canonical simulations since the coexistence chemical potential is not known a priori and, therefore, the free energy landscape has a strong underlying linear slope. The reason for this ability is the small window size and the way the free energy landscape is reconstructed. At the same time, for certain systems the small window size can also be disadvantageous. There exist transition pathways in multi-dimensional reaction coordinate space that cannot be projected in a reasonable way to a single reaction coordinate like the particle number N. In this case the small window size may suppress important fluctuations and relaxations in a second reaction coordinate. Nevertheless, the successive umbrella sampling remains one of the most powerful tools for calculating free energy landscapes if one can describe the free energy behavior in terms of a single reaction coordinate.

Case Study: Absolute Free Energy of a Hard Sphere System To demonstrate the tremendous power of the successive umbrella sampling algorithm and the high applicability of multicanonical algorithms in general, *absolute* free energies of a hard sphere system are calculated. A system of hard spheres (each with the same radius r_c) can phase separate in a liquid and a crystalline phase (fcc). In the canonical ensemble, the packing fraction $\eta = \frac{4}{3}\pi r_c^3 \frac{N}{V}$ determines whether the system is in the liquid state ($\eta \leq \eta_l \approx 0.4915$) or in the crystalline state ($\eta \geq \eta_c \approx 0.5428$) [49]. Absolute free energies are rarely accessible in typical Monte Carlo simulations. The first necessary ingredient to obtain an absolute free energy is a reference state with a precisely known reference free energy. The next step is to find a continuous path (in terms of a reaction coordinate) from this reference state to the state of interest. In the case of the considered hard sphere system the reference states are the ideal gas and the Einstein crystal, the introduction of which is deferred to the later parts of this paragraph. The free energy of the ideal gas in the canonical ensemble is

$$\beta F_{\mathrm{id}}(N, V, T) = -\ln\left(\frac{V^N}{\lambda^{3N} N!}\right) . \tag{2.11}$$

The reaction coordinate of choice is the interaction range of the potential, i. e., the particle radius r_c. For $r_c = 0$ the reference state of the ideal gas is obtained. Every $r_c \neq 0$ is directly related to a certain packing fraction η, since particle number N and volume V are assumed to be constant. The successive umbrella sampling algorithm is now used to calculated the free energy between the state with hard sphere radius r_c and the adjacent state corresponding to $r_c + \delta r_c$. By performing in this manner a free energy calculation of the range $\eta \in [0, \eta_l]$, one obtains the absolute free energy of the liquid branch of a hard sphere system within a single simulation run.

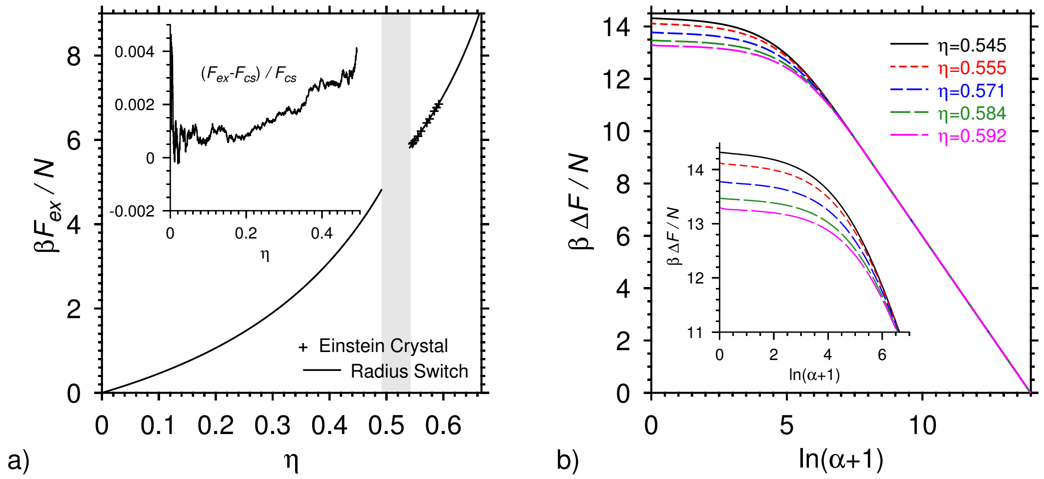

Figure 2.9.: (a) Absolute free energy per particle of a hard sphere system as function of packing fraction. The inset shows the difference of the calculated free energy to the Carnahan-Starling free energy prediction. The shaded region is the liquid-crystal coexistence region. The symbols result from the free energy difference to the Einstein crystal. (b) Free energy difference to the Einstein crystal reference state as a function of harmonic coupling strength α. The inset magnifies the upper left region.

Figure 2.9a shows as a result of such a simulation the excess free energy per particle $F_{\text{ex}}/N = F_{\text{abs}}/N - F_{\text{id}}/N$. The simulation was performed with $N = 3360$ hard spheres, which means that the successive umbrella sampling algorithm calculated precisely the absolute free energy over a range of approx. $16800\, k_B T$! The whole calculation was achieved on a single CPU core within only a couple of days. In the case of a hard sphere system, an analytical estimate of the excess free energy of the liquid branch, the so-called Carnahan-Starling equation of state, is available [73]: $F_{\text{cs}}/N = (4\eta - 3\eta^2)/(1.0 - \eta)^2$. The inset of figure 2.9a shows the relative deviation of the calculated free energy to the Carnahan-Starling expression[3].

The absolute free energy of the crystalline phase of the hard sphere system is also accessible in a slightly more complex manner. The method was proposed by FRENKEL and LADD [28, 74] and uses as a reference state the so-called Einstein crystal. The Einstein crystal is a system where every particle is pinned to a fixed position $\boldsymbol{r}_o$ via a harmonic trap $V_h(\boldsymbol{r}) = \alpha(\boldsymbol{r}_o - \boldsymbol{r})^2$. In the limit of strong coupling ($\alpha \to \infty$) this leads to the following expression of the free energy:

$$F_{\text{Ein}}(N, V, T) = U(\{\boldsymbol{r}_0\}_N) - \frac{3N}{2\beta} \ln\left(\frac{\pi}{\beta\alpha}\right) \quad , \tag{2.12}$$

where $U(\{\boldsymbol{r}_o\}_N)$ is the internal energy of the system if all particles are fixed exactly at the set of positions $\{\boldsymbol{r}_o\}_N$. Note that this position set does not necessarily need to have any crystalline structure, but can be chosen arbitrarily. Again the power of the successive umbrella sampling algorithm is used to overcome large free energy

---

[3] The origin of the small systematic deviation results most probably from the finite system size, although the Carnahan-Starling equation is also known to become less accurate at higher packing fractions.

difference between the reference state ($\alpha \to \infty$) and the desired “free” crystalline state at $\alpha = 0$. The corresponding free energy landscape is shown in figure 2.9b. Subtracting from $F_{\mathrm{Ein}}(N, V, T)$ this difference $\beta\Delta F$ as well as the ideal gas term (see Eq. 2.11) leads directly to the excess free energies shown in figure 2.9a[4]. Determining just a few of such excess free energies serves well as a further reference point for a free energy calculation based on the particle radius as it was done for the liquid phase. The result of the latter calculation is shown by the full line in the crystalline region of figure 2.9a.

This case study shows how absolute free energy landscapes as a function of “abstract” continuous reaction coordinates can be determined by successive umbrella sampling. These calculations are not only possible for hard sphere systems but rather for any particles the interaction range of which can be controlled via a parameter as it was done here for the radius.

2.6.3. Comparison between the Two Free Energy Methods

As a first conclusion, advantages and disadvantages of the previously described free energy algorithms are listed again and a meaningful combination of the two is proposed.

Successive Umbrella Sampling

- Advantages
  - works at any slope of the free energy landscape → no a priori information about the coexistence chemical potential is needed
  - boundaries of the reaction coordinate are not needed to be known in advance
  - detailed balance is fulfilled and each Monte Carlo step increases the final statistics
- Disadvantages
  - the lack of a straightforward strong parallelization scheme[5]
  - overcoming multi-dimensional free energy barriers may become difficult if one only samples in one reaction coordinate and uses small window sizes

Wang-Landau Sampling

- Advantages
  - strong parallelization scheme available (scales beyond 4000 cores because of relatively low communication effort)
  - overcoming multi-dimensional free energy barriers while sampling only along one reaction coordinate is somewhat easier
- Disadvantages

---

[4] There exist further corrections related to the change of translational entropy and due to finite size effects, which are not included here (see [28]).

[5] However, one can parallelize the successive umbrella sampling up to a certain level by using multiple independent processes which contribute to the statistics within the same window.

  - spending all the computer time in a reaction coordinate area which is not of interest if the coexistence chemical potential is not known → no convergence to the final free energy landscape
  - the convergence also breaks down if the reaction coordinate boundaries are chosen too big
  - detailed balance is only fulfilled for a weight update of $f = 0$

As one can see from this list of advantages and disadvantages, the successive umbrella sampling algorithm is the perfect choice exploring new (but relatively small) systems to get first estimates for the coexistence chemical potential and reaction coordinate boundaries. Then the parallel version of the Wang-Landau algorithm can be used together with the previous estimates for the study of larger systems.

Note that a lot of investigations were done to check whether multicanonical flat-histogram Monte Carlo methods are the optimal choice when calculating free energies. TROYER et al. point out that the flatness with respect to diffusion (tunneling rate between states) rather than the flatness of the free energy histogram itself might lead to a higher performance [75, 76].

CHAPTER

3

REVIEW OF BULK PROPERTIES

The Asakura-Oosawa model was studied extensively in the last few years. Especially the properties of the bulk case are well understood, mainly due to the work of Vink, Horbach and Binder [61, 77–79]. The phase diagram, the critical properties as well as further details like capillary waves on interfaces are reported in those references. Although it is already well studied, simulations of the AO model in the bulk represent a perfect introduction to more complicated simulations presented later in the thesis. The bulk case serves in many cases as a reference state when results from simulations in confinement need to be interpreted. Additionally, the detailed results presented in the publications make it possible to check simulation code (e.g. by locating the critical point). The continuous AO model (see section 2.2) shows qualitatively the same phase behavior as the original AO model, however, in the case of non-zero polymer-polymer interaction the phase diagram is shifted [42]. The main focus in this and in the following chapters lies on the original (purely entropic) AO model, but some results for the continuous AO model are also presented.

The current chapter also provides the nomenclature for later chapters dedicated to simulations in confinement. The results obtained by simulations presented here do not claim to be complete or detailed, but should provide a first notion about basic properties of the Asakura-Oosawa model.

3.1. Simulation Details

A mixture of colloids with radius r_c and polymers with radius $r_p = 0.8\, r_c$ are simulated within the framework of Monte Carlo simulations in a cubic box with periodic boundary conditions in all directions. The length scale in this section is the colloid radius $r_c \equiv 1$. The simulation box is split up into cells with diameter $d_{\text{cell}} \geq 2r_c$ [27]. Each particle is associated with its corresponding cell. An overlap control for a given particle with all the other particles in the simulation box is therefore reduced to an overlap check with respect to the particles in its own cell and the 26 neighboring cells. This simple trick reduces the quadratic effort to check all possible particle overlaps to a linear one.

Grand canonical simulations (constant V, T, μ_c, μ_p) are performed using rejectable canonical cluster moves (see section 2.5.1) as well as the grand canonical cluster moves from section 2.5.3. Free energy calculations are done via the successive umbrella sampling algorithm (see section 2.6.2) for the smaller systems on a single CPU and the "Wang-Landau" algorithm for larger systems on multiple CPUs (see section 2.6.1). Here, the reaction coordinate is the colloid particle number N_c and not the internal energy E as in the original formulation of the latter algorithm. The calculated weight function $w(N_c) = \ln(P(N_c))$, where $P(N_c)$ is the probability distribution of states with colloid particle number N_c, gives access to the (finite size) free energy function

$$\beta F(N_c) = -w(N_c) = -\ln(P(N_c)) \ . \tag{3.1}$$

As already mentioned earlier, the main advantage of the successive umbrella sampling algorithm is that it works at every colloid chemical potential μ_c with the same efficiency while the "Wang-Landau" algorithm needs already a relatively precise estimate of the colloid chemical potential at liquid vapor coexistence μ_c^c. Therefore, the successive umbrella sampling is a perfect "pre-sampler" to free energy calculations of large systems which then use the parallel version of the "Wang-Landau" algorithm on multiple CPUs.

3.2. Phase Separation

The AO model can phase separate in a gas-like (colloid-poor) phase and in a liquid-like (colloid-rich) phase as long as one is above the critical polymer reservoir packing fraction $\eta_{p,c}^r \approx 0.767$ (note that this value is only valid at the chosen size ratio of $q = 0.8$). The polymer reservoir packing fraction $\eta_p^r = \frac{\pi}{6}\sigma_p^3 e^{\beta\mu_p}$ (σ_p is the polymer diameter) plays a similar role as an inverse temperature $\beta = \frac{1}{k_B T}$ in energy driven systems, such as Lennard-Jones systems. The transition from the colloid-poor to the colloid-rich phase as a function of μ_c is a first order phase transition. In a finite system (with periodic boundary conditions) one observes several smeared out jumps in the derivative $\left(\frac{\partial F}{\partial N}\right)$, which correspond to the transitions between several states shown exemplary by snapshots in figure 3.1.

The periodic boundary conditions allow the system to minimize its surface free energy by "choosing" the geometry with the smallest surface. Therefore, cylinder and slab configurations can be observed at certain densities (snapshots 2, 3, 4) (also see Refs. [80–83]). The different phases can also be identified in a plot of the colloid chemical potential μ_c (Fig. 3.2) which exhibits several rounded plateaus. The rounding of the plateaus comes from the fact that the surface itself varies with the size of the droplet or the cylinder. In contrast, the slab geometry creates a flat plateau indicating that the surface area stays constant for the corresponding range of the colloid packing fraction η_c.

The black dots in figure 3.2 are a direct calculation of the chemical potential using the Widom insertion method [84]. It provides a nice consistency check that the more

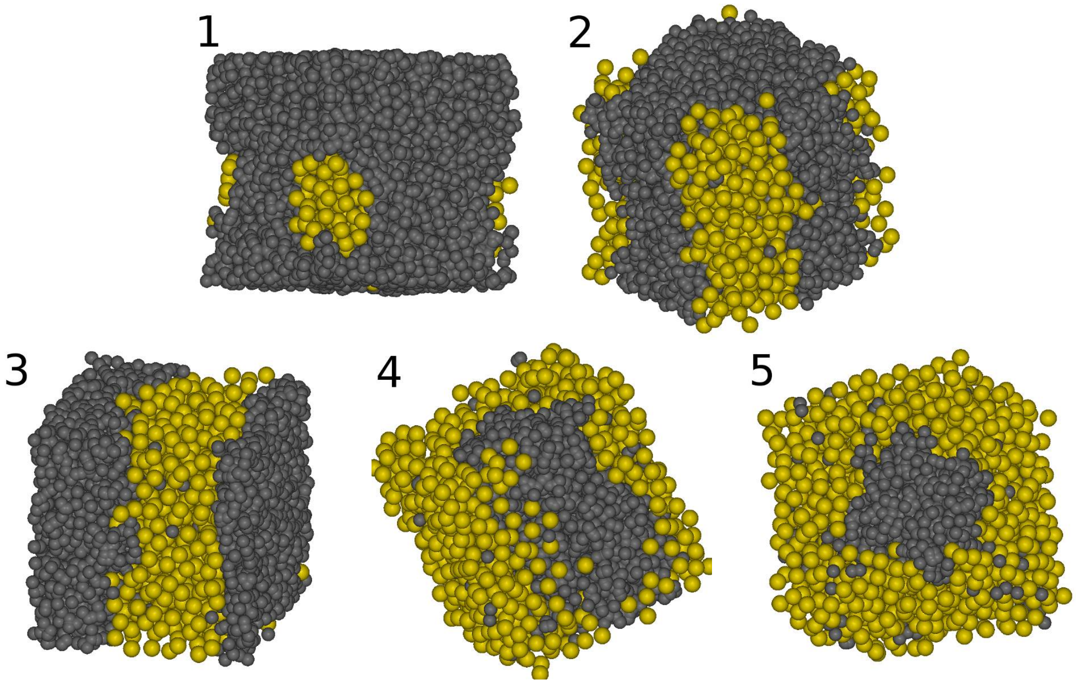

Figure 3.1.: Different (metastable) phases of the AO model in a finite system in the bulk case for $\eta_p^r = 1.30$: colloidal droplet (1), colloidal cylinder (2), slab geometry (3), cylindrical polymer-rich phase (4), polymer droplet (5).

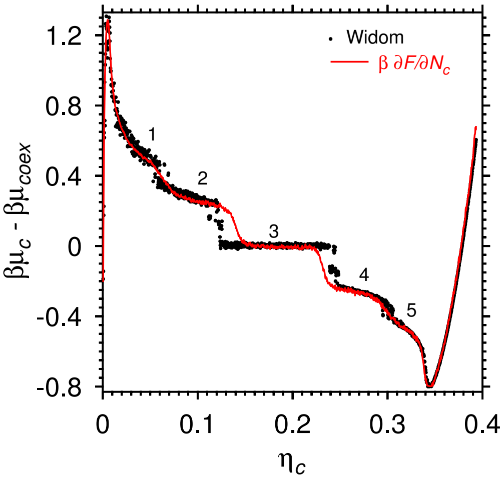

Figure 3.2: Different states of the system shown by steps of the chemical potential μ_c as a function of the colloid packing fraction η_c. The (red) full curve shows the derivative of the free energy landscape, while the (black) dots are showing data from the Widom insertion method taken as a consistency check. The numbers 1 to 5 correspond to the states shown in figure 3.1. The polymer reservoir packing fraction was $\eta_p^r = 1.30$.

complicated algorithms for determining the free energy landscape are implemented correctly. Here, the transitions seem to be sharp which is just an artifact of using only one starting configuration for each data point. During the time of the measurement the system was just not able to overcome the entropic barriers to the adjacent state by fluctuations. The derivative of the free energy landscape provides a higher accuracy and samples correctly the rounding of transitions in finite systems.

3.3. Critical Behavior

Whenever the words "critical behavior" are mentioned, one also has to mention the theory of finite size scaling which brought computational physics fundamentally to the success it has nowadays (for all the details see the original work [85–87] or compare with [88]). One of the basic aims of this theory is to relate results from simulations of typically small system sizes to predictions in the thermodynamic limit or in experiments. Especially close to criticality when the correlation length ξ starts to diverge, results from computer simulations of finite systems are no longer directly valid anymore, because a very large correlation length cannot be distinguished anymore from the diverged one.

From finite size scaling theory follows for the singular part of the free energy landscape

$$F(L,T) = L^{-(2-\alpha)/\nu}\mathcal{F}(\varepsilon L^{1/\nu}) \ ,$$

where L is the length of the system, T is the temperature and $\varepsilon = (T - T_c)/T_c$, T_c being the critical temperature. The letters α, ν, and following in the next formula β, are the so-called critical exponents defining the universality class of the system. The corresponding scaling forms for thermodynamic variables are obtained from the derivatives of F, e.g.

$$M = L^{-\beta/\nu}\mathcal{M}^0(\varepsilon L^{1/\nu}) \ .$$

Here, the magnetization M represents the order parameter of the system and $\mathcal{M}^0$ is a scaling function. This function reduces to a constant (with respect to L) at the critical temperature when $\varepsilon = 0$, so that $M \propto L^{-\beta/\nu}$. From this it is clear that ratios of momenta such as

$$\frac{\langle M^4\rangle}{\langle M^2\rangle^2} = \frac{\int M^4 P(M)\, dM}{\left(\int M^2 P(M)\, dM\right)^2} \tag{3.2}$$

become system size independent when one is exactly at $T = T_c$. Therefore, the intersection of such ratios (cumulants) for different system sizes is a fast and precise method to determine the critical point of the system of interest.

Critical Point of the AO Model Figure 3.3a shows the cumulant intersection and compares its result to the one from the literature [61, 77] (shown as horizontal line the length of which corresponds to the given error). Here, the intersection yields $\eta_p^r = 0.7670 \pm 0.0005$.

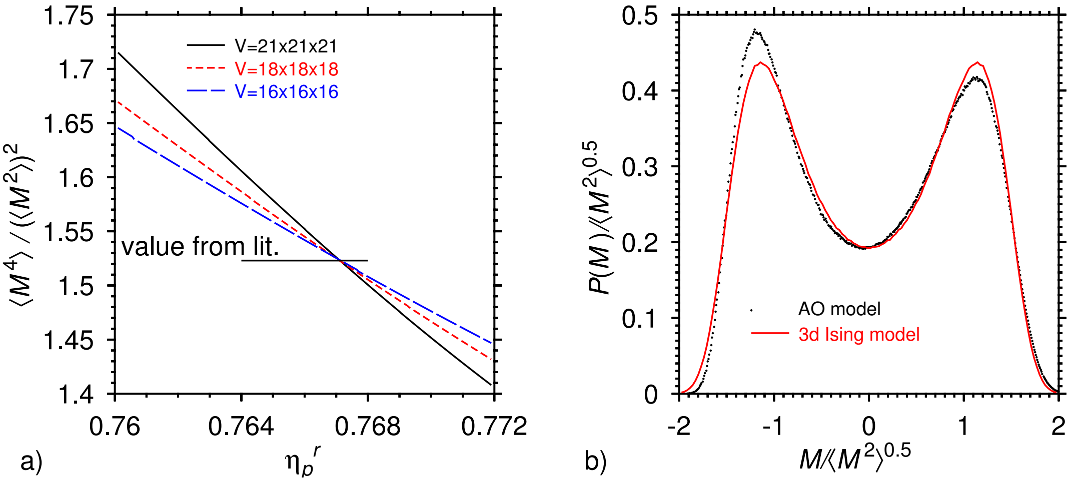

Figure 3.3.: Two approaches to estimate the critical point in the AO model. (a) Fourth order cumulant intersection. The horizontal line indicates the literature result. (b) Best agreement between rescaled order parameter distribution of the AO model with the three-dimensional Ising universality curve (red full line).

A different approach to estimate the critical point is the comparison of the rescaled order parameter distribution function $P(M)/\sqrt{\langle M^2\rangle}$, with $M = N_c - \frac{1}{2}\langle N_c\rangle$, and the three-dimensional Ising universality curve at the critical point shown in figure 3.3b. Due to the same universality class they show the best “overlap” at the critical reservoir packing fraction. The deviation between both curves is induced by the asymmetry of order parameter distribution function of the AO model. The field mixing technique [89] allows to avoid this problem.

Critical Point of the Continuous AO Model Continuous pair interactions lead to some differences in the implementation of the basic Monte Carlo moves as well as in the grand canonical cluster moves in comparison to purely entropic models. First of all, the internal energy of the system is not only zero but a continuous value so that a strict early rejection criterion as in the case of a particle overlap does not exist anymore. Second, since particles have a non-zero probability to overlap, the depletion zone is not well defined anymore, but rather a parameter in the grand canonical cluster move. In the case of the WCA potential, which mimics very well the hard sphere interaction, the native choice of the depletion zone diameter is $\sigma_{\text{depl}} = \frac{1}{2}\sigma_c + \frac{1}{2}\sigma_p$. To check the correct implementation of continuous pair interactions in the various types of Monte Carlo moves, the critical point of the continuous AO model was estimated via the cumulant intersection method (Eq. 3.2). Figure 3.4 shows the cumulant intersection result in the case of the continuous AO model with parameters $q = \sigma_p/\sigma_c = 0.8$, $\varepsilon_{cc} = \varepsilon_{cp} = 1$ and $\varepsilon_{pp} = 0.0625$. The critical point is estimated as $\eta_p^r = 1.2822 \pm 0.0005$ and agrees well with the literature value of $\eta_p^r = 1.282 \pm 0.002$ (please see the details in [42]). This shift to a higher critical polymer reservoir packing fraction in comparison to the original AO model is expected. The polymers gain less free volume when two depletion zones overlap due to their soft-core interaction. This reduces the effective depletion force, so that a higher reservoir packing fraction is needed to achieve an effective colloid attraction large enough to cause phase separation. For $\varepsilon_{pp} = 0$ the phase diagram of the original AO model is recovered almost perfectly.

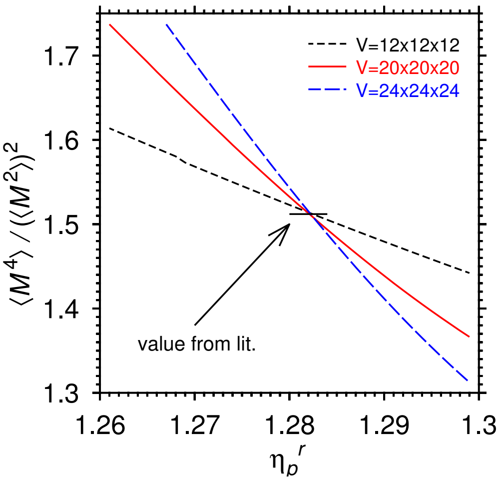

Figure 3.4: Cumulant intersection at the critical point in the case of the continuous AO model. The horizontal line indicates the location of the critical point given in the literature. See the main text for the numerical values.

3.4. Summary

The Asakura-Oosawa model exhibits a phase separation in a gas-like and liquid-like phase above a critical point of $\eta_p^r = 0.767$ ($\eta_p^r = 1.282$ in the case of the continuous AO model). Via the cumulant intersection method it is possible to extract the critical reservoir packing fraction. The agreement with the literature values and the results shown above for the Widom insertion method lead us to the conclusion that the grand canonical and canonical cluster moves were properly implemented as well as both free energy algorithms, the successive umbrella sampling and "Wang-Landau" sampling.

CHAPTER

4

CYLINDRICAL CONFINEMENT

Besides the fundamental importance for statistical thermodynamics [90–94], the confinement of fluids in narrow, cylindrical pores and microporous materials in general found a lot of interest recently [95–105]. Nanopores appear in natural rocks but also in artificial devices, such as various zeolithes used as catalysts to separate fluid mixtures. While random porosity is also an interesting topic, here, the ideal case of isolated straight pores is studied. Diameters of the order of nanometers can be experimentally realized by filled carbon nanotubes [106, 107], while diameters up to 150 μm are present in silicon wafers [108].

In general, the influence of walls changes the phase behavior strongly, especially in narrow pores. The occurrence of vapor condensation at lower chemical potentials in comparison to the bulk is known as "capillary condensation" achieved via lyophilic pore walls, and the opposite effect – "capillary evaporation" – is gained by using lyophobic pore walls [109–114]. An experimental way to access the phenomenology of cylindrical pores is the observation of adsorption hysteresis effects, where a systematical shift in comparison to the bulk critical temperature as also predicted by theories appears [115–120].

Our theoretical picture of a phase change of fluids in cylindrical confinement is rather incomplete. Kornev et al. [119] describe the condensation and respective evaporation in cylindrical pores as a morphological transition between wetting film configurations of different symmetry. This description is only valid for a pore radius $R \to \infty$ that is clearly not the case in nature or experiments. Similar problems occur in the phase diagram proposed by Liu et al. [121] where a sharp wetting transition is predicted for finite pore radii. In experiments [117] a smooth adsorption isotherm with a finite slope is observed. Non-idealities of the experimental setup like material impurities or polydispersion, which can occur for the particles or for the pore geometry, complicate the correct interpretation of this behavior. They can also draw off attention from interpreting results in the context of quasi one-dimensional confinement.

This chapter should solve the question, whether the phase changes in a cylindrical pore can be described as a sharp transition or as a rounded transition due to the statistical fluctuations in quasi one-dimensional systems.

Please see also the references [1–4] for a full comparison of the cylindrical confinement of the Asakura-Oosawa model and the Ising model which has several advantages due to its symmetries in addressing the latter question.

Since there exists a certain analogy between the quasi one-dimensional confinement of the AO model considered in this chapter and the one-dimensional Ising model, it might be helpful to mention briefly the spin configurations one observes for $T > 0$ (no external field). For any finite temperature T the correlation length of a spin domain ξ_z can be exceeded by the system dimension L. This means that the system is not in a state where all the spins are aligned, but spin up and spin down domains coexist.

4.1. Simulation Details

The cylindrical confinement is implemented via hard walls of a cylinder with radius R and length L lying with its axis on the z-axis of the coordinate system. Particles are not allowed to have positions $x^2 + y^2 \geq (R - r)^2$ (where r is the particle radius) but can “freely” move with respect to their z-coordinate. While in the bulk periodic boundary conditions were applied in every direction, here, the periodic boundary condition is only used along the cylinder axis (z-direction). The following studies are taking two different cylinder diameters $D = 2R$ into account, $D = 12$ and $D = 6$. As in the studies of the bulk case, the length scale is set by the radius of the colloids $r_c \equiv 1$.

The condition $L \gg D$ makes the canonical cluster moves in which a particle is translated at random inefficient. The small diameter of the cylinder restricts the cluster move to a colloid translation of the order of D, since taking larger translational amounts leads almost always to a rejection because the particle would leave the simulation box. Therefore, a modified version of the cluster move is used which was introduced in subsection 2.5.1 and is schematically shown in figure 2.5 on page 15. The randomly chosen colloid is moved only in the z-direction with a translational amount from the interval $[0, L/2)$. Instead of a point mirror reflection, the mirror reflection is done at the plane perpendicular to the translation vector. Of course the ordinary translational moves for polymers and colloids were additionally performed to guarantee ergodicity.

The grand canonical cluster moves are basically the same as in the bulk case. However, a small modification regarding the volume of the system improves drastically the performance. New particle positions are generated in a way that an overlap with the cylinder wall is not possible, meaning $x^2 + y^2 < (R - r)^2$. Therefore, one has to replace the system volume V in equations 2.6 and 2.7 by the reduced volume $V_r = \pi(R-r)^2 L$. Such an improvement is only possible in the case of hard walls, for finite values of continuous wall potentials the position generation has to be based on the volume of the *whole* simulation box.

Although cluster moves are used, the overall invested computer time for studies of quasi one-dimensional systems is much higher than in the bulk case, since the Monte Carlo dynamics are much slower.

4.2. Interplay of Finite Pore Length and Phase Behavior

To describe the results regarding the rounding of phase transitions in quasi one-dimensional geometries, it is important to point out the similarities and differences to the bulk case. In the bulk a well defined critical point $\eta^r_{p,c}$ exists and, by introducing the distance $t = \frac{\eta^r_p}{\eta^r_{p,c}} - 1$, one can distinguish two correlation lengths ξ_- and ξ_+ diverging as $\xi_+ \propto (-t)^{-\nu}$ coming from the one-phase region and $\xi_- \propto t^{-\nu}$ approaching the critical point from the two-phase region. Only for pore radii $R \gg \xi_+$ (for $t < 0$) and $R \gg \xi_-$ (for $t > 0$) these power laws are still valid.

Furthermore, it is important to point out that the AO model does not behave "neutral" in the case of hard walls, the colloids prefer to layer at the walls (complete wetting, compare with chapter 5). This wetting behavior leads typically to shifts of certain quantities like the coexistence chemical potential of the colloids, the coexistence densities and the critical point with respect to the bulk. It is emphasized that such effects (which occur also in a plate geometry, or spherical confinement) have to be distinguished from the one induced by the one-dimensional character of the cylindrical confinement.

At low enough polymer reservoir packing fractions the AO model in cylindrical confinement forms a mixed state (one phase region) which is homogeneous along the cylinder axis. The main focus in the following, however, lies on the polymer reservoir packing fraction region where polymers and colloids start to demix.

4.2.1. Phase Behavior in Short Pores

In short cylindrical pores, where cylinder diameter D and cylinder length L are of the same order of magnitude (or $L \gtrsim D$), the transition of the AO model from the mixed state to the demixed state is very similar to the phase transition in the bulk system and differs only through the wetting behavior. The gas-liquid phase coexistence looks typically as shown in figure 4.1. One clearly identifies the colloidal capillary bridge with curved liquid-gas interfaces at both sides.

The corresponding free energy landscape is shown in figure 4.2 and is qualitatively very similar to the one observed in the bulk. However, the typical finite size phase transition kinks (spherical droplet to cylindrical droplet to slab etc. [80–83]) are missing, and due to the colloidal wetting layer the gas peak is broadened. In short cylindrical pores the phase transition of the AO model from the gas to the liquid

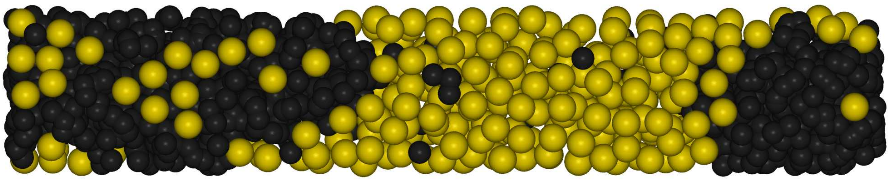

Figure 4.1.: Snapshot of gas-liquid coexistence of the Asakura-Oosawa model in a short cylindrical pore of diameter $D = 12$ and length $L = 60$ at polymer reservoir packing fraction $\eta^r_p = 1.30$.

Figure 4.2: Free energy landscape at phase coexistence of a colloid-rich and a colloid-poor phase in a cylinder of length $L = 60$, diameter $D = 12$ at a polymer reservoir packing fraction of $\eta_p^r = 1.30$.

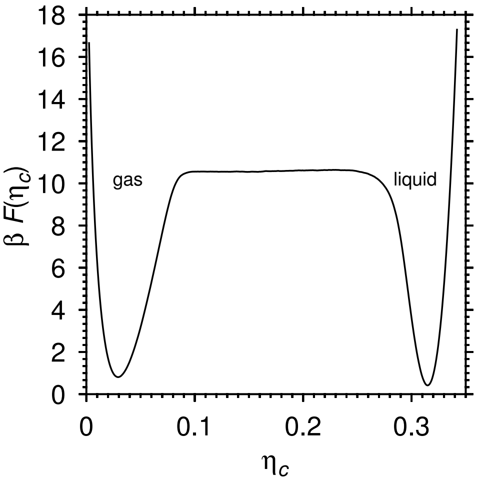

state happens via capillary condensation where the layering in the (oversaturated) gas at the walls becomes stronger and stronger until they connect in the center to a liquid phase. The liquid phase then simply grows until the interfaces connect close to the wall (polymer droplet) and eventually it fills the whole system.

The already mentioned layering of particles at flat walls is shown in figure 4.3. The parameters are chosen to be the same as in figure 4.2, but simulations were performed in a semi grand canonical ensemble, where the polymer particle number is allowed to fluctuate while the colloid particle number is fixed. The radial density profiles were recorded exactly at the colloid coexistence packing fractions in the gas phase (Fig. 4.3a) and in the liquid phase (Fig. 4.3b). The flatness of the walls causes ordering of the colloidal particles in layers (black dashed lines). The layering persists even at the center of the cylinder, but is less pronounced. A flat “bulk” density distribution is not reached in such narrow cylindrical pores. The polymers (red full lines) inherit the colloid layer structure, but are not able to form layers without the presence of colloidal particles which leads to the flat density plateau close to the cylinder axis in the case of the gas phase.

Despite the presented layering effects, the results discussed so far do not show any surprising qualitative difference to the bulk case. However, a controversy appears when thinking about the thermodynamic limit of this quasi one-dimensional system, i. e. $L \to \infty, D = \text{const}$. In this limit a phase separation cannot occur for a system with short range interactions at non-zero temperature or finite polymer reservoir packing fraction [122]. This is already shown by the analytical calculation of the one-dimensional Ising model. The fact that one sees a clear phase separation with a free energy barrier of about $10k_BT$ can only result from finite size effects. The next section indeed shows that phase transitions in quasi one-dimensional systems ($L/D \gg 1$) are qualitatively different and that bulk quantities such as critical points cannot be defined anymore.

4.2.2. Phase Behavior in Long Pores

Performing a free energy calculation close to the polymer reservoir packing fraction where the phase separation disappears leads to an interesting discovery, namely that a third minimum in the middle between the coexistence densities of the gas-like and liquid-like colloid phases appears (see Fig. 4.4a). By simply looking at a typical

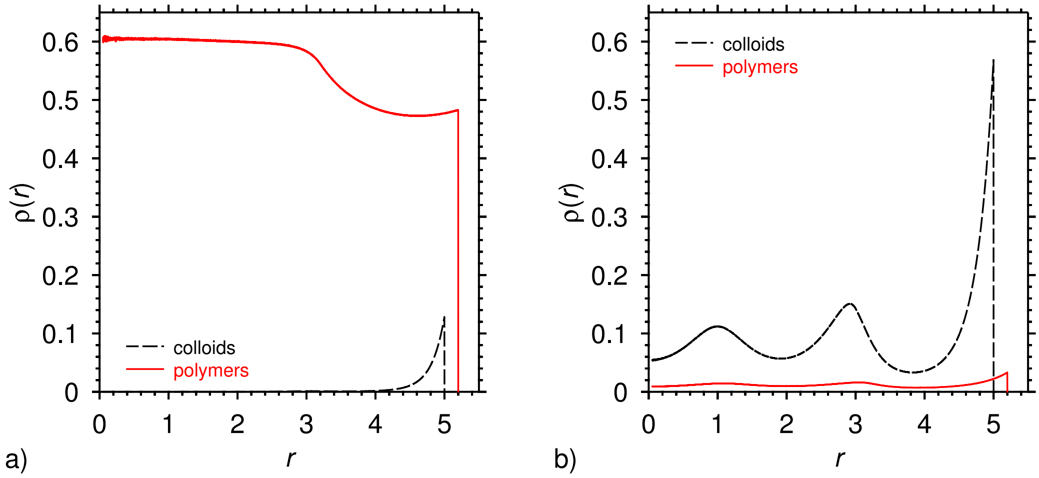

Figure 4.3.: Radial density profile of colloids and polymers plotted vs. distance from the cylinder axis for $\eta_p^r = 1.30$, $L = 60$, $D = 12$. Part (a) shows these profiles in the vapor-like phase, part (b) for the liquid-like phase. Note that in case (b) one can recognize that the polymers inherit the structure of the colloids although on their own they do not form any structure (ideal gas).

configuration in the range of states corresponding to the center minimum in $\beta F(\eta_c)$ one finds states with multiple domains of liquid and gas regions (see the snapshots in figure 4.4) with a typical distance

$$\xi_z \propto \exp(\pi R^2 \beta\gamma) \ , \tag{4.1}$$

where γ is the bulk interfacial tension between a liquid and a vapor domain. Equation 4.1 can be made plausible in the following (coarse grained) picture. The colloidal domains are treated as a one-dimensional gas of “particles” with number density $\rho = \frac{N}{L} = \xi_z^{-1}$. The free energy has two contributions, the ideal gas part and the interfacial part,

$$F_{\text{id}} \approx -Nk_BT \ln\left(\frac{e}{\rho\Lambda}\right) \tag{4.2}$$

$$F_{\text{int}} = N\gamma\pi R^2 \ , \tag{4.3}$$

Λ being the thermal wave length, $\Lambda = h/\sqrt{2\pi k_B T m}$. Equation 4.1 can now be obtained by minimizing the free energy

$$\begin{aligned} \frac{\partial(F_{\text{id}} + F_{\text{int}})}{\partial N} &= 0 \\ k_B T \ln\left(\frac{\xi_z}{\lambda}\right) &= \gamma\pi R^2 \, . \end{aligned}$$

As indicated by equation 3.1, the free energy function is equivalent to the probability distribution of the particle number, density or the packing fraction. In the probability distribution picture, peaks correspond to phases which were previously described by minima in the free energy. Figure 4.4b shows the development of the center peak of the probability distribution when varying η_p^r for $L = 180$ and $D = 12$. The free energy landscapes for $\eta_p^r = 1.075, 1.10, 1.18$ were obtained via histogram extrapolation methods based on the free energy calculation at $\eta_p^r = 1.115$. Fluctuations

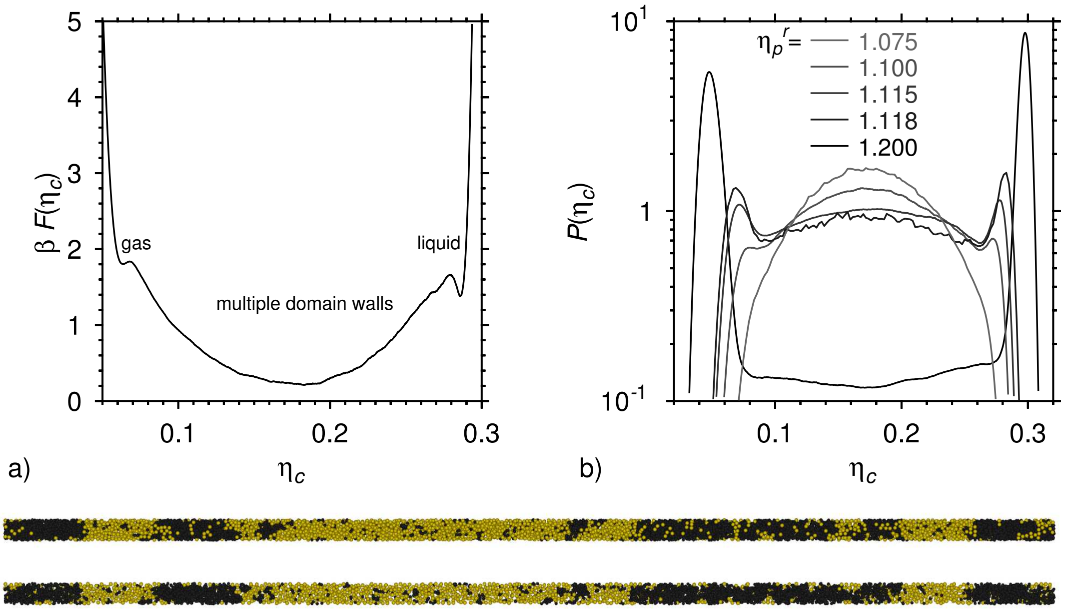

Figure 4.4.: (a) The free energy landscape of a cylinder of radius $R = 6$ and length $L = 540$ at $\eta_p^r = 1.15$. (b) Distribution $P(\eta_c)$ of the number of colloids in a cylinder of diameter $D = 12$ and length $L = 180$ (all lengths are measured in units of the colloid radius) for $\eta_p^r = 1.075$, 1.10, 1.115, 1.118, 1.20 from top to bottom at $\langle \eta_c \rangle \approx 0.175$. (at the bottom) Snapshots of the multiple domain configuration in a cylinder corresponding to the free energy calculation of figure part (a). The lower one is sliced in the middle along the long axis.

are simply due to statistical errors. Since the interfacial tension is a function of the polymer reservoir packing fraction $\gamma = \gamma(\eta_p^r)$, the variation of η_p^r leads to an effective variation of the domain correlation length ξ_z. In this sense, figure 4.4b highlights the smooth transition between three regimes, $\xi_z \lesssim L$ (single peak at $\eta_p^r = 1.075$), $\xi_z \approx L$ (three peak structure at $\eta_p^r \approx 1.115$) and $\xi_z \gtrsim L$ (double peak structure at $\eta_p^r = 1.200$).

In addition to the simulations with a cylinder diameter of $D = 12$, the system was also studied for $D = 6$. The choice of such a relatively small cylinder diameter (note that this corresponds to a width of only three colloids) reduces the number of particles to simulate and additionally increases the rounding of the phase transition. Again, the development of the center peak was recorded when varying the polymer reservoir packing fraction. A much higher accuracy could be achieved due to the lower particle numbers (see Fig. 4.5a). To emphasize the dependence of the functional form of the probability distribution on the cylinder length, figure 4.5b shows the results for this function at fixed polymer reservoir packing fraction for several choices of L. The graph identifies clearly the transition from $L \ll \xi_z$ ($L = 10$) via $L \approx \xi_z$ ($L = 100$) to $L \gg \xi_z$ ($L = 1000$).

Further insight is given by figure 4.6a and 4.6b where the first and second moment of the colloid density are plotted. The averaged density as a function of colloid chemical potential (adsorption isotherms) looks at the first view similar to the bulk case. However, the rounding of the curve disappears at rather high polymer reservoir packing fractions ($\eta_p^r \approx 1.05$) where the system is already locally ordered. As a next

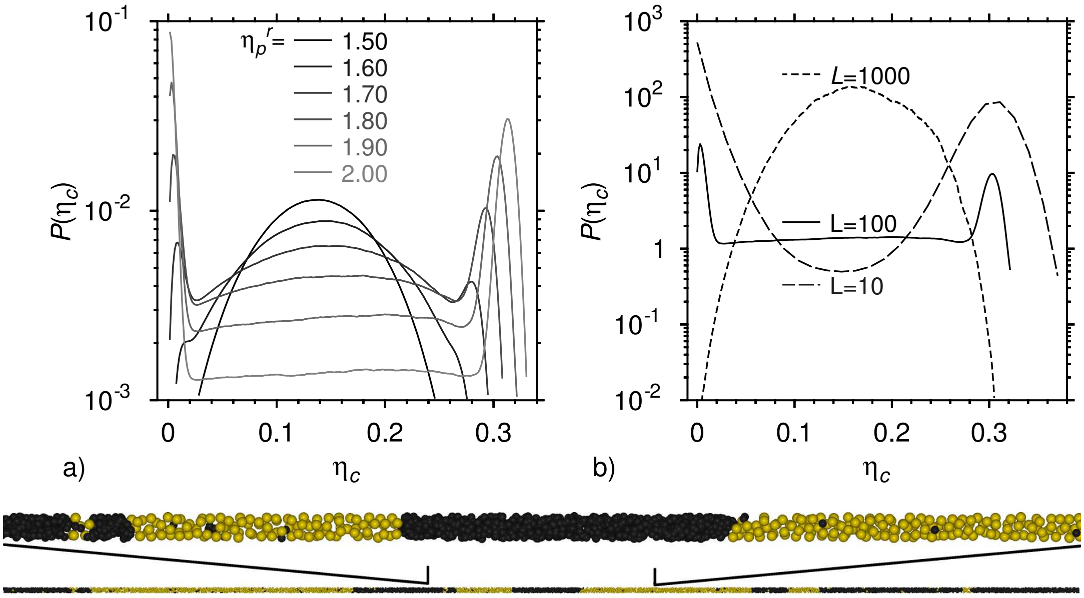

Figure 4.5.: (a) Development of the probability distribution of the colloid volume fraction $P(\eta_c)$ towards a three peak structure while decreasing η_p^r in a cylinder of diameter $D = 6$ and length $L = 100$. (b) Cylinder length dependency of the probability distribution function in a cylinder of diameter $D = 6$ at fixed polymer reservoir packing fraction $\eta_p^r = 1.90$. (at the bottom) Snapshot of the multiple domain state in the case of $D = 6$ and $L = 1000$.

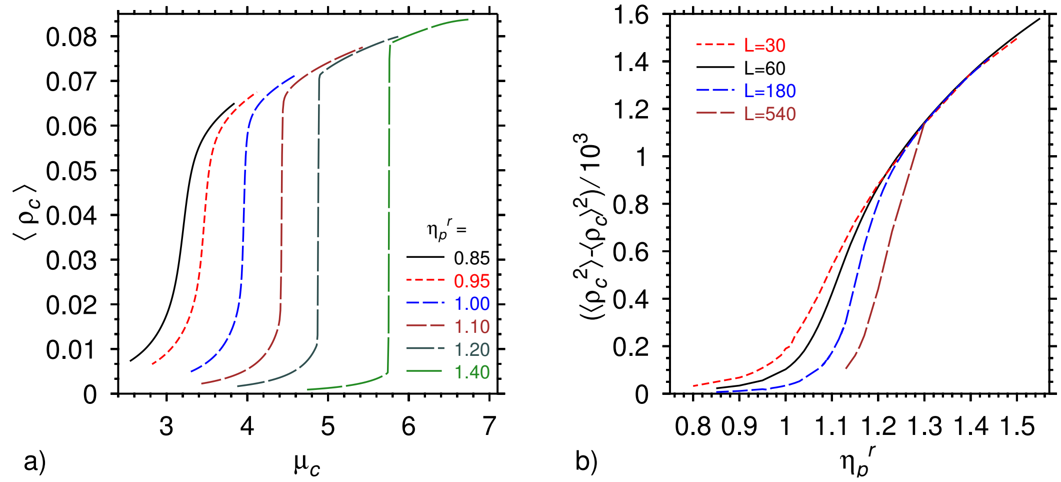

Figure 4.6.: a) First momentum (averaged colloid number density) is shown as a function of the chemical potential for different polymer reservoir volume fractions in a cylinder of diameter $D = 12$ and length $L = 60$. b) The maximum value of the density fluctuation is plotted versus η_p^r for a cylinder of diameter $D = 12$.

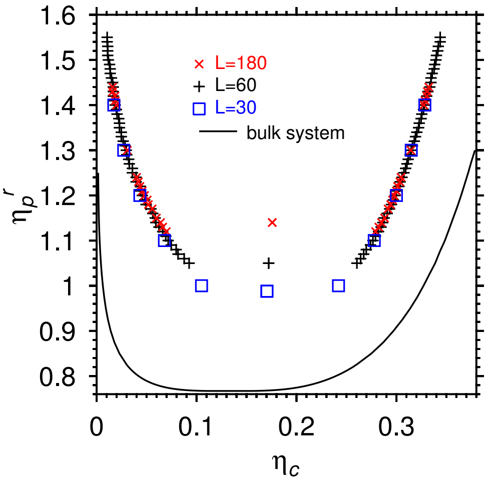

Figure 4.7: "Phase diagram" of the AO model in a cylindrical pore of diameter $D = 12$ and lengths $L = 30$, 60 and 180, as indicated. The full curve is the bulk coexistence curve [78]. Note that the points shown near $\langle\eta_c\rangle \approx 0.16$ to 0.17 mark $\eta_{p,c}^r(D, L)$ for three choices of L.

step, the colloidal density fluctuation $\Delta^2 = \langle\rho_c^2\rangle - \langle\rho_c\rangle^2$ was determined as a function of μ_c at fixed η_p^r. The chemical potential of the colloids where the maximum occurs ($\mu_c^{\max}$) gives an estimate for the coexistence chemical potential independently from the equal area rule result. When the center peak of the free energy landscape clearly dominates over the two side peaks and hence, the equal area rule cannot be successfully applied anymore, it is still possible to reweight the free energy function to $\mu = \mu_c^{\max}$ to obtain an estimate of the free energy at coexistence. The maximum $\Delta^2(\mu_c^{\max})$ is shown for several η_p^r in figure 4.6b. In contrast to the bulk no convergence to the curve of the thermodynamic limit is observed, but instead the curves shift more to the right when increasing the cylinder length. The turning points of the curves give an estimate for a pseudo-critical polymer reservoir packing fraction. However, in a finite system it is more accurate to define a pseudo-critical point via an extension of the equal area rule to three peaks. The pseudo-critical point is defined as the value of η_p^r where the probability of observing a multi-domain state overturns the probability of observing a demixed state, which means that the area under the middle peak is the same as the sum of the areas of the gas and the liquid peak. This definition was used to draw the pseudo-critical points $\eta_{p,c}^r(D, L)$ into the "phase diagram" shown in figure 4.7. The plotted binodals illustrate the shift in the coexistence densities which occurs in general for confined systems as well as the disappearance of the (global) phase separation when increasing the cylinder length.

The Disappearance of Hysteresis Effects

Another point of view on the finite size dependency is to look at the barrier height the system has to overcome at coexistence to "jump" from the gas into the multiple domain phase or from the liquid to the multiple domain phase (see Fig. 4.4b). Due to the asymmetry of the probability distribution the barrier height was averaged before being plotted (for $D = 12$) in figure 4.8. The barrier height vanishes at higher values of η_p^r when increasing the cylinder length[1].

Directly related to the barrier height and also accessible to experiments is the observation of adsorption hysteresis curves [123]. In the grand canonical ensemble this is simply the average volume fraction of colloids η_c as a function of the chemical

---

[1] The abscissa variable $1/\eta_p^r$ was chosen in order to compare qualitatively with the Ising model where the barrier height is plotted versus the temperature T [1, 2].

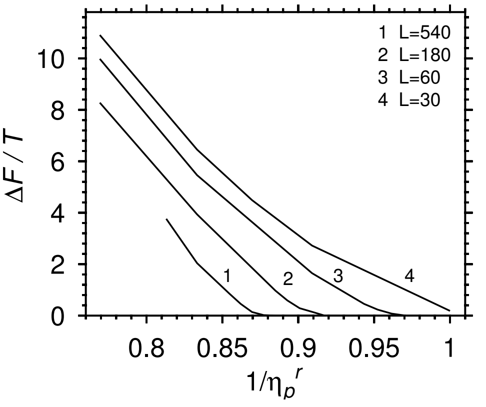

Figure 4.8: The barrier height $\Delta F/T$ for various cylinder lengths at coexistence as a function of inverse polymer reservoir packing fraction. The shown values are obtained as $\Delta F = \frac{1}{2}(\Delta F_g + \Delta F_l)$. Note that the bulk critical point in the AO model occurs at $1/\eta_p^r \approx 1.3$.

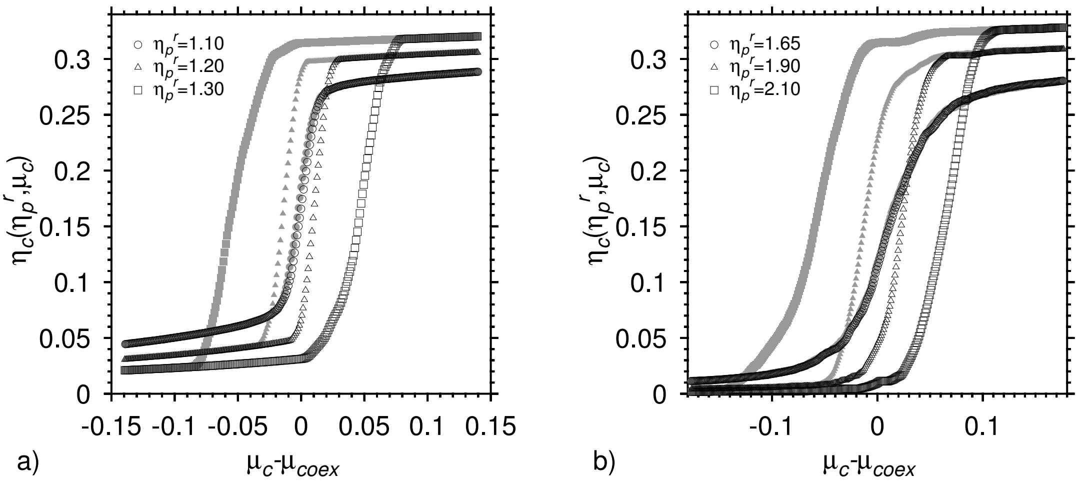

Figure 4.9.: Two hysteresis plots for the AO model. The chemical potential was varied in steps of $0.001k_BT$. Several simulation runs (up to 112) were averaged. For high polymer reservoir packing fractions large sample to sample fluctuations occur. The open symbols show data for which the chemical potential was increased stepwise while the full symbols show data for which the value of the chemical potential was decreased step by step. The plots show the disappearance of the hysteresis for a system with $D = 12$ and $L = 180$ (a) and for a system with $D = 6$ and $L = 100$ (b).

potential μ_c, where μ_c is linearly varied over time during the simulation. It is clear that at sufficiently high polymer reservoir packing fraction where the free energy landscapes possess a high free energy barrier between the two coexisting phases the function $\eta_c(\mu_c)$ follows the branches of a hysteresis curve. One can highlight the multidomain occurrence in a cylinder by looking at the behavior of such hysteresis curves. While in the bulk the hysteresis disappears at the critical temperature, in a quasi one-dimensional confinement one expects the disappearance of hysteresis effects already at the pseudo-critical point where the system is still locally ordered. This expectation is motivated by figure 4.8 in which one sees that the free energy barrier becomes very small close to the pseudo-critical points. Indeed figure 4.9 shows exactly that the hysteresis vanishes shortly before the free energy barrier disappears completely (the two peaks transform to shoulders in the free energy landscape picture). Figure 4.9b shows the hysteresis behavior in the pore of diameter $D = 6$ and has to be compared with figure 4.5a where the free energy barrier vanishes going from $\eta_p^r = 1.70$ to $\eta_p^r = 1.60$, which is in nice agreement with the collapse of the two curves in the present figure at $\eta_p^r = 1.65$. A variation of the cylinder length at a fixed η_p^r is rather difficult in the case of the AO model because the Monte Carlo relaxation time increases drastically with increasing cylinder length. In the case of the Ising model, one observes a lowering in the hysteresis critical temperature when increasing the length of the cylinder (see Refs. [1, 2]).

Some comments on the underlying Monte Carlo dynamics are necessary: As in experiments, the pronunciation of hysteresis effects is dependent on how fast and with which step size the chemical potential is varied. Therefore, there is no *exact* correspondence between the pseudo-critical points in the “phase diagram” and the value of η_p^r at which the hysteresis disappears.

4.2.3. Analysis in the Canonical Ensemble

The following technique allows to get a qualitative view of the same effects from a simple canonical ensemble or even from MD simulations. The basic idea is to equilibrate a very long cylinder at a state where multiple domains exist. Once equilibrium is reached one starts to collect data in the following manner: Separate the system in a set of subsystems which differ by their length. For example, a cylinder of length $L = 100$ can be separated into subsystem sets $\{2 \times 50,\ 3 \times 33.33,\ 4 \times 25, \ldots\}$. Within these smaller subsystems one measures the probability distribution $P(\eta_c)$ similar to grand canonical simulations. For small subsystems one gets a double peak distribution. When increasing the subsystem length, at some point more than one interface can be observed and a third peak is starting to grow in the middle.

Figure 4.10 shows clearly how the third peak appears as the length of the cylindrical subsystems is increased. One can also recognize that the system at higher polymer reservoir packing fraction keeps its double peak structure longer when the length of the subsystems is increased (especially by looking at the contour plots when the side peaks start to disappear).

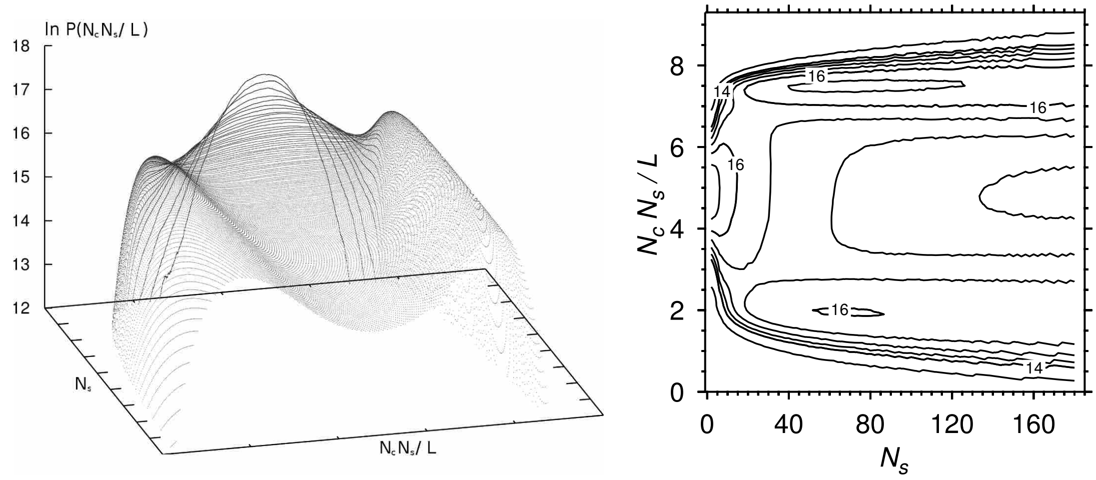

(a) Third peak development for $\eta_p^r = 1.10$.

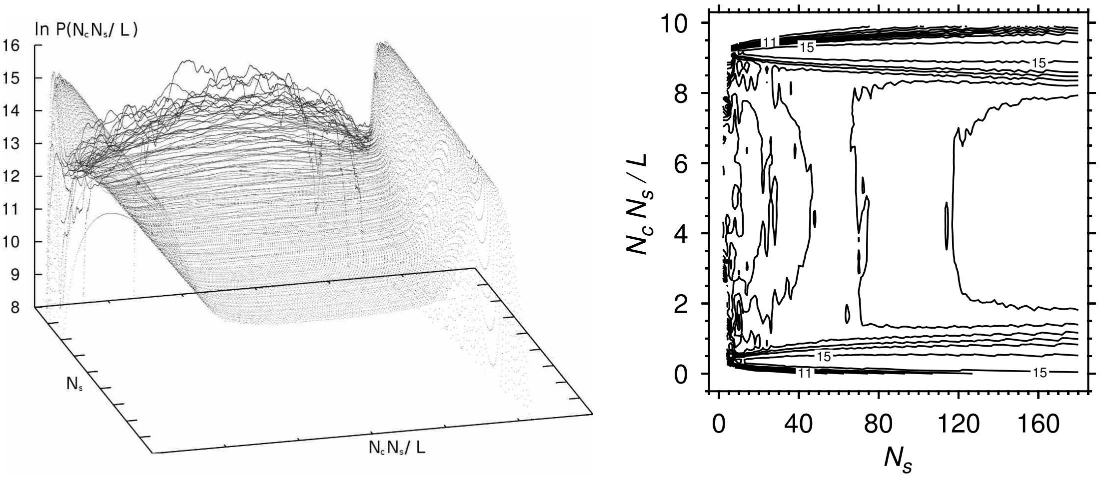

(b) Third peak development for $\eta_p^r = 1.50$.

Figure 4.10.: The growth of the middle peak from the view of the subsystem ensemble for a cylinder of a total length of $L = 1800$ and diameter $D = 12$. N_c is the number of colloids and N_s is the number of subsystems the cylinder is divided into. The height of the shown curves is the logarithm $\ln(P(N_cN_s/L))$.

4.3. Conclusion

All the graphs verify the same fundamental behavior of the AO model in a quasi one-dimensional confinement: Phase transitions in cylindrical pores are rounded and characterized by the pore radius R and the pore length L. The explanation for this lies in the correlation length ξ_z expected to vary in analogy to the one-dimensional Ising model for low temperatures and $L \to \infty$ as described by equation 4.1. The cylinder length L does not influence this correlation length in this approximation. This means that at some point the cylinder length can exceed the correlation length so that multiple domains can be formed in the pore. The typical picture that interfaces between two coexisting phases lead to free energy barriers (or areas of low probability in case of $P(\eta_z)$) does not hold in quasi one-dimensional systems with sufficiently large L. The translational entropy of interfaces grows when increasing the cylinder length while the free energy barrier height of a single interface stays constant. This interplay between the interfacial free energy and the translational entropy of the interface is finally responsible for the multiple domain states.

CHAPTER

5

SPHERICAL CONFINEMENT

The huge interest in nanomaterials and their application in science [124–126], industry and our daily life (shoe creme, food, etc.) demands understanding of their basic properties. Nanomaterials are defined as natural, incidental or manufactured materials containing particles, in an unbound state or as an aggregate or as an agglomerate where the majority of particles as well as one or more external dimensions is in the range of $1nm$ to $100nm$ (legal definition of nanomaterials from [127]). Since the size of the constituents of the material and the material itself are of the same order of magnitude, the material may exhibit completely different properties than the corresponding bulk material. The effects due to surface properties may influence the phase behavior of the system, e.g. shift the transition points, and in general the finite system size leads to a rounding of phase transitions. The influence of surface effects in small systems was studied in the case of crystallization of nanoscale liquid clusters. Already predicted 1909, the freezing transition is expected to be shifted towards lower temperatures due to higher surface free energy of the crystalline cluster in comparison to the liquid [128]. Experiments and simulations regarding gold nanoclusters confirmed the prediction [129–131]. In nanocavities the situation is similar, however, the system is not at the triple point and surrounded by a gas (as in the case of the above mentioned clusters) but is surrounded by solid walls. Especially in the case of binary mixtures where one species may favor to wet the walls, it is clear that the wetting properties of the system influence the phase behavior but at the same time also the wetting transition [132] of the system is modified by the finite size of the cavity [133] (for the case of confinement of colloid-polymer mixtures in thin films between planar walls see Ref. [31]). Here, colloid-polymer mixtures are studied confined in spherical cavities.

Understanding phase transitions in spherical confinement plays an important role, since the spherical shape of capsules appears in a wide range of applications (mini emulsions [134–136], porous networks, containers for drug delivery, etc.). As in the previous chapter, the AO interaction model is chosen as a model for colloid-polymer

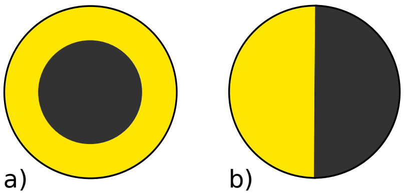

Figure 5.1: Two types of morphology for phase coexistence in spherical confinement as schematic two-dimensional sketch. (a) Complete wetting. (b) Partial wetting, "neutral" wall ($\theta = 90^o$).

mixtures and hard (structureless) walls restrict the center of particles to the volume specified by $x^2 + y^2 + z^2 < (R - \sigma_w)^2$, where R is the radius of the spherical cavity and σ_w is the wall interaction range. The unit length scale is set (in contrast to the studies in the previous chapters) by the colloid diameter $d_c = 2r_c = 1$. The aspect ratio between polymer and colloid diameter is again $q = 0.8$. Here, the phase separation of the AO model is influenced by the finite size of the sphere and the wetting properties of the binary mixture with respect to the wall. These wetting properties determine the morphology of phase coexistence. While at "neutral" walls partial wetting and, therefore, a Janus-like morphology (Fig. 5.1b) is expected, in the case of complete wetting a spherical shell structure exists at phase coexistence (Fig. 5.1a).

The structure of this chapter is two-folded. As a first step, the (finite size) "phase diagram" for wall interaction ranges $\sigma_{wc} = 0.5$ and $\sigma_{wp} = 0.4$, which correspond to the radius of the colloid or polymer respectively, is calculated. The crucial knowledge which wall interaction ranges correspond to which wetting behavior was studied within the context of a diploma thesis by collaborator ANTONIA STATT. By applying the "ensemble switch method" (introduced in chapter 6) to the polymer-rich and colloid-rich phase of the AO model it was possible to drive the system from complete wetting of the colloids via partial wetting to complete wetting of the polymers by varying the colloid-wall interaction range σ_{wc} at constant polymer-wall interaction range $\sigma_{wp} = 0.4$ (see Ref. [9]). The choice of $\sigma_{wc} = 0.5$ corresponds to the complete wetting situation and hence, morphology type "a" (Fig. 5.1a) is expected at phase coexistence. As a second step, the polymer reservoir packing fraction is fixed and the interplay of wetting and finite pore size is studied in detail regarding shifts of the phase transition.

5.1. Phase Behavior

To examine the phase behavior of the AO model under spherical confinement, the wall interaction parameters are fixed to $\sigma_{wc} = 0.5$ for the colloid-wall interaction and $\sigma_{wp} = 0.4$ for the polymer-wall interaction which corresponds to the situation of complete wetting of the colloids at the wall. As in the previous chapter, cluster move based grand canonical Monte Carlo simulations together with successive umbrella sampling or "Wang-Landau sampling" are performed to calculate free energy landscapes. Figure 5.2a shows exemplary how the transition from the polymer-rich to the colloid-rich phase proceeds at fixed $\eta_p^r = 1.40$. The transition happens in a smooth manner since finite size induced phase transitions like in the bulk such as the evaporation-condensation transition (from gas to droplet) do not appear (see also chapter 3 and references [80–83]).

In contrast to the bulk colloidal droplet formation, here, one observes the growth of

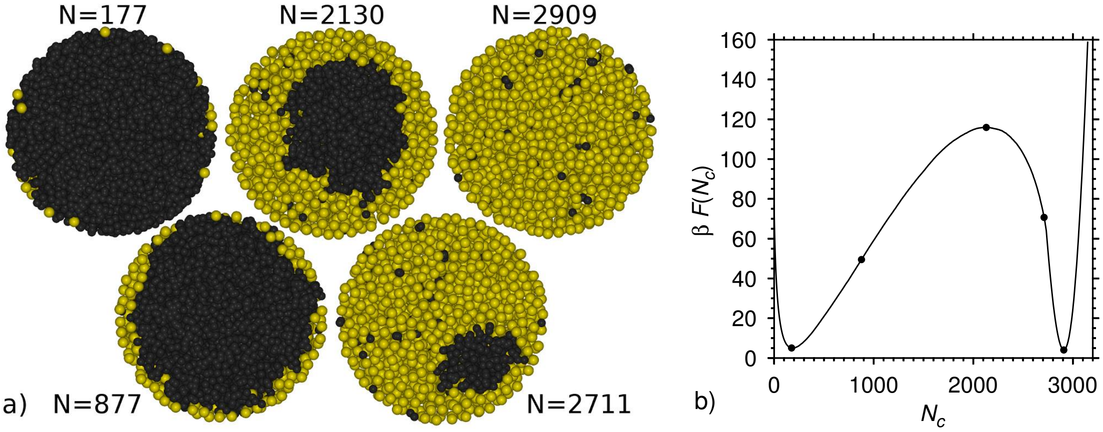

Figure 5.2.: (a) Snapshots of the gas-liquid phase coexistence in a spherical cavity of radius $R = 10$ at $\eta_p^r = 1.40$. The anterior half of the sphere is cut off, so that one looks at the center plane. The numbers close to the spheres indicate the actual number of colloids in the system. (b) Free energy landscape for the AO model under spherical confinement with radius $R = 10$ at $\eta_p^r = 1.40$ at phase coexistence. The bullets indicate the position of the snapshots in part (a) in terms of the colloid particle number.

a colloid layer which is attached to the wall. This layer is smoothly growing until the colloid-rich phase is reached. This smoothness, which can be seen directly in the free energy landscape (see Fig. 5.2b), is typical for the complete wetting behavior and does not disappear for larger spheres (also see the derivatives of free energy landscapes in the next section, Fig. 5.5b). Every change in the colloid packing fraction η_c changes the interfacial area of the two coexisting phases. Hence, the free energy barrier is relatively sharply peaked, i.e. a flat plateau cannot exist. The snapshot with colloid particle number $N_c = 2130$ illustrates nicely the type “a” morphology. One can also recognize that the polymer droplet has a certain freedom with respect to its exact position relative to the center of the cavity, but is “not allowed” to attach to the wall.

Another important aspect of the free energy function is its high degree of asymmetry. The transition kinetics are, therefore, different depending on whether one goes from the polymer-rich to the colloid-rich phase or the other way around. There exists no nucleation barrier going from the polymer-rich phase towards the coexistence region, since there is already a thin colloid layer at the walls which can grow easy. At the other side, in the case of the transition from the colloid-rich phase to the polymer-rich phase, a polymer droplet has to nucleate (in the “bulk”) and hence, the free energy exhibits a high slope at this point.

Via histogram reweighting (equal area rule) the coexistence densities can be extracted from the free energy landscapes. The phase diagram was recorded for three different sphere sizes $R = 5$, 7.5, 10. Simulations were carried out at $\eta_p^r = 0.85, 0.90, 1.00, \ldots, 1.40$. The rest of the data points was obtained via histogram extrapolation. Figure 5.3a shows the chemical potential of the colloids at coexistence μ_c for various polymer reservoir packing fractions. Over the whole range of phase coexistence, μ_c increases when increasing the radius of the cavity. This property is directly related to the complete wetting of the colloids and is discussed in more detail in the next section.

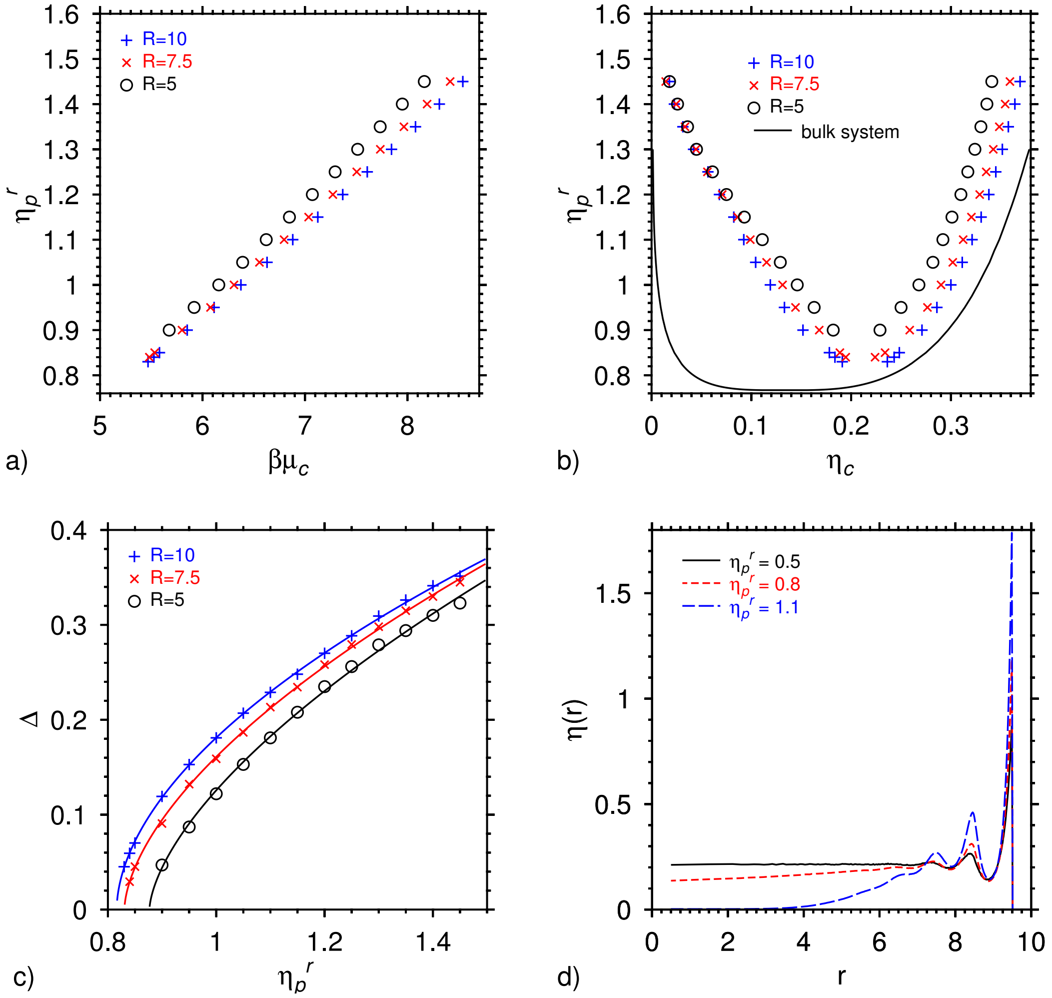

Figure 5.3.: Finite size phase diagrams for the AO model in spherical confinement (a) in the plane of $\beta\mu_c$ and η_p^r ($\beta\mu_c$ is the coexistence chemical potential of the colloids) and (b) in the plane of η_c, η_p^r. (c) Order parameter $\Delta = \eta_{c,\mathrm{liq}} - \eta_{c,\mathrm{gas}}$ as a function of polymer reservoir packing fraction. The full lines are fits $f(\eta_p^r) \propto t^\beta$, with $t = \frac{\eta_p^r}{\eta_{p,c}^r} - 1$. (d) Radial density profiles for various polymer reservoir packing fractions at $\eta_c = 0.214$ ($R = 10$).

As expected, the values for the coexistence densities lie between the binodal branches of the bulk phase diagram (Fig. 5.3b). An approach to the bulk coexistence densities when increasing R is visible, but in the case of the gas branch rather slow. The binodals end in pseudo-critical points near $\eta_p^r \approx 0.8 \ldots 0.9$. One possible way to define the position of the pseudo-critical points is to use the relation $\eta_{cl} - \eta_{cg} \propto (\eta_p^r/\eta_{p,c}^r - 1)^\beta$, where the "critical exponent" β and the "critical polymer reservoir packing fraction" $\eta_{p,c}^r$ are treated as fit parameters. Figure 5.3c illustrates the fits (full lines).

The asymmetry of the gas branch is transferred to the order parameter $\Delta = \eta_{c,\mathrm{liq}} - \eta_{c,\mathrm{gas}}$ (see Fig. 5.3c). Therefore, the function $\Delta(\eta_p^r) = \mathrm{const}(\eta_p^r/\eta_{p,c}^r - 1)^\beta$ results in a much higher exponent β in comparison to the bulk for small sphere radii. The fit parameters are given in table 5.1. Such a fit is not the only possible choice for the definition of a pseudo-critical point; observing the maximum of the density fluctuations as a function of the polymer reservoir packing fraction would be an

R	const	$\eta^r_{p,c}$	β
5	0.431(5)	0.876(5)	0.63(2)
7.5	0.415(2)	0.830(1)	0.597(8)
10	0.408(1)	0.816(1)	0.544(6)

Table 5.1: Fit parameters for the order parameter function (see the main text and figure 5.3c). The last number in brackets is the error.

alternative way (also leading to different values). In a finite system the transition from a bimodal free energy function to a unimodal free energy function is analytic which results in an effective exponent $\beta = 0.5$. Figure 5.3d shows the change in the radial density profile of the colloids when going through the critical region at fixed colloid packing fraction $\eta_c = 0.214$. One can clearly identify the transition from the homogeneous state with uniform density (apart from the walls) to the demixed state where the colloid density vanishes in the center of the cavity. Note that this behavior is only visible in the case of a second order transition to morphology type “a”, because the orientational average of $\eta(r)$ would lead to a radially constant density in morphology type “b”.

5.2. Interplay of Wetting and Finite Pore Size

As already mentioned, the transition point μ_c varies for different radii of the cavity. This quite pronounced variation is a result of the complete wetting property of the system and is expected to disappear in the case of neutral walls (90^o contact angle) as it is made plausible in the following.

5.2.1. Theoretical Aspects

The phase coexistence of the vapor (labeled as v) and the liquid (labeled as l) phase of the AO model in the bulk with free energy F_b, entropy S and volume V serves as a starting point to estimate the functional dependency $\mu_c = \mu_c(R) \equiv \mu_c^R$. The inverse temperature is set to $\beta = 1$ throughout. The free energy of the system is decomposed into bulk and surface terms

$$F(\eta_p^r, \mu_c, \sigma_{wc}, R) = V\, f_b(\eta_p^r, \mu_c) + A\, f_s(\eta_p^r, \mu_c, \sigma_{wc})\,,\ \ R \to \infty\ \ . \tag{5.1}$$

Note, however, that $f_s(\mu_c, \sigma_{wc})$ may have a residual dependence on R if one wants to use this decomposition not only in the limit $R \to \infty$ but for all R. In this case a more general Ansatz for f_s has to be chosen, e.g.

$$f_s(\eta_p^r, \mu_c, \sigma_{wc}, R) = \frac{f_s(\eta_p^r, \mu_c, \sigma_{wc})}{1 + 2\delta/R + 2(l/R)^2}\,, \tag{5.2}$$

where δ is the so-called “Tolman length” and l another length scale derived from second order terms [81]. However, this problem is disregarded here and, using $A = 4\pi R^2$ and $V = \frac{4}{3}\pi R^3$, Eq. 5.1 can be written as

$$F(\eta_p^r, \mu_c, \sigma_{wc}, R)/V = f_b(\eta_p^r, \mu_c) + \frac{3}{R} f_s(\eta_p^r, \mu_c, \sigma_{wc})\,,\ \ R \to \infty\,.$$

Using the general relations for the number density of the colloids

$$\begin{aligned}\rho_c &= -\left(\frac{\partial(F/V)}{\partial\mu_c}\right)_{\eta_p^r,\sigma_{wc}}, \quad \rho_c^b(\eta_p^r,\mu_c) = -\left(\frac{\partial f_b(\eta_p^r,\mu_c)}{\partial\mu_c}\right)_{\eta_p^r},\\ \text{and} \qquad & \rho_c^s(\eta_p^r,\mu_c,\sigma_{wc}) = -\left(\frac{\partial f_s(\eta_p^r,\mu_c,\sigma_{wc})}{\partial\mu_c}\right)_{\eta_p^r,\sigma_{wc}},\end{aligned}$$

which is the so-called surface excess density, one gets (again neglecting the residual R-dependence that ρ_c^s may have)

$$\rho_c(\eta_p^r,\mu_c,\sigma_{wc}) = \rho_c^b(\eta_p^r,\mu_c) + \frac{3}{R}\rho_c^s(\eta_p^r,\mu_c,\sigma_{wc})\,.$$

When considering the vapor-liquid phase coexistence of the AO model in the bulk, the two free energies F^v and F^l have to be equal:

$$\begin{aligned}F^v(\eta_p^r,\mu_c,\sigma_{wc},R) &= F^l(\eta_p^r,\mu_c,\sigma_{wc},R) \Leftrightarrow\\ f_b^v(\eta_p^r,\mu_c) + \frac{3}{R}f_s^v(\eta_p^r,\mu_c,\sigma_{wc}) &= f_b^l(\eta_p^r,\mu_c) + \frac{3}{R}f_s^l(\eta_p^r,\mu_c,\sigma_{wc})\,. \qquad (5.3)\end{aligned}$$

In the bulk phase coexistence occurs at μ_c^∞: $f_b^v(\eta_p^r,\mu_c^\infty) = f_b^l(\eta_p^r,\mu_c^\infty)$. Since it is reasonable to expect that for large R the capillary condensation type effects will be small, a Taylor expansion in μ_c close to μ_c^∞ is suitable:

$$\begin{aligned}f_b^v(\eta_p^r,\mu_c) &= f_b^v(\eta_p^r,\mu_c) - \rho_c^v(\eta_p^r)(\mu_c-\mu_c^\infty) \qquad (5.4)\\ f_b^l(\eta_p^r,\mu_c) &= f_b^l(\eta_p^r,\mu_c) - \rho_c^l(\eta_p^r)(\mu_c-\mu_c^\infty)\,. \qquad (5.5)\end{aligned}$$

Similarly the surface free energies are expandable as:

$$\begin{aligned}f_s^v(\eta_p^r,\mu_c,\sigma_{wc}) &= f_s^v(\eta_p^r,\mu_c^\infty,\sigma_{wc}) - \rho_s^v(\eta_p^r,\sigma_{wc})(\mu_c-\mu_c^\infty) \qquad (5.6)\\ f_s^l(\eta_p^r,\mu_c,\sigma_{wc}) &= f_s^l(\eta_p^r,\mu_c^\infty,\sigma_{wc}) - \rho_s^l(\eta_p^r,\sigma_{wc})(\mu_c-\mu_c^\infty)\,. \qquad (5.7)\end{aligned}$$

Using equations 5.4 to 5.7 in equation 5.3 yields that the transition occurs at a chemical potential μ_c^R satisfying the equation

$$\begin{aligned}(\mu_c^R-\mu_c^\infty)\left\{\rho_c^l(\eta_p^r) - \rho_c^v(\eta_p^r) - \frac{3}{R}\left[\rho_s^v(\eta_p^r,\sigma_{wc}) - \rho_s^l(\eta_p^r,\sigma_{wc})\right]\right\} &=\\ \frac{3}{R}\left(f_s^l(\eta_p^r,\mu_c^\infty,\sigma_{wc}) - f_s^v(\eta_p^r,\mu_c^\infty,\sigma_{wc})\right)&\end{aligned}$$

and hence

$$\mu_c^R = \mu_c^\infty - \frac{f_s^v(\eta_p^r,\mu_c^\infty,\sigma_{wc}) - f_s^l(\eta_p^r,\mu_c^\infty,\sigma_{wc})}{\frac{R}{3}\left(\rho_c^l(\eta_p^r) - \rho_c^v(\eta_p^r)\right) - \left[\rho_s^v(\eta_p^r,\sigma_{wc}) - \rho_s^l(\eta_p^r,\sigma_{wc})\right]}\,. \qquad (5.8)$$

Equation 5.8 is the central result which shows that $\mu_c^R - \mu_c$ is not simply proportional to $1/R$, but exhibits also a $1/R^2$ correction. This can be seen by an expansion of Eq. 5.8

$$\mu_c^R = \mu_c^\infty - \frac{3(f_s^v - f_s^l)}{\rho_c^l - \rho_c^v}\frac{1}{R} - \frac{9((f_s^v - f_s^l)(\rho_s^v - \rho_s^l))}{(\rho_c^l - \rho_c^v)^2}\frac{1}{R^2} + \mathcal{O}(1/R^3)\,. \qquad (5.9)$$

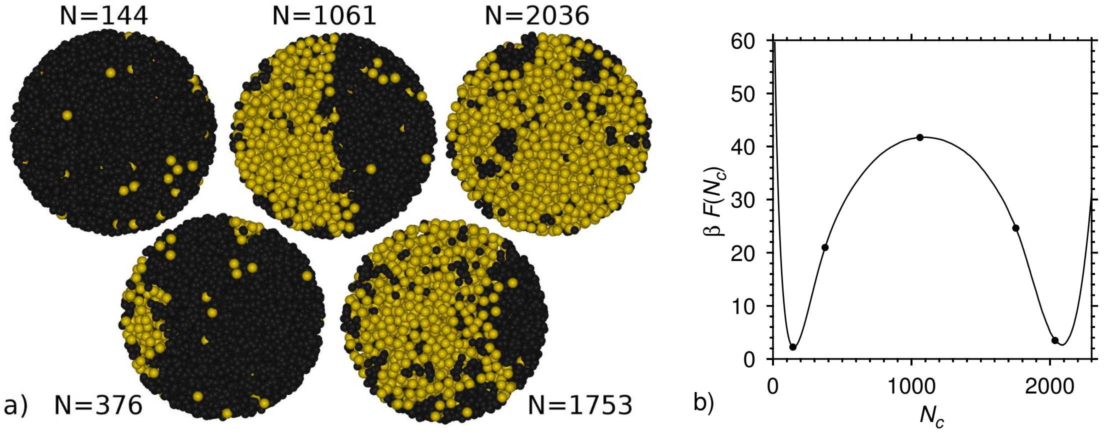

Figure 5.4.: (a) Snapshots of the gas-liquid phase coexistence in a spherical cavity of radius $R = 10$ at $\eta_p^r = 0.94$. The anterior half of the sphere is cut off, so that one looks at the center plane. The numbers close to the spheres indicate the actual number of colloids in the system. (b) Free energy landscape in the case of neutral walls ($\sigma_{wc} = 0.6755$) at $\eta_p^r = 0.94$ and $R = 10$. Full circles mark the positions of the snapshots shown in part (a).

From the expansion it is clear that for large R the vapor and liquid wall tension difference can be obtained as

$$\lim_{R\to\infty} \frac{\partial \mu_c^R}{\partial(1/R)} = -\frac{3(f_s^v - f_s^l)}{\rho_c^l - \rho_c^v}\,. \tag{5.10}$$

Of course, one has to mention, as a caveat, that the expansions Eqs. 5.4-5.7 require that quadratic terms in μ_c still are negligible. The expansion to the second order including effects related to the bulk susceptibility $\chi_b = -(\partial^2 f_b/\partial\mu_c^2)_{\eta_p^r,\mu_c=\mu_c^\infty}$ and the analogously defined surface excess susceptibilities χ_s is not carried out here.

5.2.2. Simulation Results

Equations 5.9 and 5.10 predict that in general the phase transition in spherical cavities is shifted with respect to the bulk. One can also see that in the special case of a 90^o contact angle, where $f_s^v - f_s^l = 0$, this shift should vanish. This fact and the $1/R$ and $1/R^2$ dependence of μ_c^R is addressed in the following by the calculation of free energy landscapes at fixed polymer reservoir packing fraction $\eta_p^r = 0.94$ but varying sphere radii R and colloid-wall interaction range σ_{wc}. First of all, a contact angle $\theta = 90^o$ is studied, which is expected to appear at a colloid-wall interaction range of $\sigma_{wc} \approx 0.6755$ (Ref. [9]). This special case of partial wetting is not compatible with the core-shell structure observed in Fig. 5.2a and the Janus-like (half-half) phase coexistence morphology is expected. Indeed, figure 5.4a shows the phase transition from the polymer-rich to the colloid-rich phase starting with the nucleation of a colloidal droplet at the wall ($N = 376$) and going via the Janus-like structure ($N = 1061$) to the wall-attached polymer droplet ($N = 1753$) before reaching the liquid phase. Similar to figure 5.2b the corresponding free energy function (Fig. 5.4b) exhibits a smooth behavior, however, the function is now much more symmetric and the typical property of the AO model, a narrow gas peak and a wider liquid peak, is recovered. Note that the expected kinks associated with the

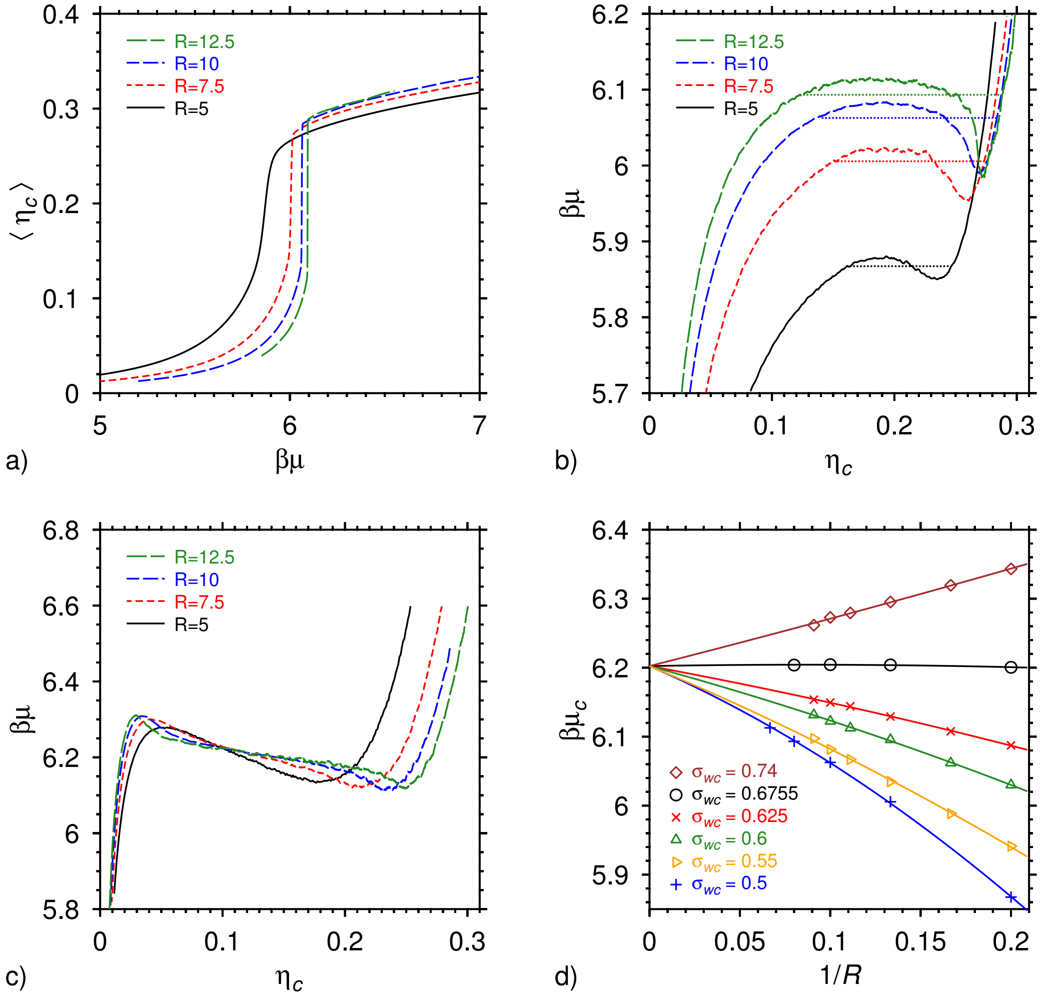

Figure 5.5.: (a) Adsorption isotherms for various radii R in the case of complete wetting. (b) Derivatives of the free energy for various cavity radii. The inflection points in (a) and the horizontal dashed lines in (b) indicate the coexistence chemical potential of the colloids μ_c^R. (c) Derivatives of the free energy as a function of colloid packing fraction η_c in the case of neutral walls. (d) Convergence behavior of the chemical potential as a function of cavity radius for various colloid-wall interaction ranges. The full lines are parabolic fits.

nucleation of the colloidal and polymer droplet at the wall are not clearly visible (although the derivative of the free energy landscape starts showing smeared out jumps in figure 5.5c, which is discussed in more detail in the next paragraphs). Well pronounced kinks in the free energy landscapes are only expected for higher polymer reservoir packing fractions and for larger sphere radii.

As a next step, the two extreme cases of complete wetting ($\sigma_{wc} = 0.5$) and the partial wetting situation with $\theta = 90^o$ are compared in more detail. Figure 5.5 illustrates the shift of the coexistence chemical potential of the colloids μ_c^R in the case of the complete wetting situation ($\sigma_{wc} = 0.5$) where the turning points of $\langle\eta_c\rangle = \frac{\pi}{6V}\int dN_c \ln F(\mu_c, N_c)N_c / \int dN_c \ln F(\mu_c, N_c)$ define μ_c^R. In figure 5.5b the axes are exchanged and $\beta\mu_c$ is directly calculated via the derivative of the free energy $\beta\mu_c = \partial F(N_c)/\partial N_c$. The coexistence densities appear at the end of the horizontal lines the height of which corresponds to the colloid chemical potential at

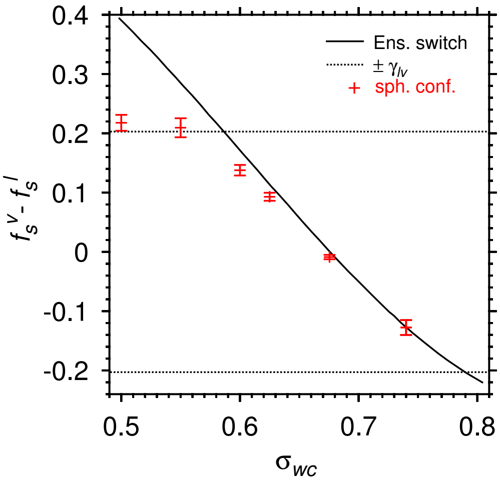

Figure 5.6: Surface free energy difference extracted from the shift in the chemical potential at coexistence in comparison to the ensemble switch method results from reference [9]. The intersection of the full line with the dashed lines marks the colloid-wall interaction range where the wetting and drying transitions happen respectively.

coexistence. The function $\mu(\eta_c)$ always shows in the center region a well defined intersection point with these lines which is directly related to the relatively sharp peak at the center of the free energy landscapes. In contrast, in the case of neutral walls (see Fig. 5.5c) the colloid chemical potential at coexistence does almost not vary with R and derivatives of the free energy landscape develop a horizontal plateau in the center when going to large cavity radii R. Furthermore, one can recognize the development of smeared out jumps at both ends of the center region indicating heterogeneous nucleation barriers. The barrier associated with the nucleation of the colloidal droplet is clearly not visible in the complete wetting situation in figure part (b).

Finally, figure 5.5d shows the coexistence chemical potential μ_c^R as a function of $1/R$ for different wetting situations, which can be directly compared with equations 5.9 and 5.10. The full lines are parabolic fits where the intersection with the ordinate was fixed to the chemical potential of the colloids at coexistence in the bulk system $\beta\mu_c^\infty = 6.2023$. The expected parabolic behavior is in good agreement with the simulation data. The slope of the fit at $\frac{1}{R} = 0$ is directly related to the surface free energy difference and, hence, can be compared with the very precise wall tension calculations in reference [9]. As coexistence density difference in the bulk the value of $\rho_c^l - \rho_c^v = 0.57442$ from reference [61] was used. Figure 5.6 shows the resulting estimate for the surface free energies for various colloid-wall interaction ranges σ_{wc}. Note that there is no tunable parameter but the extracted values are completely independent from the ensemble switch method results in reference [9]. Therefore, one can conclude that the presented theory not only qualitatively describes the shift of the transition chemical potential but is also able to give quantitative results as long as neither complete drying nor complete wetting is present. The quantitative agreement is rather surprising since a lot of approximations were made. The deviation close and above the wetting transition results from the fact that the surface excess densities were assumed to be independent of the cavity radius, which is clearly not the case when a macroscopic large wetting layer tries to form in a small spherical cavity.

5.3. Conclusion

The confinement in spherical cavities of binary systems, here a colloid-polymer mixture, which exhibit a gas-liquid phase transition, plays a crucial role with respect to the properties of the phase transition, i.e. the phase coexistence morphology. By only tuning the colloid-wall interaction it is possible to create a core-shell structure or a Janus-type-like structure when both phases coexist. Furthermore, one observes a shift of the phase transition point which is directly related to the wetting properties of the confined system. This shift depends not only linearly but also quadratically on the inverse cavity radius $1/R$ and can be quantitatively described by the presented approximate theory. This insight into the phase transition properties in spherical cavities is especially valuable within the context of nanomaterials.

CHAPTER

6

CONFINEMENT BETWEEN WALLS

In this chapter the wetting behavior of a hard sphere system and the effective Asakura-Oosawa model at flat, planar walls is investigated. Both models exhibit a first order liquid to crystal phase transition. The wetting behavior in the context of liquid-like and gas-like phases was successfully studied [9, 137–140] and is rather well understood in the picture of classical nucleation theory [141]. However, the nucleation of crystals from the fluid phase, which appears in many applications such as formation of ice crystals in the atmosphere and crystallization processes in various materials, is poorly understood. The question arises, whether the macroscopic description based on Young's equations and the classical nucleation theory which assumes a macroscopic "critical nucleus" is still valid in the case of crystalline clusters. The biggest issue might be that crystalline phases are not isotropic. The crystal plane which is involved in the interface at coexistence with the surrounding liquid in the bulk (assuming a slab geometry) is typically different from the crystal plane which favors planar flat walls. In the case of complete wetting (see Fig. 6.1b) this leads to a competition between the two different surface free energies and it is a priori not obvious which crystal orientation is thermodynamically more stable. Even the description based on surface free energies itself is uncertain, since the typically heterogeneous growth of a crystalline cluster can easily result in meta-stable but long living states which are not predicted by the net balance of all free energy contributions. Under consideration of these caveats and the recent experimental observations in the field of colloidal systems such as non-spherical, rough crystalline clusters [142], the importance of thermal fluctuations [143] and the generic similarity to crystal nucleation in metals and alloys [144], the following studies are meant to contribute to the understanding of the wetting properties of colloidal crystal phases.

As already seen in chapter 5, at phase coexistence and in the presence of confining walls, one of the two phases is typically preferred by the wall. This can be expressed by Young's equation

$$\gamma_{lg}\cos(\theta) = \gamma_{wg} - \gamma_{wl}\,, \tag{6.1}$$

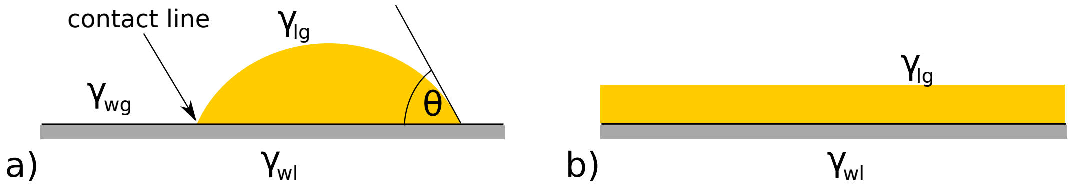

Figure 6.1.: (a) A liquid droplet surrounded by gas at the wall corresponding to a contact angle $\theta > 0^o$. (b) The complete wetting situation corresponding to $\theta = 0^o$.

which is typically formulated for a liquid droplet attached to a wall surrounded by vapor, where γ_{lg}, γ_{wg} and γ_{wl} are the liquid-gas, wall-gas and wall-liquid interfacial tensions respectively. Figure 6.1 shows the two cases of partial and complete wetting. In part (a) the condition $\left|\frac{\gamma_{wg}-\gamma_{wl}}{\gamma_{lg}}\right| \leq 1$ is fulfilled and, hence, θ can be determined by equation 6.1, while in part (b) this condition is not fulfilled and complete wetting occurs. From Eq. 6.1 it is clear that studies regarding the wetting behavior of the system of interest can be directly related to the calculation of wall tensions. One of the main tasks in this chapter is the development of a new method, the so-called ensemble switch method (section 6.1.3), which is used to determine wall tensions of both phases, the liquid phase and the crystalline phase, with a high precision.

For the hard sphere model evidence is found that complete wetting occurs when the system is confined between hard walls [34] and thus, this system is not suited to study wall attached crystalline nuclei. However, it was extensively studied in the past [26, 145–149] and therefore, will serve in this chapter as a reference system to check for the correctness of new methods. When replacing the hard walls by continuous wall interactions it is not known, in which way the wetting behavior of the system is altered. This question is answered in the following sections by investigating density profiles and by the direct calculation of wall tensions via the “ensemble switch method”. Finally, the effective AO model is investigated in a similar manner and it is shown that partial wetting occurs. The contact angle of the crystalline cluster can be influenced by changing the properties of the particle-wall interactions.

The whole studies in this chapter were performed in collaboration with DEBABRATA DEB (pressure tensor and density profile based calculations as well as direct studies of crystalline nuclei by means of geometric methods), MOHAMMAD HOSSEIN YAMANI and MARTIN OETTEL (Density Functional Theory (DFT) calculations) who are greatly acknowledged at this point for their work and helpful discussions. Especially the DFT and pressure tensor results for the hard sphere model will be present in some of the graphs providing further insight and serving as consistency checks for the ensemble switch method (for more details, see Refs. [5–8]).

6.1. Simulation Details

In the following, the simulation setup is chosen so that walls are placed at $z = \pm\frac{L_z}{2}$. Simulations are performed in the NVT-ensemble at constant particle number, simulation box volume and temperature $k_BT = 1$. In contrast to earlier chapters where a binary mixture of two particle species was studied, here, only a single particle

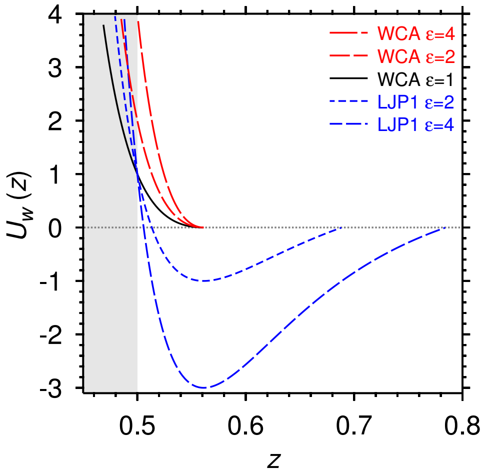

Figure 6.2: Various wall potentials (equations 6.2, 6.3 and 6.4) are shown (all with $\sigma = 0.5$). The shaded area represents the hard wall potential. The abbreviation LJP1 stands for "Lennard-Jones plus one" indicating a vertical shift by one of the ordinary Lennard-Jones potential.

type (called colloids in the following) is used. Two different pair interaction potentials between the colloids are studied, the hard sphere interaction and the effective Asakura-Oosawa interaction (see section 2.2). The unit length is the diameter (or diameter-like parameter) of the pair potential. The hard sphere model has only a single parameter, the particle diameter which is set to $\sigma = 1$ in the following. For the effective AO model the polymer reservoir packing fraction parameter is set to $\eta_p^r = 0.1$ and the ratio between polymer diameter and colloid diameter is chosen as $q = 0.15$. Phase diagrams for this parameter choices were already reported in reference [49].

6.1.1. Wall Potentials

The wall-particle pair interaction might influence the wall tensions and thus, is also expected to influence the wetting behavior, i.e. the contact angle. Therefore, various wall potentials are considered here, which are: the hard wall potential, the WCA wall potential and a shifted Lennard-Jones-like wall potential, defined as:

$$U_{w,\mathrm{hard}}(z) = \begin{cases} \infty & \text{, for } z \leq \sigma \\ 0 & \text{, else} \end{cases} , \tag{6.2}$$

$$U_{w,\mathrm{WCA}}(z,\varepsilon) = \begin{cases} 4\,\varepsilon\left[\left(\frac{\sigma}{z}\right)^{12} - \left(\frac{\sigma}{z}\right)^{6} + \frac{1}{4}\right] & \text{, for } z < 2^{1/6}\sigma \\ 0 & \text{, else} \end{cases} \tag{6.3}$$

and

$$U_{w,\mathrm{LJP1}}(z,\varepsilon) = \begin{cases} 4\,\varepsilon\left[\left(\frac{\sigma}{z}\right)^{12} - \left(\frac{\sigma}{z}\right)^{6}\right] + 1 & \text{, for } z \leq \sigma\sqrt[6]{2(\varepsilon + \sqrt{(\varepsilon-1)\varepsilon})} \\ 0 & \text{, else} \end{cases} . \tag{6.4}$$

When increasing ε in $U_{w,\mathrm{LJP1}}(z,\varepsilon)$ (from $\varepsilon = 1$) one can increase the strength of the attractive part of the potential by keeping at the same time the repulsive part so that $U_{w,\mathrm{LJP1}}(1,\varepsilon) = 1\,\forall\,\varepsilon$. Figure 6.2 illustrates the difference between the WCA potential $U_{w,\mathrm{WCA}}(z,\varepsilon)$ and the shifted Lennard-Jones potential $U_{w,\mathrm{LJP1}}(z,\varepsilon)$ with respect to the ε-dependency. Note that for $\varepsilon = 1$ the LJP1 and the WCA potential coincide.

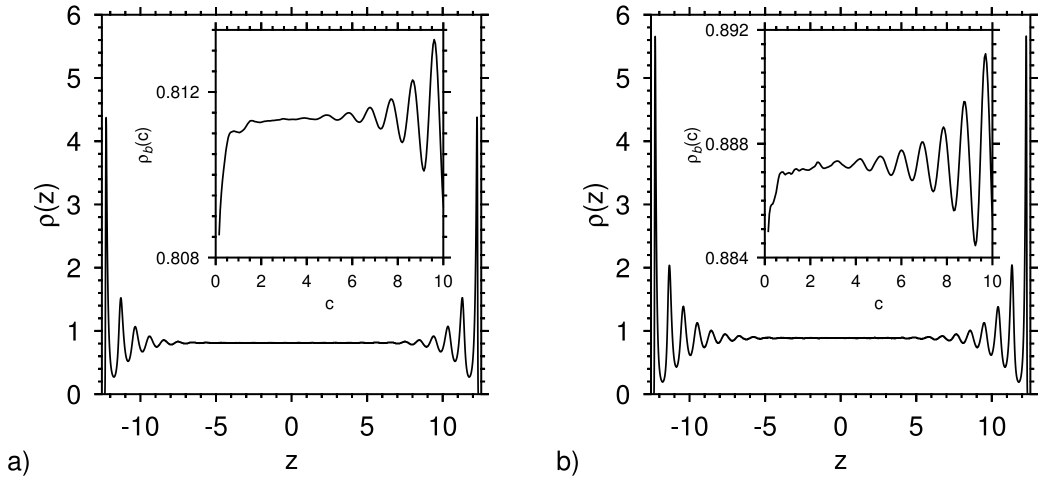

Figure 6.3.: Two density profiles of a hard sphere system for packing fractions $\eta_g \approx 0.42$ (a) and $\eta_g \approx 0.46$ (b). The wall potential is the WCA potential with $\sigma_w = 0.5$ and $\varepsilon = 1$. The linear dimensions of the simulation boxes are $L_x = L_y = 12.41786$, $L_z = 25.61184$. The insets show an estimate for the bulk density ρ_b as a function of the integration range c.

6.1.2. Density Profiles

Before proceeding with the calculation of wall tensions for investigating the wetting behavior of colloidal crystalline phases, attention has to be paid to some subtle points regarding thermodynamic quantities which have to be treated differently in comparison to the bulk situation. In the following, the hard sphere system confined between WCA walls is used as a representative example to discuss general properties of the confinement as well as to present first results regarding the influence of the wall potential. The translational invariance of the system is now broken in the z-direction so that an "origin plane" at $z = 0$ can be defined. Due to the distinguished z-axis some thermodynamic quantities become a function of the z-coordinate. A typical quantity of such a kind is the number density profile $\rho(z)$ (or the packing fraction $\eta(z) = \frac{\pi}{6}\sigma^3\rho(z)$) or the pressure of the system which is split up in parts parallel and perpendicular to the walls [150]. Figure 6.3 shows examples of density profiles in the case of a hard sphere liquid confined between two WCA walls. The walls clearly induce a layering. This layering effect decays towards the center plane of the system at $z = 0$.

The density profiles play an important role since they allow for a comparison between the Monte Carlo simulations and the density functional theory results and can also be directly used to estimate the wall tensions. Moreover, figure 6.3 points out an ambiguity which will play a crucial role in the following. In computer simulations of finite systems, there exists in general a mismatch between the global packing fraction $\eta_g = \frac{\pi}{6}\sigma^3\frac{N}{V}$, where V is the volume of the simulation box, and the so-called bulk packing fraction η_b which can be extracted from the center plateau of the density profile. While the examples in figure 6.3 suggest to simply read off the bulk density around $z \approx 0$ a closer look reveals (especially for dense systems ($\eta \approx 0.42$ to $\eta \approx 0.49$)) that still very small oscillations are visible at the plateau. The bulk

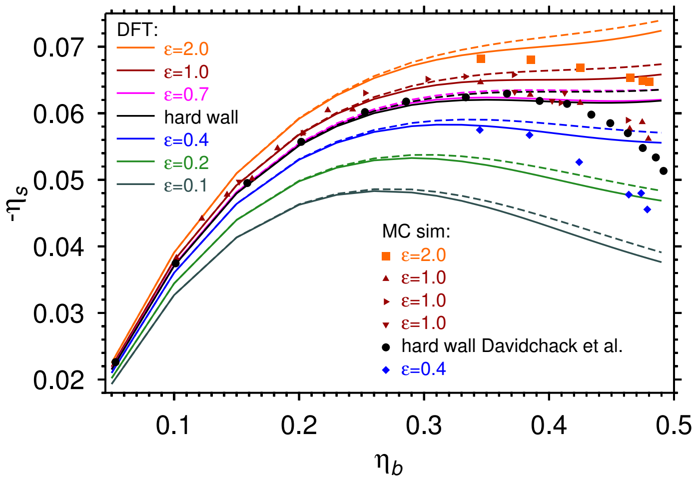

Figure 6.4.: Surface excess packing fraction η_s as a function of bulk packing fraction for hard spheres confined between WCA walls. The parameter ε of the WCA wall potential was varied as indicated. While lines represent density functional theory results, symbols indicate simulation results. In the case $\varepsilon = 1.0$ different simulation box geometries were used to check for finite size effects. Triangles pointing to the right correspond to $L_{x,y} = 5$ and $L_z = 40$. Triangles pointing down correspond to a geometry of $L_{x,y} = 13$ and $L_z = 50$. All the other symbols correspond to $L_{x,y} = 12.418$ and $L_z = 25.612$.

packing fraction can be extracted from a density profile via

$$\eta_b(c) = \frac{\pi\sigma^3}{6}\frac{\int_{-c}^{c}\rho(z)\,dz}{2c}, \tag{6.5}$$

where c sets the amount of the plateau considered for the bulk packing fraction. The insets in figure 6.3 show the influence of the integration range. While in part (a) $\rho_b(c)$ develops a plateau around $c \approx 3$, the inset of part (b) does not allow for the estimation of a value for $\rho_b(c)$ indicating that the linear dimension L_z of the simulation box is chosen still too small. A more rigorous way to define the bulk packing fraction (especially in the case of crystalline phases) is given by the limit $\eta_b = \lim\limits_{V\to\infty} \eta_g(N,V)|_{\rho_g=\text{const}}$.

Although the distance between the walls of the system shown by figure 6.3 is quite large, due to the effective thickness of the walls and the surface excess properties of the confined liquid one observes a difference of approximately 1% between global and bulk packing fractions. This issue is pointed out here, because it is the infinitely large system and, therefore, the bulk packing fraction, for which the wetting properties predicted by macroscopic theories are defined.

The influence of the variation of wall potential properties on the system can be made visible by a density profile related quantity, the so-called surface excess packing fraction η_s (which was already introduced for spherical confinement in section 5.2.1). Furthermore, this sensitive quantity allows for a first comparison between the DFT calculations and computer simulations. The surface excess packing fraction is defined as

$$\eta_s = \frac{1}{2}\int_{-L_z/2}^{L_z/2} (\eta(z) - \eta_b)\,dz\,, \tag{6.6}$$

where the factor $\frac{1}{2}$ takes the *two* walls into account. Within the context of this quantity it is important to mention the work by LAIRD and DAVIDCHACK [149], which provides highly precise estimates for the surface excess density and the wall tension in the case of hard spheres confined between hard walls. Figure 6.4 shows the literature data from reference [149] for hard spheres between hard walls in comparison to simulations results for hard spheres between WCA walls for various ε. The DFT results presented in this figures were calculated by collaborators YAMANI and OETTEL. The functional form of the excess free energy in the DFT is the so-called White Bear II functional (full lines) and its tensor modification (dashed lines). The White Bear II functional is consistent with analytic expressions for the liquid of hard spheres confined between hard walls, while the tensor modification is slightly less consistent but has the benefit to predict accurately liquid-crystal coexistence densities, bulk crystal free energies and further hard sphere crystal properties [5, 151]. The Monte Carlo simulation results for $\varepsilon = 2.0$, $\varepsilon = 0.4$ and several for $\varepsilon = 1$ in the case of $L_{x,y} = 12.418$ and $L_z = 25.612$ were provided by DEB who is acknowledged at this point. Up to a bulk packing fraction of $\eta_b \approx 0.39$ the results from DFT and from simulation agree well. Beyond this packing fraction systematic differences between theory and simulation results start to occur. The simulation results lie systematically lower and $-\eta_s$ decreases when increasing the bulk packing fraction, while all DFT results have an inflection point and even increase for the higher wall potential amplitudes. The simulation box sizes could be too small for the high packing fraction $\eta_b \gtrsim 0.46$. To rule this out, various box size were considered for WCA wall potentials with $\varepsilon = 1$ as indicated in figure 6.4. No systematic influence of the simulation box dimensions on the surface excess packing fraction are visible within the statistical errors. In addition, the data from DAVIDCHACK et al. was recorded for a system size of $L_{x,y} = 50$ and $L_z = 65$ and shows the same tendency, so that it is likely to exclude that the drop-down of $-\eta_s$ is a pure finite size effect. It is more likely that the approximate density functionals fail to predict the correct density profiles at very high packing fractions and hence, $-\eta_s$ is systematically overestimated.

Of course, differences between the DFT and the simulations with respect to the behavior of $\eta_s(\eta_b)$ will affect the wall tension prediction γ_{wl} as well. From the latter discussion one can conclude that the DFT calculations provide a valuable insight of the surface excess properties of the system and will additionally serve as an excellent consistency check for the later presented "ensemble switch method" up to a bulk packing fraction of $\eta_b \approx 0.4$. The results for the surface excess packing fraction show that the functional form of the wall potentials does modify the surface properties. Using $d\gamma \sim \eta_s(P(\eta_b))dP(\eta_b)$, where $P(\eta_b)$ is the pressure as a function of bulk packing fraction (see also [149]), it is clear that an increase of the amplitude ε of the WCA will cause an increase of the wall tension γ.

6.1.3. The Ensemble Switch Method

Within this chapter a methodology to determine wall tensions for liquid and crystalline phases is developed. The method is a modification of the thermodynamic integration method from LÖWEN [152] which was used to extract wall tensions in colloid-polymer mixtures and hard sphere crystals [153, 154].

In the original formulation by LÖWEN, the transition from a bulk system with periodic boundary conditions to a system with walls is made. The periodic boundary conditions were not modified during this process, however, in the state with completely switched on walls the interaction between particles "through" the walls were suppressed by using relatively wide walls (typically with a diameter of $\sigma = 1$). The difference between the bulk and the wall situation is represented by a parameter $\lambda \in [0, 1]$ in the Hamiltonian $\mathcal{H}(\{\boldsymbol{r}_i\}) = \mathcal{H}_b(\{\boldsymbol{r}_i\}) + \lambda \mathcal{H}_w(\{\boldsymbol{r}_i\})$. The free energy difference can therefore be integrated out by $\Delta F = \int \left\langle \frac{\partial \mathcal{H}}{\partial \lambda} \right\rangle d\lambda$. The main drawback of this method was the thickness of the walls which induces strong finite size effects since the system is compressed during the process of switching on the walls. A finite size scaling analysis to obtain the proper bulk packing fraction was not performed and the statistical errors are in general large (also in the more recent work [153, 154] where modern computers were available).

Detailed Description

The following three modifications are applied to this method to improve the quality of the results:

1. Superposition of Boundary Conditions The change in pressure when switching on wall interactions can strongly influence the free energy difference ΔF. By choosing walls of the thickness of half a particle diameter, the bulk and the wall situation become relatively similar so that the pressure difference is less pronounced. However, using thin walls automatically means that the periodic boundary conditions have to be switched on smoothly as well. This can be achieved by defining the Hamiltonian $\mathcal{H}$ of the system as a superposition (or mixture) between the Hamiltonian of the bulk system with periodic boundary conditions along the z-axis $\mathcal{H}_1$ and the Hamiltonian of the wall system without periodic boundary conditions in z-direction $\mathcal{H}_2$ ($\mathcal{H}_2$ also includes the wall potential). The mixing between these two ensembles is realized by a superposition of the form

$$\mathcal{H}(\{\boldsymbol{r}_i\}) = (1 - \kappa)\mathcal{H}_1(\{\boldsymbol{r}_i\}) + \kappa \mathcal{H}_2(\{\boldsymbol{r}_i\}) \ , \tag{6.7}$$

where $\kappa \in [0, 1]$ indicates the current mixing percentage between both ensembles the energies of which are labeled with 1 and 2. Note that compression effects can still arise, but due to the proper (smooth) handling of the periodic boundary conditions *every* wall thickness is allowed so that one can always chose a system where compression effects are minimized.

As will be explained later in more detail, equation 6.7 represents only one possibility to combine the Hamiltonians $\mathcal{H}_1$ and $\mathcal{H}_2$. Dependent on the system under investigation, a direct dependence of the Hamiltonians on κ, e.g. $\mathcal{H}_2(\kappa, \{\boldsymbol{r}_i\})$, might help to increase the smoothness of the transition from the bulk to the confined system, which is valid as long as the "pure" states are reached for $\kappa = 0$ or $\kappa = 1$ respectively. In the case of hard walls, the wall potential amplitude is set to a high but still finite value (e.g. $\varepsilon = 200 k_B T$), since otherwise the product $\kappa \mathcal{H}_2$ remains always $\kappa \mathcal{H}_2 = "\infty"$ so that a smooth transition from $\mathcal{H}_1$ to $\mathcal{H}_2$ is not possible. Similarly, the overlap penalty between hard spheres can be set to a high but finite value to allow for a proper handling of the periodic boundary conditions when the system is in a mixed state ($\kappa \approx 0.5$).

2. Calculating Free Energy Differences The free energy difference between the bulk system and the system with walls ΔF at a certain system size is obtained within a single simulation run using the "Wang-Landau-algorithm" (see chapter 2) with respect to the continuous and rather abstract reaction coordinate κ. The range of κ from zero to one is discretized into 1000 bins. While intermediate states (such as $\kappa = 0.5$) do not provide meaningful information, the free energy difference between the bulk system and the confined system $\Delta F = F(\kappa = 0) - F(\kappa = 1)$ gives an estimate for the wall surface free energy.

For dense fluid systems as well as for the crystalline phase up to 512 CPU cores were used in parallel. With this amount of processes a free energy difference ΔF can be calculated within less than 24 hours with high precision.

3. Treatment of Finite Size Effects The finite size of the simulation box influences simulation results for multiple reasons. One can distinguish between general finite size effects (which occur in almost every simulation) and confinement-specific finite size effects on free energies. Correlations between particles with their periodic images due to periodic boundary conditions, a cut off capillary wave spectrum of interfaces, a translational entropy contribution of interfaces all contribute to the first type of finite size effects. In solid structures it is also possible to introduce stress by an incorrect choice of the system size. A confinement between flat walls leads additionally to a difference between the bulk packing fraction η_b compared to the global packing fraction $\eta_g = \frac{\pi}{6}\sigma^3\frac{N}{V}$.

It is clear that one has to study carefully the finite size effects of ensemble switch simulations. However, not all finite size effects can be distinguished. The following discussion should give a feeling of the order of magnitude of the different finite size effects.

The wall tension is defined as

$$\gamma^* \equiv \beta\gamma\sigma^2 = \lim_{L_z,\, A\to\infty} \frac{\beta\Delta F(L_z, A)}{(2A)} \quad , \tag{6.8}$$

$A = L_x \times L_y$ being the area of a wall. The strongest variation of ΔF is expected with respect to the wall distance L_z. To study this behavior, the linear dimension L_z of the simulation box has to be varied while the cross section area A is kept constant. As it is shown later, in practice a linear extrapolation of $\beta\Delta F$ as a function of $1/L_z$ towards $1/L_z = 0$ allows to determine γ^*.

Application and Free Energy Results

In the following, the parameter choice and representative free energy calculation results for both interaction models and various wall interactions are presented. The main focus lies on the variation of the simulation box size and extrapolation of γ^* as stated in equation 6.8.

The *liquid* phase of both, the hard sphere model and the effective AO model, was investigated using the following relation. For every cross sectional area $A = L \times L$ the z-dimension was varied as $D = L$, $2L$, $4L$ and $D = 8L$. For the hard sphere interaction A was chosen as $A = 5 \times 5$, 6×6 or $A = 8 \times 8$. For the effective AO model A was kept constant as $A = 8.05 \times 8.05$. In the case of the *crystalline* phase the simulation box dimension has to be compatible with the fcc structure, so that possible stress of the crystal is minimized. For the crystal orientation where the (111)-plane is parallel to the walls the z-dimension was varied in the way so that 6, 12, 24, 48 or 96 lattice planes fit. The cross-sectional area for the hard sphere interaction model was chosen as $L_x \times L_y = [8.8723 \times 7.6835]$, $[8.8331 \times 7.6496]$, $[8.7807 \times 7.6043]$, $[8.7290 \times 7.5595]$, $[8.6779 \times 7.5152]$, $[8.6292 \times 7.4730]$ and for the effective AO model as $L_x \times L_y = [8.3982, 7.2730]$, $[8.3763, 7.2540]$, $[8.3544, 7.2350]$, $[8.3335, 7.2170]$, $[8.3127, 7.1990]$. In practice, the various packing fractions of the crystalline phase are set up as follows. For fixed linear dimension D the face-centered cubic (fcc) initialization had always the same number of particles. The various packing fraction values are then obtained by an appropriate definition of the unit length scale, i.e. the particle diameter. For both models, the smallest system contains only 384 particles, while the largest systems contain 6144 particles.

The parallel version of the “Wang-Landau algorithm” is used to calculate the free energy function $F(\kappa)$. The mixing parameter κ is discretized into 1000 values $\kappa_i \in [0, 1]$ and, using the Metropolis criterion, the system can move from state i to one of the adjacent states κ_{i+1} or κ_{i-1}. The linear interpolation technique (see section 2.6.1) is used for the very first weight update. From then on, single bin updates are used until the free energy function “converges” ($f = 10^{-10}$). For the largest systems up to 512 cores are used in parallel.

Figure 6.5 presents results obtained for the liquid phases of both considered interaction models. Figure 6.5a shows the free energy differences at constant global packing fraction $\eta_g = 0.4063$ in the case of the hard sphere model confined between WCA walls for the smallest investigated system size. Even at such moderate packing fraction and small system size the free energy difference is about $\beta\Delta F \approx 65\, k_BT$. This means that a free energy algorithm such as the “Wang-Landau sampling” is a mandatory necessity. From figure 6.5a an influence of the z-dimension is certainly visible. When plotting the free energy difference as a function of $\frac{1}{L_z}$, a linear fit can be used to extrapolate to $\beta\Delta F(L_z \to \infty)$. However, one has to admit that the functional dependence $\beta\Delta F(L_z)$ is not known so that the extrapolation by a linear fit could lead to systematic errors. Figure 6.5b shows examples for the linear fits. It is difficult to decide, whether a linear behavior is the correct description of the function $\beta\Delta F(1/L_z)$ since only four data points are involved. Nevertheless, a linear fit certainly serves as a first order approximation of this type of finite size effects. Part (c) and (d) of the same figure are the analogue to (a) and (b) for the effective AO model confined between LJP1 wall potentials. In contrast to part (a), the free energy function is now not monotonic anymore, but develops a minimum around $\kappa \approx 0.9$. The non-monotonic behavior is a direct result of the attractive well of the LJP1 potential. For small values of κ the diverging repulsive part of the wall potential dominates, while for $\kappa \lesssim 1$ the attractive part starts to become “active”. Figure 6.5d verifies again that a linear extrapolation of $\beta\Delta F(1/L_z)$ is sufficient to extract a precise estimate for γ.

At this point a few comments on the exact shape of the function $\beta\Delta F(\kappa)$ are necessary. Free energy algorithms such as successive umbrella sampling or the “Wang-Landau sampling” show in general the best performance when the underlying free energy landscape has an overall moderate slope as a function of the reaction coordinate of interest. In the case of the ensemble switch method it is possible to “tune” the exact form of $\beta\Delta F(\kappa)$ for all intermediate κ values, as long as the extreme case

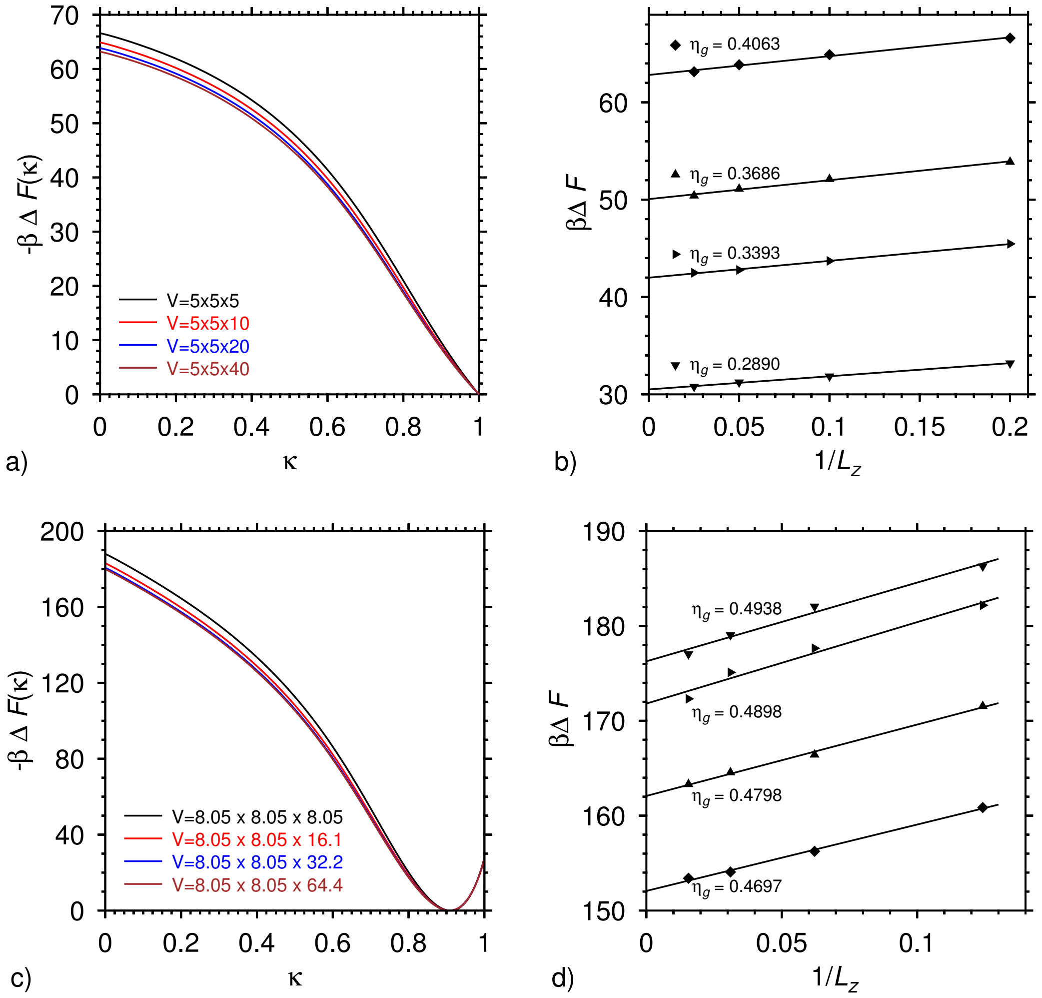

Figure 6.5.: Surface free energy results for *liquid* phases and extrapolation $L_z \to \infty$. (a) Free energy as a function of the mixing parameter κ for $\eta_g = 0.4063$ with hard sphere particle interactions and WCA wall potential ($\varepsilon_w = 1$, $\sigma_w = 0.5$). (b) Linear fit of the free energy differences obtained from plots as shown in part (a) serving as extrapolation to $L_z \to \infty$ [the upper curve with diamonds corresponds to part (a)]. The area of the wall was always $A = 5 \times 5$. (c) Free energy of the liquid phase of the effective AO model in the case of the LJP1 wall potential ($\varepsilon_w = 2$, $\sigma_w = 0.5$) at global packing fraction $\eta_g = 0.4697$. (d) Extrapolation to $L_z \to \infty$ via a linear fit for various packing fractions as indicated. The diamonds correspond to the data shown in part (c). The area of the wall was always $A = 8.05 \times 8.05$.

$\kappa = 0$ (pure bulk) and $\kappa = 1$ (full switched on walls) are not changed. To compensate the highly diverging $(1/r)^{12}$ part in the wall potentials, the wall potential amplitude ε was modified as $\varepsilon \to \kappa^{12}\varepsilon$. This leads to the smooth and modest behavior of the free energy landscapes presented in this chapter.

The crystalline structure of the effective AO model and the hard sphere model is the fcc structure. Within the context of flat walls it is known that these systems favor a crystal orientation for which the (111)-plane is parallel to the walls [34, 152] (see Fig. 6.6). In the case of crystalline phases the free energy difference $\beta\Delta F(\kappa)$ shows a much stronger dependency on the linear simulation box dimension L_z, as shown by figure 6.6a. Again a linear behavior of $\beta\Delta F(1/L_z)$ is observed, but the slope

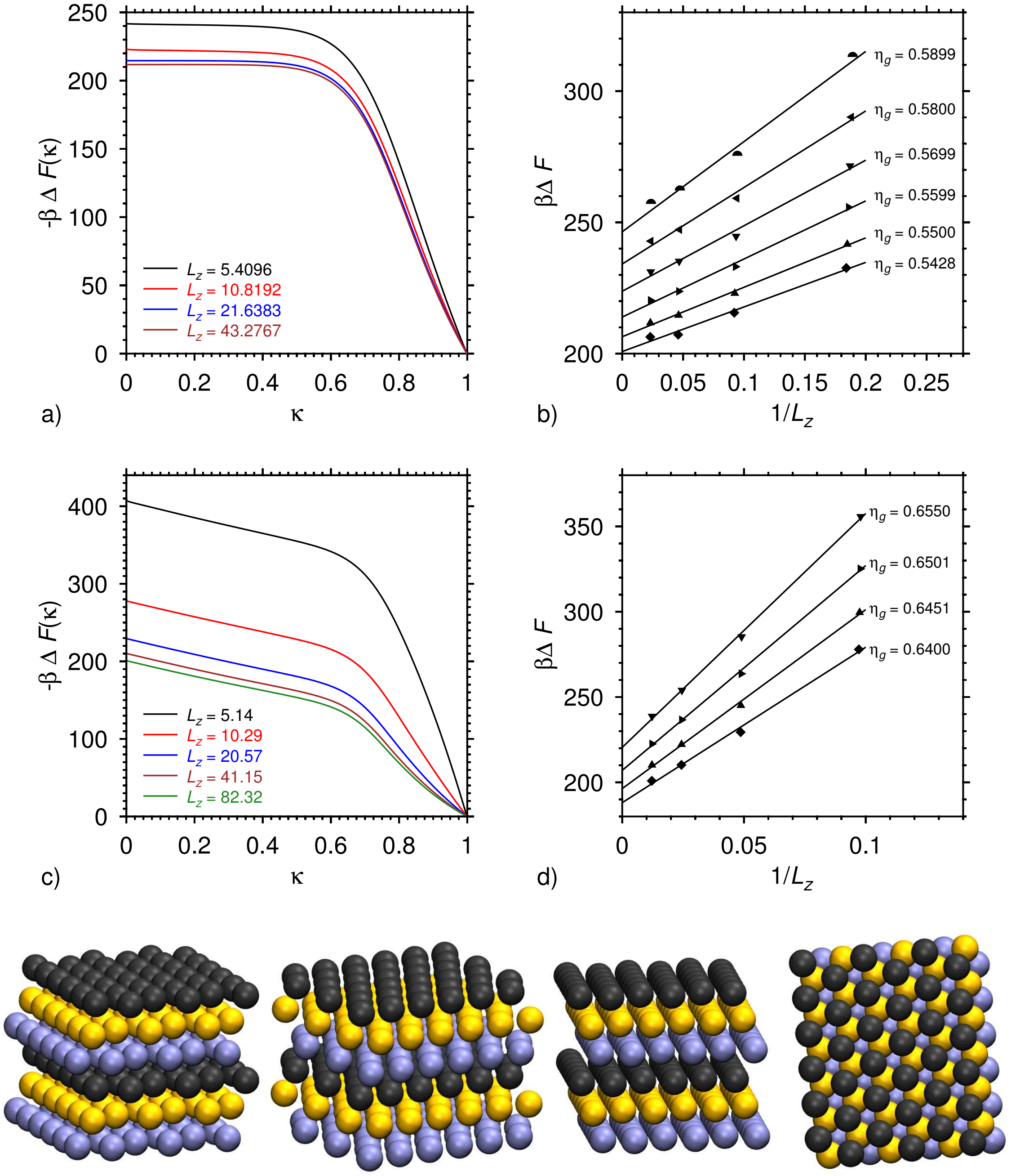

Figure 6.6.: Surface free energy results for *crystal* phases and extrapolation $L_z \rightarrow \infty$. (a) Free energy as a function of the mixing parameter κ for $\eta_g = 0.55$ with hard sphere particle interactions and WCA wall potential ($\varepsilon_w = 1$, $\sigma_w = 0.5$). (b) Linear fit of the free energy differences obtained from plots as shown in part (a) serving as extrapolation to $L_z \rightarrow \infty$ [the free energy differences from part (a) correspond to the 5th curve from the top with triangles pointing up]. (c) Free energy of the crystalline phase of the effective AO model in the case of the WCA wall potential ($\varepsilon_w = 1$, $\sigma_w = 0.5$) at global packing fraction $\eta_g = 0.64$. (d) Extrapolation to $L_z \rightarrow \infty$ via a linear fit for various packing fractions as indicated. The diamonds correspond to the data shown in part (c). (at the bottom) Various snapshots of the crystalline fcc structure. The most right picture is a topview on the fcc (111)-plane.

of the straight line fit increases drastically (Fig. 6.6b). This increase in the slope makes the extrapolation to $\frac{1}{L_z} = 0$ more sensitive resulting in larger fitting errors. In addition, it is noted that a variation of L_z in very small steps leads to a damped oscillatory behavior of $\beta\Delta F(L_z)$ corresponding to compression and stretching of the solid structure. By strictly doubling the system size from simulation to simulation one can ensure that the oscillatory stress part in $\beta\Delta F(L_z)$ has a monotonic behavior and is therefore not directly visible in figure 6.6 part (b) and (d). The extrapolation in the case of the hard sphere system to $1/L_z \to 0$ shows a slight deviation of the linear fit regarding the largest and the smallest system. This can be interpreted as evidence that a quadratic or even higher order behavior might underlie the finite size scaling. However, by simply increasing the system size further and disregarding the results for smallest system the linear behavior can be retrieved as indicated in the case of the effective AO model in figure 6.6d.

Finally, one has also to ensure that the simulation box size in x and y-direction is sufficiently large. For the liquid state the pair correlation function $g(r)$ can be used as an estimate at which distances the correlation becomes small (for a fixed packing fraction). Extracting the wall tension from too small systems (with respect to the x- and y-dimension) is expected to lead to systematic errors. In the next section the liquid branch of the wall tension of a hard sphere system confined between hard walls is compared with highly precise results from literature [149] to check for this kind of finite size effects.

6.2. Results for Hard Spheres

The ensemble switch method, as described above, allows for precise wall tension estimates which have typically a statistical error of less than 0.8%. The results by Laird and Davidchack on hard spheres between hard walls are extremely precise (with an error typically less than 0.2%) and, therefore, can serve as a reference system to check the ensemble switch method. Figure 6.7 shows the reference data (full curve) as well as the results from the ensemble mix method (symbols). The cross section area A was varied to check the influence on the wall tension estimates. The small systems ($A = 5 \times 5$) agree within the error bars with the reference data and simulations of larger systems with $A = 8 \times 8$. Using $A = 6 \times 6$ for packing fractions $\eta \gtrsim 0.42$ seems to be sufficient to calculate precisely the wall tension.

With this comparison one can conclude, on the one hand, that at sufficiently large wall surface area A the leading finite size effect is given by the variation of L_z and, on the other hand, that the ensemble switch method can produce reliable precise results for wall tensions. For the confinement of hard spheres between hard walls it is known that a complete wetting layer forms [34] and hence, this system is not suited to study crystalline wall attached clusters. As seen in figure 6.4, the wall potential amplitude of the WCA wall potential has a strong influence on the surface properties of the hard sphere system and the question arises whether it is possible to obtain partial wetting for a hard sphere system by only changing this wall potential parameter.

To investigate the wetting behavior of the hard sphere system, the wall tensions at bulk coexistence densities have to be determined. The coexistence densities of the hard sphere system are $\eta_l = 0.492$ for the liquid and $\eta_c = 0.545$ for the crystalline

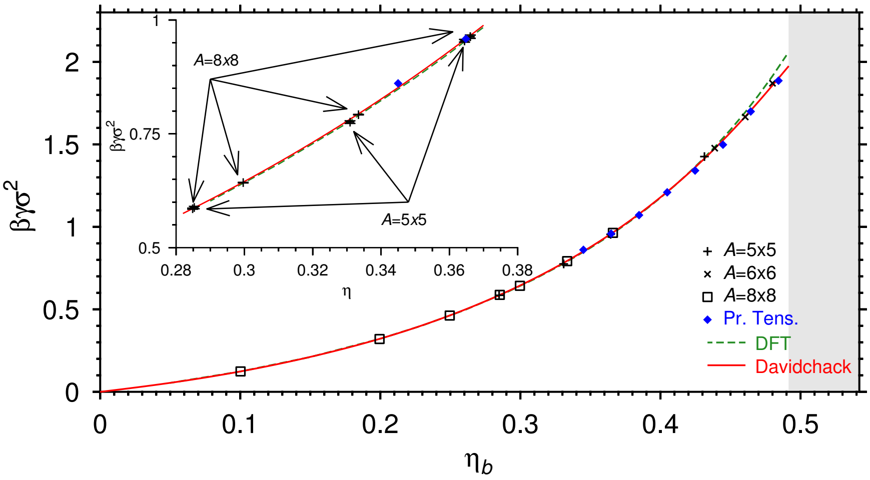

Figure 6.7.: Wall tension of the hard sphere model confined between hard walls ($\sigma_w = 0.5$) as a function of packing fraction. The shaded area marks the beginning of the coexistence region of the liquid and crystalline phase for hard spheres. The full curve corresponds to the data of DAVIDCHACK [149] (interpolation via cubic splines), the dashed line is the DFT result (White Bear II functional), the blue diamonds are pressure tensor calculations and the black symbols show the result of the ensemble switch method for different cross sections A respectively.

phase [49]. The wall potential amplitude ε was varied as $\varepsilon = 0.25,\ 0.5,\ 1.0,\ 2.0,\ 4.0$. Various ensemble switch simulations close to the coexistence densities were performed for every wall potential amplitude. Figure 6.8a shows the result for the liquid phase and demonstrates that it is possible to modify the wall tension when varying ε. The DFT results (provided by YAMANI and OETTEL) agree well with the simulation results up to a bulk packing fraction of $\eta_b \approx 0.45$. From this point on, the simulation results are systematically lower as expected from the investigation of the surface excess packing fraction η_s. In addition, pressure tensor results (provided by coworker DEB) are included in the graph which agree also well with the "ensemble switch" results.

To derive a contact angle via Young's equation (Eq. 6.1), one does not only need the wall tensions but additionally the liquid-crystal interfacial tension γ_{lc}, which is in general difficult to obtain. Two methods are common to calculate the interfacial tension. In the wave fluctuation method the interfacial stiffness $\widetilde{\gamma}_{lc}$ with respect to various possible orientations of the crystal can be calculated. The interfacial tensions of the different crystal orientations are then extracted via a cubic harmonics expansion (see Ref. [155]). Furthermore, there also exists the cleaving wall method where the work which it costs to separate and connect the liquid and the crystalline phase is directly related to the corresponding wall tension. Between different authors and different methods the results for the interfacial tension vary. Latest results from 2010 [156] are $\gamma^{111} = 0.5416$, $\gamma^{110} = 0.5590$ and $\gamma^{100} = 0.5820$. The interfacial stiffness is estimated as $\widetilde{\gamma}_{lc} = 0.49$ (ZYKOVA-TIMAN et al.) or as $\widetilde{\gamma}_{lc} = 0.44$ (LAIRD et al.) [49, 148]. Figure 6.8b focuses on the coexistence region (note the break in the abscissa scale) and allows for analyzing the wetting behavior of the system by means of Young's equation. Although the absolute values of the wall tension are strongly influenced by the applied WCA wall potential, the variation in γ_{wl} seems to be identical to the variation in γ_{wc}^{111} within the errors of the calculation. Therefore,

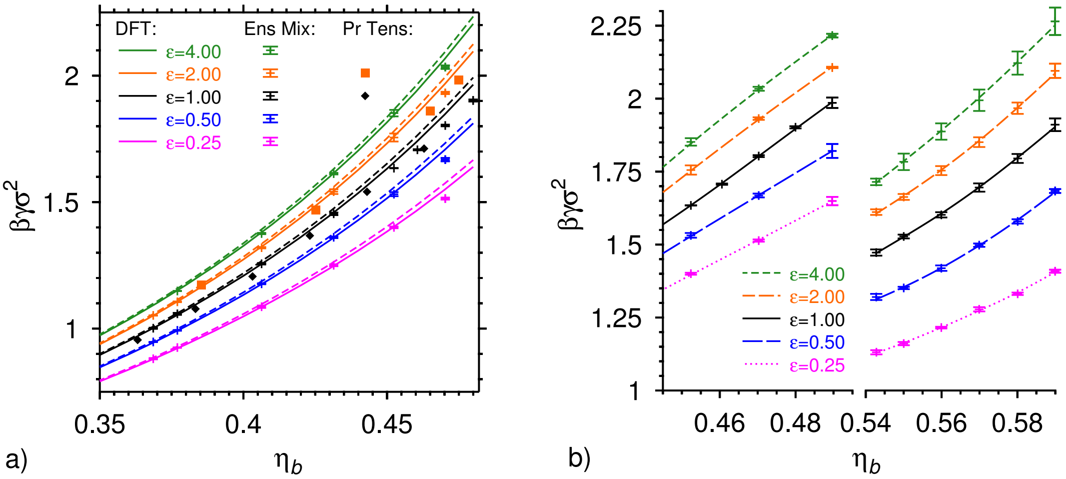

Figure 6.8.: Wall tension of the hard sphere model confined between WCA walls ($\sigma_w = 0.5$) as a function of packing fraction. Part (a) focuses on the liquid phase while part (b) shows the densities close to the coexistence region. At the liquid branches (a) three different data sets are compared: DFT-calculations, the ensemble mix method and the pressure tensor method. In (b) only the results from the ensemble mix method are shown.

ε	0.25	0.5	1.0	2.0	4.0
γ_{lw}	1.649 ± 0.014	1.821 ± 0.024	1.986 ± 0.018	2.107 ± 0.002	2.216 ± 0.006
γ_{wc}^{111}	1.131 ± 0.007	1.321 ± 0.011	1.473 ± 0.011	1.611 ± 0.010	1.715 ± 0.011
$\Delta\gamma$	0.518 ± 0.016	0.500 ± 0.026	0.513 ± 0.021	0.496 ± 0.010	0.501 ± 0.013

Table 6.1.: Wall tension estimates for the hard sphere model confined between WCA walls close to the coexistence densities at $\eta_l = 0.4915$ and $\eta_c = 0.5428$. In all the cases the contact angle is $\Theta \gtrsim 0^o$.

the wetting behavior is not (or only weakly) influenced by such modifications of the wall potential. Furthermore, the difference of the wall tensions $\Delta\gamma = \gamma_{wl} - \gamma_{wc}^{111}$ is similar to the estimates of the liquid-crystal interfacial tension: For hard spheres confined between WCA walls complete wetting or partial wetting with very small contact angles occurs (see also table 6.1).

6.3. Results for the Effective AO Model

The hard sphere interaction model together with WCA walls did not allow for a convenient study of contact angles of crystalline clusters since the influence of the wall amplitude ε on the difference $\Delta\gamma = \gamma_{wl} - \gamma_{wc}^{111}$ is rather weak and the system stays in the region of complete wetting or partial wetting with tiny contact angles. In contrast, the effective Asakura-Oosawa (eff. AO) model is expected to show large enough contact angles of crystalline "nuclei" so that a detailed study on the relation between colloid-wall interaction and the contact angle seems to be more promising. Zykova-Timan et al. studied the bulk properties of this model in the NPT en-

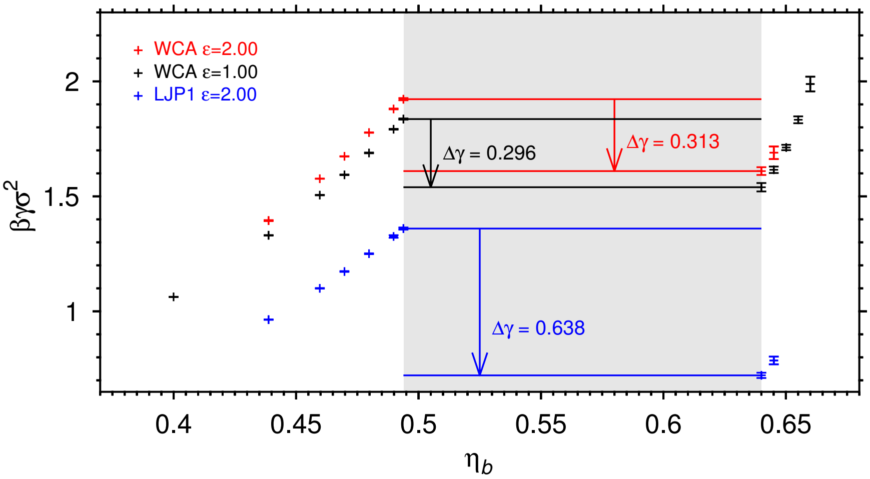

Figure 6.9.: Wall tension results obtained by the ensemble mix method close to the liquid crystal coexistence area of the effective AO model confined between various wall types as indicated.

semble [49]. The effective AO model undergoes a first order phase transition from a liquid to a crystalline fcc phase. The liquid-crystal interfacial stiffness $\tilde{\gamma}_{lc} = 0.95$ was extracted via the capillary wave analysis [49] and is the only estimate for the interfacial tension at the moment. The liquid and crystal coexistence densities are $\eta_l = 0.494$ and $\eta_c = 0.64$ respectively.

As in the previous section, the wall tensions of the liquid and crystalline phase were calculated via the ensemble switch method. Additionally to the WCA wall interaction the so-called LJP1 wall potentials (see Eq. 6.4) with an attractive well were used to influence the wetting behavior.

In comparison to the hard sphere system, the crystal coexistence density of the effective AO model is even higher which leads to very small translational amounts in the canonical moves and, hence, the computational effort increases drastically. Due to the higher densities and the increased interaction range of the pair potential, slightly larger simulation boxes were chosen in comparison to the previous "ensemble switch" studies.

Figure 6.9 shows the results for the obtained wall tensions. All the wall tensions are in general lower than in the hard sphere case. Table 6.1 shows the results for various wall potentials and crystal orientations at the coexistence densities. One can see again that the variation of the wall potential has a strong influence on the wall tension, however, in the case of the WCA wall potential the difference $\Delta\gamma = \gamma_{lw} - \gamma_{cw}^{111}$ does vary only weakly again. In contrast, the variation to the LJP1 wall potential could increase the difference and, hence, reduces the contact angle. Using the interfacial stiffness from [49] as a first estimate for the interfacial tension as $\gamma_{lc} \approx 0.95$ one can derive via Young's equation (6.1) a contact angle of $\theta \approx 72°$ in the case of WCA walls and $\theta \approx 48°$ for the LJP1 potential with $\varepsilon = 2$. The reduction of the contact angle can be understood in the following phenomenological picture: The attractive part of the wall potential causes the dense crystalline phase to gain more potential energy in comparison to the liquid phase. A crystalline nucleus consisting of a fixed number of particles therefore tries to flatten more at the wall than the surrounding liquid which leads to a reduction of the contact angle θ.

Table 6.2: Wall tension estimates for the effective AO model at the coexistence densities $\eta_l = 0.494$ and $\eta_c = 0.64$. For γ_{cw}^{110} complete wetting of the liquid is expected.

WCA $\varepsilon = 1$	γ_{lw}	1.836 ± 0.003	
	γ_{cw}^{111}	1.540 ± 0.019	$\Theta \approx 72^o$
	γ_{cw}^{100}	1.82 ± 0.051	$\Theta \approx 89^o$
	γ_{cw}^{110}	2.94 ± 0.2	
WCA $\varepsilon = 2$	γ_{lw}	1.923 ± 0.005	
	γ_{cw}^{111}	1.610 ± 0.017	$\Theta \approx 71^o$
LJP1 $\varepsilon = 2$	γ_{lw}	1.360 ± 0.004	
	γ_{cw}^{111}	0.722 ± 0.012	$\Theta \approx 48^o$

Since it is in general possible to attach crystalline nuclei also with the (110)- or (100)-plane at the wall, a rough estimate of the wall tensions for these crystal orientations at the crystal coexistence density were calculated. Especially for the (110)-plane, which is very “rough”, the procedure of switching on walls leads to an immense amount of stress, so that free energy differences of the order of $6000\, k_B T$ appear for the smallest systems. It is questionable whether a simple linear fit procedure still covers the finite size effects properly, in fact, the data for the (110)-orientation suggests a more quadratic behavior. The resulting values for the wall tensions are given in table 6.1.

The derived contact angles of $\theta \approx 72^o$ for WCA wall interactions and $\theta \approx 90^o$ for the (100)-plane (note in table 6.1 $\gamma_{lw} - \gamma_{cw}^{100} \approx 0$) agree almost exactly with the contact angles obtained by geometrical methods (see Ref. [8]). Such a high consistency between the two independent measurements of the contact angles is rather unexpected since, on the one hand, the geometric method based on crystalline cluster identification and sphere-cap fitting contains a certain freedom regarding the choice of parameters (which slightly influence the contact angle estimate) and, on the other hand, the contact angle calculation presented above is based on the interfacial stiffness rather than the interfacial tension of the liquid-crystal interface. Nevertheless, evidence is found that the macroscopic picture of heterogeneous crystal nucleation at planar, flat walls still holds to a high degree although the anisotropy, inhomogeneity and the other implications that were mentioned at the beginning of this chapter are disregarded in this formalism.

6.4. Conclusion

The topic of heterogeneous nucleation of crystalline clusters was addressed by Monte Carlo simulations in an (extended) NVT ensemble within the theoretical framework of a surface free energy based macroscopic picture. By comparison with literature results, density functional theory and pressure tensor calculations it was shown that the “ensemble switch” method predicts reliable values for the surface free energies of liquids and crystals confined between planar walls. Hard spheres in the crystalline phase are predicted to show complete wetting or only tiny contact angles with respect to repulsive WCA walls independent of the applied degree of repulsion at the walls. In the effective Asakura-Oosawa model crystalline clusters with a contact angle of $\theta \approx 71^o$ are expected. The introduction of an attractive well close to the wall allows for the reduction of the contact angle. Comparison with the direct observation of crystalline clusters and analysis via geometric methods (by collaborator DEB [8]) yields that the simple picture of a surface free energy balance of wall attached nuclei can still provide quantitative insight into the problem of heterogeneous crystalline nucleation.

CHAPTER

7

MULTI PARTICLE COLLISION DYNAMICS (MPCD)

In mesoscale simulations where molecular details play an important role for the dynamics, a simple continuum description based on the Navier-Stokes equations is not sufficient anymore. Also a fully atomistic approach is not well suited since only the short time behavior is accessible with present-day computers due to the high number of microscopic degrees of freedom. There exist multiple algorithms addressing the key feature of mesoscale systems, which is the interplay between thermal fluctuations and hydrodynamic interactions. All these algorithms like Dissipative Particle Dynamics (DPD) [157–159], Lattice Boltzmann (LB) [160–162] and also MPCD introduced by MALEVANETS and KAPRAL [163, 164] (also known under the name Stochastic Rotation Dynamics (SRD)) try to average out the microscopic degrees of freedom to get a high computational efficiency by using a coarse grained approach for the solvent.

The MPCD algorithm is well suited for Reynolds and Perclet numbers of the order of 0.1 to 10 and has within this range a lot of advantages in comparison to alternative methods. It is an easy to implement and fast approach having explicit (but coarse grained, ideal) solvent particles for which analytic expressions, e.g. transport coefficients, exist.

The basic idea is to combine the ordinary velocity Verlet based Molecular Dynamics (MD) simulations of so-called “fluid” or “embedded” particles with a simplified and coarse grained solvent model. The solvent is represented by point-like non-interacting particles. The coupling of the fluid particles to the solvent is achieved by the exchange of momentum between solvent particles and fluid particles within collision steps[1]. The local conservation of momentum and mass of the MPCD algo-

---

[1] This is the simplest and computationally inexpensive way to couple both particle species. However, there exist also more sophisticated approaches where an explicit pair interaction model

rithm is the crucial ingredient to obtain hydrodynamics in the simulation.

The MPCD algorithm is highly extensible to various thermostats [165, 166] as well as constraints like walls and obstacles [167, 168]. The simplicity of the inclusion of walls and obstacles is one of its strongest features. Furthermore, the possibility to switch off the hydrodynamics by maintaining the thermodynamic fluctuations [169] makes the MPCD algorithm a powerful tool to study the influence of hydrodynamics on the kinetics of complex fluids.

This chapter is structured as follows. First, the integration scheme of Molecular Dynamics simulations is introduced, then the MPCD algorithm including various thermostat versions and boundary conditions is described in detail. After this, two case studies are presented, Poiseuille flow of the solvent in narrow channels and the dynamics of a single fluid tracer particle embedded in solvent.

7.1. MD Integration Scheme

The following paragraphs briefly elucidate some important aspects of MD simulations following references [28, 170]. While Monte Carlo methods are based on a stochastic trajectory in phase space, in Molecular Dynamics simulations the classical trajectories of particles based on Newtons second law are calculated. In contrast to Monte Carlo methods, Molecular Dynamics simulations are typically used to extract (additionally to equilibrium quantities) transport properties of classical many-body systems. The word “classical” already anticipates at which length and time scales the MD simulation scheme is useful.

The basic idea behind MD simulations is to integrate Newtons equations of motion

$$m_i \ddot{\boldsymbol{r}}_i = \boldsymbol{F}_i \quad ,$$

where m_i is the mass of the particle i and $\boldsymbol{F}_i$ is the force acting on this particle. In this approach it is assumed that the force $\boldsymbol{F}_i$ can be extracted via $-\nabla U_i = \boldsymbol{F}_i$ from an N-particle potential of the general form

$$U(\{\boldsymbol{r}_i\}) = \sum_i u_1(\boldsymbol{r}_i) + \frac{1}{2}\sum_{i \neq j} u_2(\boldsymbol{r}_i, \boldsymbol{r}_j) + \dots \quad , \tag{7.1}$$

where ... stands for three-body interactions like bond angle potentials and higher order interactions. The term $u_1(\boldsymbol{r}_i)$ corresponds to an external field or walls, while $u_2(\boldsymbol{r}_i, \boldsymbol{r}_j)$ corresponds to pair interactions. The labels $1, 2$ at u represent at the same time the principal order of the numerical effort of the operation to calculate those interactions in a computer simulation.

There exist multiple algorithms how to integrate Newtons equations of motion within a small time interval δt (the so-called MD time step). One of the most simplest of these algorithms is the so-called velocity Verlet algorithm [171] which defines the propagation of a particle in phase space via

$$\begin{aligned} \boldsymbol{r}_i(t+\delta t) &= \boldsymbol{r}_i(t) + \boldsymbol{v}_i(t)\delta t + \frac{\boldsymbol{F}_i(t)}{2m_i}\delta t^2 && (7.2) \\ \boldsymbol{v}_i(t+\delta t) &= \boldsymbol{v}_i(t) + \frac{\boldsymbol{F}_i(t+\delta t) + \boldsymbol{F}_i(t)}{2m_i}\delta t \quad . && (7.3) \end{aligned}$$

---

between fluid and solvent particles is applied.

Implementing these two equations (together with a force calculation and boundary conditions) is enough to perform MD simulations in the NVE ensemble where the total energy $E_{\text{tot}} = E_{\text{pot}} + E_{\text{kin}}$ is a constant over all times and, hence, represents a control variable to check a proper implementation (especially when taking parallelization schemes into account, see section 2.6.1.2 for the corresponding figure).

7.2. The MPCD Algorithm

Long range correlations due to hydrodynamics are obtained by conservation of mass and momentum. All hydrodynamic interaction (HI) methods fulfill those conservation laws. Lattice methods are fast but break the Galilean invariance and have the disadvantage that there is no "natural" way to couple the solutes such as colloids and polymers to the solvent. The same problem also occurs when confinement is considered. Ripoll and Winkler [172] studied carefully the solvent properties such as transport coefficients using the MPCD approach. Dependent on the parameters a gas-like or a fluid-like behavior can be modeled by the MPCD solvent which is characterized by the Schmidt number measuring the ratio between viscous and diffusive transport [172, 173].

In addition to the aforementioned MD steps for embedded particles, the basic structure of all MPCD algorithms consists of two steps, which are presented here in their original formulation (SRD) in the micro canonical ensemble:

1. **Collision step:** update the velocities of the solvent particles in each cell by a rotation of their relative velocities:

   $$\boldsymbol{v}_i = \boldsymbol{u} + \mathcal{R}(\alpha)\delta\boldsymbol{v}_i \ , \tag{7.4}$$

   where $\boldsymbol{u}$ is the mean velocity in the cell, $\delta\boldsymbol{v}_i = \boldsymbol{v}_i - \boldsymbol{u}$ and $\mathcal{R}(\alpha)$ is a rotation matrix with angle α around a randomly chosen rotation axis. In this collision step the fluid particles are integrated, which is explained later in more detail (see section 7.2.2).

2. **Streaming step:** update the particle positions and velocities of the solvent particles by the standard velocity Verlet algorithm:

   $$\boldsymbol{r}_i(t+\tau) = \boldsymbol{r}_i(t) + \boldsymbol{v}_i(t)\tau + \frac{1}{2}\frac{\boldsymbol{F}_e(t)}{m_s}\tau^2 \tag{7.5}$$

   $$\boldsymbol{v}_i(t+\tau) = \boldsymbol{v}_i(t) + \frac{1}{2m_s}\left[\boldsymbol{F}_e(t) + \boldsymbol{F}_e(t+\tau)\right]\tau \ . \tag{7.6}$$

   $\boldsymbol{F}_e$ is an external force, m_s the mass of a solvent particle and τ the collision time step, which in case of an embedded MD fluid (see section 7.4) can be related to the MD time δt as $\tau = I \cdot \delta t$ with I being a positive integer.

These two basic steps describe clearly in which theoretical picture the solvent is treated in MPCD algorithms. Within a single cell hydrodynamic interactions are not resolved. Instead, collisions between solvent particles are treated stochastically. The streaming step does not contain forces between solvent particles, which expresses the continuous character of the solvent. Using a whole set of collision cells together with the streaming steps, describes hydrodynamics for length scales beyond the collision cell dimension a. If the linear cell dimension a is chosen that large that a solvent particle remains over several streaming steps within the same cell and typically "collides" with the same neighboring solvent particles, the Galilean invariance is broken and the algorithm fails, i.e. the solvent particles become strongly correlated. The so-called mean free path $\lambda = \tau\sqrt{k_BT/m_s}/a$, m_s being the mass of a single solvent particle, can be used as a measure for the validity of the algorithm when considering transport coefficients or any other measurement where a solvent mass is involved. For instance, the presence of a thermostat or an external force will define the solvent mass and thus, the condition $\lambda > 1$ should be fulfilled. However, there exists a nice workaround of this algorithmic drawback, which is the shift of the center of the cell system by a vector whose components are drawn randomly from the interval $[-a, a]$. This simple trick restores Galilean invariance by ensuring that within the collision of a solvent particle the mean velocity is composed of the velocities of *different* neighboring particles every collision step [174].

7.2.1. Solvent Thermostats

Three different thermostats were implemented and tested for the solvent, the Efficient Cell Level Thermostating (ECLT) [175] and the Maxwell-Boltzmann-Statistics thermostat (MBS) [176], which are a direct extension of the SRD algorithm, and an Anderson-Thermostat referred to as MPC-AT [165, 177].

MPC-AT Thermostat The MPC-AT was introduced 2002 by GOMPPER et al. [165, 177] and follows a route different to the original SRD algorithm. No rotation of relative velocities is performed, but new relative velocities $\boldsymbol{v}_i^r$ are generated based on a Maxwell-Boltzmann distribution with variance $\sigma^2 = k_BT/m_s$. The collision rule is then

$$\boldsymbol{v}_i = \boldsymbol{u} + \boldsymbol{v}_i^r - \frac{1}{M}\sum_{j=1}^{M} \boldsymbol{v}_j^r \ , \tag{7.7}$$

M being the number of particles in the considered cell. The MPC-AT approach can be extended to also conserve angular momentum, which plays an important role especially for anisotropic particles. The only drawback of the MPC-AT is the rather expensive generation of Gaussian random numbers (three per particle in every collision step).

ECLT Thermostat 2005 HECHT et al. introduced the efficient cell level thermostat ECLT. The original idea of the rotation of the relative velocities in the SRD algorithm is sustained, but additionally a velocity rescaling is applied with a certain acceptance probability. This cell-wise thermostating does not change the viscosity of the fluid and preserves the parameter α which represents an important solvent parameter for fine-tuning solvent properties. It was reported to have a fast equilibration time and was successfully applied for the study of sedimentation of charged colloids [175]. Please see also the full review [178] or the original article [175] for further details of the algorithm.

Efficient Cell Level Thermostating (ECLT)

1. Choose a real number ψ from the interval $[1, 1+c]$ at random, where c is the "strength" of the thermostat typically of the order of $c \approx 0.1$.
2. Generate with probability $\frac{1}{2}$ the scaling factor $S = \psi$ or $S = 1/\psi$ respectively.
3. Calculate the acceptance probability $p = \min(1, A)$ with $A = S^{3(M-1)} \exp\left(-\frac{1}{2k_BT}\sum_{1=1}^{M} m_i(\boldsymbol{v}_i - \boldsymbol{u})^2(S^2-1)\right)$, where M is the number of particles in the current cell.
4. Perform a stochastic rotation with the rescaled rotation matrix $S\mathcal{R}$ if a uniform random number $\varepsilon \in [0, 1)$ is smaller than p, otherwise perform a (usual) stochastic rotation with $\mathcal{R}$.

MBS Thermostat Eventually 2010 the so-called Maxwell-Boltzmann-Statistics thermostat (MBST) was proposed by Gompper et al. and represents from all of the so-far introduced thermostats the fastest in terms of reaching the desired target temperature which is an important feature when a system undergoes a quench. The relative velocities of the particles in the MPC cell are rotated and rescaled in every collision step. Similar to the ECLT the rotation angle α is preserved as a tunable parameter of solvent properties. The velocity rescaling factor ξ is created by two types of kinetic energies, the relative local kinetic energy of the cell $E_k = \frac{1}{2}\sum_i m_i(\Delta\boldsymbol{v}_i)^2$ and the target local kinetic energy E_k' which is taken from a gamma distribution:

$$P(E_k') = \frac{1}{E_k'\Gamma(f/2)}\left(\frac{E_k'}{k_BT}\right) e^{-E_k'/(k_BT)} \quad . \tag{7.8}$$

Here, $f = 3(M-1)$ is the number of degrees of freedom of the system and $\Gamma(x)$ is the gamma function. The rescaling factor ξ is then calculated as

$$\xi = \sqrt{E_k'/E_k} \quad . \tag{7.9}$$

During every SRD collision step the relative particle velocities are then additionally rescaled as $\Delta\boldsymbol{v}_i \to \xi\Delta\boldsymbol{v}_i$. Note that the formulation in this order has a numerical instability for $E_k = 0$, since then $\xi \to \infty$ and the product $\xi\Delta\boldsymbol{v}_i$ is not defined anymore. Of course, $E_k = 0$ is equivalent to $\Delta\boldsymbol{v}_i = 0\,\forall i$ and hence $\Delta\boldsymbol{v}_i$ does not need to be rescaled or rotated.

NOHI Thermostat Another very important thermostat type is the NOHI thermostat, where NOHI stands for "no hydrodynamic interactions". It allows to switch off hydrodynamics while the thermal fluctuations still remain [169]. Instead of explicit solvent particles, the the mean momentum $\boldsymbol{P}$ taken from a Maxwell-Boltzmann distribution with variance $\sigma^2 = m_sMk_BT$ and zero mean is used. This way of solvent treatment is much faster than all the other MPC thermostats, because no solvent particles are needed in the simulation anymore. They are completely represented by their mass m_s and their average number per cell M. Of course, this thermostat is only useful when particles embedded in the solvent are present (see section 7.4).

7.2.2. Fluid Solvent Coupling

The coupling of the solvent to fluid particles is one of the strongest features of MPCD algorithms in contrast to other methods, especially lattice methods, since the coupling happens in a very "native" way. The most simple technique is the following: Fluid particles are integrated in the collision steps, which means that they are associated to solvent cells and the mean velocity of the cell is the mass weighted average of all velocities being part of the cell. All the previously presented formulas stay exactly the same where M is now the total number of particles in the cell (including fluid particles) and the average velocity is $\boldsymbol{u} = \sum_{i=1}^{M} m_i \boldsymbol{v}_i / \sum_{i=1}^{M} m_i$, m_i being the mass of either a solvent particle or a fluid particle respectively. This leads to a momentum transfer from the fluid to the solvent. The velocity of fluid particles is updated in the same way as the velocity of the solvent particles (either by the SRD technique or within the context of the thermostats). This leads to a momentum transfer from the solvent to the embedded fluid particles $\Delta \boldsymbol{p} = (\boldsymbol{v}' - \boldsymbol{v}_{\text{old}}) m_f$. The collision step is the only point where both particle species are coupled. Until the next collision fluid particles are treated via the velocity Verlet integration procedure and the solvent particles stream interactionless.

The frequency at which collision steps are performed defines the solvent viscosity, as it will be shown in section 7.3. The integration time step of the velocity Verlet integration of the fluid particles is independent from this choice. However, the frequency of MPCD collision steps has to be an integer multiple of the MD time step.

7.2.3. Boundary Conditions

The behavior of the solvent close to boundaries like planar walls plays an important role with respect to the hydrodynamics and is not as trivial to implement as it might look in the first place. In general, one has to distinguish between stick, perfect slip and partial slip boundary conditions. Since the solvent is treated as a set of point-like non-interacting particles, the collision with a wall is treated in a geometric manner within the streaming step. However, the collision step also has to be modified as it will be explained in the following paragraphs.

Perfect Slip Boundaries The perfect slip boundary is easy to realize. Solvent particles which would pass through the wall within a streaming time step are specularly reflected at the wall. In case of planar walls, chosen perpendicular to the z-axis and located at $\pm\frac{L_z}{2}$, this means that the z-component of the velocity is modified as $v_z \to -v_z$. Denoting the particle position after the streaming as $\boldsymbol{r}^o$, which lies outside of the simulation box, the new particle position after the reflection is calculated as $r_z^n = 2w_z - r_z^o$, where $w_z = \pm\frac{L_z}{2}$ depending whether the particle penetrated the upper or the lower wall.

Stick Boundaries In contrast to the slip boundary specular reflection, here, the so-called bounce back rules inspired by other mesoscale methods (Lattice-Boltzmann) are applied. In the case of planar walls the bounce back rule leads to $\boldsymbol{v} \to -\boldsymbol{v}$. With the notation $\boldsymbol{r}^b$ for the solvent particle position before the streaming step (the

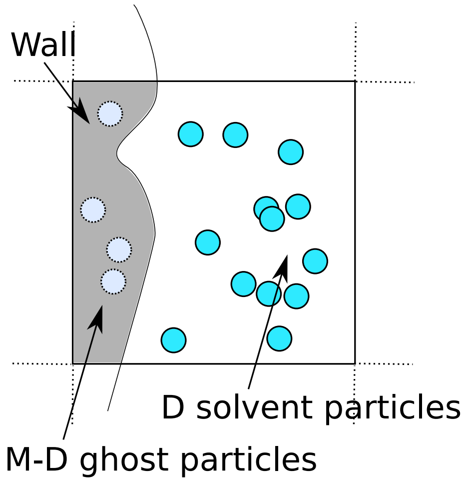

Figure 7.1: Schematic representation of a collision cell which intersects with a wall. A certain number of ghost particles are added to recover the mean number of particles per cell M.

other labels are the same as in the previous paragraph) the new particle position is calculated as

$$\boldsymbol{r}^n = 2\left[\boldsymbol{r}^b + (\boldsymbol{r}^o - \boldsymbol{r}^b)\frac{w_z - r_z^b}{r_z^o - r_z^b}\right] - \boldsymbol{r}^o\,.$$

With this simple bounce back rule one could in principle already simulate no-slip boundary conditions. However, for more complicated shaped boundaries than planar walls as well as for the necessary shift of the cell system (see the beginning of section 7.2) it is unavoidable to have partially occupied collision cells. These cells cause the appearance of spurious slip at the wall. In this case so-called bulk filling rules have to be applied to guarantee no-slip boundaries. A number of ghost particles is generated to counterbalance the difference from the mean solvent particle number per cell M (see the scheme in Fig. 7.1). The velocities of the ghost particles are drawn from a Maxwell-Boltzmann distribution with variance $\sigma^2 = k_B T/m_s$. There are various modifications to this simple bulk filling rule to improve the properties of the solvent close to walls, which includes for example a symmetrization or the precise calculation of the occupied volume fraction by the wall in each cell (see [173] for a systematic study of MPC solvents at various types of boundaries).

Partial Slip Boundaries A simple method to control the amount of slip at a surface for solvent particles was introduced as *Method 2* in reference [173]. One just selects with a certain probability Γ perfect slip or stick boundaries. This technique allows a continuous crossover from stick boundary conditions to perfect slip boundaries and naturally fits, as a stochastic but momentum conserving method, into the framework of the MPCD simulation technique.

7.3. Case Study: Poiseuille Flow of Solvent

Poiseuille flow in channels can be used to determine the viscosity of the solvent in a fast and reliable way. Furthermore, it gives insight regarding the effects of the implemented boundary conditions (no-slip, partial slip). By applying a constant pressure gradient or alternatively a constant external force parallel to the walls a Poiseuille flow can be accomplished.

Due to the local conservation of momentum and energy the SRD algorithm is directly related to the Navier-Stokes equations, and hence, assuming a constant density, the Navier-Stokes equations for incompressible (Newtonian) fluids serve as a starting point for the derivation of a viscosity measurement:

$$\begin{aligned} \rho(\partial_t + \langle \boldsymbol{u}|\nabla\rangle)\boldsymbol{u} &= -\nabla p + \eta\nabla^2\boldsymbol{u} + \rho\boldsymbol{F}/m_s & (7.10)\\ \langle\nabla|\boldsymbol{u}\rangle &= 0\ . & (7.11)\end{aligned}$$

Here, $\boldsymbol{u}$ is the velocity field, p is the pressure, η is the viscosity and $\boldsymbol{F}$ is an external force. The equation is easy to solve under the condition to have only an external force term $\rho\boldsymbol{F}/m_s = \rho\boldsymbol{g} = \rho g\boldsymbol{e}_x$ and that one is interested in a steady-state solution of the following form:

$$\boldsymbol{u}(t,x,y,z) = u(z)\boldsymbol{e}_x$$

Then equation 7.11 is fulfilled and equation 7.10 reduces to:

$$-\frac{\rho g}{\eta} = u''(z)\ ,$$

which leads with the no-slip boundary conditions $u\left(z = \pm\frac{L}{2}\right) = 0$ to the solution

$$u(z) = -\frac{\rho g}{2\eta}\left(z^2 - \frac{L^2}{4}\right)\ . \tag{7.12}$$

An extension including a slip length at the boundaries can be derived as

$$u(z) = -\frac{\rho g}{2\eta}\left(z^2 - \frac{L^2}{4}\right) + \frac{\rho g s L}{2\eta}\ , \tag{7.13}$$

where s is the slip length (please compare with [179] for a more detailed description). For cylindrical confinement one obtains

$$u(r) = -\frac{\rho g}{4\eta}\left(R^2 - r^2\right)\ ,$$

r being the radial component of the cylindrical coordinates.

The viscosity η can also be predicted for the MPCD solvent model. The kinematic viscosity $\nu = \eta/\rho$ (with $\rho = N_s/a^3$) can be described by kinetic theory of two parts (for more details see [180–184]), a collision part

$$\frac{\nu_{\text{coll}}}{\sqrt{k_B T a^2/m}} = \frac{1}{\lambda}\frac{(1-\cos\alpha)}{18}\left(1 - \frac{1}{\rho}\right) \tag{7.14}$$

and a kinetic part

$$\frac{\nu_{\text{kin}}}{\sqrt{k_B T a^2/m}} = \lambda\left[\frac{1}{(4 - 2\cos\alpha - 2\cos 2\alpha)}\frac{5\rho}{\rho - 1} - \frac{1}{2}\right]\ , \tag{7.15}$$

where α is the rotation angle (see subsection 7.2), λ is the mean free path ($\lambda = \tau\sqrt{k_B T/ma^2}$), a is the size of the collision cell and ρ is the number density of the solvent. This rotation angle dependent results are valid for both the ECLT

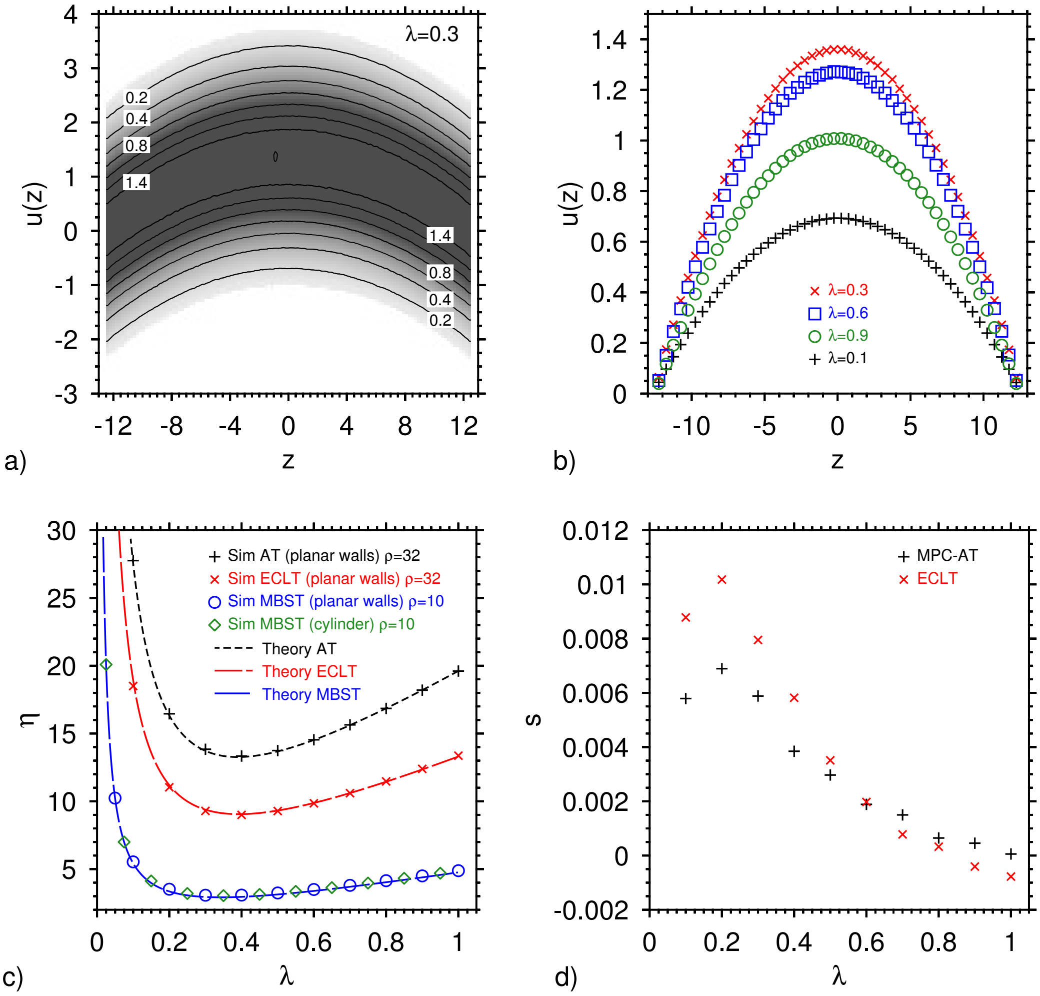

Figure 7.2.: Relation of parabolic flow profiles to the viscosity and slip length. In part (a) one can see a typical probability distribution $P(u, z)$ with $\int\int P(u, z)\, du\, dz = 1$ of a velocity profile for $\lambda = 0.3$ using the ECLT. Contours of constant probability from 0.2% up to 1.4% are shown. The maximum in the dark area in the center corresponds to 1.636%. Part (b) shows different velocity profiles in a channel using the ECL thermostating. Part (c) shows the viscosity obtained by fitting equation 7.13 to the velocity profiles and compares with theory. Part (d) shows the slip length obtained from the same fit. Further details are given in the text.

and MBST algorithms. In the case of an MPC-AT thermostat one expects for the viscosity contributions [185]:

$$\eta_{\mathrm{coll}} = \frac{m_s(N_s - 1 + e^{-N_s})}{12a\tau} \tag{7.16}$$

and

$$\eta_{\mathrm{kin}} = \rho k_B T \tau \left(\frac{N_s}{N_s - 1 + e^{-N_s}} - \frac{1}{2} \right) \quad . \tag{7.17}$$

With equation 7.13 it is possible to extract the solvent viscosity via the fit to velocity profiles obtained by simulations of plane Poiseuille flow induced by a constant external force. This results can then be compared directly to the above presented theoretical predictions.

To study the Poiseuille flow, the simulation box was chosen as $L_x = L_z = 25$ and $L_y = 10$ with walls at $z = \pm L_z/2$ in the unit length scale of $a = 1$. The mass of the solvent was set to $m_s = 1$ and the density was $\rho = 32$ or $\rho = 10$. By keeping the temperature fixed at $k_B T = 1$ the mean free path becomes identical to the collision time $\lambda = \tau$. Figure 7.2a shows a typical velocity probability distribution in the channel in x-direction. By averaging over the ordinate one can then obtain parabolic velocity profiles shown in figure 7.2b. From these parabolic profiles the viscosity η and the slip length s is extracted by fitting equation 7.13 to the data sets. Part (c) of the same figure shows the results for the viscosity in case of an MPC-AT, the ECL thermostat and the MBS thermostat. The dashed lines correspond to the theoretical curves of equations 7.14 and 7.15 for the ECLT/MBST data and equations 7.16 and 7.17 for the AT data. In both cases the theory perfectly agrees without the use of fitting parameters with the simulation viscosity results. In case of the MBST thermostat the cylindrical confinement was also used to calculate the solvent viscosity shown by the open diamond symbols in figure 7.2c.

Figure 7.2d shows the slip length obtained from the fits in the case of $\rho = 32$. The slip length is of the order of 10^{-2} and varies only slightly with λ. By increasing the wall distance or increasing the number density ρ it is possible to minimize further the appearance of a slip length.

7.4. Case Study: Influence of Hydrodynamics on a Tracer Particle

The properties of the solvent in the bulk or in confinement are already an interesting topic on their own (see, for instance, [167, 168] or [173]). Now, one can go a step further and put a single heavy fluid tracer particle in the solvent and investigate the influence of hydrodynamic interactions on the embedded particle motion.

A convenient way to measure the hydrodynamic contribution to the diffusion of a single embedded particle is the calculation of the velocity auto-correlation function

$$C_v(t) = \frac{\langle \boldsymbol{v}(t) \cdot \boldsymbol{v}(0) \rangle}{\langle \boldsymbol{v}^2(0) \rangle} \quad , \tag{7.18}$$

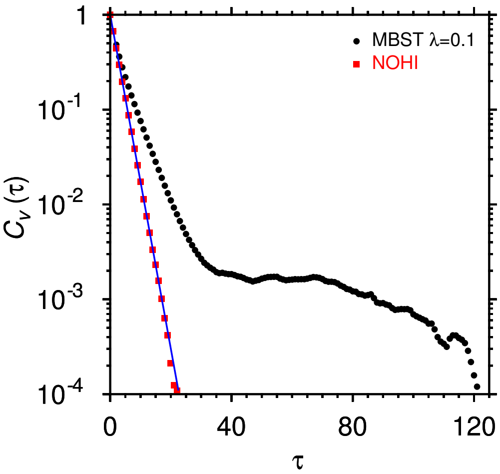

Figure 7.3: Velocity auto-correlation function for a single heavy tracer particle with and without hydrodynamic interactions. The straight line renders the exponential decay (Eq. 7.19). The solvent density was set to $\rho = 10$. The rotation angle was $\alpha = \pi/2$ and the tracer particle mass was $m_f = \rho m_s$. Note that the kinks and fluctuations from $\tau = 40$ on are due to low statistics.

where the average $\langle \ldots \rangle$ can be interpreted either as an average over independent runs or as re-definitions of the time step $t = 0$ within the same trajectory. Under the molecular-chaos assumption one expects an exponential decay of $C_v(t)$ (see [172])

$$C_v(\tau = I \cdot t) \simeq (1-\gamma)^\tau, \quad \gamma = \frac{2}{3}(1-\cos(\alpha))\frac{m_s\rho}{m_s\rho + m_f} \quad . \tag{7.19}$$

Figure 7.3 shows the time dependence of the velocity auto-correlation function of a single tracer particle of mass $m_f = \rho m_s$ in the case of an MBS thermostat (MBST) and for switched off hydrodynamics (NOHI). The hydrodynamic influence on the velocity auto-correlation is clearly visible and drops below 10^{-4} only after 120 collisions. Furthermore, the graph verifies the thermal motion of the tracer particle in the case of switched off hydrodynamic interactions as predicted by equation 7.19. A comparison of the diffusion coefficient

$$D = \frac{1}{3}\int_0^\infty \langle \boldsymbol{v}(t)\cdot\boldsymbol{v}(0)\rangle dt \to \frac{1}{3}\left(\frac{1}{2}\langle \boldsymbol{v}^2(0)\rangle + \sum_{I=1}^{\infty}\langle \boldsymbol{v}(I\cdot\tau)\cdot\boldsymbol{v}(0)\rangle\right)\tau \tag{7.20}$$

for both cases leads to $(D_{\mathrm{MBST}} - D_{\mathrm{NOHI}})/D_{\mathrm{NOHI}} \approx 0.43$, so an enhancement of 43% of the hydrodynamics in comparison to Brownian motion with respect to the diffusion.

7.5. MPCD Parallelization

There exist multiple ways how a typical Molecular Dynamics simulation program could be parallelized to use more than a single CPU core at the same time. The basic idea of all those techniques is that parts of a program which do not influence each other can be executed at the same time. For instance, it could be that the calculation of the force between two particles has so many contributions that every contribution could be calculated by an own core (force decomposition). In the case of the typically short ranged potentials within this work such a parallelization is not efficient, of course. However, there are two techniques which do perform efficiently, namely, the particle decomposition based on shared memory, and the domain decomposition [186, 187] based on message passing. Note that both techniques have to be applied for the MD part and the solvent part of the simulation in a different manner.

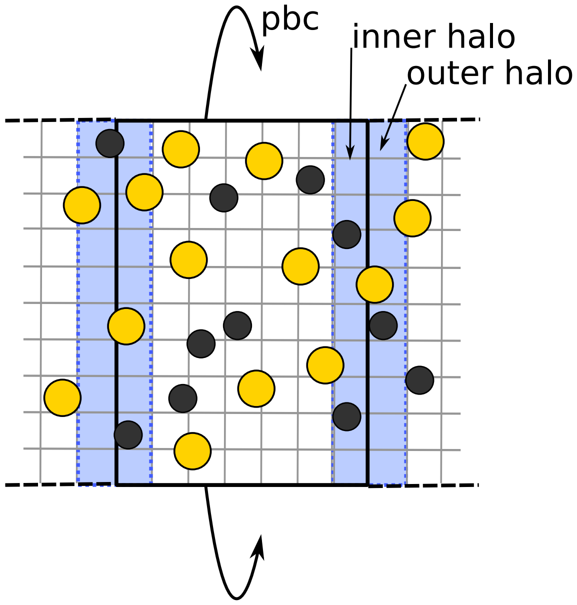

Figure 7.4: Domain decomposition scheme for velocity Verlet steps visualizing the halos with respect to the domain in the center. The inner and outer halo layers coincide with the boundaries of the MD particle cell system (drawn in light gray). Here, a one-dimensional slice decomposition is shown. Instead of periodic boundaries (indicated as "pbc") walls can also be applied.

7.5.1. Parallelization via Message Passing

Molecular Dynamics Part Using the domain decomposition technique means to separate the simulation box into smaller domains (slices, cubes, etc.) in which the majority of particles is independent from particles in other simulation box parts with respect to the force calculation. Each domain is associated to one process. For short range interactions it is obvious that every particle has a radius beyond which it cannot influence other particles anymore (cutoff radius of the pair potential). This idea goes back to the year 1959 [27] and is used already in serial code where the particles are always part of a cell system with cell diameters $d_{\text{cell}} \geq \max[\{r_{\text{cut},a}\}, a \text{ labels the pair potential}]^2$. Instead of calculating the distances (and forces) to all particles, only the particles in the own and the neighboring cells have to be taken into account.

This cell system sets the width of the so-called halo layers in a domain decomposition parallelization (see Fig. 7.4). From the point of view of the center domain in figure 7.4 the particles in the outer halo have to be known, since they can potentially contribute to the force a particle feels close to the domain borders. At this point the message passing comes into play. Before any force can be calculated, each process has to send its particle positions of the inner domain halos to the processes of the neighboring domains and has to receive the information about the outer halos. After this send-receive communication every process has all the information needed to update the forces of all particles inside its own domain. When the new forces of all particles are determined, the particles move according to the Verlet rules (see section 7.1). The particles which now lie outside of the domain have to be sent to the corresponding neighboring domains and can subsequently be removed from memory.

In this work a one-dimensional (via slices) and a two-dimensional (via cuboids) domain decomposition is mainly used. The one-dimensional decomposition has the disadvantage that the message lengths (which scale with the domain cross sectional

---

[2] The cell system for the MD particles is just a technical detail to improve the performance of the force calculation and should not be mistaken for the solvent collision cell system.

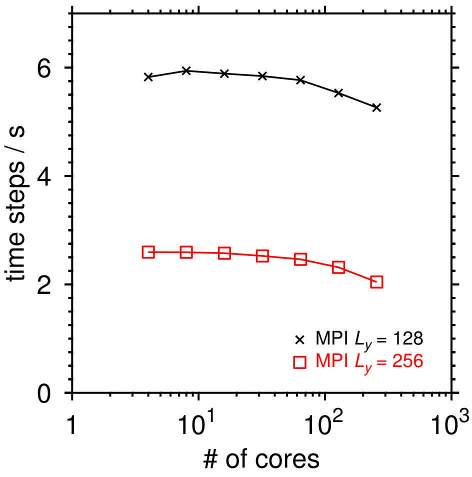

Figure 7.5: Weak scaling plot of the one-dimensional domain decomposition parallelization on *Juropa*. The system size per process is constant in this plot. From the left to the right the following numbers of cores were used: 4, 8, 16, 32, 64, 128, 256. The slice dimension was $L_x \times L_y \times L_z = 4 \times 128 \times 5$ and $L_x \times L_y \times L_z = 4 \times 256 \times 5$ as indicated.

area) is larger than in a two- or three-dimensional decomposition, however, it has the advantage that only a single send-receive operation is needed since no corners are present. As a general rule one should always prefer the higher-dimensional decomposition, but sometimes the system under study itself can also favor lower-dimensional decomposition as in the case of the parallel walls confinement or the cylindrical confinement.

Solvent Part The aforementioned domain decomposition scheme only treats MD particles (colloids and polymers). The solvent particles are handled in a slightly different way. At this point Godehard Sutmann has to be greatly acknowledged for his ideas, help and long discussions regarding the parallelization of the MPC part. Please see the corresponding reference [188].

First of all, the random shift vector $\boldsymbol{a}_0$ of the MPC cell system is generated by the root process and sent to all other processes. Then, particles are sorted into this shifted cell system. The shift leads to the situation that particles do not have an associated cell in the current domain and have to be sent to the neighboring domains. This is done in an ordered manner. First, a send-receive along the x-axis is performed, then along the y-axis and so on. This guarantees that all particles are placed in the proper cells. The MPC cell algorithm of choice is used to update all of the solvent velocities. The new calculated velocities are sent back in the inverse order, so first the z, then the y and finally the x-axis. This sequenced send-receive technique treats the corners properly. The subsequent MPC streaming step is handled as the streaming in the case of the MD particles.

Figure 7.5 shows how far one can go in terms of CPU cores with reasonable losses in performance in case of the one-dimensional domain decomposition. The quadratic geometry of the systems is reached for 32 and 64 processes for $L_y = 128$ and $L_z = 256$ respectively.

Probing the Correct Implementation

Velocity Verlet Integration Molecular Dynamics simulations in the NVE ensemble were tested in two ways. The sum of kinetic and potential energy is conserved in the NVE ensemble and should not systematically vary, if the integration time step was chosen to be small enough. As a test a colloid-polymer mixture (continuous AO

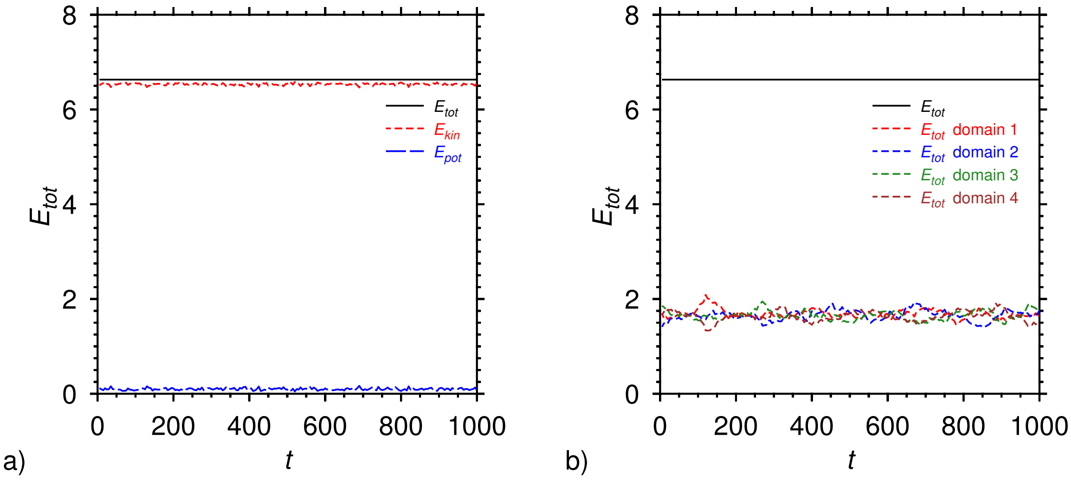

Figure 7.6.: Conservation of total energy E_{tot} in an NVE simulation which was split up into domains to run in parallel. A random configuration of colloids and polymers in a elongated cuboid box with walls was chosen for initialization. The time step was chosen as $\delta t = 0.002$. Part (a) shows the contribution of kinetic and potential energy. Part (b) shows the contribution from the different domains to the total energy.

model, see section 2.1) was considered. Figure 7.6 shows such a check of the parallel implementation of the velocity Verlet algorithm. From figure part (a) it is nicely visible how the (fluctuating) potential and kinetic energy sum up to the constant total energy E_{tot}. In part (b) of the same figure the total kinetic energy is shown for each subdomain separately. Although fluctuating within a subsystem, the total energy as a sum over all domains is again a constant. This leads to the conclusion that, on the one hand, the integration time step was chosen small enough (for the considered pair interactions) and, on the other hand, the domain decomposition via message passing was implemented correctly.

Solvent Coupling A similar test can be performed to check whether the collisional coupling between MD and solvent particles was properly implemented. Again the total energy $E_{\text{tot}} = E_{\text{kin,fluid}} + E_{\text{kin,sol}} + E_{\text{pot}}$ is a conserved quantity in the case of the SRD algorithm in a bulk system[3]. Figure 7.7 is the analog to figure 7.6b and verifies the conservation of the total energy within the domain decomposition parallelization.

7.5.2. Parallelization via Shared Memory

Molecular Dynamics Part The second technique which was implemented is the particle decomposition via shared memory. The forces acting on each particle can be calculated independently from the force calculations for other particles. Such calculations are done typically in large *for*-loops. Different loop parts are treated by different processes (threads). Program parts where multiple threads need write access at the same time at the same memory area are treated in parallel via the

---

[3] Note that bulk filling rules for under-occupied MPC cells would already destroy the conservation of energy.

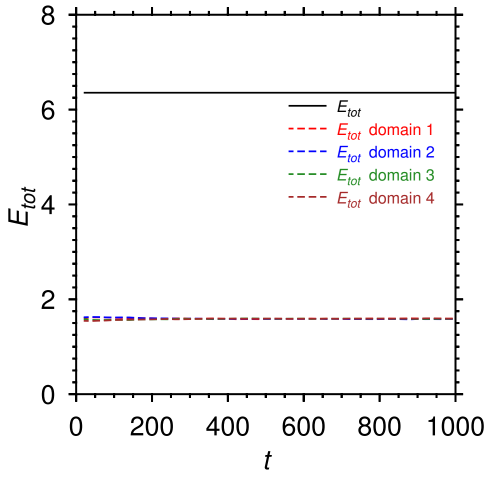

Figure 7.7: Energy conservation and equipartition of energy across different domains. The solvent acts as a strong thermostat, so that only up to time $t = 200$ small fluctuations are visible within the subdomains.

openMP reduction operations (for instance the kinetic or potential energy). The association to MD cells cannot be parallelized in such a simple way (linked list access) and is executed serially. This is not a drawback since the particle insertion is a rather fast operation in comparison to the velocity Verlet step. Furthermore, tasks are distributed to threads in a scheduled manner using an exponential decay of the partial task size. Such a scheduling scheme minimizes the idle-time tasks have to wait for each other.

Solvent Part In case of the solvent collision step there exists no default openMP reduction operation which could handle the simultaneous array write access when sorting in the particles into MPC cells. A simple data structure is needed to solve this issue. In the serial code each MPC cell owns an array to sort in the solvent and MD particles before performing the stochastic collision. To do this in parallel, every MPC cell gets now as many arrays as threads are present, so that every process has its own private array. This technique is visualized by figure 7.8. This simple trick is really crucial for the shared memory parallelization, since the number of solvent particles which have to be shifted and sorted in is typically of the order of millions and thus, a serial execution of this code block would drastically slow down the whole program.

For comparison the shared memory parallelization performance is shown together with the message passing parallelization results in a strong scaling plot (see Fig. 7.9). Even though there is almost no serial part left in the particle decomposition parallelization, the performance cannot compete with the domain decomposition via message passing. The main reason is that the particle memory is not spatially ordered and, therefore, is accessed in a random manner. The odd performance drop-down for six cores can be understood when one looks how the Intel Nehalem 8-core nodes access their memory. The Nehalem unit is split up in two quad-cores each of which have access to “their own” half of the global memory. In the case of 6 cores, two cores can access some memory only via communication with the neighboring quad-core unit. The six core data point represents the most unbalanced memory access. In the case of the domain decomposition small deviations from the almost linear behavior are expected since the cell system diameters depend on the used domain slice width. In practice, both versions of parallelization were used for different tasks. Most often, the domain decomposition scheme was used since it shows the better performance

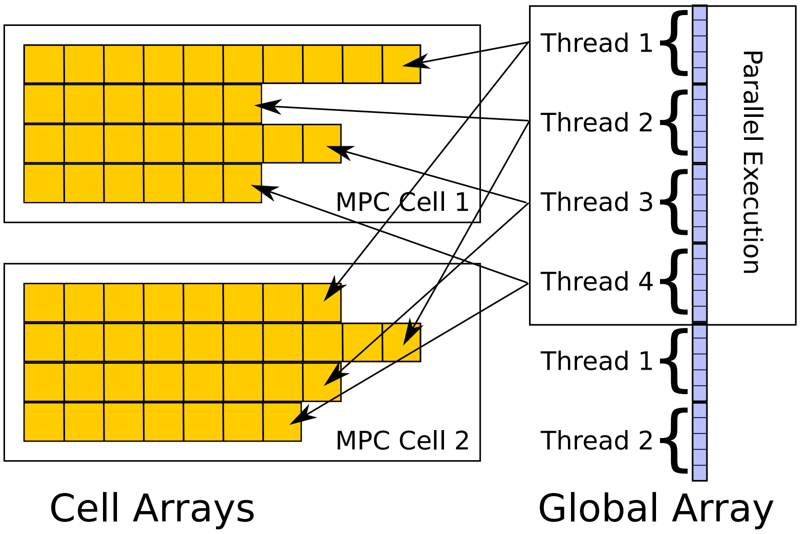

Figure 7.8.: Shared memory parallelization scheme for particle insertion into MPC cells. Here, four threads are shown which can fill up two MPC cells at the same time. A square represents the memory allocated for one particle. All particles (typically in the order of 10 millions) have to be sorted from the "global array " into cell arrays. Every thread obtains in each MPC cell a dynamical particle array of its own.

Figure 7.9: Strong scaling comparison between the domain decomposition (Message Passing) and the particle decomposition (shared memory) parallelization scheme. The underlying system was an AO mixture in the two-phase region between two walls a distance $L_z = 5$ apart from each other ($L_x = L_y = 96$). The blue dashed line represents a perfectly linear scaling. The error of the data points is of the order of the symbol size.

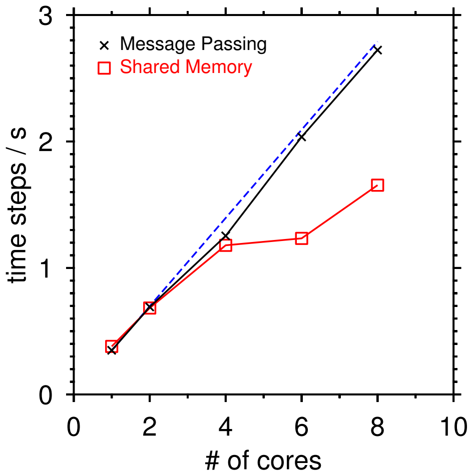

and is not restricted to the size of a node. However, since particles of the same type are only distinguishable by their position in memory, the division of the system in subdomains, which particles often enter and leave, leads to the loss of their discernability. For measurements of quantities such as auto-correlation functions for which the particles have to be distinguishable the shared memory parallelization scheme was applied.

Hybrid simulations where a particle decomposition via a shared memory parallelization is done additionally within a domain of a domain decomposition parallelization scheme make sense up to the number of cores which have direct access to the same range of global memory. For instance, an AMD 12-core Magny Cours unit is split up into two six-core units which have direct access to their part of the memory. In this case one would expect a linear scaling up to six cores.

7.6. Conclusion

In this chapter the MPCD algorithm was introduced. Multiple thermostats were implemented and compared in their properties and their performance. It was shown that the solvent viscosity (Schmidt number) can be controlled by the parameters of the algorithm and agree very well with the theoretical predictions. The same measurement confirms that perfect stick boundary conditions for hard walls can be achieved by bounce back and bulk filling rules. Furthermore, the coupling between the solvent and embedded particles was introduced and the influence of hydrodynamics on an embedded heavy tracer particle could be measured. It was possible to implement two different parallelization schemes, from which the domain decomposition scheme can be applied to multiple nodes and therefore, is expected to work on hundreds or thousands of CPU cores.

CHAPTER

8

SPINODAL DECOMPOSITION IN THIN FILMS

After a quench of a multi-component system from a homogeneous state into a phase diagram region of phase coexistence the system becomes unstable with respect to the initially homogeneous state and phase separation takes place via the “spinodal decomposition” mechanism. Due to density fluctuations the system breaks up into mesoscopic domains ($\gtrsim$ particle diameter) aspiring to further growth. Besides the technological importance like the production of alloys, porous membranes or polymer foams, the pattern formation mechanism represents a generic process in condensed matter. Particularly the case of thin films becomes important in the context of nanotechnology and at the same time remains a challenging problem with respect to our theoretical understanding. This is due to a competition of interface and bulk behavior leading to complex phenomena like wetting, prewetting and layering transitions. Spinodal decomposition in quasi two-dimensional systems is especially interesting from the experimental point of view where binary mixtures are often confined between substrates (typically favored by only one of the two components of the binary mixture). Colloid-polymer mixtures are perfectly suited to study the spinodal decomposition mechanism via experiments, since the μm-sized colloids can be observed directly by confocal microscopy. The *static properties* of colloid-polymer mixtures could be successfully investigated via coarse grained models such as the AO model or its extension (see next section and reference [42]), but the *dynamics* are controlled by the solvent particles below the nanometer size. The MPCD technique is able to model such systems in which length scales from nanometers (solvent) up to 100 μm or more (macroscopic pattern formation) need to be considered simultaneously. Figure 8.1 shows a typical snapshot from a spinodal decomposition simulation using the MPCD technique. Three different length scales are visible: point-like solvent particles (small blue spheres), fluid particles (yellow and black spheres) and the macroscopic domains consisting of fluid particles.

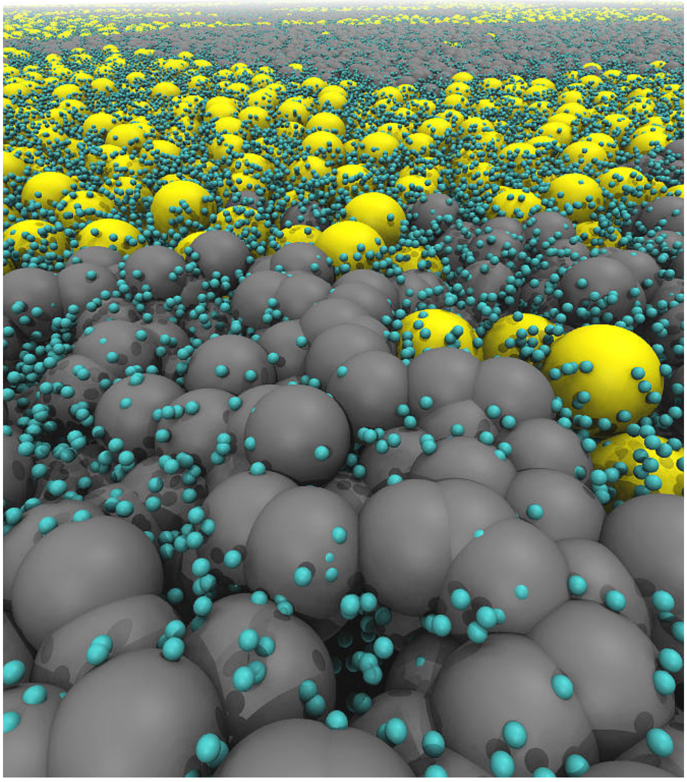

Figure 8.1: Typical snapshot of a colloid-polymer mixture during the demixing process. The small particles (blue) represent the point-like solvent particles. The black particles are the polymers and the yellow particles are the colloids. A small part of the upper layer of solvent particles is not shown to improve the visibility of the colloid-polymer domain structure.

In this chapter the dynamics of spinodal decomposition in binary fluids is investigated by using the MPCD algorithm which allows for switching off hydrodynamic interactions. In contrast to a lot of theoretical and numerical studies which were done in the past and used to predict universality (see next section for an overview), here an intrinsically asymmetric binary colloid-polymer mixture confined between planar walls (which are favored by the colloids) is studied. Such a model, for which no symmetry with respect to interactions is left over anymore, and for which the dimensionality is neither pure three-dimensional nor pure two-dimensional, is much closer to the "real" experiments, and the question arises whether a universal phase separation behavior can still be expected.

8.1. Aspects of Phase Separation Kinetics

This section shall serve as a brief summary of what is known about spinodal decomposition from the theoretical point of view, from the point of view of numerical investigations and also from the perspective of experiments. In binary fluid mixtures, one observes a self-similarity during the coarsening process, which means that typical snapshots of the demixing pattern at different times can be mapped onto each other by zooming in or out. This type of universality is typically described by the growth of a characteristic length scale $l_d(t)$ over time t after the quench from the one-phase region into the two-phase region. As will be discussed just below, within certain time regimes a simple power law description $l_d(t) \sim t^n$ of the average domain size is found, where n is the so-called "growth exponent". However, to which degree of universality such simple formulas are valid is a current debate, especially when thinking about typical experimental setups. Even when confining a monolayer of fluid particles, the system behaves still three-dimensional on the length scale of the solvent particles. Of course, also effects from gravitation, polydispersity, impurities or non-idealities regarding the flatness of the confining walls are often present in experiments.

Spinodal Decomposition in three dimensions Following the review from Bray [189], one expects in the case of a binary liquid mixture in the bulk for the average domain size three different growth law regimes, which can be made plausible by dimensional arguments. In general, one distinguishes between two classes of dynamical models. The time evolution of a non-conserved order parameter ϕ is

$$\partial_t \phi \sim \frac{\delta F[\phi]}{\delta \phi} \ , \tag{8.1}$$

where $F[\phi]$ is the free energy functional of this order parameter. Such dynamics equations with additional noise terms are called "model A" within the framework of critical dynamics and represent a simple gradient descent. It can be used to describe, for instance, a transition from the gas to the liquid phase. For the case of phase separation after a quench, the order parameter is conserved and the dynamic equation ("model B") can be written as a continuity equation

$$\partial_t \phi \sim -\nabla \cdot \boldsymbol{j} \tag{8.2}$$

with a current $\boldsymbol{j} = \lambda \nabla \frac{\delta F}{\delta \phi}$. The functional derivative $\frac{\delta F}{\delta \phi}$ can be interpreted as the chemical potential $\mu \equiv \frac{\delta F}{\delta \phi}$ so that equation 8.2 results into a diffusion equation

$$\partial_t \phi \sim \lambda \Delta \mu \ . \tag{8.3}$$

Equation 8.3 is extended by an "advective" term taking into account the transport of the order parameter by hydrodynamic flow:

$$\partial_t \phi + \boldsymbol{v} \nabla \phi \sim \lambda \Delta \mu \ ,$$

where $\boldsymbol{v}$ is the local velocity of the fluid. This velocity field follows from the Navier-Stokes equations in the case of an incompressible fluid as

$$\rho \left(\partial_t \boldsymbol{v} + (\boldsymbol{v} \cdot \nabla) \boldsymbol{v} \right) = \eta \nabla^2 \boldsymbol{v} - \nabla p - \phi \nabla \mu \ . \tag{8.4}$$

Here, η is the fluid shear viscosity, p is the pressure and ρ is the density. The last term is the driving force and is equivalent to the free energy difference the fluid follows when the chemical potential μ is varied.

In the overdamped limit (viscous hydrodynamics) the left hand side of equation 8.4 can be neglected and with p and $\mu \sim \frac{\gamma}{L}$ (where γ is the interfacial tension) and $v \sim \frac{L}{t}$ it yields

$$\frac{\eta}{Lt} \sim \frac{\gamma}{L^2} \ \Rightarrow L \sim \frac{\gamma}{\eta} t \ . \tag{8.5}$$

The latter equation represents the viscous growth law and serves from now on to define the validity regimes of the two further growth laws.

Equation 8.3 is valid when the advective term is negligible resulting in the diffusive growth law

$$\frac{1}{t} \sim \lambda \frac{\gamma}{L^3} \ \Rightarrow L \sim (\lambda \gamma t)^{1/3} \ . \tag{8.6}$$

This is only valid when $\lambda\Delta\mu \gg \boldsymbol{v}\cdot\nabla\phi$ which leads with the same dimensional estimates and the result of equation 8.5 to $L \ll (\lambda\eta)^{1/2}$. For the last possible growth law one considers the case when the inertial term in the Navier-Stokes equation dominates over the viscous part, so that

$$\rho\frac{L}{t^2} \sim \frac{\gamma}{L^2} \;\Rightarrow L \sim \left(\frac{\gamma}{\rho}t^2\right)^{1/3} \tag{8.7}$$

follows as the inertial growth law. This is valid, if $\rho\left(\partial_t\boldsymbol{v} + (\boldsymbol{v}\cdot\nabla)\boldsymbol{v}\right) \gg \eta\nabla^2\boldsymbol{v}$ which leads using again the result of equation 8.5 to $\rho\frac{L}{t^2} \gg \frac{\gamma}{L^2} \;\Rightarrow L \gg \frac{\eta^2}{\rho\gamma}$. With $L \equiv l_d(t)$ one can summarize the scaling laws of the average domain size in binary liquids including hydrodynamic interactions as

$$l_d(t) \propto \begin{cases} (D\gamma t)^{1/3}\ , & L \ll (D\eta)^{1/2} \\ \frac{\gamma}{\eta}t\ , & (D\eta)^{1/2} \ll L \ll \frac{\eta^2}{\rho\gamma} \\ (\gamma/\rho)^{1/3}t^{2/3}\ , & L \gg \frac{\eta^2}{\rho\gamma} \end{cases}\ . \tag{8.8}$$

For a more detailed review of these growth laws and further aspects of spinodal decomposition in three dimensions see the work from SIGGIA [190], FURUKAWA [191, 192] and the more recent review from KENDON et al. [193, 194]. The latter present Lattice Boltzmann simulation results of high quality which confirm very convincingly the viscous ($\sim t$) and the inertial regime at late times ($\sim t^{2/3}$). They point out a wide crossover regime over multiple decades of time from the power law exponent $n = 1$ to $n = 2/3$. The investigated time regime and system size is only possible to access via mesoscale methods such as Lattice Boltzmann. Reaching this late time regime using conventional MD simulation techniques is a very challenging task at current state-of-the-art computers [195]. The derivation of growth laws based on dimensional analysis is pointed out by GRANT and ELDER to be not rigorous [196]. They criticize that the simple dimensional arguments lead wrongly to the late time power law with exponent 2/3. They claim that the growth exponent is bounded to $n \leq 1/2$ because the increase in the Reynolds number at late times causes turbulence and hence, will not allow for exponents larger than 1/2. Despite these critics, the growth laws of equation 8.8 were often verified in computer simulations, and also in experiments a rather high exponent of $n \approx 0.8$ was observed [197].

Spinodal Decomposition in two dimensions The process of spinodal decomposition of binary mixtures in two dimensions is much less understood than in three dimensions. Although a lot of theoretical and numerical investigations were performed, a whole zoo of power law exponents was obtained raising the question whether one can talk at all about universality in spinodal decomposition kinetics. A few examples are presented and commented in the following. The already mentioned study by FURUKAWA [191] is also valid in two dimensions and hence, predicts a growth law with exponent $n = 2/3$ for late times. FURUKAWA's numerical investigations indeed confirm this prediction but also point out that for a high viscosity, where a so-called double phase separation morphology is seen, the universality vanishes [198]. While for the early states where the system still behaves diffusive the $n = 1/3$ power law is also expected for two-dimensional systems, as soon as hydrodynamic mechanisms play a role, the droplet diffusion-coagulation mechanism with $n = 1/d$, $d = 2$ should dominate which agrees with the prediction by GRANT et al. of $n = 1/2$ (for concentrated mixtures) and a crossover at late times to $n = 1/3$ (for dilute mixtures, Lifshitz-Slyozov mechanism) [199]. The morphology of the demixing pattern is reported to have a strong influence on the growth mechanism. While a percolating pattern which is typically achieved for symmetric 50%-50% binary mixtures (often called "critical") shows an $n = 2/3$ power law, off-critical concentration ratios can lead to $n = 1/2$ or $n = 1/3$ [200, 201]. WAGNER et al. report that for binary mixtures, in which both species have different dynamics and at the same time show a droplet morphology at 50%-50% mixture, a viscous regime with $n = 1$ is recovered which later crosses over into a $n = 2/3$ regime, very similar to three dimensions. Finally, TANAKA et al. as well as WAGNER et al. argue that there cannot exist a universality in the true sense of the word, since the observed growth laws depend too strongly on the underlying viscosity [202, 203]. REITH et al. [204] did quenches close to the critical point and point out that even in the supercritical region the growth of critical fluctuations shows power law behavior but only well inside the two phase region it is possible to observe an $n = 1/2$ power law. As a last example the work of CHEN et al. shall be mentioned [205]. In their numerical investigations of two-dimensional polymer blends they are able to switch off hydrodynamics. For 50%-50% mixtures they find $n \approx 1/2$ with hydrodynamics and $n \approx 1/3$ (which is much closer to $1/4$ when one looks at the data) without hydrodynamics. As soon as droplet patterns are reached they find always $n \approx 1/3$ $(1/4)$. They also comment on the so-called "pinning" effect which was observed in experiments [206] as a sudden tremendous slowdown in dynamics which was later explained by CRIST as a "shock" due to a morphological crossover from a percolation to a droplet pattern [207].

Spinodal Decomposition in quasi two dimensions With all the controversial aspects mentioned above in mind a few results from numerical investigations of the quasi two-dimensional setup, where x- and y-dimensions are huge in comparison to the z-dimension of the system, are discussed in the following. One expects a two-dimensional behavior in the spinodal decomposition process as soon as the average domain size exceeds the smallest lateral dimension of the system. RAMACHANDRAN et al. studied via DPD simulations a pure two-dimensional fluid layer (in the x, y-plane) which is surrounded by solvent with respect to the z-dimension [23]. Independent of the concentration ratio they find a power law with $n = 1/3$ when a solvent is present in the third dimension and $n = 1/2$ when they restrict the system to purely two dimensions. They predict that the presence of additional walls perpendicular to the z-axis leads to a power law with $n = 1/4$. DAS et al. studied a binary Lennard-Jones fluid confined between two walls, where the "A-particles" favor the walls [208]. For droplet structures they find a growth law exponent of $n = 2/3$ at late times and conclude that this behavior may be only a transient or that the wetting influences the growth dynamics. Finally, HORE and LARADJI provide a very detailed study by means of DPD simulations on quasi two-dimensional systems where wetting layers are present [209]. Similar to DAS et al. they find for the droplet morphology fast growth exceeding even $n = 1$ at an intermediate time regime, which crosses over into the $n = 1/3$ power law at late times. They explain this as a result of the wetting layer backflow. Furthermore, for the case of "neutral" walls and percolation pattern, they studied the influence of stick and slip boundary conditions and find that in the case of stick boundary conditions correlations are screened which leads to a smaller growth law exponent $n = 1/3$ in contrast to slip boundaries $n = 1/2$.

All these various findings and possible growth mechanisms make clear how complex the situation of phase separation kinetics is in general and for quasi two-dimensional confinement in particular. It becomes apparent that universality in the strong classical sense, meaning parameter insensitive power laws, may not exist for binary fluids in quasi two-dimensional confinement. However, it might be possible to categorize the various observed power laws and, therefore, predict for well-defined setups which growth mechanism and regularities are expected.

8.2. Phase Diagram

Before one can start studying the spinodal decomposition of the continuous AO model confined between planar walls, one has to know the phase diagram. The bulk phase diagram can only serve as a rough orientation, but important effects like the asymmetric preference of particle species to the walls (which are located at $\pm L_z/2$) are not covered. Therefore, a phase diagram has to be recorded separately for every wall distance D one is interested in. The WCA potential is used for the particle-wall interaction with $\sigma_{wc} = 0.5$ and $\sigma_{wp} = 0.4$. The wetting behavior of the continuous AO model was studied in high detail at fixed $\eta_p^r \approx 1.57$ [9]. For the wall-particle interaction ranges chosen above, complete wetting was found and is also expected to be present for higher values of η_p^r. Figure 8.2 shows the binodal in the case of wall distances $D = 5$ and $D = 10$. Please note that all packing fractions result from the number densities by using the effective diameter $d_{\text{eff}} = 1.01557\sigma$, σ being the parameter in the corresponding potential, as $\eta = \rho\frac{\pi}{6}d_{\text{eff}}^3$. Some of the grand canonical Monte Carlo simulations simulations were performed by collaborator Antonia Statt who is acknowledged at this point.

Figure 8.2d shows estimates for the free energy landscapes for wall distance $D = 1.5$. Such a small wall separation leads to an almost pure two-dimensional system, since colloids and polymers do not fit on top of each other anymore. The depletion force seems to be smaller than in three-dimensional systems. To be able to see a clear phase separation extremely high polymer reservoir packing fraction of $\eta_p^r \gtrsim 3.5$ are needed. Although at $\eta_p^r = 4$ the coexistence density minima are well separated the resulting interfacial tension is only around $\gamma \approx 0.1$. When increasing the polymer reservoir packing fraction to $\eta_p^r = 5$ the interfacial tension is increased by a factor of five to $\gamma \approx 0.5$. The colloid and polymer densities, on the other hand, are only 6% and 15% respectively higher. These values are in general important since they define the validity regimes of the power laws (see Eq. 8.8). Assuming a constant shear viscosity η and mass density ρ, an increase of the interfacial tension lowers the length scale from which on the inertial growth regime dominates.

8.3. Simulation Details

Quenching Procedure The word “quench” refers to an instantaneous or very quick change of system parameters so that the system is positioned in a region

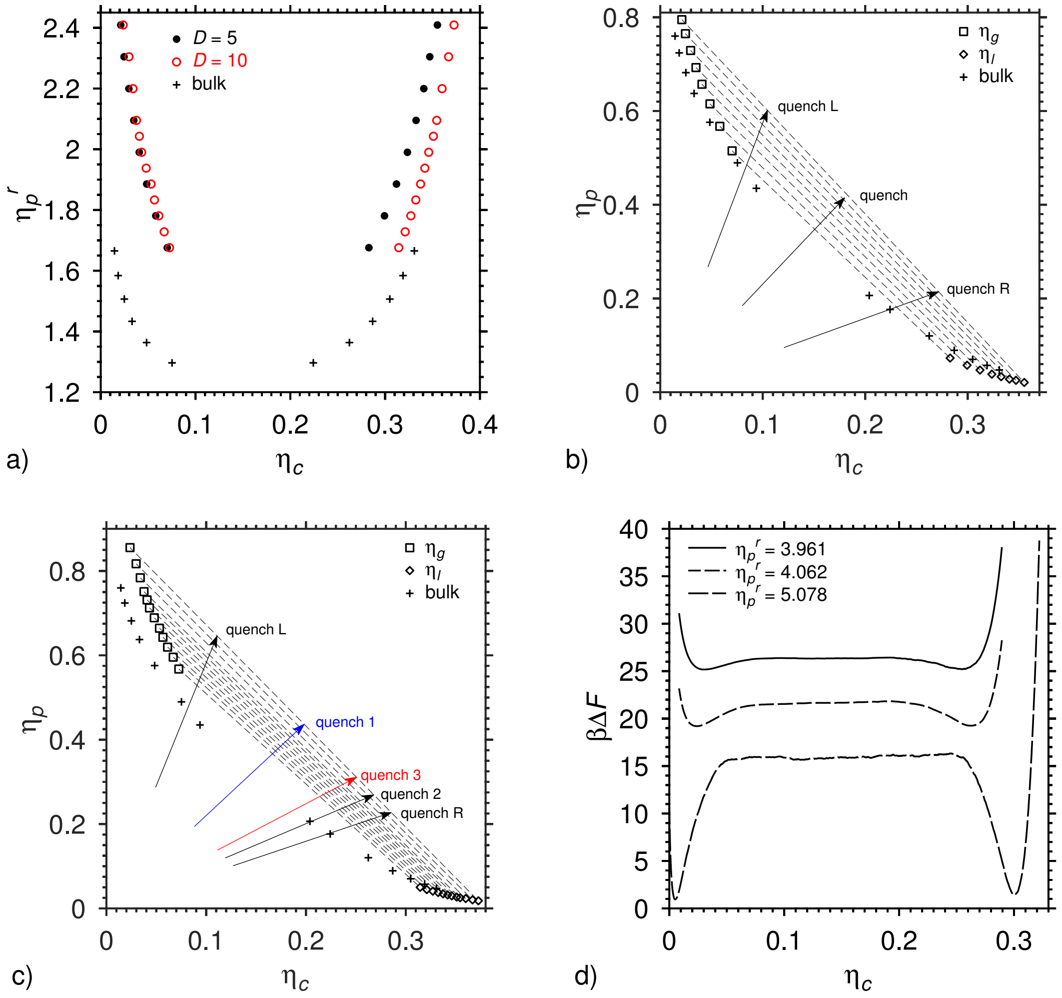

Figure 8.2.: (a) Phase diagram of the continuous AO model confined between planar walls a distance D apart. The wall potential is the WCA potential with $\sigma_w = 0.5$. Two different choices of $D = 5$ and $D = 10$ as well as the bulk data from [42] are shown. (b) Phase diagram of the continuous AO model in the plane of polymer packing fraction η_p and colloid packing fraction η_c for distance $D = 5$. (c) Same as (b) but for $D = 10$. (d) Free energy landscapes for $L_x = 20$, $L_y = 60$ and $D = 1.5$ for various η_p^r as indicated.

of the phase diagram its current configuration does not belong to. Such a jump from one region in the phase diagram to another region of the phase diagram can be achieved via a change in temperature, pressure or volume depending on which ensemble is considered. In the actual case of the continuous AO model a simple change of the temperature variable is undesirable, since this model represents an entropic system where the polymer reservoir packing fraction plays the role of an inverse temperature. Changing the polymer particle number in the simulation leads to the desired quench, but there is no well-defined rule how additional polymers should be inserted. Therefore, a volume quench is used, which means a change in both the polymer packing fraction *and* the colloid packing fraction. This is achieved by an initial simulation in a much larger simulation box with same wall distance D. The coordinates of a typical snapshot of this simulation are then rescaled with respect to their x- and y-coordinates to fit into the smaller target simulation box corresponding to the target packing fractions. In the case of MPCD simulations, the solvent particle coordinates are kept constant so that the solvent density is not changed during this quench procedure[1]. Resulting overlaps between particles (which lead to numerical instabilities of the integration scheme due to tremendous forces) are the drawback of the volume quench and need a subtle treatment, for instance, by force limitations during the velocity Verlet steps. In practice only a few of this restricted integration steps (if ever) are needed, since the solvent particles act as a very strong thermostat.

Parameter Choice The parameter space of the actual system under study is immense even when disregarding technical parameters like the integration time step and parallelization related parameters. The parameters for the static properties of the model are fixed throughout the MPCD simulations which are exactly the parameters which define the phase diagram (see section 2.2 and 8.2). The unit length scale is the colloid diameter σ_{cc} in the colloid-colloid WCA-interaction potential.

The choice of the parameters which influence the dynamics directly[2] needs a few comments and remarks. The mass of a polymer was set equal to the mass of a colloid ($m_p = m_c = 1$), which means with respect to the SRD algorithm that the solvent cannot directly distinguish between the species of MD particles. However, the soft interaction potential of the polymers allows for multiple polymers per solvent cell, while the “hard” interactions between colloids suppress the occurrence of multiple colloids in an MPC cell. Of course, it is desirable to study the influences of the mass difference in binary mixtures on the dynamics (especially when taking HI into account), but this remains a future project. Another parameter, which has to be chosen carefully, is the MPC cell dimension. This dimension sets the lower boundary for the resolution of hydrodynamic effects, since within such a cell there are only *stochastic* collisions. This means, on the one hand, the smaller this cell size the better hydrodynamic influences can be studied at small length scales. On the other hand, the simple velocity coupling (see section 7.4), in which solvent particles can stream through MD particles, anyway makes a correct hydrodynamic description below the order of MD particle sizes impossible. As a compromise, here,

---

[1] Solvent particles that lie outside the simulation box are removed. Then the desired solvent density is matched by either adding a few solvent particles at random or deleting them respectively.

[2] Note that also parameters such as the wall distance or the relative percentage of the particle species influence the dynamics strongly.

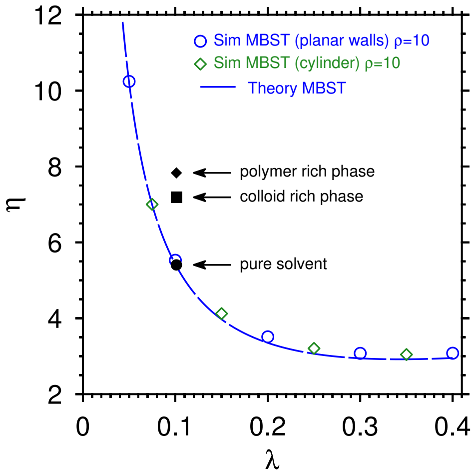

Figure 8.3: Zoomed in version of figure 7.2c. The bullet symbol with label "pure solvent" represents a measurement using the same parameters as in the spinodal decomposition studies. Additionally, the viscosity estimates of the polymer-rich phase and the colloid-rich phase (see coexistence densities in the phase diagram, Fig. 8.2b) are shown.

$L_x = L_y$	D	σ_{cc}, ε_{cc}	σ_{cp}, ε_{cp}	σ_{pp}, ε_{pp}	σ_{wc}, ε_{wc}	σ_{wp}, ε_{wp}
256; 512	1.5; 5; 10	1, 1	0.9, 1	0.8, 0.0625	0.5, 1	0.4, 1
m_c, m_p	m_s	N_s	a, α	δt	τ	T, therm.
1, 1	0.025	10	0.5, $\pi/2$	0.002	0.008	1, MBST; NOHI

Table 8.1.: General parameter setup for the study of spinodal decomposition in thin films. Multiple entries per field are separated by commas while values which were varied are separated by semicolons. The MBST thermostat allows for different boundary conditions of solvent particles (see the details in the main text).

a lateral cell dimension of $a = 0.5$ was selected. The next point is to decide for a certain solvent number density. The solvent number density defines the quality of the approximation of the MPC solvent to a realistic solvent (remember that one solvent particle in the simulation represents a group of solvent particles in reality). Especially the compressibility ($\sim 1/\rho_s$) rises when choosing low solvent densities. Successful simulations were reported for solvent densities from $\rho_s = 10$ up to $\rho_s = 32$ per cell volume. With the choice of $a = 0.5$, $\rho_s = 10$ leads to an overall density of $\rho_s^{\text{tot}} = 80$ and therefore, represents a relatively high value so that compressibility effects should be negligible. Additionally to the solvents density, the mass of solvent particles has to be chosen. A rule of thumb says that the mass of one MD particle should be similar to the sum of solvent particle masses it interacts with. A solvent mass of $m_s = 0.025$ means a total solvent mass of $m_c^{\text{tot}} = 0.25$ per cell or $m_V^{\text{tot}} = 2$ per unit volume and hence, represents a reasonable choice to fulfill this rule of thumb.

With all these parameters fixed, the collision time step τ determines the solvent viscosity via the mean free path $\lambda = \tau\sqrt{k_B T/(m_s a^2)}$. With the choice of $\tau = 4 \times 0.002 = 0.008$ this results in $\lambda \approx 0.1$ so that the viscosity yields (see Fig. 8.3) $\eta = \rho_{s,c}\eta^* \approx 5.4$. As one can see from figure 8.3 this choice of mean free path and corresponding viscosity belongs to the collision dominated part and therefore, belongs to the regime of high Schmidt numbers. Table 8.1 gives a summary of the parameters to be considered in the simulation. Additionally, one should keep in mind the polymer and colloid particle numbers which define the position in the phase diagrams and control the morphology and therefore, the dynamics of phase separation.

Technical Details The huge system size makes it almost impossible to run a simulation on a single core; the memory needed exceeds 6 GB or more, which means on current computer architectures that an inter-CPU communication is needed when memory is accessed (see the scaling breakdown in figure 7.9). Despite such a slowing down due to architectural limits, the typical performance a single core achieves is of the order of $2 \cdot 10^{-5} t$ per second (AMD interlagos architecture, $V = 256 \times 256 \times 10$), where t is the MD unit time. Simulating a range of $t \sim 10^5$ would lead to a real-time of approximately 150 years. Even though this is the most extreme example in terms of system size and time range considered in this thesis, it clearly points out the necessity of a highly parallelized implementation of the algorithms. Certain system dynamics of interest are expected to follow power laws $\mathcal{O}(t) \sim t^n$ with $n \lesssim 1$, where $\mathcal{O}$ stands for a typical observable of interest like the average structure size l_d. This expectation leads to the following choice for data output. For the early times the simulation runs on "only" 256 cores and writes to the hard disk positions and velocities of the colloids and polymers every $t = 12$ MD unit times. Then the number of cores per lateral dimension is doubled as well as the time when coordinates are written out leading to 1024 cores and $t = 48$. The latest stages in the simulations are accessed via 4096 cores and $t = 192$. This leads to a balanced communication, input-output to calculation time ratio and therefore, to an (almost) linear strong scaling behavior. In practice, checkpointing (to continue a simulation) comes additionally into play for which also the solvent particle positions and velocities have to be written out from time to time leading to full-information snapshots of a typical size of 2 to 9 GB. Figure 8.4 shows the performance development of typical simulation runs ($V = 256 \times 256 \times 10$) on the super computer HERMIT (CRAY XE6). The performance is always set by the slowest process, which is typically the process corresponding to the domain with the largest particle number. In the case of spinodal decomposition the polymer regions with almost four times more particles than present in colloid regions cause the general dropdown of the performance over MD time t due to their growth. This problem of load imbalance could be solved by the virtualization of MPI-ranks which then can be dynamically distributed to individual processors [210]. However, this needs a moderate redesign of the code and is known for compatibility issues depending on the super computer platform, so that its implementation is deferred to the future. From the graph it is clear that the MD part of the algorithm (which is the costly part when using the NOHI thermostating) is responsible for the breakdown in performance. The large dropdown in performance going from 1024 to 4096 cores can be explained by the MD cell system change from $l_{c,\mathrm{MD}} = 1.14$ (1.5% larger than the cutoff radius) to $l_{c,\mathrm{MD}} = 1.33$ (18.5% larger than the cutoff radius). This means that approximately 1.4 times more particles are selected as potential contributors to the force calculation of a single particle which fits well to the change in performance[3].

Extracting Structural Information The most common structural information is obtained by measuring position correlations in real or momentum space. While in soft matter physics colloidal particles are directly observable via confocal microscopy and therefore, an access to real space analysis is possible, in condensed matter physics, on the molecular level, scattering methods such as x-ray scattering, which

---

[3] The value 1.4 comes from the area comparison $l^2_{c,4096}/l^2_{c,1024}$ since the z-dimension of the MD cell system stays unchanged.

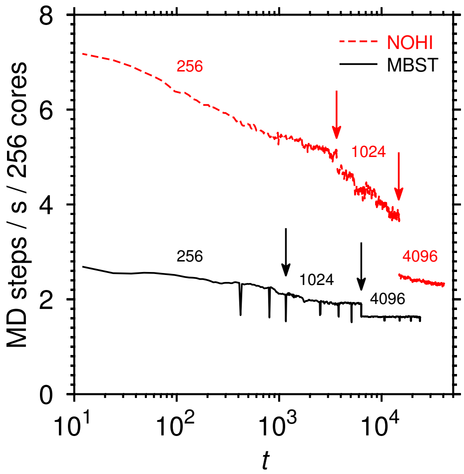

Figure 8.4: Performance of the MPCD simulations on the super computer HERMIT. Arrows indicate a change in the number of used cores. The overall performance for 1024 cores and 4096 cores was divided by 4 and 16 respectively. The sharp minima in the MBST data correspond to checkpoints where a full snapshot is written to the hard disk. For further details see the main text.

correspond to momentum space, are the preferred choice. In computer simulations both methods are applicable and both have their advantages and disadvantages. The calculation of pair correlation functions is a rather slow process of quadratic numerical effort. The smooth behavior of the resulting $g(r)$-curves allows for a precise detection of the average domain size by reading off the second intersection of $g(r)$ with the horizontal line at $c = 1$. Only for very early times the oscillations of the order of the particle-particle distance complicate the situation, since multiple intersections can occur (see Fig. 8.5a, $t = 60$). For such short times the general trend of the pair correlation function has to be fitted and the intersection between the fit and $c = 1$ can be regarded as a typical length scale. In general, the structure factor shows a more noisy signal (even though it was averaged over the same number of runs) but can clearly distinguish between typical inner particle distances $q \approx 6.2$ and the larger patterns within the demixing process ($q < 1$) (see Fig. 8.5b). Note that both, the pair correlation function and the structure factor, can hardly distinguish between different morphologies e.g. droplet patterns or bicontinuous percolation-like patterns.

In the following, the average domain size during spinodal decomposition is measured

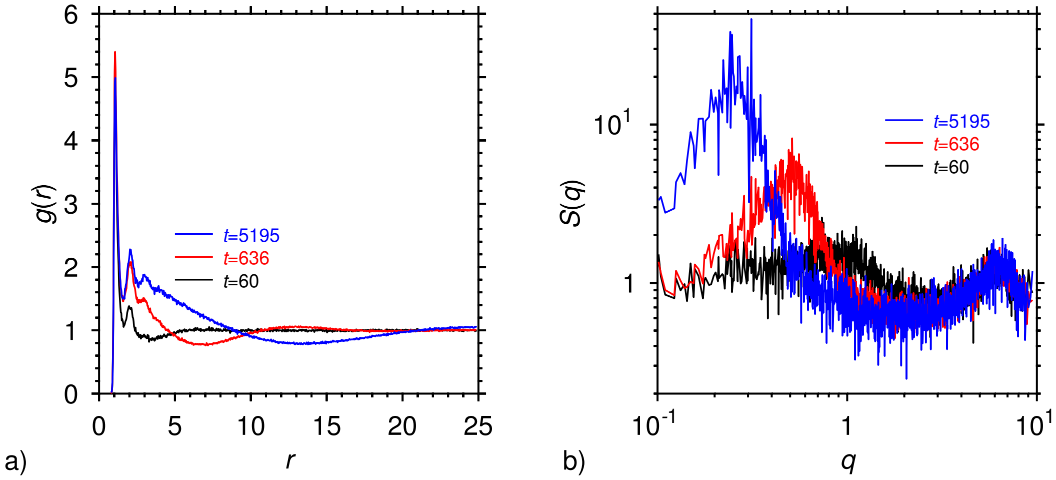

Figure 8.5.: Colloid position correlations in direct (a) and momentum space (b) for the case for the demixing process of a colloid-polymer mixture in quasi two-dimensional confinement (see section 8.4).

using the pair correlation function instead of the structure factor, since it is the average domain size for *later* times that can be determined with high precision and which is expected to show a universal behavior. In quasi two-dimensional geometries there exist multiple ways how to define a meaningful version of this quantity. Here, the distances are measured in thin slices parallel to the walls. Only the slices close to the center are taken into account to exclude the wetting effects close to the walls. For instance, for the wall distance $D = 10$ seven slices with a width of 0.5 in the range $z \in [-1.75, +1.75]$ were used. In each slice a quasi two-dimensional pair correlation function is calculated taking only x- and y-components of the particle positions into account. The seven resulting pair correlation functions are then averaged and the intersection with $c = 1$ is read off. This is done for every time step within every independent run. The value of the intersection point r_{c1} can be related to the average domain size l_d using the structure factor peaks. When comparing the peak positions (using $2\pi/q = r$) with the intersection points, the relation $l_d = 2.5r_{c1}$ seems to be a reasonable choice.

8.4. Film Thickness D=5

The first system under consideration has a wall distance $D = 5$. Apart from the investigation of spinodal decomposition, the system also introduces the nomenclature and the typical choice of parameters which can be varied to influence the phase separation dynamics. The simulation box size is chosen as $V = 256 \times 256 \times 5$. In the following it is assumed that finite size effects set in at an average structure size of the minority phase of $l_d^{\max} \approx L/4$ so that the time regime, where this structure size is exceeded, does not need to be accessed. The quench is performed into a phase diagram region of critical composition of both phases, which means a packing fraction ratio of approximately $\frac{1}{2}(\eta_c^g + \eta_c^l)$ for the colloids and $\frac{1}{2}(\eta_p^g + \eta_p^l)$ for the polymers, where $\eta^{g/l}$ are the gas and liquid coexistence packing fractions respectively (see Fig. 8.2b). The main focus lies on the influence of hydrodynamic effects on the domain growth behavior. In the case of included hydrodynamics (via the MBS thermostat) two different choices of boundary conditions were studied, stick boundaries and slip boundaries (see section 7.2.3). By simply looking at snapshot series (Fig. 8.6) a qualitative picture evolves how domain growth proceeds for different solvent properties. In the very beginning a bicontinuous structure of interconnecting domains is visible. At later times the number of droplets of the colloid-rich phase (white areas) dominates in comparison to the number of droplets of the polymer-rich phase (black areas). The fastest domain growth is seen for the case of hydrodynamics in combination with perfect slip boundary conditions (left column). In the case of hydrodynamics with perfect stick boundary condition the whole process is distinctively slowed down (middle column). When hydrodynamic interactions are switched off completely (right column) the system exhibits the slowest dynamics of pattern formation.

While the snapshots visualize nicely the dynamics in the lateral dimensions, they do not give insight into the dynamics perpendicular to the walls. Figure 8.7a shows the changes over time of the colloidal density profiles perpendicular to the walls. The height of the colloid layer peak at the wall varies in a non-monotonic way, which is shown for all three solvent implementations in figure 8.7b. This special

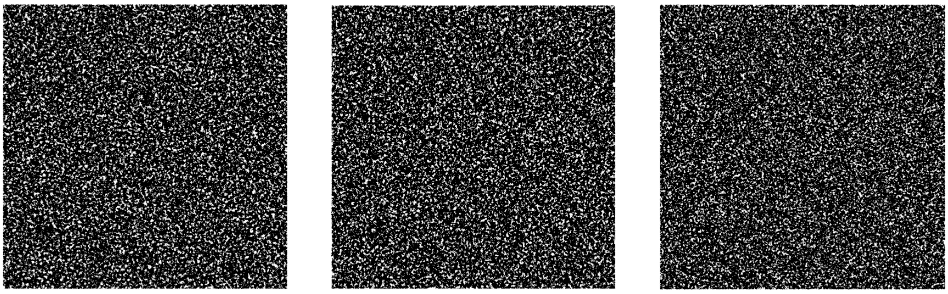

(a) time $t = 12$

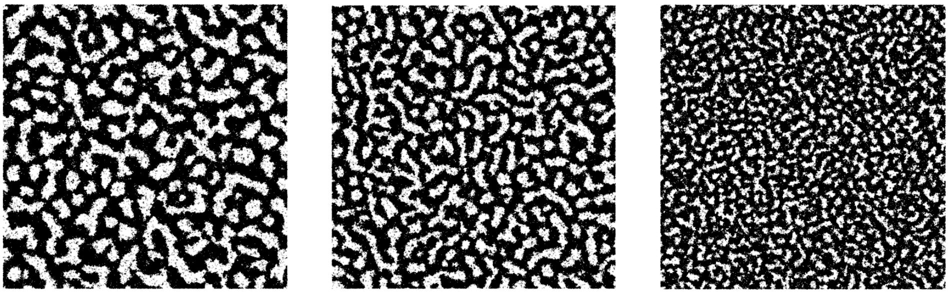

(b) time $t = 1200$

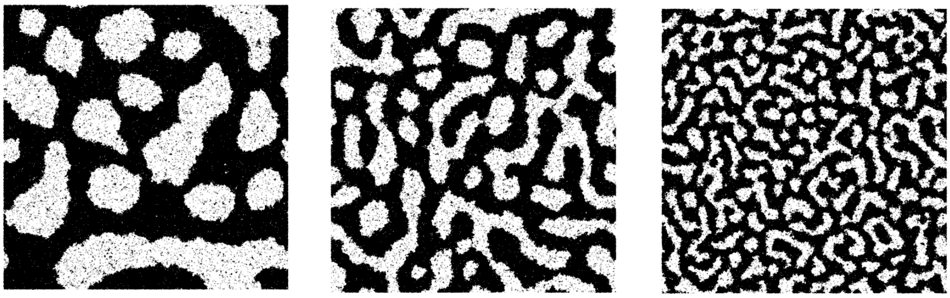

(c) time $t = 12000$

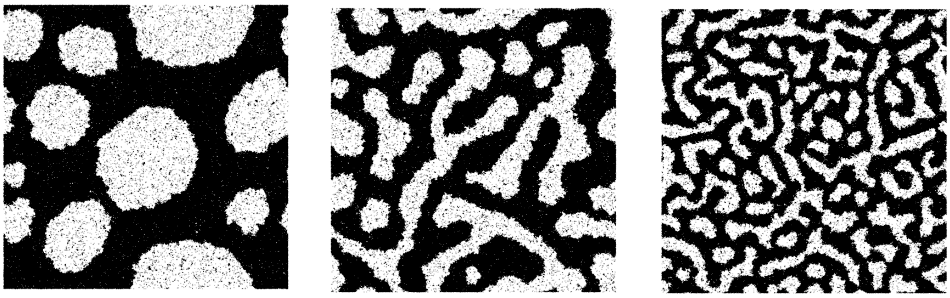

(d) time $t = 30000$

Figure 8.6.: Snapshot series of the demixing process. Only the polymers are shown (black dots). Time increases from top to bottom. The left series corresponds to hydrodynamics with perfect slip boundary conditions (MBST slip). The middle column corresponds to hydrodynamics with stick boundary conditions (MSBT stick) and the right column corresponds to switched off hydrodynamics (NOHI).

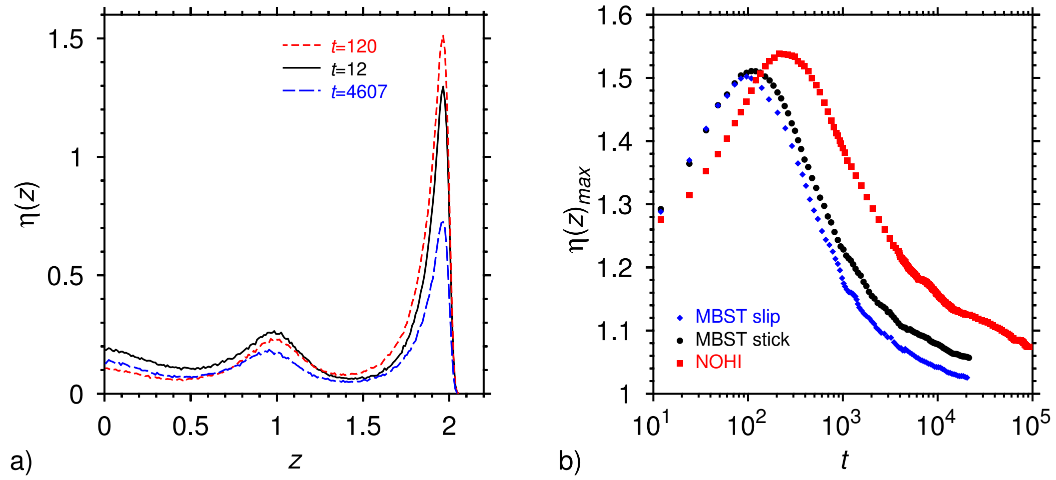

Figure 8.7.: (a) Typical density profiles of the colloids along the z-axis at different times as indicated (MBST). (b) Height of the first colloid layer peak as a function of time.

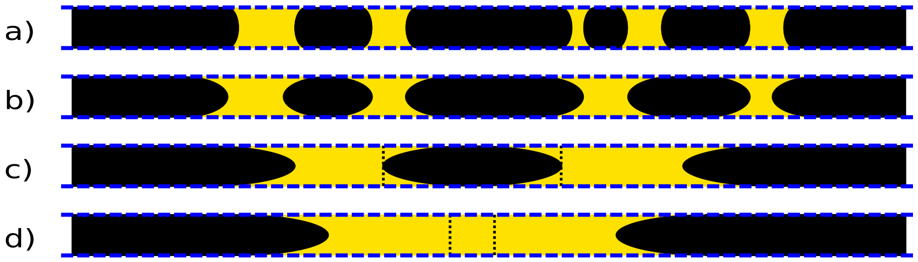

Figure 8.8.: Schematic representation of the different processes influencing the particle distribution perpendicular to the walls in a narrow quasi two-dimensional system. (a) Particles rapidly form groups of the size of wall separation and connect to the walls. (b) The strong depletion force acting at the colloids (yellow areas) leads to a further flow of this species to the walls. (c) Domains combine but the colloids still move into the direction of the walls. (d) Saturation of the colloidal drift towards the walls and further connection of domains redistributing colloid layers close to the walls among the center region (indicated by the yellow area enclosed by vertical dotted lines).

type of dynamics can be explained by an interplay of a flow of the colloids towards the walls due to the intrinsic depletion force which saturates at some moment and the connection of colloidal domains redistributing the colloid layer remnants (see Fig. 8.8). While the growth of the colloid layer at the walls is a direct result of the intrinsic particle dynamics, the “backflow” is an effective movement resulting from the combination of colloidal domains. For the polymers this results in flows of the opposite direction. As long as one stays in a symmetric bicontinuous domain structure there is no reason why these two flows should enhance the coarsening process at later times, but rather one anticipates a compensation, so that at the end power laws typical for two-dimensional systems are expected.

However, the form of the interconnection patterns of the colloid-rich and polymer-rich regions does depend on time. This means that the percolation threshold, where the system switches from a symmetric bicontinuous pattern to a droplet pattern, which depends in two dimensions only on the underlying viscosity of both phases

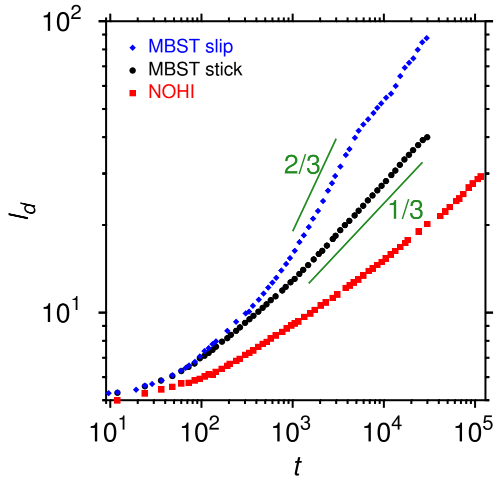

Figure 8.9: Development of the average domain size l_d over time. Both lines show the the power laws $l_d \propto t^n$, with $n = 2/3$ and $n = 1/3$ respectively. The symbols correspond to the first zero-crossing $r = r_{c1}$ of $h(r) = g(r) - 1$ via $l_d = 2.5 r_{c1}$.

and the concentration ratio, might be shifted in either direction. These effects shall be rather weakly pronounced in the case of $D = 5$, but are expected to play a more important role when increasing the wall distance D, e.g. $D = 10$.

Finally, the average domain size as a function of time was measured as described in the previous section. Figure 8.9 shows this quantity for the three different choices of solvent implementation in analog to the corresponding snapshot series. As expected, hydrodynamics drastically speed up the whole process. However, the predicted late time behavior with power law exponent $n = 2/3$ for two dimensions is only visible for perfect slip boundary conditions and only over a short range of time before one sees a break down to $n \approx 1/3$ again. The reason for this becomes clear from the snapshots where one identifies that the approximately bicontinuous structure changes more and more to a round droplet structure where the Lifshitz-Slyozov mechanism dominates again. The stick boundary case never evolves this power law but follows with high precision the $n = 1/3$ power law behavior, although the morphology as a function of domain size l_d is the same as in the case of perfect slip boundary conditions. This discovery can be understood when one asks the question, over which lateral distance a velocity correlation in the solvent persists. A solvent particle “travels” typically a distance of the order D until it collides with the walls. Since bounce back rules are applied to model the stick boundary condition, the velocity of the solvent particle is inverted, and the velocity auto-correlation dies rapidly out. This screening effect is shown in more detail in figure 8.10 where the velocity auto-correlation function in the xy-plane is compared for several choices of pore widths D with stick boundary conditions and perfect slip boundary conditions. This investigation shows clearly that in the case of perfect slip even in a narrow pore of $D = 1.5$ the expected long time tail behavior is established rapidly, while for the stick boundary condition the velocity auto-correlation is strongly screened for $D = 5$ and gets even negative for $D = 2.5$ or $D = 1.5$ (full symbols).

This finding is a very distinct detail of quasi two-dimensional systems confined between walls in comparison to the pure two-dimensional case. Even though in an experiment it might be possible to have a colloid-polymer monolayer, the solvent will still exhibit three-dimensional dynamics. The solvent slip length determines over which range of average structure size the observation of the inertial regime ($n = 2/3$) is possible at all.

The domain growth behavior for switched off hydrodynamics (NOHI in Fig. 8.9)

Figure 8.10: Two-dimensional velocity auto-correlation function for various wall distances D and boundary conditions as indicated. Full symbols mark negative values, i.e. an anti-correlation of the velocity over time.

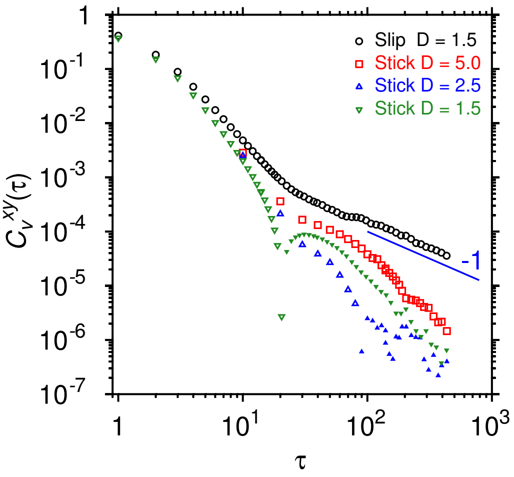

Figure 8.11: Comparison of the domain growth for two different solvent density parameters ρ_s for the NOHI thermostat as indicated. The inset shows the effective exponent $n_e = \log_{10}(l_d(10t)/l_d(t))$ as a function of inverse domain size at time t.

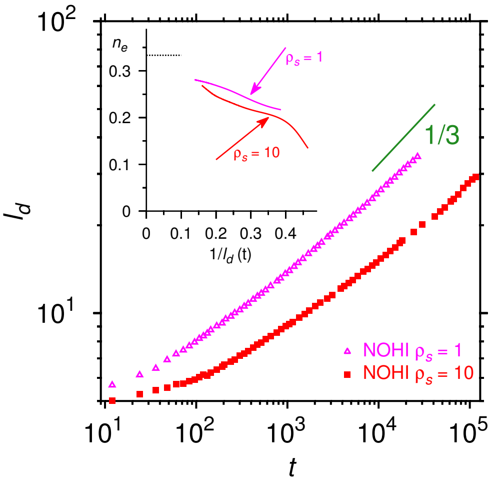

needs still to be commented. As expected from the previously shown snapshots, the average domain size shows the slowest growth behavior over time. No scaling behavior is observed, but rather a huge transient towards $n \approx 1/3$. In order to distinguish between this assumed transient behavior and a possible late time behavior with an exponent of $n = 1/4$, which was also reported in literature regarding the two-dimensional compressible Ising model [211], another series of simulation runs using the NOHI thermostat is performed, but now with a solvent density per cell of $\rho_s = 1$. This choice effects the viscosity of the solvent and hence, influences the time scale of the simulation so that a more advanced coarsening is accessible with less computational effort as shown in figure 8.11. The data observed for $\rho_s = 1$ shows again a very slow growth of the effective exponent n_e towards $n = 1/3$. The inset of the same figure emphasizes this by plotting the effective exponent n_e as a function of $1/l_d(t)$. This makes it possible to extrapolate to $l_d(t) \to \infty$. Both curves clearly exceed the $n = 1/4$ power law and tend towards $n = 1/3$ (dotted line) at late times.

The last point which shall be addressed for film thickness $D = 5$ is the influence of the colloid-polymer concentration ratio (at fixed η_p^r) on the spinodal decomposition kinetics. As mentioned above, the coarsening pattern morphology is crucial for the observed growth laws and, therefore, one expects for strongly "off-critical" quenches, where droplet patterns are present, that the Lifshitz-Slyozov mechanism dominates. In general, the question of the possibility of enhanced domain growth due to wetting layer backflow can be concerned for "off-critical" quenches. However,

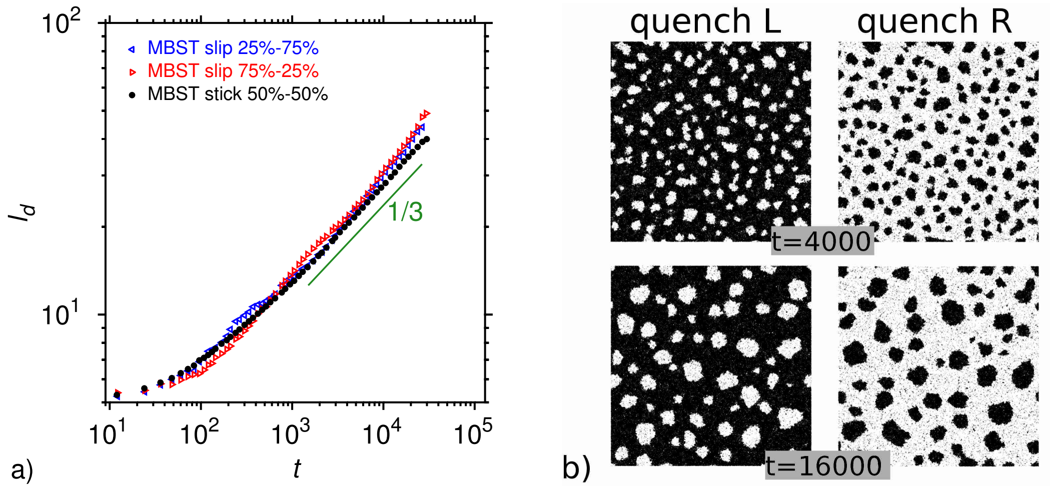

Figure 8.12.: (a) Domain growth for off-critical quenches in the case of slip boundary conditions. For comparison the curve resulting from a critical concentration ratio with stick boundary conditions is also shown. (b) Typical snapshots for the two different colloid-polymer concentration ratios.

in the case of $D = 5$ colloid wetting layers do simply not fit so that only small remnants are visible at the colloid domains (as already insinuated by figure 8.8). Figure 8.12a shows the result for off-critical quenches to the left (label “quench L” in Fig. 8.2b) and to the right (label “quench R”) in comparison to the center quench. The snapshots in the same figure part (b) demonstrate that even at intermediate times ($t \approx 4000$) no bicontinuous structure evolved. First of all, it is remarkable that both data sets for the off-critical mixtures fall on top of each other, although there is a difference in dynamics of both phases. Second, in comparison to the data series of the critical quench for stick boundary conditions the $n = 1/3$ scaling behavior is only slightly exceeded, so that one can conclude that in the case of $D = 5$ there is no pronounced evidence for an enhancement of the demixing dynamics due to wetting layer backflow.

Before going on to a wall separation of $D = 10$, the results for film thickness $D = 5$ are briefly summarized: For bicontinuous coarsening patterns the domain growth law universality of purely two-dimensional systems is found. However, the domain structure is influenced by the underlying dynamics perpendicular to the walls so that a percolating structure may vanish over time. Furthermore, the boundary conditions of the solvent play a crucial role. Only in the case where hydrodynamic interactions are not screened (perfect slip boundaries) the $l_d \sim t^{1/3}$ power law is exceeded. The suppression of hydrodynamic interactions slows the process of spinodal decomposition drastically down and a large transient region towards a power law exponent of $n = 1/3$ is present.

8.5. Film Thickness D=10

Increasing the wall distance from $D = 5$ to $D = 10$ is expected to enhance the influence of the dynamics perpendicular to the walls on the coarsening pattern. Indeed, the “critical” quench (labeled as “quench 1” in Fig. 8.2c) leads even at early times to a pure colloidal droplet structure which persists over time (see Fig. 8.13a).

To obtain a bicontinuous structure further concentration ratios were studied labeled as "quench 2" and "quench 3" in Fig. 8.2c. While the simulation run corresponding to "quench 2" shows an almost perfectly symmetric percolation pattern at intermediate times around $t \approx 1500$, at later times ($t \approx 6700$) the system switches to a polymer droplet structure. Finally, although not as symmetrical as "quench 2" at intermediate times, the bicontinuous structure of "quench 3" remains stable up to $t \approx 9000$ (not shown). To save computer time these results were obtained from single runs using slip boundary conditions.

The obvious change in the pattern morphology can be quantified by using the so-called Euler characteristic χ. The Euler characteristic is a topological invariant and was originally developed to characterize polyhedra by comparing the occurrence of vertices, edges and faces. Continuous structures such as spheres, toruses etc. can be discretized using polygons or in the most simple case cubes or squares in two dimensions, respectively. Once discretized, it is possible to define Euler characteristics for the originally continuous structures. In two dimensions every droplet contributes with $\chi = 1$, every hole with $\chi = -1$ and a bicontinuous structure has $\chi = 0$.

Here, a simple mapping on the two-dimensional Ising model is performed and the Euler characteristic is calculated following references [212, 213]. Such mapping procedures from densities of continuous systems to Ising systems have typically a free parameter, the threshold when a local density corresponds to "spin up" and not to "spin down". By changing this threshold only a bit, χ shifts up or down. Another subtle point is the generation of "noise pixels" due to fluctuations in the local density which are not intended to contribute to χ. Both influences are minimized by using a relatively large area ($A_l = 4 \times 4$ in units of the colloid diameter) to estimate the local density (noise reduction). Then the distribution of densities over all such areas is analyzed. When the system is demixed and the average structure size exceeds noticeably $A_l = 4 \times 4$, the density distribution shows a double peak structure the peak positions of which correspond to local, time dependent coexistence densities $\eta^g_{\mathrm{loc}}(t)$ and $\eta^l_{\mathrm{loc}}(t)$ for either particle species. The mean $\frac{1}{2}(\eta^g_{\mathrm{loc}}(t) + \eta^l_{\mathrm{loc}}(t))$ is then used as a time dependent threshold for the spin mapping procedure. Figure 8.13a shows the Euler characteristics for colloids and polymers as a function of time for the three considered quenches. The asymmetry between the Euler characteristic of the polymer-rich phase and the Euler characteristic of the colloid-rich phase at the early stages results from the wetting of the colloids at the walls and disappears when the average domain size exceeds clearly $D = 10$. From then on the initial number of colloidal droplets is decreasing over time and at the late stages saturates to the morphology which is visible in the snapshots in Fig. 8.13a. One can also see the crossover from a percolation pattern to droplets of the polymer-rich phase in the case of quench 2.

Figure 8.13b shows the average structure size as a function of time for these single simulation runs. The first quench, which corresponds to a droplet structure, exceeds at late times the $n = 1/3$ power law, giving first evidence that wetting layer effects might accelerate the demixing dynamics. The dynamics of quench 2 show an interesting break-off close to $t \approx 4000$. This "pinning effect" is known from experiments [206] to happen when one crosses the percolation threshold. The system remains "shocked" until it continues to follow a power law behavior. The data corresponding to quench 3 shows the fastest ($n = 2/3$ like) power law behavior at late times, which fits to the fact that χ is closest to a percolation structure at late times for quench

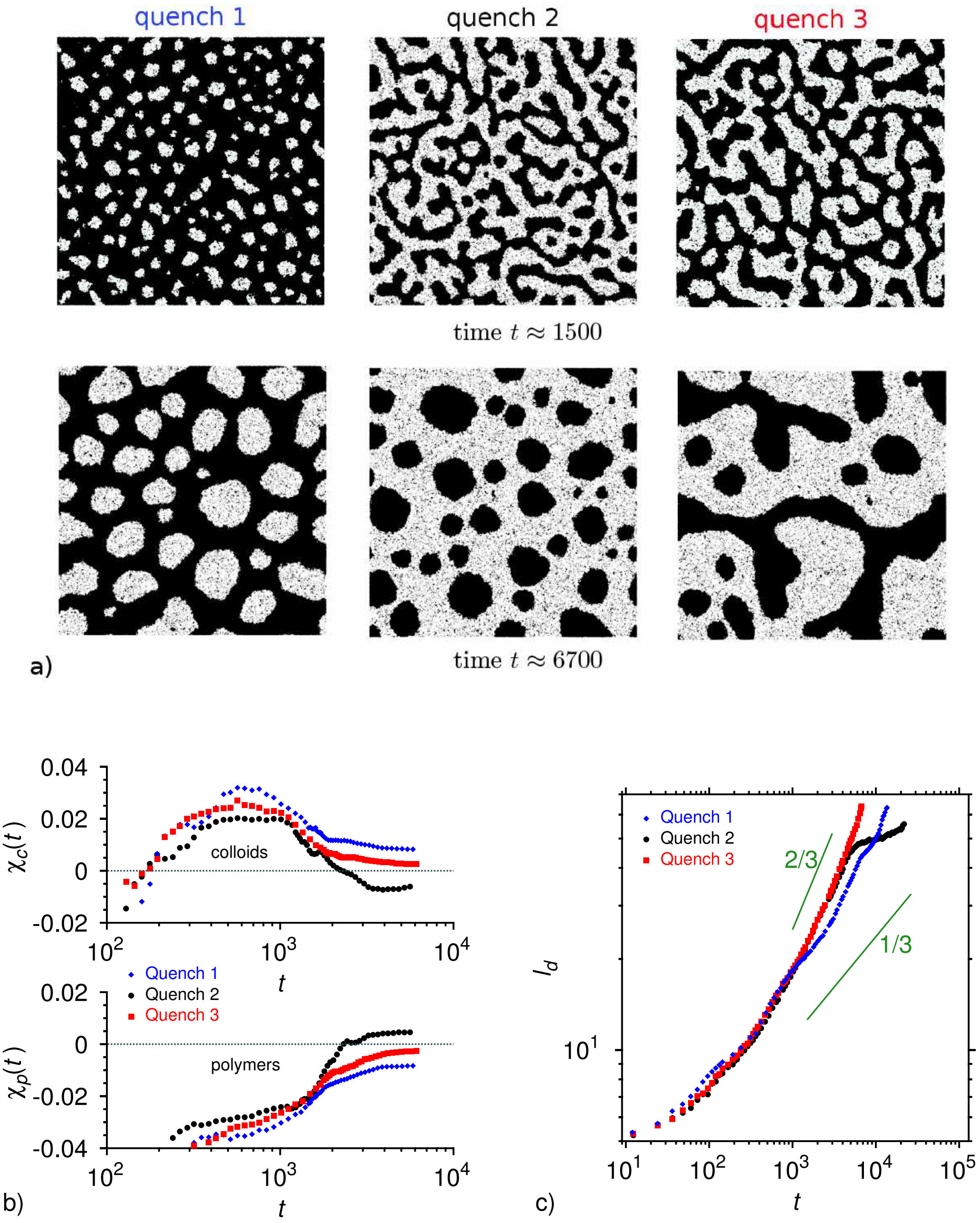

Figure 8.13.: (a) Snapshot series of the demixing process for various concentration ratios. Only the polymers are shown (black dots). The perfect slip boundary condition was used. Concentration ratios correspond to the quench 1 to quench 3 as indicated in Fig. 8.2c. (b) Euler characteristic for colloid and polymer pattern at various concentration ratios using the MBS thermostat with slip boundaries. (c) The average domain size l_d for the three different colloid-polymer concentrations obtained from a single run as a function of time. As a guide for the eye power laws with different slopes are included.

3. All these various findings make clear that for $D = 10$ the concentration ratio plays a dominant role with respect to the scaling behavior. However, since only data from single simulation runs are presented, one has to be careful with a quantitative interpretation of the results by means of power law exponents. For instance,

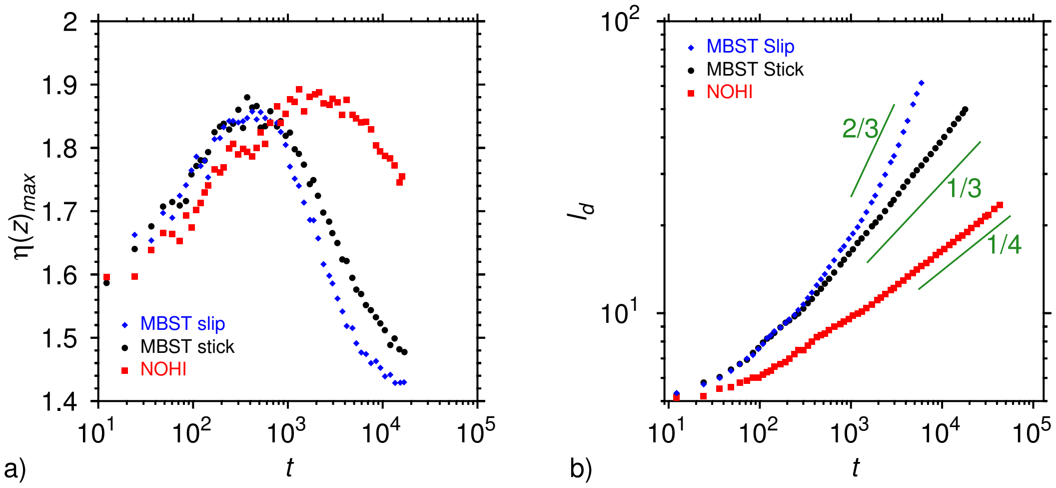

Figure 8.14.: (a) Maximum height of the colloid wall layer peak as a function of time for quench 3. Note that only two simulation runs were averaged, so that the fluctuations of the data points result from the statistical error. (b) Domain growth for slip and stick boundary conditions as well as switched off hydrodynamics for the “quench 3” concentration ratio.

the exact time at which the percolation threshold is crossed (quench 2 data series) depends on the current fluctuations and hence, is expected to differ from simulation run to simulation run. It is questionable whether “pinning effects” are visible at all when one averages over enough independent runs. In fact, one is more likely to see a reduced effective growth law exponent. The concentration ratio used for quench 3 is the only one which seems to be reasonably well suited for probing the influence of hydrodynamics on the coarsening dynamics as done for $D = 5$. In the next paragraph the “quench 3” setup is used when comparing the various solvent setups, MBST slip, stick and switched off hydrodynamic interactions.

The period of time over which the growth and decrement of the colloid layer at the walls takes place is extended in comparison to the wall distance $D = 5$, but shows the same qualitative behavior as shown in figure 8.14a. Eventually, figure 8.14b presents the results for the domain growth behavior. The results are in qualitative agreement with the scaling laws obtained for wall distance $D = 5$, but the data series with included hydrodynamic interactions show both an enhancement over the $n = 2/3$ and $n = 1/3$ power law behavior respectively. In principle, such effects can result for two different reasons: three-dimensional viscous hydrodynamics behavior (transient with $n \lesssim 1$) or enhancement by wetting layers. The first reason can be ruled out, since the average domain length scale at which the enhancement is present exceeds clearly the wall distance $D = 10$. Therefore, it is likely that domain growth profits from the presence of wetting layer remnants.

To study the latter aspect of a possible speed-up in the domain growth dynamics in more detail, the spinodal decomposition of off-critical pure droplet states is investigated. The dynamics in droplet pattern are expected to follow the $n = 1/3$ power law behavior, independent of the fact whether the polymers or the colloids form the minority phase. This was indeed observed for wall distance $D = 5$ (see Fig. 8.12). In the case of $D = 10$ the wetting layer remnants are stronger developed and a possible influence has to be more pronounced. When arguing that wetting layer remnants

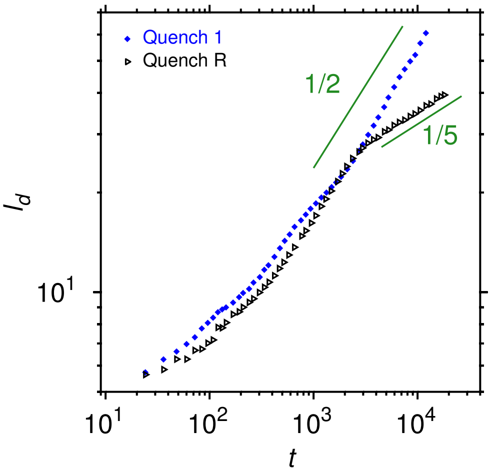

Figure 8.15: Comparison between domain growth behavior of off-critical quenches showing a colloidal droplet structure (quench 1) and a polymer droplet structure (quench R), both times using slip boundary conditions. The oscillations in the quench 1 data series up to $t \approx 1000$ are present in every run and do not average out. The errors are much smaller than the symbol size in this regime.

of the colloid-rich phase enhance the domain growth of colloidal droplets, one has to postulate that in the contrary case where the polymers form the droplets no enhancement or even a slow down has to be recognizable. Figure 8.15 confirms this presumption. The data series for the colloidal droplet pattern exceeds clearly the power law with exponent $n = 1/3$ (quench 1) and at the same time the data series for the concentration ratio where polymer droplets are present shows a distinct slow down at late stages. From these findings it is clear that the violation of the $n = 1/3$ power law reported for quasi two-dimensional systems in the literature [208, 209] are related to the wetting properties of the system. However, the terminus “wetting layer backflow” which suggest in a sense an active mechanism has to be used with caution. Rather the picture of a particle redistribution in a geometric manner, when two domains connect, emerges (as proposed by scheme 8.8).

8.6. Film Thickness D=1.5

To clarify further the role of the quasi dimensionality, i.e. the influence of the wall distance D, the last simulation series presented in this chapter are performed in a system of size $V = 512 \times 512 \times 1.5$. Since particles cannot use anymore the dimension perpendicular to the walls to pass each other, the system is almost two-dimensional. The asymmetry with respect to the wall preference of the colloid particle species is highly suppressed now, and a critical quench is expected to produce a rather stable bicontinuous structure over a wide range of time scales. This section focuses on the question whether the so far observed results depend on the z-dimension, i.e. a three-dimensional hydrodynamics, or if they constitute a two-dimensional behavior. The hydrodynamics in the case of $D = 1.5$ are almost two-dimensional since only three MPC cells fit between the walls. Stick boundary conditions will lead to a strong hydrodynamic screening of the order of $D = 1.5$, so that the difference between included HI with stick boundaries and switched-off HI is expected to be smaller than observed in the previous sections for $D = 5$ and $D = 10$. For slip boundary conditions two-dimensional hydrodynamic interactions are recovered resulting in $l_d \sim t^{1/2}$ [214], or, when reaching the inertial regime ($l_d \gg \frac{\eta^2}{\rho\gamma}$), in $l_d \sim t^{2/3}$ [191]. Two different quenches are considered in the following. While both are critical, the underlying polymer reservoir packing fractions are very different corresponding to the free energy landscapes presented in figure 8.2d with polymer reservoir packing

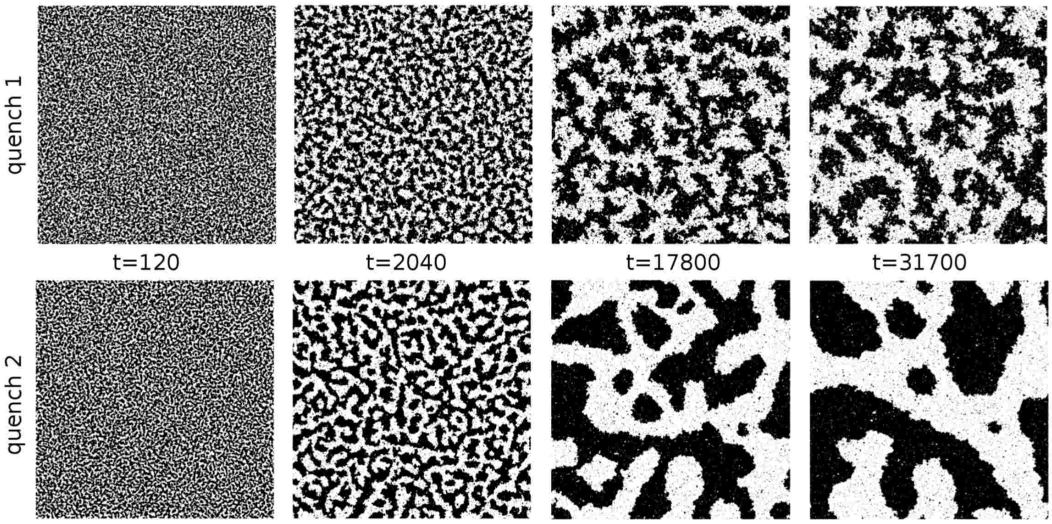

Figure 8.16.: Comparison of the domain growth pattern for two different polymer reservoir packing fractions. "quench 1" corresponds to $\eta_p^r \approx 4$ and "quench 2" corresponds to $\eta_p^r \approx 5$. In both cases the MBS thermostat with slip boundary conditions was used.

fractions $\eta_p^r \approx 4$ and $\eta_p^r \approx 5$. The polymer reservoir packing fraction of $\eta_p^r \approx 4$ corresponds to the coexistence diameters of $N_c = 103552$ colloids and $N_p = 503648$ polymers. The interfacial tension is tiny ($\gamma \approx 0.1$) which induces very frayed interfaces between colloid-rich and polymer-rich areas (see the snapshot series "quench 1" in figure 8.16). For $\eta_p^r \approx 5$ the particle numbers are $N_c = 109507$ and $N_p = 579610$. The interfacial tension is $\gamma \approx 0.5$. The higher surface tension leads to much sharper interfaces as seen in Fig. 8.16 ("quench 2").

Already visible from these series of snapshots is that the domain growth dynamics are accelerated in the case of "quench 2". At MD time $t = 31700$ individual domains are even that large for "quench 2" that they already interconnect with themselves via the periodic boundary conditions. As soon as such a connection appears, dynamics can be extremely accelerated because the system can very efficiently minimize the interfacial area by aligning the interfaces parallel to the x or y-axis. Then further growth of this domain happens essentially in a one-dimensional manner leading to a slow down in the phase separation dynamics. Thus, this type of finite size effects leads to oscillations in the observed domain growth. Percolation patterns are most sensitive to this kind of finite size effects because they have the largest interfacial area. It is essential to look carefully at snapshot series and the average domain size extracted from *single* runs, since the oscillations can easily be misinterpreted as "pinning effects" or can lead to artificial effective exponents when averaging over multiple runs. Data corresponding to an average domain size $l_d \gtrsim 100$ are not taken into account in the following.

In figure 8.17 the average domain size is shown as a function of MD time. Part (a) shows the quench to $\eta_p^r \approx 4$ ("quench 1") and part (b) shows the results for the quench to $\eta_p^r \approx 5$. In both cases the hydrodynamic interactions play a tremendous role. As expected from the previous studies ($D = 5, 10$), switching off the hydrodynamic interactions leads to the slowest dynamics with respect to $l_d(t)$. As before, the corresponding curves slightly exceed the $n = 1/4$ power law. Hydrodynamics

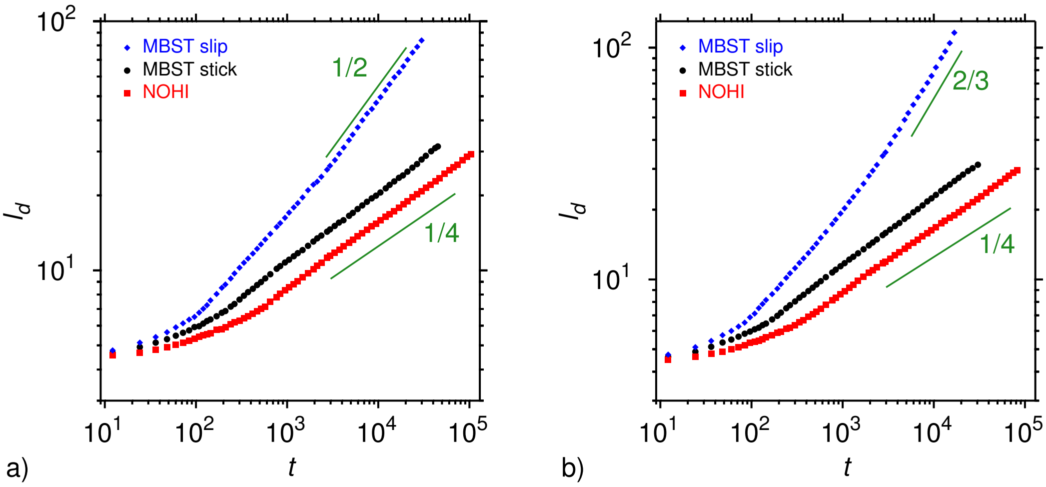

Figure 8.17.: Average domain size l_d as a function of time for three different solvent properties at polymer reservoir packing fraction $\eta_p^r \approx 4$ (a) and $\eta_p^r \approx 5$ (b).

combined with stick boundary conditions do clearly accelerate the demixing process, but, due to the extreme screening by the presence of the walls, the function $l_d(t)$ shows qualitatively the same behavior as for switched off hydrodynamics. Finally, slip boundary conditions lead to the fastest growth showing a power law behavior of $l_d \sim t^{1/2}$ in the case of $\eta_p^r \approx 4$ (Fig. 8.17a) and $l_d \sim t^{2/3}$ for $\eta_p^r \approx 5$ (Fig. 8.17b). As motivated in the beginning of this section, this difference is due to the enhanced gas-liquid interfacial tension γ for the deeper quench ($\eta_p^r \approx 5$) in comparison to "quench 1" ($\eta_p^r \approx 4$). The inertial regime $l_d \gg \frac{\eta^2}{\rho\gamma}$ is reached earlier and hence the $n = 2/3$ power law becomes visible. These observations fit nicely in the theoretical picture and expectations which evolved already from the results obtained for wall distances $D = 5$ and $D = 10$.

8.7. Conclusion

The Multi Particle Collision Dynamics mesoscale simulation method is well-suited to study spinodal decomposition kinetics. The overall number of particles can exceed 50 millions due to the substantial amount of explicitly included solvent particles. However, the usage of parallel computation techniques alleviates the accompanying problems to some extent and allows for a detailed study of phase separation over multiple time and length scales. This way the influence of hydrodynamics on the dynamics of phase separation can be investigated in detail.

The presented results for three different solvent properties, different wall distances and various phase separation morphologies lead to the conclusion that there exists universal behavior in quasi two-dimensional systems of intrinsically asymmetric binary mixtures. However, in contrast to pure two-dimensional and particularly three-dimensional systems, the distinct dynamics perpendicular to the walls limits the range in time over which power law predictions based on two dimensions or three dimensions are observable. In addition, the boundary condition of the solvent, which is not present in systems which are either strictly two-dimensional or three-dimensional without confinement, strongly influences the hydrodynamic interaction range. The outcome of the presented simulation runs points out that stick boundary conditions lead to a screening of hydrodynamic interactions on the scale of the wall distance D. In this case power laws based on long range hydrodynamic interactions such as the inertial late time behavior predicted by FURUKAWA [192] can only be visible for respectively large wall separations. When setting the slip length to infinity by using perfect slip boundary conditions, hydrodynamic interactions become long ranged again, and evidence for the inertial regime is found.

As in strictly two-dimensional or three-dimensional systems, the spinodal decomposition kinetics of quasi two-dimensional systems is strongly influenced by the underlying demixing pattern morphology. In addition to the fluid viscosity imbalance, slow non-monotonic dynamics perpendicular to the walls influence the structure of the phase separation patterns over time. As long as the system shows a percolating domain structure the domain growth laws for pure two-dimensional systems with included hydrodynamic interactions are recovered, namely, the droplet diffusion-coagulation mechanism for $l_d \ll \frac{\eta^2}{\rho\gamma}$ [214] or FURUKAWA's inertial growth law as soon as the inertial regime is entered ($l_d \gg \frac{\eta^2}{\rho\gamma}$). When hydrodynamic interactions are switched off and the system behaves purely diffusive, a slow transient to the $l_d \sim t^{1/3}$ power law is obtained.

Furthermore, the possibility of an enhancement of the spinodal decomposition kinetics by "wetting layer backflow" could be verified for the largest wall distance of $D = 10$. When the droplets forming the *minority* phase favor the walls, the domain growth clearly exceeds the $n = 1/3$ power law behavior. In contrast, when the *majority* phase does favor the walls, the phase separation is drastically slowed down. The picture which is proposed for this finding is that of a simple redistribution of wetting layer remnants of domains leading to an effective backflow when they interconnect.

CHAPTER

9

SUMMARY & OUTLOOK

The phase behavior of a model colloid-polymer mixture, the Asakura-Oosawa model, under various types of confinement was studied by Monte Carlo simulations. The calculation of free energy functions played a key role in the investigation of the phase behavior throughout all the different types of confinement. It was shown that a system which is confined to a quasi one-dimensional geometry exhibits a "phase behavior" which is qualitatively different from a bulk system or a system confined in a plate geometry. As soon as the correlation length ξ_z is exceeded by the length of the cylindrical pore, the system does not stay in the pure gas or the pure liquid state, but instead forms multiple coexisting domains of both phases. Thus, for very long cylindrical pores the phase separation into vapor-like and liquid-like phases takes place in two steps: When the bulk correlation length is of the same order as the cylinder radius, phase separation occurs on a local scale. Moving further into the region where phase separation occurs in the bulk, the system develops long quasi one-dimensional domains (whose length ξ_z is controlled by the bulk interfacial tension). Only when this length exceeds the length of the cylindrical pore, one obtains a state with uniform density in z-direction. As a next step, the Asakura-Oosawa model system was investigated in even lower-dimensional confinement, in spherical cavities. It was demonstrated that the "phase transition point" (in terms of the colloid chemical potential) is directly related to the wetting properties of the binary mixture at the walls as well as to the radius R of the spherical cavity. By expanding free energy expressions for the case $R \to \infty$ it was possible to show that the shift of the transition point is controlled by the contact angle between the gas-liquid interface and the wall. Two different cases of phase coexistence morphologies were pointed out, the core-shell structure and the Janus-type structure. These findings are believed to be especially important to the field of nanomaterials and are intended to inspire further experiments. Eventually, a method to calculate wall tensions for liquids and crystalline phases was developed and applied to the hard sphere system and the effective AO model confined between planar walls. The obtained wall tension results were used to estimate the contact angle of heterogeneous wall attached crystalline nuclei by means of Young's equation. It was shown that the wall potential in general influences the wall tensions and particularly that by introducing an attractive well the contact angle is modified in the case of the effective AO model. These findings are intended to motivate further comparative studies such as the direct observation of crystalline wall attached nuclei [8] as well as experiments to understand in more detail the topic of heterogeneous nucleation especially with respect to the validity of the macroscopic description based on Young's equation.

The last part of this work addresses dynamics with a special focus on the influence of hydrodynamic interactions on the phase separation kinetics of colloid-polymer mixtures confined between planar walls. It was shown that the Multi Particle Collision Dynamics algorithm is well suited to tackle this issue, since its mesoscale picture of the colloidal suspension provides enough details about the solvent properties and at the same time is efficient to study spinodal decomposition over multiple decades in time. The obtained results lead to the conclusion that in the case of a quasi two-dimensional confinement of an intrinsically asymmetric binary mixture universality regimes exist, the exact form of which depends on the specific setup. For very small wall distances D the theoretically predicted power law behavior is obtained, while the wetting properties and the dynamics perpendicular to the walls start to gain influence and hence modify the power law forms when D is increased. Hydrodynamic long range interactions in quasi two-dimensional systems can only build up when the perfect slip boundary condition is applied to the solvent. Phase separation kinetics in quasi two-dimensional systems are highly complex due to the interplay of wetting and the finite system size and the regimes of universal behavior are found to depend strongly on the chosen setup.

Overall this work demonstrates that confining geometries strongly influence the phase behavior of the system in comparison to the bulk and lead to interesting and complex phenomena in equilibrium as well as in the dynamics of the system due to the interplay of surface and finite size effects.

APPENDIX

A

ON THE PHASE BEHAVIOR OF TETRAPODS

The following project was undertaken under the supervision of Prof. Erik Luijten during my visit at Northwestern University, Chicago (October the 18th, 2010 - December the 17th, 2010).

The recent progress in the production of nanoscale and mesoscale material building blocks with different shapes [215, 216] is expected to strongly expand the variety of materials. Understanding the exact influence of the shape on the self-assembly properties and phase behavior is crucial if one wants to predict features of new materials. This chapter focuses on building blocks consisting of colloidal particles which are known to show a broad range of self assembled structures [217] or even quasi crystalline structures [218].

Very promising candidates for the design of new materials are building blocks with tetrahedral geometry, i.e. tetrapods, which could be synthesized successfully over a wide range of aspect ratios [219, 220]. Figure A.1 shows how tetrapod structures

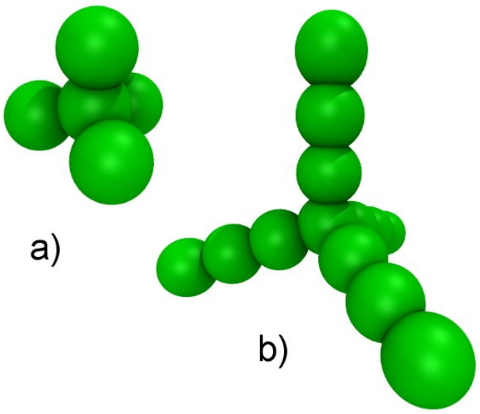

Figure A.1: Snapshots of tetrapods consisting of spherical colloids:
(a) arm length $l_a = 1$,
(b) arm length $l_a = 3$

can be built by spherical colloids. The arm length l_a is the number of colloids in one branch which is attached to the colloidal seed in the center. In the following, the unit length scale is set by the colloid monomer diameter. Three different tetrapod conformations are considered here: While the distance between the centers of colloidal monomers is always chosen to be the same as the colloid diameter, the arm length is varied as $l_a = 1, 2, 3$.

In the following, the phase behavior of two tetrapod models is obtained with two methodologies. First, Monte Carlo simulations are performed where the interconnection between colloidal monomers is rigid and pair interactions of monomers of the same tetrapod are suppressed. Second, Molecular Dynamics simulations on graphic processing units (GPUs) are undertaken, where stiff bond potentials and stiff bond angle potentials were applied between the colloidal spheres. In the case of the Molecular Dynamics simulations the monomer-monomer interaction within the same tetrapod is included.

A.1. Monte Carlo Simulations

Studying the phase behavior of binary mixtures with a high size asymmetry between the two components becomes more difficult when arbitrary shapes of the particles are allowed, especially when one wants to perform grand canonical cluster moves from section 2.5.3. For simple shapes, like spherocylinders, one can easily extend this cluster move type but when looking at even more complex shapes, like tetrapods, it is technically difficult to extend the grand canonical cluster move, since the generation of random coordinates for the depletant particles in the particle deletion move becomes difficult. In general, the additional rotational degree of freedom reduces a lot the acceptance probability for particle insertions and the question arises, if studies based on a canonical move set might be better suited in this case. SINKOVITS and LUIJTEN generalized the canonical rejection free geometric cluster algorithm (see section 2.5.2) for arbitrarily shaped anisotropic particles [221, 222]. In this generalization self-inverse symmetry operations such as mirror reflections at a pivot point or reflections at a plane are implemented on a hyperspherical geometry (see section 2.3.2) which is needed to maintain the self-inverse character of the transformations. Simulations on hypersphere surfaces were introduced by CAILLOL as a method to handle long range Coulomb interactions of charged particles [50, 51, 53]. He also studied particles with Lennard-Jones interaction potentials on hyperspherical surfaces and proposed an empirical correction to the potential to suppress curvature related effects [52] which is particularly important when being close to the critical region of the system.

It has been shown that the combination of the so-called restricted Gibbs ensemble with the geometric cluster algorithm allows for an efficient calculation of phase diagrams [223, 224]. Due to the highly structured and modularized code provided by DANIEL SINKOVITS, it was possible to include the restricted Gibbs ensemble structure in a fast and time efficient manner. DANIEL SINKOVITS and ERIK LUIJTEN are greatly acknowledged at this point for their help and never-ending will of answering questions regarding the technical and physical details. In the restricted Gibbs ensemble two simulation boxes (or hypersphere surfaces) are present and, additionally to canonical moves in the separate boxes, particle moves between both simulation boxes are attempted[1].

Simulation Details and Results

Two different setups for the investigation of the tetrapod phase behavior are regarded in the following, a single component system where the monomers interact via a version of the Lennard-Jones potential and a tetrapod-polymer mixture using the Asakura-Oosawa interaction model. To compare between both setups qualitatively, the inverse temperature $\beta = \frac{1}{k_B T}$ is used in analogy to the polymer reservoir packing fraction η_p^r as a parameter for the phase diagrams in case of the Lennard-Jones interaction model. All simulations take place on a four-dimensional hypersphere surface, where the hypersphere has a radius of $R = 6$. The studies of the single component system are used in the following to explain the simulation procedure details for the restricted Gibbs ensemble.

The Lennard-Jones pair interactions between the colloidal monomers, as proposed by Caillol, is

$$W_{\mathrm{LJ}}(i,j) = \begin{cases} 4\left[\left(\frac{\sigma}{R\sin r_{ij}}\right)^{12} - \left(\frac{\sigma}{R\sin r_{ij}}\right)^{6}\right] & \text{, for } r_{ij} < r_c/R \\ 0 & \text{, else} \end{cases}, \tag{A.1}$$

where R is the radius of the hypersphere, σ the monomer diameter ($\sigma = 1$) and $r_{ij} = R\arccos(\boldsymbol{r}_i \cdot \boldsymbol{r}_j / R^2)$ is the distance between particle i and particle j. Here, the cutoff radius is set to $r_c = 2.5$. When the system undergoes a phase separation in the restricted Gibbs ensemble, the densities observed in both simulation boxes do in general not correspond to the coexistence densities but rather to a respectively oversaturated or undersaturated state, because both the volume *and* the total particle number are fixed. This comes from the fact that in restricted Gibbs ensemble Monte Carlo simulations no explicit interface of the coexisting phases is present and that the system favors the oversaturated and undersaturated phase states over the additional creation of an interface in one of the simulation boxes. The so-called intersection method [225] is used to obtain the “true” coexistence densities from a series of simulation runs at different total tetrapod number N_0. Figure A.2a illustrates this method for the choice of tetrapods with arm length $l_a = 1$. For every inverse temperature β up to thirty choices of N_0 were simulated. These simulations are independent from each other and therefore, can be performed simultaneously. The average particle numbers in both boxes N_- and N_+ are recorded and plotted once versus N_0 and once versus $2N_0 - 2N_\pm$. The resulting intersection of both curves marks then the true coexistence particle numbers at the ordinate. From the example plot in figure A.2 one determines $N_{c-} = 72$ and $N_{c+} = 408$ leading with $V = 2\pi^2 R^3 = 4263.67$ to the monomer packing fractions $\eta_g = 0.044$ and $\eta_l = 0.251$. The snapshot (Fig. A.2b) verifies that the extracted coexistence densities correspond to a gas-liquid phase coexistence, since no ordered structures are visible.

This intersection technique is performed also for all choices of arm length $l_a = 1, 2, 3$ as well as for the AO interaction model with $a_l = 1$. For this interaction model the

---

[1] Volume exchange moves are not allowed in this restricted version of the Gibbs ensemble, since the mirror reflection operations in the cluster moves only work when the volume of both simulation boxes is equal.

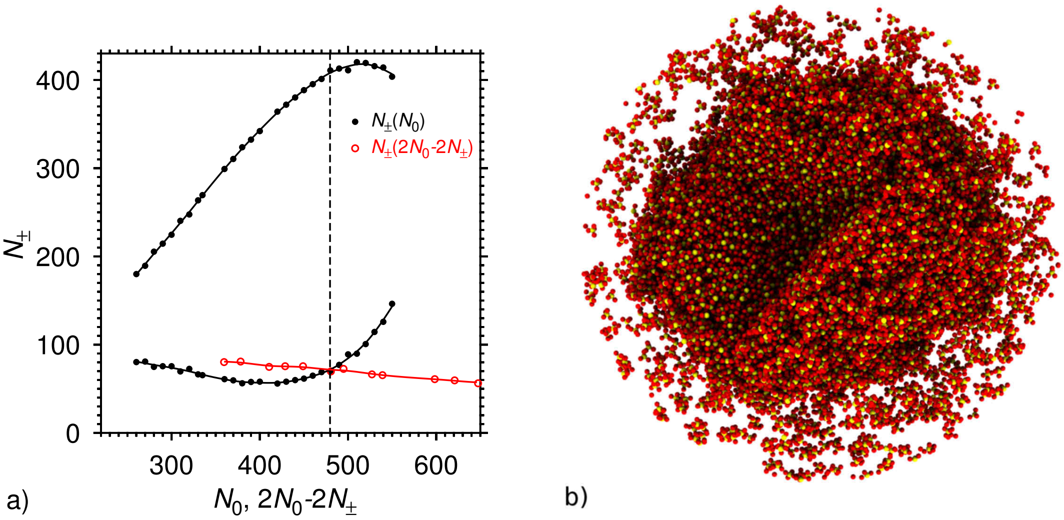

Figure A.2.: (a) Intersection method for tetrapods of arm length $l_a = 1$ on the surface of a hypersphere with radius $R = 6$ ($\beta = 0.52$). N_0 is the total number of particles simulated, while $N_\pm$ are the particle numbers corresponding to the peaks in the probability distribution function. The full lines are a guide to the eye. (b) Snapshot taken out of a canonical simulation showing a liquid droplet of tetrapods with arm length $a_l = 1$ surrounded by the coexisting gas. The center particles of the tetrapods are colored in yellow. A wedge was cut out of the configuration to allow a view inside the droplet.

ratio of the polymer diameter to the colloidal monomer diameter is set to $q = 0.8$, as in the previous chapters, and the polymer reservoir packing fraction is varied to obtain the phase diagram. The resulting phase behavior of the tetrapods is summarized in figure A.3.

Figure A.3a shows three binodals in the case of the modified Lennard-Jones model for different arm lengths, as indicated. The coexistence densities are shown as a function of the inverse temperature $\beta = \frac{1}{k_B T}$. For arm length $a_l = 1$ and $a_l = 2$ a region of phase coexistence is visible for $\beta \gtrsim 0.5$ and $\beta \gtrsim 0.42$ respectively. For arm length $a_l = 3$ only a few data points are shown which correspond to several computational expensive "test"-runs. The equilibration time as well as the correlation between configurations increase drastically when increasing the arm length. Therefore, the quality of the data, especially for the liquid branches, is expected to become less precise in the case of arm length 2 and 3. Part (b) of the same figure presents the binodal for tetrapods of arm length $a_l = 1$ in the case of the Asakura-Oosawa model. One can clearly recognize the same qualitative behavior in comparison to the Lennard-Jones interaction model (part (a)). In the case of the binary tetrapod-polymer mixture the rejection free cluster algorithm develops its full power. The computational effort for a pair of coexistence density points did not increase much ($\lesssim 10\%$).

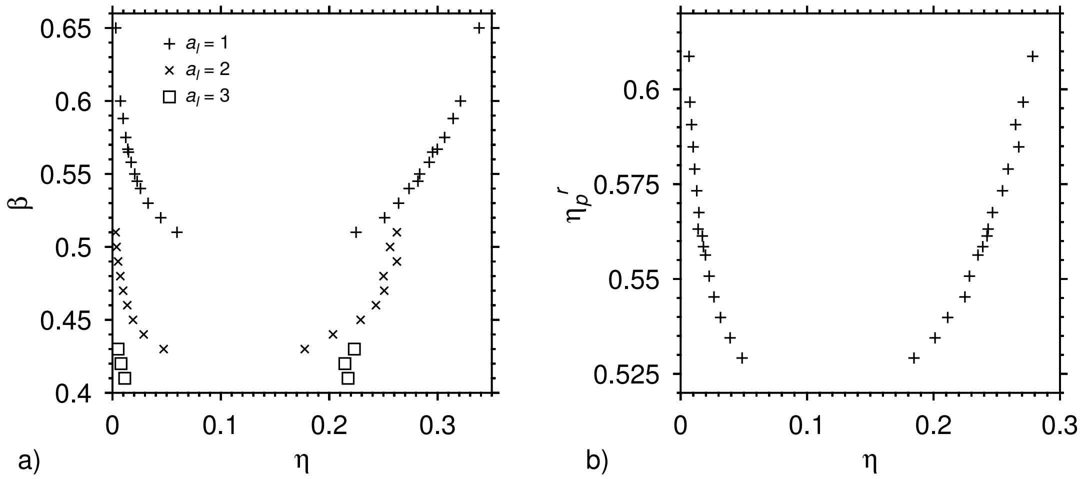

Figure A.3.: (a) Phase diagram of tetrapods with modified Lennard-Jones potential (Eq. A.1), where η is the monomer packing fraction. The arm length varies as indicated. The radius of the hypersphere is fixed to $R = 6$. (b) Binodal for tetrapods of arm length $a_l = 1$ using an Asakura-Oosawa model for several polymer reservoir packing fractions η_p^r.

A.2. Molecular Dynamics Simulations

As an alternative approach to study the phase behavior of tetrapods, the single component setup (without polymers) is investigated by means of Molecular Dynamics simulation based on the velocity Verlet algorithm (see section 7.1). The simulations take place in a standard cuboid simulation box. The tetrapod model is slightly modified. The colloidal monomer interaction potential is again the Lennard-Jones pair potential with cutoff radius $r_c = 2.5$ (without curvature correction expression) but interactions between monomers of the same tetrapod are not excluded anymore. In addition, strong harmonic bond potentials $V(r) = \frac{1}{2}k_b(r - \sigma)^2$ with spring constant $k_b = 600$ as well as bond angle potentials $V(r) = \frac{1}{2}k_a(\theta - \theta_0)^2$ with $k_a = 600$ and $\theta_0 = 2.0944$ for the connections of monomers to the center and $\theta_0 = \pi$ for connections within one arm are used. These connections between the monomers take a proper transfer of momentum within a tetrapod into account. The unit length scale is set by the monomer diameter $\sigma \equiv 1$.

The simulations are performed on a graphic card (NVIDIA GTX 580) using the open source Molecular Dynamics implementation HOOMD [226]. The velocity Verlet algorithm allows in contrast to ordinary Monte Carlo simulations a position update of all the particles simultaneously. This feature enables Molecular Dynamics simulations to be performed in a parallel manner on the multiple compute units which modern graphic cards provide. In case of the simple one component setup of the tetrapod ensemble this technique is expected to perform even better than the geometric cluster algorithm. Of course, as soon as a second particle species (with a relatively small particle diameter) comes into play, this advantage is lost, and the geometric cluster algorithm will outnumber Molecular Dynamics simulations with respect to the performance.

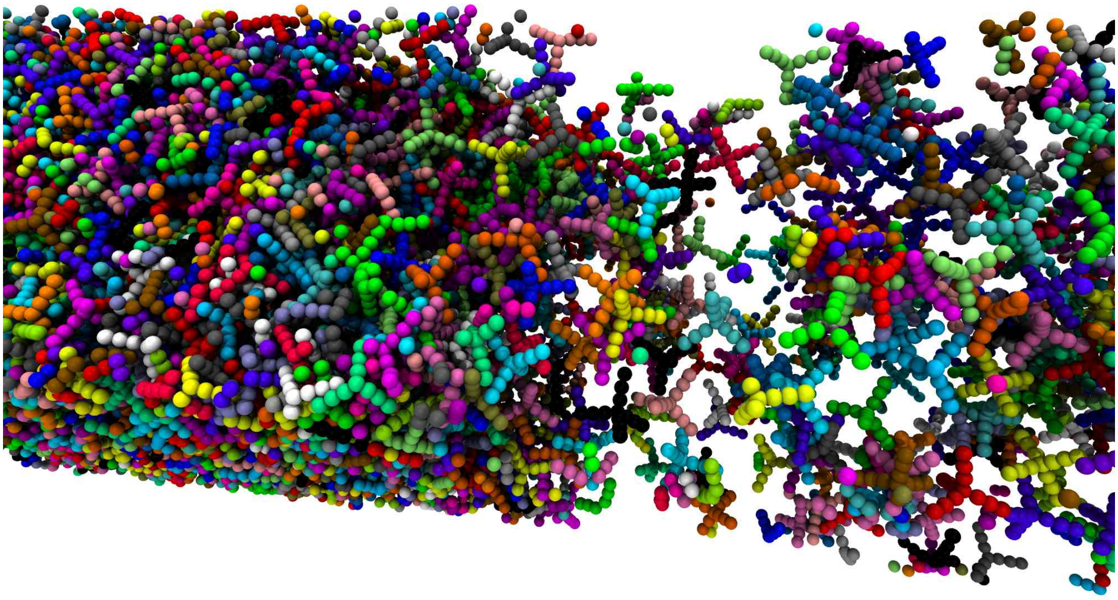

Figure A.4.: Snapshot of the coexistence interface between the liquid (left) and the gas (right) phase of tetrapods of arm length $a_l = 3$ simulated via canonical MD on a GTX 580 GPU. The different colors serve for the distinction of the individual tetrapods.

Simulation Details and Results

Simulations are performed at constant temperature using the Nosé-Hover thermostat with time constant $\tau = 0.005$. The integration time step is chosen as $\Delta t = 0.0001$. To extract properly the coexistence densities, an elongated simulation box with volume $V = 30 \times 30 \times 120$ is chosen. When the total particle number in the system is close to the coexistence diameter, a slab configuration evolves (see Fig. A.4). The elongated simulation box assures that the system maintains the slab configuration even when the total particle number does not exactly correspond to the coexistence diameter. The volume which both phases occupy simply adjusts, but the coexistence densities remain unchanged.

After equilibration of the system to a certain temperature a production run is performed in which configurations are written out. The last configuration of such a production simulation run can be used as a starting point for the next considered temperature to reduce the equilibration time. The configurations are then analyzed via sub-boxes. The simulation box is virtually divided into cubic subsystems and for every subsystem a probability distribution $P(\eta)$ (where η is the monomer packing fraction in the system) is recorded. To increase the statistics, especially for larger subsystems, all the coordinates of a configuration are shifted between 300 and 1000 times randomly. One typically ends up in an asymmetric double peak structure of $P(\eta)$ where the peak positions with respect to η mark the coexistence packing fractions as illustrated by figure A.5. In contrast to probability distributions from grand canonical Monte Carlo simulations, the plateau between the two peaks does not give any further information such as the interfacial free energy. The probability distribution shows only a weak sub-box size dependency, which is recognizable in the shape of the peaks as well as in the absolute positions of the peak maxima. Since

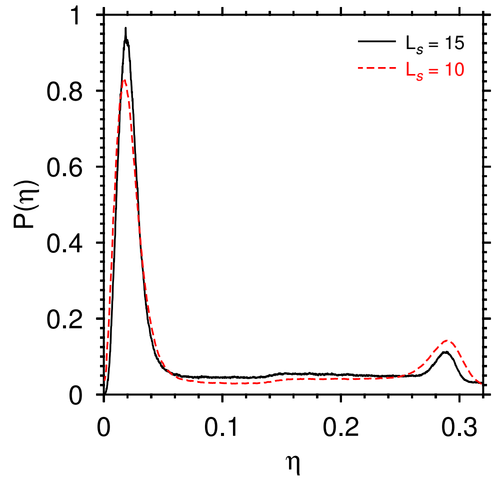

Figure A.5: Probability distribution $P(\eta)$ in subsystems with tetrapods of arm length $l_a = 1$. The inverse temperature is $\beta = 0.62$. L_s is the linear dimension of the cubic subsystems.

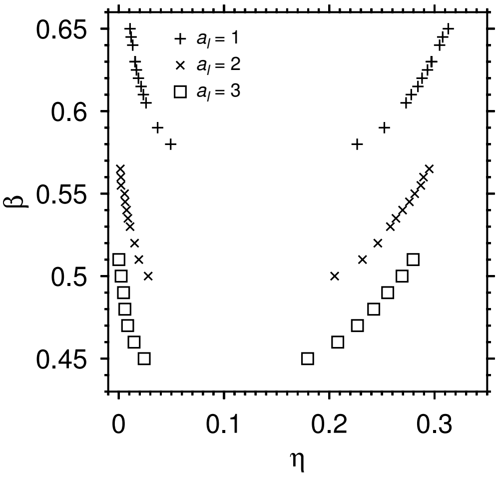

Figure A.6: Binodals extracted from the sub-box analysis of Molecular Dynamics simulations of tetrapods of various arm lengths a_l as indicated. The simulation box size was in all three cases $V = 30 \times 30 \times 120$. The dimension of the sub-box was chosen as $V = 15 \times 15 \times 15$.

the probability distribution for the larger sub-box ($L_s = 15$) can more accurately resolve the gas phase, the coexistence densities resulting from the sub-box analysis of length $L_s = 15$ are used in the following.

As for the Monte Carlo simulations on the hypersphere three different choices of the arm length were considered, $a_l = 1, 2, 3$. The total number of tetrapods was chosen as $N(a_l = 1) = 4698$, $N(a_l = 2) = 2610$ and $N(a_l = 3) = 1566$. Figure A.6 shows the final result for the phase diagram. First of all, the qualitative behavior is the same as for the Monte Carlo simulations, but the curves are stretched by a factor of approximately 1.12. Such a difference was expected, since two different models with a different number of degrees of freedom were used. When one compares the high density branches, especially for arm length $a_l = 2$ and $a_l = 3$, one can suspect that the Monte Carlo simulations slightly underestimate the liquid coexistence density.

A.3. Conclusion

It was shown that the geometric cluster algorithm together with the restricted Gibbs ensemble is a powerful tool to study anisotropic particles via Monte Carlo simulations, especially when an explicit depletant particle species is present in the simulation. Tetrapods modeled by colloidal spheres with a repulsive core interaction followed by an attractive part show the following phase behavior. For high temperatures (or low η_p^r in the case of the Asakura-Oosawa interaction model) the system is in a homogeneous state. When the temperature is lowered, the system demixes into a vapor-like and a liquid-like phase. The phase diagram was recorded for three different arm lengths of the tetrapods which all show a gas-liquid phase transition. Systems containing tetrapods with longer arms start to phase separate at higher temperatures (lower η_p^r) in comparison to tetrapods with shorter arms. In addition, the monomer packing fraction η at coexistence is smaller for longer arm lengths. In contrast to simpler shapes such as spherocylinder, no evidence for orientational order in the considered interval of η was found.

These observations might motivate further studies of tetrapod systems with higher values for a_l with a special focus on the phase behavior in the region where the system starts to demix. This is closely related to the question whether for $\beta = 0$ this kind of phase separation can be observed or, similarly, whether a purely repulsive tetrapod system can show a vapor-liquid phase transition for long enough arms. But also the results obtained for the system based on the Asakura-Oosawa model represents a good starting point for further investigations. Keeping the arm length a_l fixed but lowering the aspect ratio between polymer diameter and monomer diameter q, can result in an interesting phase behavior, such as directional ordering or the formation of gel-like structures.

BIBLIOGRAPHY

[1] D. Wilms, A. Winkler, P. Virnau, and K. Binder, "Rounding of phase transitions in cylindrical pores," *Phys. Rev. Lett.*, vol. 105, p. 045701, 2010.

[2] A. Winkler, D. Wilms, P. Virnau, and K. Binder, "Capillary condensation in cylindrical pores: Monte Carlo study of the interplay of surface and finite size effects," *J. Chem. Phys.*, vol. 133, p. 164702, 2010.

[3] D. Wilms, A. Winkler, P. Virnau, and K. Binder, "Monte Carlo simulations of the 2d-Ising model in the geometry of a long stripe," *Comput. Phys. Commun.*, vol. 182, pp. 1892 – 1895, 2011.

[4] K. Binder, P. Virnau, D. Wilms, and A. Winkler, "Spurious character of singularities associated with phase transitions in cylindrical pores," *Eur. Phys. J. - Special Topics*, vol. 197, pp. 227–241, 2011.

[5] D. Deb, A. Winkler, M. H. Yamani, M. Oettel, P. Virnau, and K. Binder, "Hard sphere fluids at a soft repulsive wall: A comparative study using Monte Carlo and density functional methods," *J. Chem. Phys.*, vol. 134, p. 214706, 2011.

[6] D. Deb, D. Wilms, A. Winkler, P. Virnau, and K. Binder, "Methods to compute pressure and wall tension in fluids containing hard spheres," *Int. J. Mod. Phys.*, (Submitted), 2012.

[7] D. Deb, D. Wilms, A. Winkler, P. Virnau, and K. Binder, "Monte Carlo studies of interfacial free energies in colloidal suspensions," *NIC Symposium 2012 Proceedings*, p. 235, 2012.

[8] D. Deb, A. Winkler, P. Virnau, and K. Binder, "Simulation of fluid-solid coexistence in finite volumes: A method to study the properties of wall-attached crystalline nuclei," *J. Chem. Phys.*, vol. 136, p. 134710, 2012.

[9] A. Statt, A. Winkler, P. Virnau, and K. Binder, "Controlling the wetting properties of the Asakura-Oosawa model and applications to spherical confinement," *J. Phys.: Condens. Matter*, vol. 24 (in press), 2012.

[10] T. Graham, "Liquid diffusion applied to analysis," *Phil. Trans. Roy. Soc.*, vol. 151, p. 183, 1861.

[11] D. Aarts, M. Schmidt, and H. Lekkerkerker, “Direct visual observation of thermal capillary waves,” *Science*, vol. 304, pp. 847–850, 2004.

[12] H. Lekkerkerker, V. de Villeneuve, J. de Folter, M. Schmidt, Y. Hennequin, D. Bonn, J. Indekeu, and D. Aarts, “Life at ultralow interfacial tension: wetting, waves and droplets in demixed colloid-polymer mixtures,” *Eur. Phys. J. B*, vol. 64, pp. 341–347, 2008.

[13] J. Hernandez-Guzman and E. R. Weeks, “The equilibrium intrinsic crystal-liquid interface of colloids,” *P. Natl. Acad. Sci. USA*, vol. 106, p. 15298, 2009.

[14] J. J. Crassous, H. Dietsch, P. Pfleiderer, V. Malik, A. Diaz, L. A. Hirshi, M. Drechsler, and P. Schurtenberger, “Preparation and characterization of ellipsoidal-shaped thermosensitive microgel colloids with tailored aspect ratios,” *Soft Matter*, vol. 8, pp. 3538–3548, 2012.

[15] A. Elaissari, ed., *Colloidal Polymers: Synthesis and Characterization.* Marcel Dekker Ltd, 2003.

[16] R. Xie, U. Kolb, and T. Basche, “Design and synthesis of colloidal nanocrystal heterostructures with tetrapod morphology,” *Small*, vol. 2, pp. 1454–1457, 2006.

[17] B. A. Baker and V. T. Milam, “DNA density-dependent assembly behavior of colloidal micelles,” *Langmuir*, vol. 26, pp. 9818–9826, 2010.

[18] J. Schwarz-Linek, G. Dorken, A. Winkler, L. G. Wilson, N. T. Pham, C. E. French, T. Schilling, and W. C. K. Poon, “Polymer-induced phase separation in suspensions of bacteria,” *EPL*, vol. 89, p. 68003, 2010.

[19] J. Schwarz-Linek, A. Winkler, L. G. Wilson, N. T. Pham, T. Schilling, and W. C. K. Poon, “Polymer-induced phase separation in Escherichia coli suspensions,” *Soft Matter*, vol. 6, pp. 4540–4549, 2010.

[20] J. A. N. Zasadzinski and R. B. Meyer, “Molecular imaging of tobacco mosaic virus lyotropic nematic phases,” *Phys. Rev. Lett.*, vol. 56, pp. 636–638, 1986.

[21] J. Bryngelson, J. Onuchic, N. Socci, and P. Wolynes, “Funnels, pathways, and the energy landscape of protein-folding - a synthesis,” *Proteins-Structure Function and Genetics*, vol. 21, pp. 167–195, 1995.

[22] J. Neder, B. West, P. Nielaba, and F. Schmid, “Coarse-grained simulations of membranes under tension,” *J. Chem. Phys.*, vol. 132, p. 115101, 2010.

[23] S. Ramachandran, S. Komura, and G. Gompper, “Effects of an embedding bulk fluid on phase separation dynamics in a thin liquid film,” *EPL*, vol. 89, p. 56001, 2010.

[24] J. L. McWhirter, H. Noguchi, and G. Gompper, “Deformation and clustering of red blood cells in microcapillary flows,” *Soft Matter*, vol. 7, pp. 10967–10977, 2011.

[25] N. Metropolis, A. Rosenbluth, M. Rosenbluth, A. Teller, and E. Teller, “Equation of state calculations by fast computing machines,” *J. Chem. Phys.*, vol. 21, pp. 1087–1092, 1953.

[26] B. Alder and T. Wainwright, “Phase transition for a hard sphere system,” *J. Chem. Phys.*, vol. 27, pp. 1208–1209, 1957.

[27] B. J. Alder and T. E. Wainwright, “Studies in Molecular Dynamics. i. general method,” *J. Chem. Phys.*, vol. 31, pp. 459–466, 1959.

[28] D. Frenkel and B. Smit, *Understanding Molecular Simulation.* Academic Press, London, 2002.

[29] L. Greenemeier, "Study says carbon nanotubes as dangerous as asbestos," http://www.scientificamerican.com/, 2008.

[30] A. De Virgiliis, R. L. C. Vink, J. Horbach, and K. Binder, "Colloid-polymer mixtures between asymmetric walls: Evidence for an interface localization transition," *Europhys. Lett.*, vol. 77, p. 60002, 2007.

[31] K. Binder, J. Horbach, R. Vink, and A. De Virgiliis, "Confinement effects on phase behavior of soft matter systems," *Soft Matter*, vol. 4, pp. 1555–1568, 2008.

[32] R. L. C. Vink, A. De Virgiliis, J. Horbach, and K. Binder, "Phase diagram and structure of colloid-polymer mixtures confined between walls," *Phys. Rev. E*, vol. 74, p. 031601, 2006.

[33] Y. Song, E. Mason, and R. Stratt, "Why does the Carnahan-Starling equation work so well," *J. Phys. Chem.*, vol. 93, pp. 6916–6919, 1989.

[34] M. Dijkstra, "Capillary freezing or complete wetting of hard spheres in a planar hard slit?," *Phys. Rev. Lett.*, vol. 93, p. 108303, 2004.

[35] A. Einstein, "On the theory of Brownian movement," *Ann. d. Phys.*, vol. 322, pp. 549–560, 1905.

[36] P. Langevin, "Theory of Brownian motion," *C. R. Acad. Sci.*, vol. 146, p. 530, 1908.

[37] J. Perrin, *Brownian Motion and Molecular Reality.* Taylor & Francis, London, 1910.

[38] F. Oosawa and S. Asakura, "Surface tension of high-polymer solutions," *J. Chem. Phys.*, vol. 22, p. 1255, 1954.

[39] S. Asakura and F. Oosawa, "Interaction between particles suspended in solutions of macromolecules," *J. Polym. Sci.*, vol. 33, pp. 183–192, 1958.

[40] A. Vrij, "Polymers at interfaces and interactions in colloidal dispersions," *Pure Appl. Chem.*, vol. 48, pp. 471–483, 1976.

[41] S. M. Ilett, A. Orrock, W. C. K. Poon, and P. N. Pusey, "Phase behavior of a model colloid-polymer mixture," *Phys. Rev. E*, vol. 51, pp. 1344–1352, 1995.

[42] J. Zausch, P. Virnau, K. Binder, J. Horbach, and R. L. Vink, "Statics and dynamics of colloid-polymer mixtures near their critical point of phase separation: A computer simulation study of a continuous Asakura-Oosawa model," *J. Chem. Phys.*, vol. 130, p. 064906, 2009.

[43] J. D. Weeks, D. Chandler, and H. C. Andersen, "Role of repulsive forces in determining the equilibrium structure of simple liquids," *J. Chem. Phys.*, vol. 54, pp. 5237–5247, 1971.

[44] D. Chandler, J. D. Weeks, and H. C. Andersen, "Van der Waals picture of liquids, solids, and phase transformations," *Science*, vol. 220, p. 787, 1983.

[45] D. M. Heyes and H. Okumura, "Equation of state and structural properties of the Weeks-Chandler-Andersen fluid," *J. Chem. Phys.*, vol. 124, p. 164507, 2006.

[46] P. Bolhuis and A. Louis, "How to derive and parameterize effective potentials in colloid-polymer mixtures," *Macromolecules*, vol. 35, pp. 1860–1869, 2002.

[47] S. Asakura and F. Oosawa, “Interaction between particles suspended in solutions of macromolecules,” *J. Polym. Sci.*, vol. 33, pp. 183–192, 1958.

[48] M. Dijkstra, R. van Roij, R. Roth, and A. Fortini, “Effect of many-body interactions on the bulk and interfacial phase behavior of a model colloid-polymer mixture,” *Phys. Rev. E*, vol. 73, p. 041404, 2006.

[49] T. Zykova-Timan, J. Horbach, and K. Binder, “Monte Carlo simulations of the solid-liquid transition in hard spheres and colloid-polymer mixtures,” *J. Chem. Phys.*, vol. 133, p. 014705, 2010.

[50] J. M. Caillol and D. Levesque, “Numerical simulations of homogeneous and inhomogeneous ionic systems - an efficient alternative to the Ewald method,” *J. Chem. Phys.*, vol. 94, p. 597, 1991.

[51] J. M. Caillol, “A new potential for the numerical simulations of electrolyte-solutions on a hypersphere,” *J. Chem. Phys.*, vol. 99, p. 8953, 1993.

[52] J. M. Caillol, “Critical-point of the Lennard-Jones fluid: A finite-size scaling study,” *J. Chem. Phys.*, vol. 109, p. 4885, 1998.

[53] J. M. Caillol, “Numerical simulations of Coulomb systems: A comparison between hyperspherical and periodic boundary conditions,” *J. Chem. Phys.*, vol. 111, p. 6528, 1999.

[54] V. I. Manousiouthakis and M. W. Deem, “Strict detailed balance is unnecessary in Monte Carlo simulation,” *J. Chem. Phys.*, vol. 110, pp. 2753–2756, 1999.

[55] R. H. Swendsen and J.-S. Wang, “Nonuniversal critical-dynamics in Monte-Carlo simulations,” *Phys. Rev. Lett.*, vol. 58, p. 86, 1987.

[56] U. Wolff, “Collective Monte-Carlo updating for spin systems,” *Phys. Rev. Lett.*, vol. 62, p. 361, 1989.

[57] J. P. Wittmer, P. Beckrich, H. Meyer, A. Cavallo, A. Johner, and J. Baschnagel, “Intramolecular long-range correlations in polymer melts: The segmental size distribution and its moments,” *Phys. Rev. E*, vol. 76, p. 011803, 2007.

[58] C. Dress and W. Krauth, “Cluster algorithm for hard spheres and related systems,” *J. Phys. A-Math. Gen.*, vol. 28, pp. 597–601, 1995.

[59] J. Liu and E. Luijten, “Rejection-free geometric cluster algorithm for complex fluids,” *Phys. Rev. Lett.*, vol. 92, p. 035504, 2004.

[60] J. Liu and E. Luijten, “Generalized geometric cluster algorithm for fluid simulation,” *Phys. Rev. E*, vol. 71, p. 066701, 2005.

[61] R. Vink and J. Horbach, “Grand canonical Monte Carlo simulation of a model colloid-polymer mixture: Coexistence line, critical behavior, and interfacial tension,” *J. Chem. Phys.*, vol. 121, p. 3253, 2004.

[62] D. Ruelle, *Statistical Mechanics Rigorous Results.* World Scientific, Imperial College Press, 1969.

[63] B. Berg and T. Neuhaus, “Multicanonical algorithms for 1st order phase-transitions,” *Phys. Lett. B*, vol. 267, p. 249, 1991.

[64] B. Berg and T. Neuhaus, “Multicanonical ensemble - a new approach to simulate 1st-order phase-transitions,” *Phys. Rev. Lett.*, vol. 68, p. 9, 1992.

[65] A. M. Ferrenberg and D. P. Landau, “Critical behavior of the three-dimensional ising model: A high-resolution Monte Carlo study,” *Phys. Rev. B*, vol. 44, pp. 5081–5091, 1991.

[66] F. Wang and D. P. Landau, “Efficient, multiple-range random walk algorithm to calculate the density of states,” *Phys. Rev. Lett.*, vol. 86, pp. 2050–2053, 2001.

[67] F. Wang and D. P. Landau, “Determining the density of states for classical statistical models: A random walk algorithm to produce a flat histogram,” *Phys. Rev. E*, vol. 64, p. 056101, 2001.

[68] S.-H. Tsai, F. Wang, and D. P. Landau, “Uncovering the secrets of unusual phase diagrams: Applications of two-dimensional Wang-Landau sampling,” *Braz. J. Phys.*, vol. 38, pp. 6–11, 2008.

[69] C. Zhou and J. Su, “Optimal modification factor and convergence of the Wang-Landau algorithm,” *Phys. Rev. E*, vol. 78, p. 046705, 2008.

[70] R. V. Craiu, J. Rosenthal, and C. Yang, “Learn from thy neighbor: Parallel-chain and regional adaptive MCMC,” *J. Am. Stat. Assoc.*, vol. 104, pp. 1454–1466, 2009.

[71] P. Virnau and M. Muller, “Calculation of free energy through successive umbrella sampling,” *J. Chem. Phys.*, vol. 120, pp. 10925–10930, 2004.

[72] P. Virnau, *Monte-Carlo-Simulationen zum Phasen- und Keimbildungsverhalten von Polymerlösungen.* PhD thesis, Johannes Gutenberg-Universität Mainz, 2003.

[73] G. A. Mansoori, N. F. Carnahan, K. E. Starling, and J. T. W. Leland, “Equilibrium thermodynamic properties of the mixture of hard spheres,” *J. Chem. Phys.*, vol. 54, pp. 1523–1525, 1971.

[74] D. Frenkel and A. Ladd, “New Monte-Carlo method to compute the free-energy of arbitrary solids - application to the fcc and hcp phases of hard-spheres,” *J. Chem. Phys.*, vol. 81, pp. 3188–3193, 1984.

[75] P. Dayal, S. Trebst, S. Wessel, D. Wurtz, M. Troyer, S. Sabhapandit, and S. Coppersmith, “Performance limitations of flat-histogram methods,” *Phys. Rev. Lett.*, vol. 92, p. 097201, 2004.

[76] Y. Wu, M. Korner, L. Colonna-Romano, S. Trebst, H. Gould, J. Machta, and M. Troyer, “Overcoming the slowing down of flat-histogram Monte Carlo simulations: Cluster updates and optimized broad-histogram ensembles,” *Phys. Rev. E*, vol. 72, p. 046704, 2005.

[77] R. Vink and J. Horbach, “Critical behaviour and interfacial fluctuations in a phase-separating model colloid-polymer mixture: grand canonical Monte Carlo simulations,” *J. Phys.: Condens. Matter*, vol. 16, pp. 3807–20, 2004.

[78] R. L. C. Vink, J. Horbach, and K. Binder, “Critical phenomena in colloid-polymer mixtures: Interfacial tension, order parameter, susceptibility, and coexistence diameter,” *Phys. Rev. E*, vol. 71, p. 011401, 2005.

[79] R. L. C. Vink, J. Horbach, and K. Binder, “Capillary waves in a colloid-polymer interface,” *J. Chem. Phys.*, vol. 122, p. 134905, 2005.

[80] L. G. MacDowell, V. K. Shen, and J. R. Errington, “Nucleation and cavitation of spherical, cylindrical, and slablike droplets and bubbles in small systems,” *J. Chem. Phys.*, vol. 125, p. 034705, 2006.

[81] B. J. Block, S. K. Das, M. Oettel, P. Virnau, and K. Binder, “Curvature dependence of surface free energy of liquid drops and bubbles: A simulation study,” *J. Chem. Phys.*, vol. 133, p. 154702, 2010.

[82] M. Schrader, P. Virnau, and K. Binder, “Simulation of vapor-liquid coexistence in finite volumes: A method to compute the surface free energy of droplets,” *Phys. Rev. E*, vol. 79, p. 061104, 2009.

[83] L. MacDowell, P. Virnau, M. Muller, and K. Binder, “The evaporation/condensation transition of liquid droplets,” *J. Chem. Phys.*, vol. 120, pp. 5293–5308, 2004.

[84] B. Widom, “Some topics in the theory of fluids,” *J. Chem. Phys.*, vol. 39, pp. 2808–2812, 1963.

[85] M. E. Fisher, *Critical Phenomena.* Academic Press, London, 1971.

[86] V. Privman, ed., *Finite Size Scaling and Numerical Simulation of Statistical Systems.* World Scientific, Singapore, 1990.

[87] K. Binder, *Computational Methods in Field Theory.* Springer, Berlin, 1992.

[88] D. P. Landau and K. Binder, *A Guide to Monte-Carlo Simulations in Statistical Physics.* Cambridge University Press, New York, 3rd ed., 2009.

[89] N. B. Wilding and A. D. Bruce, “Density fluctuations and field mixing in the critical fluid,” *J. Phys.: Condens. Matter*, vol. 4, p. 3087, 1992.

[90] J. S. Rowlinson and B. W, *Molecular Theory of Capillarity.* Oxford Univ. Press, Oxford, 1982.

[91] C. A. Croxton, ed., *Fluid Interfacial Phenomena.* Wiley, New York, 1985.

[92] J. Charvolin, J.and Joanny and J. Zinn-Justin, eds., *Liquids at Interfaces.* North-Holland, Amsterdam, 1990.

[93] D. Henderson, ed., *Fundamentals of Inhomogeneous Fluid.* M. Dekker, New York, 1992.

[94] K. Binder, D. P. Landau, and M. Müller, “Monte Carlo studies of wetting, interface localization and capillary condensation,” *J. Stat. Phys.*, vol. 110, p. 1411, 2003.

[95] L. Gelb, K. Gubbins, R. Radhakrishnan, and M. Sliwinska-Bartkowiak, “Phase separation in confined systems,” *Rep. Progr. Phys,*, vol. 62, p. 1573, 1999.

[96] M. Schön and S. Klapp, *Reviews in Computational Chemistry*, vol. 24. John Wiley & Sons, 2007.

[97] I. Brovchenka and A. Oleinikova, *Interfacial and Confined Water.* Elsevier Science, 2008.

[98] S. J. Gregg and K. S. W. Sing, *Adsorption, Surface Area, and Porosity.* Academic Press, New York, 2nd ed., 1982.

[99] A. Liapis, ed., *Fundamentals of Adsorption.* Engineering Foundation, New York, 1987.

[100] J. Fraissard, ed., *Physical Adsorption, Theory, and Applications.* Kluwer Acad. Publ., Dordrecht, 1997.

[101] F. Rouquerol, J. Rouquerol, and K. Sing, *Adsorption by Powders and Porous Solids: Principles, Methodology, and Applications.* Academic Press, San Diego, 1999.

[102] T. Thorsen, S. Maerkl, and S. Quake, “Microfluidic large-scale integration,” *Science*, vol. 298, p. 580, 2002.

[103] A. Meller, “Dynamics of polynucleotide transport through nanometre-scale pores,” *J. Phys.: Condens. Matter*, vol. 15, p. 581, 2003.

[104] I. M. Squires and S. R. Quake, “Microfluidics: Fluid physics at the nanoliter scale,” *Rev. Mod. Phys.*, vol. 77, p. 977, 2005.

[105] E. Wolf, *Nanophysics and Nanotechnology.* Wiley-VCH, Weinheim, Germany, 2004.

[106] S. Inoue, N. Ichikuni, T. Suzuki, T. Uemtsu, and K. Kaneko, “Capillary condensation of n-2 on multiwall carbon nanotubes,” *J. Phys. Chem. B*, vol. 102, p. 4689, 1998.

[107] M. Meyyappan, ed., *Carbon Nanotubes: Science and Applications.* CRC, Boca Raton, 2004.

[108] Z. Yu, H. Gao, W. Whu, H. Ge, and S. Chou, “Fabrication of large area subwavelength antireflection structures on Si using trilayer resist nanoimprint lithography and liftoff,” *J. Vac. Sci. Technol. B*, vol. 21, p. 2874, 2003.

[109] W. T. Thomson and L. Kelvin *Philos. Mag.*, vol. 42, p. 448, 1871.

[110] M. E. Fisher and H. Nakanishi, “Scaling theory for the criticality of fluids between plates,” *J. Chem. Phys.*, vol. 75, p. 5857, 1981.

[111] H. Nakanishi and M. E. Fisher, “Critical-point shifts in films,” *J. Chem. Phys.*, vol. 75, p. 3279, 1983.

[112] R. Evans, U. Marini Bettolo Marconi, and T. P., “Capillary condensation and adsorption in cylindrical and slit-like pores,” *J. Chem. Soc., Faraday Trans.*, vol. 82, p. 1763, 1986.

[113] G. S. Heffelfinger, F. van Swol, and K. E. Gubbins, “Liquid-vapor coexistence in a cylindrical pore,” *Mol. Phys.*, vol. 61, p. 1381, 1987.

[114] R. Evans, “Fluids adsorbed in narrow pores: phase equilibria and structure,” *J. Phys.: Condens. Matter*, vol. 2, p. 8989, 1990.

[115] G. Mason, “A model of adsorption-desorption hysteresis in which hysteresis is primarily developed by the interconnections in a network of pores,” *Proc. R. Soc. London, Ser. A*, vol. 390, p. 47, 1983.

[116] G. S. Heffelfinger, F. van Swol, and K. E. Gubbins, “Adsorption hysteresis in narrow pores,” *J.Chem. Phys.*, vol. 89, p. 5202, 1988.

[117] K. Morishige and M. Shikimi, “Adsorption hysteresis and pore critical temperature in a single cylindrical pore,” *J. Chem. Phys.*, vol. 108, p. 7821, 1998.

[118] K. Morishige and M. Ito, “Capillary condensation of nitrogen in mcm-41 and sba-15,” *J. Chem. Phys.*, vol. 117, p. 8036, 2002.

[119] K. G. Kornev, I. K. Shingareva, and A. V. Neimark, “Capillary condensation as a morphological transition,” *Ad. Coll. Interface Sci.*, vol. 96, p. 143, 2002.

[120] A. Vishnyakov and A. V. Neimark, “Studies of liquid-vapor equilibria, criticality, and spinodal transitions in nanopores by the gauge cell Monte Carlo simulation method,” *J. Phys. Chem. B*, vol. 105, p. 7009, 2001.

[121] A. J. Liu, D. J. Durian, E. Herbolzheimer, and S. A. Safran, “Wetting transitions in a cylindrical pore,” *Phys. Rev. Lett.*, vol. 65, pp. 1897–1900, 1990.

[122] V. Privman and M. E. Fisher, “Finite-size effects at 1st-order transitions,” *J. Stat. Phys.*, vol. 33, p. 385, 1983.

[123] P. C. Ball and R. Evans, “Temperature-dependence of gas-adsorption on a mesoporous solid - capillary criticality and hysteresis,” *Langmuir*, vol. 5, p. 714, 1989.

[124] E. Wolf, *Nanophysics and Nanotechnology.* Wiley-VCH,Weisheim, 2002.

[125] Y. Champion and H. Fecht, *Nano-Architectured and Nano-Structured Materials.* Wiley-VCH,Weisheim, 2004.

[126] C. Rao, A. Müller, and A. Cheetham, *The chemistry of nanomaterials: Synthesis, properties and applications*, vol. 1. Wiley-VCH,Weisheim, 2006.

[127] European Commssion, “Definition of a nanomaterial,” http://ec.europa.eu/environment/chemicals/nanotech, 2011.

[128] P. Pawlow, “Über die Abhängigkeit des Schmelzpunktes von der Oberflächenenergie eines festen Körpers ,” *Z. phys. Chem*, vol. 65, pp. 545–548, 1909.

[129] Buffat P. and Bonel J.P, “Size effect on the melting temperature of gold particles,” *Phys. Rev. A*, vol. 13, pp. 2287–2298, 1978.

[130] F. Ercolessi, W. Andreoni, and E. Tosatti, “Melting of small gold particles: Mechanism and size effects,” *Phys. Rev. A*, vol. 66, pp. 911–914, 1991.

[131] E. Mendez-Villuendas and R. Bowles, “Surface nucleation in the freezing of gold nanoparticles,” *Phys. Rev. Lett.*, vol. 98, p. 185503, 2007.

[132] S. Dietrich, “Wetting Phenomena in Phase Transitions and Critical Phenomena, edited by Domb, C. and Lebowitz, J.L. ,” *Academic Press, New York*, vol. 12, pp. 2–218, 1988.

[133] K. Binder, “Phase transitions in reduced geometry,” *Annu. Rev. Phys. Chem.*, vol. 43, pp. 33–59, 1992.

[134] M. Antonietti and K. Landfester, “Polyreactions in miniemulsions,” *Prog. Polym. Sci.*, vol. 27, pp. 689–757, 2002.

[135] K. Landfester, A. Musyanovych, and V. Mailänder, “From polymeric particles to multifunctional nanocapsules for biomedical applications using the miniemulsion process,” *J. Polym. Sci., Part A: Polym. Chem.*, vol. 48, pp. 493–515, 2010.

[136] K. Landfester, “The generation of nanoparticles in miniemulsions,” *Advanced Materials*, vol. 13, pp. 765–768, 2001.

[137] D. Winter, P. Virnau, and K. Binder, “Monte Carlo test of the classical theory for heterogeneous nucleation barriers,” *Phys. Rev. Lett.*, vol. 103, p. 225703, 2009.

[138] D. Winter, P. Virnau, and K. Binder, “Heterogeneous nucleation at a wall near a wetting transition: A Monte Carlo test of the classical theory,” *J. Phys.: Condens. Matter*, vol. 21, p. 464118, 2009.

[139] S. K. Das and K. Binder, “Does Young’s equation hold on the nanoscale? a Monte Carlo test for the binary Lennard-Jones fluid,” *Europhys. Lett.*, vol. 92, p. 26006, 2010.

[140] S. K. Das and K. Binder, “Simulation of binary fluids exposed to selectively adsorbing walls: a method to estimate contact angles and line tensions,” *Mol. Phys.*, vol. 109, pp. 1043–1056, 2011.

[141] D. Kashchiev, *Nucleation, Basic Theory with Applications.* Butterworth-Heinemann, Oxford, 2000.

[142] U. Gasser, E. Weeks, A. Schofield, P. Pusey, and D. Weitz, "Real-space imaging of nucleation and growth in colloidal crystallization," *Science*, vol. 292, pp. 258–262, 2001.

[143] P. Schall, I. Cohen, D. Weitz, and F. Spaepen, "Visualizing dislocation nucleation by indenting colloidal crystals," *Nature*, vol. 440, pp. 319–323, 2006.

[144] D. M. Herlach, I. Klassen, P. Wette, and D. Holland-Moritz, "Colloids as model systems for metals and alloys: A case study of crystallization," *J. Phys.: Condens. Matter*, vol. 22, p. 153101, 2010.

[145] W. Wood and J. Jacobson, "Preliminary results from a recalculation of the Monte Carlo equation of state of hard spheres," *J. Chem. Phys.*, vol. 27, pp. 1207–1208, 1957.

[146] W. Hoover and F. Ree, "Melting transition and communal entropy for hard spheres," *J. Chem. Phys.*, vol. 49, p. 3609, 1968.

[147] R. L. Davidchack and B. B. Laird, "Crystal structure and interaction dependence of the crystal-melt interfacial free energy," *Phys. Rev. Lett.*, vol. 94, p. 086102, 2005.

[148] R. L. Davidchack, J. R. Morris, and B. B. Laird, "The anisotropic hard-sphere crystal-melt interfacial free energy from fluctuations," *J. Chem. Phys.*, vol. 125, p. 094710, 2006.

[149] B. B. Laird and R. L. Davidchack, "Calculation of the interfacial free energy of a fluid at a static wall by Gibbs–Cahn integration," *J. Chem. Phys.*, vol. 132, p. 204101, 2010.

[150] F. Varnik, J. Baschnagel, and K. Binder, "Molecular Dynamics results on the pressure tensor of polymer films," *J. Chem. Phys.*, vol. 113, pp. 4444–4453, 2000.

[151] M. Oettel, S. Goerig, A. Haertel, H. Loewen, M. Radu, and T. Schilling, "Free energies, vacancy concentrations, and density distribution anisotropies in hard-sphere crystals: A combined density functional and simulation study," *Phys. Rev. E*, vol. 82, p. 051404, 2010.

[152] M. Heni and H. Löwen, "Interfacial free energy of hard-sphere fluids and solids near a hard wall," *Phys. Rev. E*, vol. 60, pp. 7057–7065, 1999.

[153] A. Fortini, M. Dijkstra, M. Schmidt, and P. P. F. Wessels, "Wall-fluid and liquid-gas interfaces of model colloid-polymer mixtures by simulation and theory," *Phys. Rev. E*, vol. 71, p. 051403, 2005.

[154] A. Fortini and M. Dijkstra, "Phase behaviour of hard spheres confined between parallel hard plates: Manipulation of colloidal crystal structures by confinement," *J Phys : Condens Matter*, vol. 18, p. L371, 2006.

[155] T. Zykova-Timan, R. Rozas, J. Horbach, and K. Binder, "Computer simulation studies of finite-size broadening of solid-liquid interfaces: From hard spheres to nickel," *J. Phys.: Condens. Matter*, vol. 21, p. 464102, 2009.

[156] R. L. Davidchack, "Hard spheres revisited: Accurate calculation of the solid-liquid interfacial free energy," *J. Chem. Phys.*, vol. 133, p. 234701, 2010.

[157] P. Hoogerbrugge and J. Koelman, "Simulating microscopic hydrodynamic phe-

nomena with Dissipative Particle Dynamics," *Europhys. Lett.*, vol. 19, pp. 155–160, 1992.

[158] P. Espanol, "Hydrodynamics from Dissipative Particle Dynamics," *Phys. Rev. E*, vol. 52, pp. 1734–1742, 1995.

[159] P. Espanol and P. Warren, "Statistical-mechanics of Dissipative Particle Dynamics," *Europhys. Lett.*, vol. 30, pp. 191–196, 1995.

[160] X. W. Shan and H. D. Chen, "Lattice Boltzmann model for simulating flows with multiple phases and components," *Phys. Rev. E*, vol. 47, pp. 1815–1819, 1993.

[161] G. Mcnamara and G. Zanetti, "Use of the Boltzmann-equation to simulate lattice-gas automata," *Phys. Rev. Lett.*, vol. 61, pp. 2332–2335, 1988.

[162] X. He and L. Luo, "Theory of the lattice Boltzmann method: From the Boltzmann equation to the lattice Boltzmann equation," *Phys. Rev. E*, vol. 56, pp. 6811–6817, 1997.

[163] A. Malevanets and R. Kapral, "Mesoscopic model for solvent dynamics," *J. Chem. Phys.*, vol. 110, pp. 8605–8613, 1999.

[164] A. Malevanets and R. Kapral, "Solute Molecular Dynamics in a mesoscale solvent," *J. Chem. Phys.*, vol. 112, pp. 7260–7269, 2000.

[165] H. Noguchi, N. Kikuchi, and G. Gompper, "Particle-based mesoscale hydrodynamic techniques," *EPL*, vol. 78, p. 10005, 2007.

[166] I. O. Goetze, H. Noguchi, and G. Gompper, "Relevance of angular momentum conservation in mesoscale hydrodynamics simulations," *Phys. Rev. E*, vol. 76, p. 046705, 2007.

[167] A. Lamura, G. Gompper, T. Ihle, and D. Kroll, "Multi-particle collision dynamics: Flow around a circular and a square cylinder," *Europhys. Lett.*, vol. 56, pp. 319–325, 2001.

[168] A. Lamura and G. Gompper, "Numerical study of the flow around a cylinder using multi-particle collision dynamics," *Eur. Phys. J. E*, vol. 9, pp. 477–485, 2002.

[169] M. Ripoll, R. G. Winkler, and G. Gompper, "Hydrodynamic screening of star polymers in shear flow," *Eur. Phys. J. E*, vol. 23, pp. 349–354, 2007.

[170] J. Dont, G. Gompper, P. Lang, D. Richter, M. Ripoll, and R. Willbold, *Macromolecular Systems in Soft and Living Matter*. Forschungszentrum Jülich GmbH, 2011.

[171] L. Verlet, "Computer "experiments" on classical fluids. i. thermodynamical properties of Lennard-Jones molecules," *Phys. Rev.*, vol. 159, pp. 98–103, 1967.

[172] M. Ripoll, K. Mussawisade, R. G. Winkler, and G. Gompper, "Dynamic regimes of fluids simulated by multiparticle-collision dynamics," *Phys. Rev. E*, vol. 72, p. 016701, 2005.

[173] J. K. Whitmer and E. Luijten, "Fluid-solid boundary conditions for multiparticle collision dynamics," *J. Phys.: Condens. Matter*, vol. 22, p. 104106, 2010.

[174] T. Ihle and D. Kroll, "Stochastic rotation dynamics: A Galilean-invariant mesoscopic model for fluid flow," *Phys. Rev. E*, vol. 63, p. 020201, 2001.

[175] M. Hecht, J. Harting, T. Ihle, and H. Herrmann, "Simulation of claylike colloids," *Phys. Rev. E*, vol. 72, p. 011408, 2005.

[176] C. C. Huang, A. Chatterji, G. Sutmann, G. Gompper, and R. G. Winkler, “Cell-level canonical sampling by velocity scaling for multiparticle collision dynamics simulations,” *J. Comput. Phys.*, vol. 229, pp. 168–177, 2010.

[177] E. Allahyarov and G. Gompper, “Mesoscopic solvent simulations: Multiparticle-collision dynamics of three-dimensional flows,” *Phys. Rev. E*, vol. 66, p. 036702, 2002.

[178] G. Gompper, T. Ihle, D. M. Kroll, and R. G. Winkler, “Multi-particle collision dynamics - a particle-based mesoscale simulation approach to the hydrodynamics of complex fluids,” *Adv. Polym. Sci.*, vol. 221, p. 1, 2009.

[179] E. Lauga and C. Cossu, “A note on the stability of slip channel flows,” *Physics of Fluids*, vol. 17, p. 088106, 2005.

[180] A. Malevanets and R. Kapral, “Mesoscopic model for solvent dynamics,” *J. Chem. Phys.*, vol. 110, pp. 8605–8613, 1999.

[181] A. Malevanets and R. Kapral, “Solute Molecular Dynamics in a mesoscale solvent,” *J. Chem. Phys.*, vol. 112, pp. 7260–7269, 2000.

[182] T. Ihle and D. M. Kroll, “Stochastic rotation dynamics. i. formalism, Galilean invariance, and Green-Kubo relations,” *Phys. Rev. E*, vol. 67, p. 066705, 2003.

[183] T. Ihle and D. M. Kroll, “Stochastic rotation dynamics. ii. transport coefficients, numerics, and long-time tails,” *Phys. Rev. E*, vol. 67, p. 066706, 2003.

[184] T. Ihle, E. Tüzel, and D. M. Kroll, “Equilibrium calculation of transport coefficients for a fluid-particle model,” *Phys. Rev. E*, vol. 72, p. 046707, 2005.

[185] H. Noguchi and G. Gompper, “Transport coefficients of off-lattice mesoscale-hydrodynamics simulation techniques,” *Phys. Rev. E*, vol. 78, p. 016706, 2008.

[186] S. Y. Liem, D. Brown, and J. H. R. Clarke, “Molecular Dynamics simulations on distributed memory machines,” *Comput. Phys. Commun.*, vol. 67, pp. 261 – 267, 1991.

[187] D. Brown, J. H. R. Clarke, M. Okuda, and T. Yamazaki, “A domain decomposition parallelization strategy for Molecular Dynamics simulations on distributed memory machines,” *Comput. Phys. Commun.*, vol. 74, pp. 67 – 80, 1993.

[188] G. Sutmann, R. Winkler, and G. Gompper, “Simulating hydrodynamics of complex fluids: Multi-Particle Collision Dynamics coupled to Molecular Dynamics on massively parallel computers.” (in preparation).

[189] A. Bray, “Theory of phase-ordering kinetics,” *Advances in Physics*, vol. 43, pp. 357–459, 1994.

[190] E. D. Siggia, “Late stages of spinodal decomposition in binary-mixtures,” *Phys. Rev. A*, vol. 20, pp. 595–605, 1979.

[191] H. Furukawa, “Effect of inertia on droplet growth in a fluid,” *Phys. Rev. A*, vol. 31, pp. 1103–1108, 1985.

[192] H. Furukawa, “Role of inertia in the late stage of the phase separation of a fluid,” *Physica A*, vol. 204, pp. 237–245, 1994.

[193] V. Kendon, M. Cates, I. Pagonabarraga, J. Desplat, and P. Bladon, “Inertial effects in three-dimensional spinodal decomposition of a symmetric binary fluid mixture: a lattice Boltzmann study,” *Journal Of Fluid Mechanics*, vol. 440, pp. 147–203, 2001.

[194] V. Kendon, J. Desplat, P. Bladon, and M. Cates, “3D spinodal decomposition in the inertial regime,” *Phys. Rev. Lett.*, vol. 83, pp. 576–579, 1999.

[195] L. Yelash, P. Virnau, W. Paul, K. Binder, and M. Mueller, “Spinodal decomposition of polymer solutions: A parallelized Molecular Dynamics simulation,” *Phys. Rev. E*, vol. 78, p. 031801, 2008.

[196] M. Grant and K. Elder, “Spinodal decomposition in fluids,” *Phys. Rev. Lett.*, vol. 82, pp. 14–16, 1999.

[197] T. Hashimoto, “Small-angle neutron scattering studies of dynamics and hierarchical pattern formation in binary mixtures of polymers and small molecules,” *J. Polym. Sci., Part B: Polym. Phys.*, vol. 42, pp. 3027–3062, 2004.

[198] H. Furukawa, “Spinodal decomposition of two-dimensional fluid mixtures: A spectral analysis of droplet growth,” *Phys. Rev. E*, vol. 61, pp. 1423–1431, 2000.

[199] M. Miguel, M. Grant, and J. Gunton, “Phase-separation in 2-dimensional binary fluids,” *Phys. Rev. A*, vol. 31, pp. 1001–1005, 1985.

[200] J. Farrell and O. Valls, “Spinodal decomposition in a two-dimensional fluid model,” *Phys. Rev. B*, vol. 40, pp. 7027–7039, 1989.

[201] J. Farrell and O. Valls, “Spinodal decomposition in a 2-dimensional fluid model - heat, sound, and universality,” *Phys. Rev. B*, vol. 42, pp. 2353–2362, 1990.

[202] H. Tanaka and T. Araki, “Phase inversion during viscoelastic phase separation: Roles of bulk and shear relaxation moduli,” *Phys. Rev. Lett.*, vol. 78, pp. 4966–4969, 1997.

[203] A. Wagner and J. Yeomans, “Breakdown of scale invariance in the coarsening of phase-separating binary fluids,” *Phys. Rev. Lett.*, vol. 80, pp. 1429–1432, 1998.

[204] D. Reith, K. Bucior, L. Yelash, P. Virnau, and K. Binder, “Spinodal decomposition of polymer solutions: Molecular Dynamics simulations of the two-dimensional case,” *J. Phys.: Condens. Matter*, vol. 24, p. 115102, 2012.

[205] H. Chen and A. Chakrabarti, “Hydrodynamic effects on domain growth in off-critical polymer blends,” *J. Chem. Phys.*, vol. 108, pp. 6006–6013, 1998.

[206] J. Lauger, R. Lay, and W. Gronski, “The percolation-to-cluster transition during spinodal decomposition of an off-critical polymer mixture - observation by light-scattering and optical microscopy,” *J. Chem. Phys.*, vol. 101, pp. 7181–7184, 1994.

[207] B. Crist, “On "pinning” domain growth in two-phase polymer liquids,” *Macromolecules*, vol. 29, pp. 7276–7279, 1996.

[208] S. Das, S. Puri, J. Horbach, and K. Binder, “Spinodal decomposition in thin films: Molecular-Dynamics simulations of a binary Lennard-Jones fluid mixture,” *Phys. Rev. E*, vol. 73, p. 031604, 2006.

[209] M. J. A. Hore and M. Laradji, “Dissipative particle dynamics simulation of the interplay between spinodal decomposition and wetting in thin film binary fluids,” *J. Chem. Phys.*, vol. 132, p. 024908, 2010.

[210] L. V. Kale, E. Bohm, C. L. Mendes, T. Wilmarth, and G. Zheng, “Programming Petascale Applications with Charm++ and AMPI,” in *Petascale Computing: Algorithms and Applications* (D. Bader, ed.), pp. 421–441, Chapman & Hall / CRC Press, 2008.

[211] S. J. Mitchell and D. P. Landau, "Phase separation in a compressible 2D Ising model," *Phys. Rev. Lett.*, vol. 97, p. 025701, 2006.

[212] K. Mecke, "Morphological characterization of patterns in reaction-diffusive systems," *Phys. Rev. E*, vol. 53, p. 4794, 1996.

[213] K. Mecke, "Morphological characterization of spinodal decomposition kinetics," *Eur. Phys. J. B*, vol. 8, p. 99, 1999.

[214] K. Binder, "Theory for dynamics of clusters. II. critical diffusion in binary-systems and kinetics of phase separation," *Phys. Rev. B*, vol. 15, pp. 4425–4447, 1977.

[215] Y. Sun and Y. Xia, "Shape-controlled synthesis of gold and silver nanoparticles," *Science*, vol. 298, pp. 2176–2179, 2002.

[216] S. Chen, Z. L. Wang, J. Ballato, S. H. Foulger, and D. L. Carroll, "Monopod, bipod, tripod, and tetrapod gold nanocrystals," *Journal of the American Chemical Society*, vol. 125, pp. 16186–16187, 2003.

[217] S. N. Fejer, D. Chakrabarti, and D. J. Wales, "Self-assembly of anisotropic particles," *Soft Matter*, vol. 7, pp. 3553–3564, 2011.

[218] D. V. Talapin, E. V. Shevchenko, M. I. Bodnarchuk, X. Ye, J. Chen, and C. B. Murray, "Quasicrystalline order in self-assembled binary nanoparticle superlattices," *Nature*, vol. 461, pp. 964–967, 2009.

[219] L. Manna, E. Scher, and A. Alivisatos, "Synthesis of soluble and processable rod-, arrow-, teardrop-, and tetrapod-shaped CdSe nanocrystals," *J. Am. Chem. Soc.*, vol. 122, pp. 12700–12706, 2000.

[220] L. Manna, D. Milliron, A. Meisel, E. Scher, and A. Alivisatos, "Controlled growth of tetrapod-branched inorganic nanocrystals," *Nat. Mater.*, vol. 2, pp. 382–385, 2003.

[221] D. W. Sinkovits, S. A. Barr, and E. Luijten, "Rejection-free Monte Carlo scheme for anisotropic particles," *J. Chem. Phys.*, vol. 136, p. 144111, 2012.

[222] D. W. Sinkovits and E. Luijten, "Nanoparticle-Controlled Aggregation of Colloidal Tetrapods," *Nano Lett.*, vol. 12, pp. 1743–1748, 2012.

[223] J. Liu, N. B. Wilding, and E. Luijten, "Simulation of phase transitions in highly asymmetric fluid mixtures," *Phys. Rev. Lett.*, vol. 97, p. 115705, 2006.

[224] D. J. Ashton, J. Liu, E. Luijten, and N. B. Wilding, "Monte Carlo cluster algorithm for fluid phase transitions in highly size-asymmetrical binary mixtures," *J. Chem. Phys.*, vol. 133, p. 194102, 2010.

[225] D. J. Ashton, N. B. Wilding, and P. Sollich, "Fluid phase coexistence and critical behavior from simulations in the restricted Gibbs ensemble," *J. Chem. Phys.*, vol. 132, p. 074111, 2010.

[226] J. A. Anderson, C. D. Lorenz, and A. Travesset, "General purpose Molecular Dynamics simulations fully implemented on graphics processing units," *J. Comput. Phys.*, vol. 227, pp. 5342 – 5359, 2008.